Tuning the Spin-Orbit Coupling and the Spin Dynamics of Atomic Chains on Superconductors

Dissertation

zur Erlangung des Doktorgrades
an der Fakultät für Mathematik, Informatik und
Naturwissenschaften im Fachbereich Physik
der Universität Hamburg

vorgelegt von

Philip Beck

aus Hamburg

- Hamburg, 2022 -

GUTACHTER DER DISSERTATION:

Prof. Dr. R. Wiesendanger

PD Dr. J. Wiebe

VORAUSSICHTLICHE MITGLIEDER DER PRÜFUNGSKOMMISSION:

Prof. Dr. R. Wiesendanger

PD Dr. J. Wiebe

Prof. Dr. T. Wehling

Prof. Dr. N. Huse

Prof. Dr. M. Potthoff

DATUM DER DISPUTATION:

28.10.2022

VORSITZENDER DER PRÜFUNGSKOMMISSION:

Prof. Dr. M. Potthoff

VORSITZENDER DES PROMOTIONSAUSSCHUSSES:

Prof. Dr. W. J. Parak

DEKAN DER MIN-FAKULTÄT:

Prof. Dr.-Ing. N. Ritter

Abstract

The ever-growing demand for high-performance computational power can no longer be met by the miniaturization of existing Si-based integrated circuit technology. New approaches that replace the electrical charge as the information carrier such as nanospintronics or overall new computing schemes such as quantum computation are promising technological routes to address these issues and are at the heart of modern physics research. While research towards quantum computation has made large leaps forward in recent years, it also became apparent that the decoherence time of the so-far realized qubits is too short. A heavily pursued approach to solve this issue is the use of topologically protected qubits that rely on exotic non-Abelian Majorana bound states (MBS), which can be realized as excitations in condensed-matter systems e.g. at the boundaries of topological superconductors.

This Ph.D. thesis addresses the experimental realization and fundamental properties of both technological concepts (nanospintronics and topological qubits) in the platform of artificial atomic spin chains assembled on the surfaces of *s*-wave superconductors. The methods of scanning tunneling microscopy (STM) and - spectroscopy (STS) are employed to construct such chains and different operational modes are used to investigate their magnetic and electronic properties as well as their spin dynamics. The experiments are carried out in a setup with a base temperature of 320 mK and an external magnet capable of applying a 12 T magnetic field.

Three material systems are investigated in the course of this thesis in order to determine suitable properties for the realization of MBS in spin chains on superconductors. These properties are closely linked to the local bound states that magnetic adatoms induce in superconductors — Yu-Shiba-Rusinov (YSR) states — as well as their magnetic and electronic

interactions in ensembles of multiple adatoms, which give rise to Shiba bands. The first material platform investigated in this thesis are single adatoms, artificial dimers, and chains of Mn adatoms on Nb(110). The platform is characterized by an unprecedented energy resolution in STS experiments and a highly reproducible control and fabrication of nanostructures tailored from individual adatoms. This enables the indirect observation of Shiba band formation in momentum space and reveals the effect of SOC on these bands — a topological gap in a Shiba band. The experiments reveal that a low SOC is the limiting factor, preventing the realization of a large topological gap hosting isolated MBS in this material platform.
A comparative study on similar Mn structures on Ta(110) is performed to further investigate the role of SOC, which is enabled by the fact that the main significant differences between niobium and tantalum are their atomic masses and their SOC strengths. A comparison of similar Mn chains and Shiba bands on both substrates reveals that the size of the topological gap can indeed be increased by heavy substrates.
This highlights that proximitized films of a high-Z layer on Nb(110) can be ideal substrates for Shiba chains to realize isolated MBS, which is the third material platform investigated in this thesis. It is demonstrated that Fe chains on one atomic layer of Au on Nb(110) can be tailored into a single Shiba band regime.
Last, the spin dynamics of antiferromagnetically coupled spin chains on Ta(110) are investigated using time-resolved spin-polarized STM. By tuning external parameters, such as the magnetic field, we drive the system from the quasiclassical case into the decoupled quantum limit, where the chain is largely decoupled from itinerant quasiparticles of the metallic substrate by the superconducting gap. We conclude that spin chains on superconductors are promising systems for future studies of quantum coherence effects.

Zusammenfassung

Die immer zunehmende Nachfrage nach höherer Rechenleistung kann nur noch bedingt durch eine Verkleinerung von lithographisch hergestellten integrierten Schaltkreisen gestillt werden. Neue Ansätze schlagen daher vor, die elektrische Ladung durch den Elektronenspin als Informationsträger zu ersetzen (Nanospintronik) oder aber quantenmechanische Zustände zur Informationsverarbeitung zu nutzen (Quantencomputer). Die Erabeitung solcher Konzepte ist zu einem der wichtigsten Forschungsschwerpunkte der modernen Festkörperphysik geworden. In den letzten Jahren wurden erhebliche Fortschritte hinsichtlich des Baus von Quantencomputern erzielt. Allerdings hat sich herausgestellt, dass die Kohärenzzeiten von gängigen Qubits zu kurz sind. Daher wird mit Nachdruck an topologisch geschützten Qubits geforscht, welche die nicht-Abelschen Eigenschaften von sogenannten Majorana-Moden (MM) nutzen sollen. Im Forschungsbereich der kondensierten Materie wurde das Auftreten solcher Moden an den Grenzflächen von topologischen Supraleitern vorhergesagt.
Diese Dissertation befasst sich mit beiden obengenannten Konzepten (Nanospintronik und MM) durch die Erforschung von atomaren Spinketten auf den Oberflächen von konventionellen Supraleitern. Die atomaren Ketten werden mit Hilfe eines Rastertunnelmikroskops (RTM) fabriziert — künstliche Strukturen werden Atom für Atom mit der Spitze des RTM gebaut — und anschließend mittels Rastertunnelspektroskopie untersucht. Zusätzlich werden magnetische Spitzen eingesetzt, um Spin-sensitive und zeitabhängige Messungen der elektronischen Struktur durchzuführen. Die Experimente wurden in einem RTM mit einer Basistemperatur von 320 mK und einem supraleitenden Magneten (< 12 T) durchgeführt. Im Rahmen dieser Arbeit wurden drei verschieden Probensysteme untersucht um günstige Eigenschaften einer Spinkette hinsichtlich der Realisie-

rung von MM zu finden. Diese Eigenschaften werden vor allem bestimmt durch die lokal gebundenen Zustände, welche magnetische Verunreinigungen auf Supraleitern induzieren — sogenannte Yu-Shiba-Rusinov (YSR) Zustände — und von deren elektronischen und magnetischen Wechselwirkungen in größeren künstlichen Strukturen, wodurch sogenannte Shiba-Bänder entstehen. Zunächst werden einzelne Mn Adatome, künstliche Dimere und Ketten aus Mn auf Nb(110) untersucht. Diese Plattform ermöglicht insbesondere die Herstellung von defektfreien atomaren Spinketten und eine hervorragende Energieauflösung bei der spektroskopischen Untersuchung dieser Ketten, was bei bisherigen Systemen nicht möglich war. Diese Vorzüge erlauben eine indirekte Messung der Bandstruktur von eindimensionalen Ketten im Impulsraum, wodurch das Auftreten einer topologischen Energielücke in einem Shiba-Band nachgewiesen werden konnte. Allerdings zeigen die Experimente auch, dass die Spin-Bahn-Kopplung (SBK) in diesem System zu niedrig ist, um eine genügend große topologische Energielücke zu erzeugen, die isolierte MM beherbergt.
Um den Einfluss der SBK auf Shiba-Bänder zu untersuchen, wird eine Vergleichsstudie mit strukturell identischen Mn Ketten auf Ta(110) durchgeführt. Da Niob und Tantal sehr ähnliche physikalische Eigenschaften haben, mit Ausnahme der atomaren Massenzahl und der SBK, können Änderungen der Shiba-Bandstruktur auf eben diese Größen zurückgeführt werden. So wird experimentell gezeigt, dass die Größe der topologischen Bandlücke in der Tat von der Stärke der SBK abhängt.
Diese Erkenntnis zeigt, dass ultradünne Filme schwerer metallischer Elemente (z.B. Gold oder Iridium), welche auf Nb(110) epitaktisch gewachsen werden, vielversprechende Substrate zur Realisierung von isolierten MM in Shiba-Ketten sind, da diese eine hohe SBK mit der großen Energielücke des Niobs vereinen. Solche Substrate sind die dritte Materialplattform, die in dieser Arbeit untersucht wird. Es wird gezeigt, dass es möglich ist, defektfreie eindimensionale Spinketten auf solchen Heterostrukturen zu konstruieren, die exakt ein niedrigenergetisches

dispersives Shiba-Band besitzen.
Des weiteren wird die Dynamik von antiferromagnetischen Spinketten auf Supraleitern mit zeitaufgelöster Spin-sensitiver RTM untersucht. Es konnte gezeigt werden, dass die Spinkette durch Ändern des Magnetfeldes von einen quasiklassischen Néel-Zustand in einen Quantenspinzustand überführt werden kann, bei dem die Spins durch die Energielücke des Substrats weitestgehend von den Substratelektronen abgekoppelt sind. Zukünftig könnten mit solchen Spinketten daher interessante Quantenkohärenz-Experimente durchgeführt werden.

Contents

Abbreviations

DFT	density functional theory
DM	Dzyaloshinskii-Moriya
DOS	density of states
fcc	face-centered cubic
hcp	hexagonal close-packed
FFT	fast Fourier transformation
KKR	Korringa-Kohn-Rostoker
LDOS	local density of states
QPI	quasiparticle interference
RKKY	Ruderman-Kittel-Kasuya-Yosida
rms	root mean square
SP-STM	spin-polarized scanning tunneling microscopy
SP-STS	spin-polarized scanning tunneling spectroscopy
SOC	spin-orbit coupling
STM	scanning tunneling microscope
STS	scanning tunneling spectroscopy
TMR	tunnel magnetoresistance
UHV	ultra-high vacuum
MBS	Majorana bound states
YSR	Yu-Shiba-Rusinov
1D	one-dimensional
2D	two-dimensional
FM	ferromagnetically
AFM	antiferromagnetically

TBM	tight-binding model
MSH	magnet-superconductor hybrid
2DEG	two-dimensional electron gas
ARPES	angle-resolved photoemission spectroscopy
SC	superconductivity
SIS	superconductor-insulator-superconductor
BCS	Bardeen-Cooper-Schrieffer
N	normal metal
N/S	normal metal-superconductor
BdG	Bogoliubov-de-Gennes
PMMs	precursors of Majorana modes
MMs	Majorana modes
TSC	topological superconductivity
VASP	Vienna Ab-initio Simulation Package
LEED	low-energy electron diffraction
ML	monolayer
VT-STM	variable-temperature scanning tunneling microscope
bcc	body-centered cubic
fcc	face-centered cubic
MARs	multiple Andreev reflections
XMCD	X-ray magnetic circular dichroism
ESR	electron spin resonance
MAE	magnetic anisotropy energy

1 Introduction

In order to handle the ever-growing demand for high-performance computational power of industrial and scientific applications, an increasing amount of supercomputers with higher performances are continuously being built[1]. As those facilities consume huge amounts of electrical power for processing and cooling[2] — in 2006 data center computing made up 1.5 % of the total U.S. electricity consumption[3] — physical sciences have undergone a quest to develop novel and more efficient classical computing schemes[4] as well as completely new approaches such as quantum computation[5]. The latter offers a pathway to solve certain optimization problems considerably faster and more efficient than conventional computers can. Furthermore, simulations of quantum mechanical systems that are currently way out of reach due to their complexity, may be envisioned[6]. While significant steps forward are being made using superconducting qubits to construct an universal quantum computer[7], no ideal general purpose qubit platform has emerged so far, which is partly related to the varying technical requirements depending on the specific anticipated use (universal quantum computer, quantum simulator, quantum annealing etc.)[5]. One issue which unites current technologies is the interaction of qubits with their environment, leading to the decoherence of the quantum states.

A so far only theoretically proposed idea to address this issue is topological quantum computation[8,9]. In recent years topology has emerged as a key concept in condensed matter physics[10]. In particular, it states that a given system with a non-trivial topology in the bulk must have boundary modes at the edges/surfaces of the system, as enforced by the bulk-boundary correspondence[11]. Hence, these states are protected by

the topology of a given system and are not destroyed by small perturbations.
A beautiful example are quantum wells of CdTe-HgTe-CdTe, where the inner material (HgTe) has an inverted band gap with respect to the outer material (CdTe), making them topologically distinct. Therefore, helical edge states must appear at the interfaces and must display the quantum spin Hall effect[12–14]. For the purpose of topological quantum computation a special kind of boundary modes, called Majorana bound states (MBS), are required, which are predicted to occur on the boundaries of topological superconductors. The trait which makes them desirable for topological quantum computation is the fact that MBS are neither fermions nor bosons, but non-Abelian anyons. Upon exchanging two particles, the former two (fermions and bosons) are characterized by a multiplication of the wavefunction with a phase factor. However, considering the latter type (non-Abelian anyons), the wavefunction is multiplied by a unitary matrix, which is an operation that does not commute. Hence, after interchanging two MBS twice the final state will not be the initial state[15,16]. If one could realize a device where it is possible to exchange multiple MBS, one could change the system between multiple degenerate ground states and thereby encode and process quantum information without the aforementioned problems of decoherence that conventional computation schemes are struggling with[8].
Multiple solid-state systems have been proposed to host topological superconductivity (TSC) and MBS, most of which include a spin-polarized one-dimensional (1D) or two-dimensional (2D) system which is subject to large spin-orbit coupling (SOC) and is proximitized by an s-wave superconductor[17,18]. Some examples are a strong topological insulator coupled to an $s-$wave superconductor[17,19,20], materials with a Dirac-like surface state being intrinsically superconducting[21–24], semiconductor nanowires proximity coupled to an s-wave superconductor exposed to an external B-field[25–31] and magnetic chains on s-wave superconductors[32–39].

Although many experimental works suggest the observation of MBS in this variety of systems, the clear unambiguous demonstration of a MBS in a hard topological gap is still lacking. In fact the field has recently undergone many controversies on experiments claiming the observation of MBS or some of their key signatures[40] (see for example the retraction of a paper on the quantized conductance in semiconductor nanowires[41] or reproducibility issues of the same platform[42,43]). Furthermore, publications on Fe(Te,Se) are suspected to only show cherry-picked data[44] following a novel study indicating that trivial bound states of magnetic impurities might be the origin for the observed physics after all[24].
In this thesis I focus on the approach of 1D magnetic chains on *s*-wave superconductors, which are investigated using a scanning tunneling microscope (STM) and scanning tunneling spectroscopy (STS)[45,46]. This technique enables the imaging of surfaces with high vertical and lateral resolution on the atomic scale and can even include magnetic contrast on this scale, if spin-polarized tips are used[47,48]. The method is then referred to as spin-polarized scanning tunneling microscopy (SP-STM), which can also be employed to record magnetic signals in the time domain giving rise to measurements of the spin dynamics of nanomagnets[49–51]. Furthermore, STS enables spatially resolved measurements of the local density of states (LDOS) as a function of energy, using the spectroscopic mode. Employing the method of STM tip-induced atom manipulation[52], it is possible to construct atomically precise nanostructures in an atom-by-atom approach. Therefore, one can study artificial structures which are free from defects and impurities, providing another advantage over other static measurement methods.
Following the original proposals to realize MBS in magnetic adatom chains deposited on *s*-wave superconductors[32–34,36–38], a tremendous experimental effort to craft such model systems and study them using STM and STS has started. Initially, it was found that chains of Fe/Pb(110) and Fe/Re(0001) display first indications of MBS in STS measurements[53–57] — zero-energy states localized on the chain's edges. However, the former

system of self-organized Fe chains on Pb(110) suffers from an unclear chain geometry, intermixing of Fe and Pb, and the lacking reproducibility of MBS signatures, which are only observed for few chains[54]. While the latter sample system Fe/Re(0001) resolves this issue through a fabrication of the adatom chains using STM tip-induced atom manipulation, the low critical temperature of Re makes it difficult to clearly pinpoint the physical origin of spectroscopic features[55,58]. Consequently, new material systems hosting structurally well-defined magnetic chains produced by STM tip-induced atom manipulation with a large *s*-wave gap of the substrate are required to enable the unambiguous identification of in-gap features in STS measurements.
As I will show in this thesis, recent experimental work demonstrates that the use of Nb(110) as the substrate for magnetic chains resolves both issues[59–63]. However, it was also shown that the SOC strength might be too low in the investigated structures to open large topological gaps in all relevant bands (see Section 4.2). Therefore, it is the primary aim of this thesis to gain an understanding on the role of SOC in magnetic adatom chains and to develop routes and techniques which increase the SOC in these structures. Additionally, we perform first time-resolved SP-STM measurements to characterize the spin dynamics of magnetic adatom chains coupled to a superconductor.
The basic theoretical concepts and models which are used throughout this thesis are introduced in Chapter 2, where I focus on the two phenomena of magnetism and superconductivity. The discussion of their interplay at the atomic scale, which gives rise to Yu-Shiba-Rusinov (YSR) states as well as the coupling of YSR states to Shiba bands in chains and their topological properties are in the focus of the first half of the chapter. Theoretical consideration of the spin dynamics of antiferromagnetically (AFM) coupled magnetic chains on superconducting and metallic substrates make up the second part of this chapter.
Chapter 3 is an introduction to the aforementioned powerful experimental tools of STM and STS, where I lay the physical foundation for both

methods and I present the two experimental setups that are used throughout this thesis. Additionally, I introduce the ultra-high vacuum (UHV)-based sample preparation of Ta(110) and Nb(110), using the former as an example. Afterwards, I demonstrate the reproducibility of STM tip-induced atom manipulation for Mn adatoms on Ta(110).
The experimental results are separated into two chapters which deal with different physical properties of artificial magnetic adatom chains on superconducting substrates. In general, Chapter 4 presents multiple STM and STS studies on the YSR states and Shiba bands of single magnetic adatoms, artificial dimers and chains on *s*-wave superconductors, where each section focuses on one particular effect related to SOC. To begin with, I reveal a SOC-induced effect in the YSR states of AFM coupled dimers of Mn on Nb(110). Afterwards, I present two examples of chains using the same material platform, where SOC is definitely present, but eventually it is too low to observe MBS in a hard topological gap. The successive sections present novel approaches which may increase SOC by engineering special chain geometries or by using high-Z materials as the substrate, which are superconducting themselves or by proximity to another material. Indeed I demonstrate that the latter two approaches are promising, as it is possible to increase the topological gap size of Shiba bands by choosing a high-Z substrate and since it is possible to tailor defect-free single Shiba band systems on a proximitized thin film.
The second experimental chapter (Chapter 5) is devoted to measuring the spin dynamics of AFM coupled magnetic chains on Ta(110) using the random telegraph noise method[49,50]. Since Ta is a type-I superconductor we can abruptly switch the substrate from it superconducting state to the metallic phase by applying an external B-field. Different types of STM tips and a clever engineering of their magnetic state enables us to investigate adatom chains in different limits i.e. the quantum case where the chain is largely screened from any external perturbations and the quasiclassical case where the chain collapses into a bistable magnetic ground state[64,65].

2 Theoretical background

This chapter introduces the basic theoretical concepts and models, which are necessary to understand the motivation and experimental approach of the work presented in this thesis. I begin by presenting single atom magnetism, in particular focusing on magnetic anisotropy, the exchange coupling between impurities and the origin/role of SOC in Section 2.1. Afterwards, I proceed with the introduction of another major physical property relevant to this thesis, namely superconductivity (SC). In particular, Section 2.2 introduces the phenomenology of SC, the microscopic origin and the proximity effect. The section is concluded by covering essential physical properties of magnet-superconductor hybrid (MSH) structures in the limit of single atoms and 1D chains, which are the basis for a large extent of this thesis. Section 2.3 is a short introduction on spin dynamics, which focuses on the magnetization switching in AFM coupled spin chains.

2.1. Single atom magnetism

Since the experimental approach discussed in this thesis is of bottom-up nature, it is quite instructive to start the discussion of magnetism at the single atom level: The electronic ground state of a not too heavy ($Z < 75$) multi-electron atom is obtained by following Hund's rules for the outermost shell, with decreasing priority of the rules[66,67]:

I the total spin momentum $|S| = |\sum m_s|$ is maximized

II the orbital momentum $|L| = |\sum m_l|$ is maximized and

III if the shell is half-filled or less, L and S couple antiparallel ($J = |L - S|$) or in the other case they couple parallel ($J = |L + S|$).

To calculate the total magnetic moment $\hat{\mathbf{m}}$ of a given species, one adds up the contributions of total orbital angular momentum $\mathbf{L}$ and total spin momentum $\mathbf{S}$ to obtain the total angular momentum $\mathbf{J} = \mathbf{L} + \mathbf{S}$, which in turn can be plugged into

$$\mathbf{m} = g\mu_B \mathbf{J}, \tag{2.1}$$

where $\mu_B = \frac{e}{2m_e}\hbar \approx 5.79 \cdot 10^{-5}\,\mathrm{eV/T}$ is the Bohr magneton and g is the Landé or g-factor given by

$$g = \frac{3}{2} + \frac{1}{2}\frac{S(S+1) - L(L+1)}{J(J+1)}, \tag{2.2}$$

which reduces to $g = 1$ for sole orbital momentum or to $g = 2$ for sole spin momentum[68,69]. However, this momentum is subject to change, once a single atom adsorbs on a solid surface, where a hybridization with the substrate may lead to charge transfer and the Coulomb interaction with the electronic environment of the substrate atoms leads to a crystal-field splitting of the magnetism-carrying $d-$ or $f-$orbitals[68].
As discussed above, the spin-related properties of multi-electron atoms or ions are usually described by the quantum mechanical states $|L, M_L\rangle$ and $|S, M_S\rangle$ for the orbital states and the spin states, respectively. In the case of a $3d$ transition metal atom adsorbed on a surface, where it is coordinated by the substrate atoms, the orbital momentum is typically largely quenched by the crystal field. The small remaining orbital momentum and SOC lead to a magnetic anisotropy of the system. Such systems are usually well described by an effective spin Hamiltonian with a multiplicity of $2S + 1$[70]. In the following, I will discuss two important contributions to such a Hamiltonian. In particular I will consider a Heisenberg Hamiltonian with

- magnetic anisotropy

- exchange interactions with neighboring spins,

while keeping a particular focus on the types of systems studied in this thesis. A more general overview, which does not focus on metallic surface magnetism and one-dimensional systems, can be found in textbooks as Ref. [68].

2.1.1. Magnetic anisotropy

A systematic way to describe the contributions to the magnetic anisotropy, including the particular coordination environment and symmetry of a magnetic atom, is provided by the Stevens operators, which have to be taken into account up to a certain order, depending on the particular system[71,72]. The simplest Hamiltonian for geometries with uniaxial symmetry is

$$\hat{H}_{\text{spin}} = D\hat{S}_z^2, \tag{2.3}$$

where $\hat{S}_z$ is the $z-$component spin operator. If the particular system has an orthorhombic distortion, as it is the case for a rhombic pyramidal geometry with a C_{2v} point group, an additional term

$$E(\hat{S}_x^2 - \hat{S}_y^2) \tag{2.4}$$

has to be added to the effective spin Hamiltonian of Equation 2.3. The relevant point groups of systems discussed in this thesis are C_{3v} (to lowest order only Equation 2.3) and C_{2v} (Equations 2.3 and 2.4)[70,73].
The effect of these terms on a spin system can be illustrated quite easily. E.g., if we neglect the transversal anisotropy term E and only consider the uniaxial term, then the constant D determines whether it is an easy-axis ($D < 0$) system or and easy-plane ($D > 0$) system.

2.1.2. Interactions between magnetic atoms

An intriguing consequence of the observation of magnetic order is that one has to treat it quantum mechanically to obtain a good understanding of its origin. This is apparent from the conclusion that single atoms/ions have magnetic moments on the order of μ_B. However, the dipolar interactions at spacings equal to typical lattice constants can not account for energy values of $\sim 300\,\mathrm{K}$, which would be required to explain the observation of room temperature ferromagnetism in a classical picture. Eventually, it was found that the responsible interaction for the strong coupling of magnetic moments is the quantum mechanical exchange interaction.
As an instructive approach to understand it origin, we can consider a two-atom system with two electrons, which results in a Hamiltonian with two kinetic energy terms and sums over the Coulomb interactions of each electron with each core and the other electron. In the latter case, the Coulomb interaction is given by $\hat{V}_C(\mathbf{r},\mathbf{r}') = \frac{e^2}{4\pi\epsilon_0|\mathbf{r}-\mathbf{r}'|}$, where ϵ_0 is the vacuum permittivity. The two electron wave function is then given by

$$\begin{aligned}\Psi(\mathbf{r},\mathbf{r}') = c_I\phi_L(\mathbf{r})\phi_L(\mathbf{r}') + c_{II}\phi_L(\mathbf{r})\phi_R(\mathbf{r}') \\ +c_{III}\phi_R(\mathbf{r})\phi_L(\mathbf{r}') + c_{IV}\phi_R(\mathbf{r})\phi_R(\mathbf{r}').\end{aligned} \tag{2.5}$$

The resulting Hamiltonian is a 4×4 matrix, where each element consists of multiple two-electron integrals. Apart from the hopping integral (commonly t), which evaluates the kinetic energy between two wave functions and which can be imagined as the tunneling of an electron from one Wannier wave function to the other, there are two important terms. To begin with, there is the Coulomb integral

$$U = \int\int \phi_L^*(\mathbf{r})\phi_L^*(\mathbf{r}')\hat{V}_C(\mathbf{r},\mathbf{r}')\phi_L(\mathbf{r})\phi_L(\mathbf{r}')\mathrm{d}V\mathrm{d}V' \tag{2.6}$$

and there is the direct exchange integral

$$J_D = \int\int \phi_L^*(\mathbf{r})\phi_R^*(\mathbf{r}')\hat{V}_C(\mathbf{r},\mathbf{r}')\phi_L(\mathbf{r}')\phi_R(\mathbf{r})\mathrm{d}V\mathrm{d}V'. \tag{2.7}$$

The former can be imagined in a classical framework, where it corresponds to the Coulomb repulsion of two electrons. The latter, however, has no intuitive meaning. A solution of the system for its eigenfunctions and eigenenergies, yields four solutions. By applying the Pauli principle, stating that the total wave function of a Fermion, including the spin wave function, which is not included in Equation 2.5, must be antisymmetric under exchange, we conclude that there are three solutions with symmetric orbital wave functions describing AFM ordered spins and one solution with an antisymmetric orbital wave function describing ferromagnetically (FM) aligned spins. The eigenenergies of these states are shown as a function of the hopping parameter t in Figure 2.1a. The exchange constant J is defined as half of the energy difference between the lowest-lying AFM state and the FM state, which is given by

$$J = J_D + \frac{U}{4} - \sqrt{t^2 + \frac{U^2}{16}}. \tag{2.8}$$

From this definition we find that $J > 0$ favors FM order and $J < 0$ favors AFM configurations.
In the Heisenberg model one neglects the two wave functions with doubly occupied orbitals (terms I and IV in Equation 2.5), due to their strong Coulomb repulsion (large U). One can then expand Equation 2.8 for small t/U and obtain

$$J = J_D - \frac{2t^2}{U}. \tag{2.9}$$

The aforementioned Coulomb interactions of the Hamiltonian, which act on the orbital part of the wave function, are summarized in the exchange constant J which is passed over to an effective spin Hamiltonian that

does not act on the orbital parts, but only on the spin part of the wave function.
Now that we have a general understanding of the exchange interaction's origin in two-atom systems, we can define a Heisenberg Hamiltonian[68,73]

$$\hat{H} = -2 \sum_{i>j} J_{ij} \hat{\mathbf{S}}_i \cdot \hat{\mathbf{S}}_j, \tag{2.10}$$

where we sum over all spins and their interactions, considering every interaction only once, which explains the origin of the factor 2. It should be noted that there are multiple ways to define the exchange energy and the sum in Equation 2.10, which can result in different factors and signs in the representation of the Hamiltonian.
Writing Equation 2.10 in its most general form, one obtains an exchange tensor, such that the Hamiltonian can be rewritten in a form where the different contributions to the exchange interaction are separated into the following terms

$$\hat{H} = \frac{1}{2} \sum_{i \neq j} J_{ij} \hat{\mathbf{S}}_i \cdot \hat{\mathbf{S}}_j + \frac{1}{2} \sum_{i \neq j} \mathbf{D}_{ij} \cdot (\hat{\mathbf{S}}_i \times \hat{\mathbf{S}}_j) + \frac{1}{2} \sum_{i \neq j} \hat{\mathbf{S}}_i \cdot J_{ij}^{\text{aniso}} \cdot \hat{\mathbf{S}}_j. \tag{2.11}$$

where J_{ij} is the isotropic exchange interaction, $\mathbf{D}_{ij}$ is the Dzyaloshinskii-Moriya (DM) vector and J_{ij}^{aniso} is the symmetric anisotropic exchange interaction[73,74].
The DM interaction plays an important role in systems with broken inversion symmetry and sizable SOC, while it is compensated in systems with inversion symmetry[75,76]. From its term in Equation 2.11, it is evident that it favors a perpendicular alignment of the spins, which depends on the orientation and strength of the DM vector $\mathbf{D}_{ij}$. Please note that the connection of the DM interaction and SOC is established in Subsection 2.1.3. Besides the frustration of exchange interactions between nearest and next-nearest neighboring spins[77–79], the DM interaction is the driving term for non-collinear magnetic ground states[80–84].

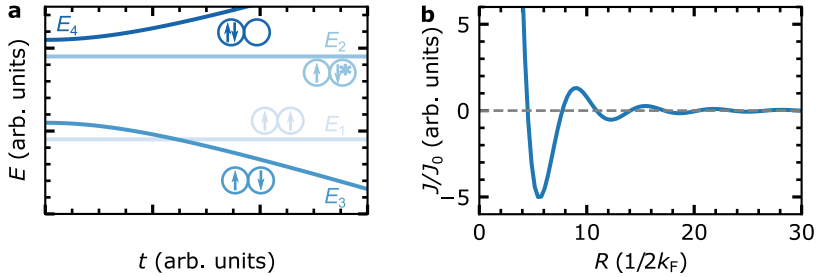

Figure 2.1.: a Eigenenergies of the two-atom system with two electrons, depending on the hopping parameter t, where the exchange integral J_D and the Coulomb integral U are constants. E_1 and E_3 are the lowest-lying FM- and AFM ground states used for the definition of the exchange energy J in Equation 2.8. **b** Distance dependence of the Ruderman-Kittel-Kasuya-Yosida (RKKY) interaction.

Another important aspect of the atomic interactions for the systems studied in this thesis are the different types of exchange interactions. So far, I discussed the direct exchange between two magnetic atoms. However, one should also consider possible superexchange which is mediated by an interstitial ion between the two spin-carrying atoms[85–87] and the RKKY interaction, which is mediated by the conduction electrons of the host[88–90]. The latter can be derived by treating a free electron gas with magnetic perturbations. In the framework of second order perturbation theory, one obtains a distance-dependent exchange coupling[68]

$$J(R) = J_0^2 \frac{2k_F R\cos(2k_F R) - \sin(2k_F R)}{(2k_F R)^4} \tag{2.12}$$

where R is the distance between the two interacting atoms, k_F is the Fermi wave vector of the conduction electron system and J_0 is the strength of the local exchange between the atom and the conduction electrons. This relation is illustrated in Figure 4.5b, where once can clearly see the oscillatory behavior of the exchange constant J, which has also been found in experiments[91,92]. In contrast to Equation 2.12, k_F is not isotropic in

real systems. Therefore, the RKKY contribution to the exchange coupling depends strongly on the crystallographic direction. The flexibility of the exchange which this direction- and distance-dependence offers, can be used to tailor non-collinear magnetic ground states as, e.g. spin spirals[93].

2.1.3. Spin-orbit coupling effects at metallic surfaces

As I will discuss in Section 2.2, SOC plays a crucial role for the phenomenon of topological superconductivity. Overall, there are multiple mechanisms contributing to SOC in solid state systems: contributions from atomic SOC , potential gradients at surfaces/interfaces leading to an effective SOC and intrinsic structural inversion symmetry breaking, which leads to SOC -like terms as well. I will discuss the origin of each mechanism in the following subsections. To get an instructive understanding of the topic, let us consider SOC from atomic contributions. In the succeeding section I will move on to discuss SOC in metallic systems and at interfaces. I conclude by linking SOC to the DM interaction.

Atomic origin of spin-orbit coupling

A mathematical approach to SOC is the derivation of the Pauli equation from the Dirac equation of an electron in a vector potential $\mathbf{A}$ in the non-relativistic limit, which is expressed by:

$$\begin{aligned}[\varepsilon + eV(\mathbf{x}) - \frac{1}{2m}(\hat{\mathbf{p}} + \frac{e}{c}\mathbf{A}(\mathbf{x}))^2 + \frac{1}{2m_0c^2}(\varepsilon + eV(\mathbf{x}))^2 \\ + i\frac{e\hbar}{(2m_0c)^2}\mathbf{E}(\mathbf{x})\cdot\hat{\mathbf{p}} - \mu_B\hat{\boldsymbol{\sigma}}\cdot\mathbf{B}(\mathbf{x}) - \frac{e\hbar}{(2m_0c)^2}\hat{\boldsymbol{\sigma}}\cdot(\hat{\boldsymbol{\nabla}}V\times\hat{\mathbf{p}})]\psi = 0\end{aligned} \tag{2.13}$$

Here $\epsilon = \epsilon' - m_0c^2$ is the particle energy reduced by the rest mass energy, c is the speed of light, V is a scalar potential, $\mathbf{A}$ is an external vector

potential, $\mathbf{E}(\mathbf{x})$ is the electric field, and $\hat{\boldsymbol{\sigma}}$ is the vector containing the Pauli spin matrices. For a detailed derivation see Ref.[11].
To extract the physical meaning of Equation 2.13, let us ascribe the terms to well known effects and discuss the remainder: The first three terms correspond to a regular Schrödinger equation which includes an external vector potential $\mathbf{A}$, while the next two terms can be considered as relativistic corrections to the Schrödinger equation which do not act on the spin. The following expression is the Zeeman term, which is well known from non-relativistic quantum mechanics. However, the last term is a novel type of interaction. It couples the electron's spin to its orbital motion, which is exactly the term describing SOC.
A common intuitive understanding of SOC in atomic physics is obtained by imagining that an electron is moving in the electric field $\mathbf{E} = \nabla V$ near the core of an atom in the global frame of reference. A relativistic Lorentz transformation to the electron's frame of reference gives rise to an effective $\mathbf{B}$ field, which in turn acts on the electron's spin. In atomic physics this effect explains the lifted degeneracy of, e.g., p states with $P_{3/2}$ and $P_{1/2}$, also known as the fine structure[94]. The size of the splitting between the two levels scales with $\propto Z^4$[11,69].

Spin-orbit coupling in metallic systems

From the previous subsection we have obtained the understanding that a potential gradient perpendicular to the momentum of an electron gives rise to an effective $\mathbf{B}$ field in the electron's frame of reference. If we look for such potential gradients in condensed matter systems, we can think of a two-dimensional electron gas (2DEG) in III-V heterostructures[95], or more generally surfaces and interfaces, where the space-inversion symmetry is always broken[96]. The SOC contributions, which are induced by such potential gradients at surfaces and interfaces are referred to as Rashba SOC.

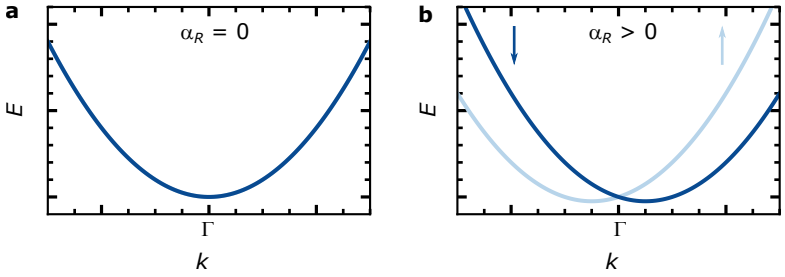

Figure 2.2.: a and **b** Eigenenergies of the Rashba Hamiltonian for a metallic surface state (Equation 2.14) without SOC ($\alpha_R = 0$) and for finite SOC ($\alpha_R > 0$), for any cut of the two-dimensional **k** space, that includes Γ. Color coded arrows indicate the spin of the band.

Let us now consider the example of a metallic surface state, where Rashba SOC gives rise to a Hamiltonian similar to the last term of Equation 2.13, which reduces to[97,98]

$$\hat{H}_R = \frac{\hbar^2 \mathbf{k}_\parallel^2}{2m^*} + \alpha_R(k_y\hat{\sigma}_x - k_x\hat{\sigma}_y). \tag{2.14}$$

Here, m^* is the effective electron mass in this band, $\mathbf{k}_\parallel = (k_x, k_y, 0)$ and α_R is the Rashba parameter, which accounts for the strength of the SOC. The effect of this term on a metallic surface state, considering a finite value of Rashba SOC , is shown in Figure 2.2. The parabolic bands of opposite spin are shifted in opposite directions of the **k**-space and their band bottom is offset compared to the case without SOC.
Therefore, the effect of SOC on band structures seems to be well known[99]. However, in reality it is challenging to predict the strength of SOC effects, i.e. to estimate the size of α_R prior to studying a given system experimentally. This is already evident from rather simple and well studied systems such as the surface states of Au(111) and Ag(111). For gold, the Rashba splitting of the surface state is observable in angle-resolved photoemis-

sion spectroscopy (ARPES) measurements[100,101], while it is not resolved for silver[102], which has a similar surface state. The potential gradient can be estimated by the potential change from the vacuum level to the bottom of the surface state band —approximated by the work function Φ — and the potential change occurs on a length scale of about the Fermi wavelength $\sim \lambda_F$, yielding $(\hat{\nabla} V)_z \sim \Phi/\lambda_F$[11]. Therefore, this effect can only explain a SOC-induced splitting of the surface state of Au(111) on the order of $\alpha_R |\mathbf{k}_\parallel| \sim 1 \cdot 10^{-6}$ µeV[11,103]. This is in strong contrast to the experimentally observed energy splitting of 110 meV at the Fermi wave vector of Au(111).

Furthermore, the difference of the atomic masses (Z values) between Ag and Au can not explain the drastically different size of the Rashba splitting, either. Eventually, it was found that it is rather the product of atomic SOC and the asymmetry of the wave function under consideration that is decisive[104]. For the case of Au(111) and Ag(111) it was shown that the difference in d_{z^2} admixture to the p_z-like surface state explains the drastically different SOC, as it is much larger for the Au(111) surface than for Ag(111). It was even shown, that in a single layer of Ag on Au(111), the Rashba splitting is expected to be enhanced, as the d states of the Au substrate induce a larger d_{z^2} character in the surface state[103].

In conclusion, the effect of SOC on a particular system such as a surface state splitting — or as I will show later, the opening of a topological gap in magnetic chains on a s-wave superconductor— can be described quite well. However, an estimation of the expected SOC strength in a given system, which goes beyond an evaluation of the atomic contributions ($\propto Z^4$), is very difficult and might require an ab initio based theoretical study[105,106] of the particular system, as illustrated in the example above.

The relation of SOC and DMI

In Subsection 2.1.2 I introduced the DM interaction as an anisotropic interaction contributing to the exchange and argued that a broken space inversion symmetry is required. In this section, I will proceed to show that it depends on the SOC of the host in a system of two magnetic impurities, coupled via the RKKY interaction of a metallic substrate with strong SOC[107].

Consider two magnetic atoms, located on a substrate of heavy impurities. For the sake of simplicity one reduces the system down to both magnetic atoms and one heavy substrate atom. Then, it can be shown that the resulting spin Hamiltonian is dominated by

$$\hat{H}_{DM} = -V(\xi)\frac{\sin(k_F(R_A + R_B + R_{AB}) + \eta)\mathbf{R}_A \cdot \mathbf{R}_B}{R_A R_B R_{AB}}(\mathbf{R}_A \times \mathbf{R}_B)(\hat{\mathbf{S}}_A \times \hat{\mathbf{S}}_B) \tag{2.15}$$

where $\mathbf{R}_A$ and $\mathbf{R}_B$ are the vectors from the non-magnetic atom to the respective magnetic one with lengths R_A and R_B, R_{AB} is the distance between both magnetic impurities, η is a phase shift and $V(\xi)$ is proportional to the SOC strength of the non-magnetic atom[108].

Apart from the dependence of the DM interaction on SOC of the non-magnetic host, which is evident from Equation 2.15, a few symmetry considerations of the problem and favorable spin configurations are accessible as well. Let us consider magnetic adatoms on a surface (defined as the $x-y-$plane) and that the non-magnetic heavy substrate atom is displaced from the connecting line of the two magnetic atoms in z-direction: If the spins $\hat{\mathbf{S}}_A$ and $\hat{\mathbf{S}}_B$ lie in-plane, their cross product results in a vector that is perpendicular to $\mathbf{R}_A \times \mathbf{R}_B$. Therefore, there would be no DM interaction contribution to the exchange. However, if the spins have large out-of-plane contributions, $\hat{\mathbf{S}}_A$ and $\hat{\mathbf{S}}_B$ and $\mathbf{R}_A \times \mathbf{R}_B$ are no longer perpendicular and a finite DM interaction is present, driving the spins into perpendicular alignment[109].

More generally, one has to take into account that every non-magnetic substrate atom adds a contribution to the DM vector which is proportional to the first, spin-independent part of Equation 2.15. Due to the symmetry of the problem defined above, the DM vector will have a component of zero in the direction of the connecting line of atom A and B (x-direction). Due to the broken inversion symmetry at the surface, the component of the DM vector in z-direction is small. Approximately, the DM vector will have its largest component in the y-direction. Therefore, the Hamiltonian in Equation 2.15 favors a perpendicular spin alignment in the $x-z-$plane considering the system described above.

2.2. Superconductivity and its interaction with magnetism

The following section introduces important theoretical concepts related to SC which are necessary to understand the experimental results of this thesis. In the description of this effect, I will proceed analogously to the historical development of the field where the phenomenology was studied first (Subsection 2.2.1) and only later an adequate microscopic theory was found (Subsection 2.2.2). Afterwards, I will introduce the SC proximity effect in Subsection 2.2.3, which is a crucial concept for many of the ideas realized in this thesis. At last I will introduce the basic concepts of the interaction of magnetism with SC at the single atom level in Subsection 2.2.4 and for larger structures of 1D chains in Subsection 2.2.6. In an intermediate section I will discuss the basics of MBS in condensed matter systems (Subsection 2.2.5).

2.2.1. Phenomenology of superconductivity

Generally, superconductors are a class of materials which are characterized by the following list of properties. If they are cooled below a critical temperature T_C:

- the electrical resistance of the sample drops to zero in the superconducting state, which was the first experimental manifestation of SC and its observation was awarded with the Nobel prize of physics in 1913[110]
- magnetic flux is expelled from the SC, as long as it doesn't exceed a certain field strength, which is called the Meissner-Ochsenfeld effect[111]
- a SC has a gap of quasiparticle excitations with a width of 2Δ around the Fermi level.

Above the critical temperature T_C, SCs behave like regular metals or even heavily doped semiconductors. A phenomenological description of the Meissner-Ochsenfeld effect was derived from the Maxwell equations in the framework of the London theory, where screening currents on the surface of a SC explain the expelled magnetic flux in the bulk of a given sample. However, the theory lacks a microscopic origin, which was realized much later.
Another important property of SC is the distinction of type I and type II superconductors, which was experimentally motivated in the 1930's[112–114] but realized only much later[115]. While type I superconductors are characterized by a single critical field B_C, above which the superconducting state is destroyed, there are two critical fields for type II superconductors $B_{C,1}$ and $B_{C,2}$. Below a field of $B_{C,1}$, the superconductor reacts to a B field by expelling it from the sample through screening currents. Between $B_{C,1}$ and $B_{C,2}$ tubes of normal-conducting regions penetrate the superconductor — so-called vortices — which allow magnetic flux to locally penetrate

the sample. At fields above $B_{C,2}$, the superconducting state is quenched. A prediction of a particular superconductor's type can be obtained by the Ginzburg-Landau parameter, which is given by

$$\kappa = \frac{\lambda}{\xi}, \tag{2.16}$$

where λ is the London penetration depth, the distance at which an external magnetic field is screened, measured from the surface to the bulk of a given material, and ξ is the coherence length of the SC. Below a critical Ginzburg-Landau parameter $\kappa = \frac{1}{\sqrt{2}}$[116] one expects a type I superconductor, while a parameter larger than that results in a type II superconductor[114].

2.2.2. Microscopic model of superconductivity

The microscopic model, which was successful in describing SC — the Bardeen-Cooper-Schrieffer (BCS) theory named after its three authors[117] — relies on the formation of bound electron pairs below a material specific critical temperature T_C. These pairs are called Cooper pairs, and for $T = 0\,\mathrm{K}$ they occupy the same ground state due to their bosonic nature. The formation of Cooper pairs below T_C is the underlying reason for superconductivity in all types of superconductors. However, the pairing mechanism can vary under the condition that the Cooper pair wave functions are antisymmetric under exchange of the two electrons, as governed by the fermionic nature of the electrons making up the Cooper pairs:
The pairing mechanism is called conventional SC or *s*-wave, if the total spin $S = 0$ (antisymmetric) and the total angular momentum $L = 0$ (symmetric) of the Cooper pair both add to zero. Another pairing state is characterized by a spin-triplet state $S = 1\hbar$ and an uneven total angular momentum $L = 1\hbar$, referred to as *p*-wave[118]. If one takes the time-

dependence of the pairing into account, which can be even and odd as well, it is possible to further classify the pairing mechanisms. A review on the resulting odd-frequency SC in 1D systems is given in Ref. [119].
An important step towards the BCS theory was Cooper's demonstration that electrons near the Fermi surface can form pairs in the presence of even a weak attractive potential at sufficiently low temperatures[120]. This attractive potential between electrons is assumed to be mediated by electron-phonon interactions in BCS-like superconductors, which is motivated by experimental observations of an isotope effect on the critical temperature T_C[121,122]. Even up-to-date, this property is sometimes used as a hallmark to determine the origin of the coupling mechanism in novel superconductors[123].
An accurate derivation of the BCS theory is given in Refs. [118, 124]. In the following I will highlight the most important approaches and steps. As an instructive starting point of the BCS theory, one may consider the reduced BCS Hamiltonian, in which the creation and annihilation operators $\hat{c}^\dagger_{\mathbf{k}\sigma}$ and $\hat{c}_{\mathbf{k}\sigma}$ create/annihilate quasiparticles with an effective mass m^*, a momentum of $\mathbf{k}$ and spin σ:

$$\hat{H}_\mathrm{R} = \sum_{\mathbf{k},\sigma} \xi_{\mathbf{k}} \hat{c}^\dagger_{\mathbf{k}\sigma} \hat{c}_{\mathbf{k}\sigma} + \sum_{\mathbf{k},\mathbf{k}'} V_{\mathbf{k}\mathbf{k}'} \hat{c}^\dagger_{\mathbf{k}'\uparrow} \hat{c}^\dagger_{-\mathbf{k}'\downarrow} \hat{c}_{-\mathbf{k}\downarrow} \hat{c}_{\mathbf{k}\uparrow} \tag{2.17}$$

in which $\xi_{\mathbf{k}} = \frac{\hbar^2 k^2}{2m^*} - E_\mathrm{F}$ and $V_{\mathbf{k}\mathbf{k}'}$ is the attractive potential of an electron with momentum $\mathbf{k}$ and $\mathbf{k}'$ which will be further defined later. The ansatz for the many-body wave function in the BCS theory is given by

$$\Psi_\mathrm{BCS} = \prod_{\mathbf{k}} (u_{\mathbf{k}} + v_{\mathbf{k}} \hat{c}^\dagger_{\mathbf{k}\downarrow} \hat{c}^\dagger_{-\mathbf{k}\uparrow}) \, |\Phi_0\rangle \tag{2.18}$$

where $|\Phi_0\rangle$ is the vacuum state and $u_{\mathbf{k}}$, $v_{\mathbf{k}}$ are complex probability amplitudes, which describe the unoccupied and occupied pair-states around the Fermi energy with the normalization condition $|u_{\mathbf{k}}|^2 + |v_{\mathbf{k}}|^2 = 1$. The

ground-state energy is then calculated to be

$$E = \langle \Psi_{\mathrm{BCS}} \mid \hat{H}_{\mathrm{R}} \mid \Psi_{\mathrm{BCS}} \rangle = 2\sum_{\mathbf{k}} |v_{\mathbf{k}}|^2 \xi_{\mathbf{k}} + \sum_{\mathbf{k},\mathbf{k}'} V_{\mathbf{k}\mathbf{k}'} v_{\mathbf{k}}^* u_{\mathbf{k}} v_{\mathbf{k}'} u_{\mathbf{k}'}^* \tag{2.19}$$

which can then be minimized with respect to $u_{\mathbf{k}}$ and $v_{\mathbf{k}}$

$$|v_{\mathbf{k}}|^2 = \frac{1}{2} \cdot [1 - \frac{\xi_{\mathbf{k}}}{\sqrt{|\Delta|^2 + \xi_{\mathbf{k}}^2}}] \tag{2.20}$$

and

$$|u_{\mathbf{k}}|^2 = \frac{1}{2} \cdot [1 + \frac{\xi_{\mathbf{k}}}{\sqrt{|\Delta|^2 + \xi_{\mathbf{k}}^2}}] \tag{2.21}$$

where $\Delta_{\mathbf{k}}$ is the gap function defined as $\Delta_{\mathbf{k}} = -\sum_{\mathbf{k}'} V_{\mathbf{k}\mathbf{k}'} u_{\mathbf{k}'} v_{\mathbf{k}'}$. The Equations 2.20 and 2.21 are plotted in Figure 2.3a. It is apparent that the quasiparticles are dominantly electron-like below the Fermi level and dominantly hole-like above it. Near E_{F}, $|u_{\mathbf{k}}|^2$ and $|v_{\mathbf{k}}|^2$ are smeared out in a range of $\Delta_{\mathbf{k}}$.

As the attractive interaction between the electron pairs is phonon-mediated for conventional *s*-wave superconductors, it is reasonable to assume the pairing potential to be of the form

$$V_{\mathbf{k}\mathbf{k}'} = \begin{cases} -V & \text{for } |\xi_{\mathbf{k}}| \text{ and } |\xi_{\mathbf{k}'}| \leq \hbar\omega_{\mathrm{D}} \\ 0 & \text{for } |\xi_{\mathbf{k}}| \geq \hbar\omega_{\mathrm{D}} \text{ or } |\xi_{\mathbf{k}'}| \geq \hbar\omega_{\mathrm{D}}, \end{cases} \tag{2.22}$$

where ω_{D} is the Debye frequency of the phonons. Electrons within a range of $\pm\hbar\omega_{\mathrm{D}}$ around the Fermi energy are subject to $-V$ and no pairing potential is assumed otherwise.

From this consideration one can calculate the condensation energy, i.e. the energy gained by the pairing. It is given by $-N_{\mathrm{N}}(E_{\mathrm{F}}) \cdot \Delta^2/2$, where $N_{\mathrm{N}}(E_{\mathrm{F}})$ is the normal state DOS at the Fermi energy. It is apparent that a large DOS and a large pairing-interaction V favor the condensation energy.

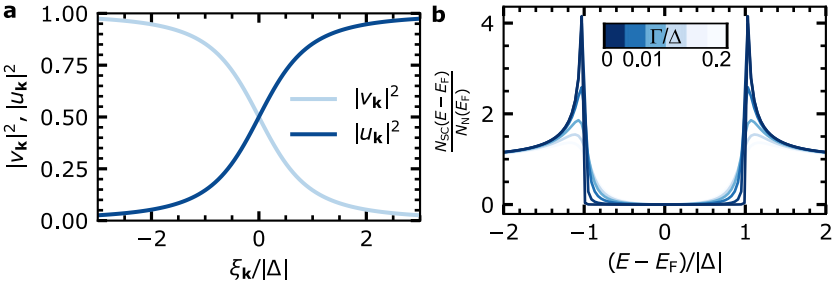

Figure 2.3.: **a** Absolute squares of the probability amplitudes u_k and v_k for unoccupied and occupied pair-states around the Fermi energy according to Equation 2.21 and Equation 2.20. **b** Plots of the density of states (DOS) of excited quasiparticles for a superconductor around the Fermi level, without broadening $\Gamma/\Delta = 0$ (darkest curve) according to Equation 2.24 and for finite values of Γ/Δ according to the Dynes function Equation 2.25.

The energy necessary to break a Cooper pair into two quasiparticles of momentum $\mathbf{k}$ is given by

$$\epsilon_\mathbf{k} = \sqrt{\xi_\mathbf{k}^2 + \Delta^2} \tag{2.23}$$

which illustrates that quasiparticles have a minimum energy of Δ[118,124]. One remaining open point is the DOS of a superconductor close the to Fermi level, which is directly measurable in STS experiments (Subsection 3.1.1). The normal state DOS is assumed to be approximately constant $N_N(E) = N_N(E_F)$, as we are only considering a small energy window. From Equation 2.23 we have concluded that quasiparticles have a minimum energy of $\pm\Delta$. Therefore, a region of the size of $\pm\Delta$ forms around the Fermi energy, where no quasiparticle states are available — the energy gap of the superconductor. For energies larger than $|\Delta|$, the DOS is given by

$$N_{SC}(E - E_F) = N_N(E_F) \cdot \frac{E - E_F}{\sqrt{(E - E_F)^2 - \Delta^2}} \tag{2.24}$$

Plots of the DOS are shown in Figure 2.3b. From Equation 2.24 one can see that there are singularities in the DOS at $E - E_F = \pm\Delta$ for zero temperature/broadening. In real systems, which are subject to broadening due to finite temperatures and due to the measurement set-up a more accurate description is obtained by the Dynes function[125]

$$\frac{N_{SC}(E - E_F)}{N_N(E_F)} = sign(E)\mathrm{Re}[\frac{E - i\gamma}{\sqrt{E^2 + 2i\gamma - \Delta^2}}] \tag{2.25}$$

where Γ is a phenomenological broadening parameter. The effect of this parameter is displayed in Figure 2.3b. Measurements of the superconducting energy gap in superconductor-insulator-superconductor (SIS) tunnel junctions can be seen as further evidence for the correctness of the BCS theory[126–128]. Additionally, very recent experiments using shot noise STM on a SC demonstrate that the charge transport inside the superconducting gap occurs in packages of $2e$, which can be seen as direct evidence of Cooper pairs[129].

2.2.3. Proximity effect

Already quite early after the discovery of SC in some metals, experiments using tunneling spectroscopy demonstrated that a normal metal (N) brought into contact with a SC leads to superconducting correlations in N, even if it doesn't host attractive pairing interactions on its own[130,131]. This phenomenon — called proximity effect — is not entirely understood yet. However, a basic understanding of it may be obtained by considering Andreev reflections at the normal metal-superconductor (N/S) interface[132,133]. Further, the framework of nonequilibrium SC[134] can be used to explain some experiments[135]. While there are claims that some observations are not describable in this theory[136], they should not be overextended, as the experiments can also be explained by the very poor sample quality and tip effects.

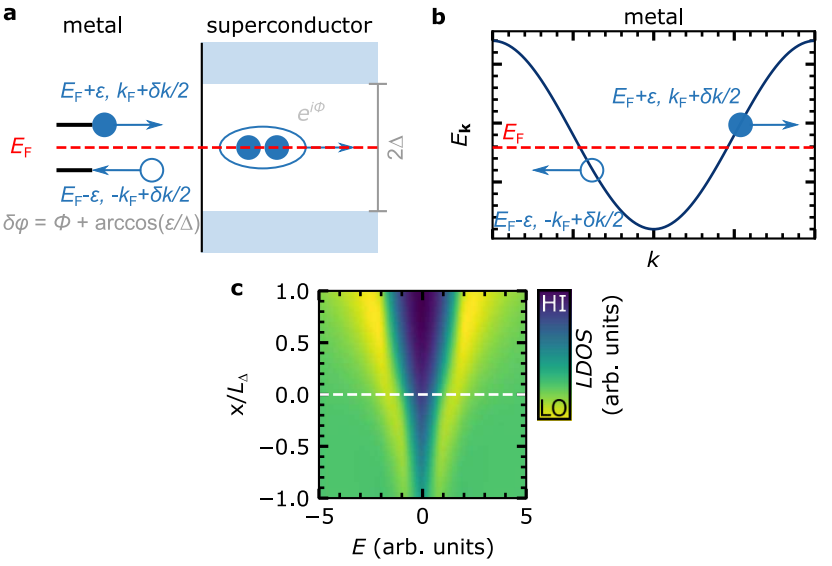

Figure 2.4.: a Sketch of the Andreev process, in which an incident electron (filled blue sphere) in the N region is reflected from the N/S interface as a hole (empty sphere) and a Cooper pair is transfered to the SC . **b** Band structure of a normal metal, in which the electron and hole states of the particles involved in the Andreev reflection are marked. It is apparent that the wave vectors are mismatched by $\delta k = 2\epsilon/\hbar v_F$. **c** Solution of the Usadel equation (Equation 2.27) for $\theta(x,E)$, where constants are assumed for D and γ_{SF}. x is normalized to the coherence length L_ϵ evaluated at the energy Δ. The white line marks the N/S interface.

Andreev reflections[137] are two-electron transport processes occuring at N/S interfaces. At energies above/below $\epsilon > |E_F \pm \Delta|$ single particle transport between a N and a SC may occur as usual. However, for energies lower than $\epsilon < |E_F \pm \Delta|$, these processes are forbidden, as there are no states in this energy region of the SC. Taking two-particle processes into account, the transport mechanism illustrated in Figure 2.4a is possible: An electron propagating towards the N/S interface can be transferred to the SC, if there is a second electron transferred through the interface, with which it may form a Cooper pair. This process is similar to the reflection of a hole to the N region, which maintains charge conservation. Further, the reversed process is possible as well, i.e. an Andreev reflection from a hole to an electron. It should be noted, that a perfect reflection is only possible for particles at E_F, as illustrated in Figure 2.4b. As the metal is not particle-hole symmetric, the incident electron ($E_F + \epsilon$, $k_F + \delta k/2$) and the reflected hole ($E_F - \epsilon$, $-k_F + \delta k/2$) have mismatched wave vectors.
Regarding the proximity effect, the important characteristic of Andreev reflections is the phase coherence of the process. As illustrated in Figure 2.4a, the reflected hole has a fixed phase change of $\delta\varphi = \Phi + \arccos(\epsilon/\Delta)$ in comparison to the incident electron. There is one contribution from the fixed macroscopic phase of the superconductor Φ and another energy-dependent phase contribution $\arccos(\epsilon/\Delta)$, which results in a phase shift of $\pi/2$ for $\epsilon = 0$. The length scale of this phase coherence of reflected holes and electrons in the N is the value that eventually determines the spatial extent of the proximity effect. After a length of $L_\epsilon = \sqrt{\hbar\mathfrak{D}/\epsilon}$, where $\mathfrak{D}$ is the diffusion constant, coherence is lost and interference effects no longer occur.
As long as electrons and holes maintain a phase-coherence in the N one obtains finite values of the condensation amplitude F

$$F = \sum_{E>0} v^*(\mathbf{r})u(\mathbf{r})[1 - 2f(E)], \tag{2.26}$$

where $f(E)$ is the Fermi-Dirac distribution. It is apparent from Equation 2.26 that there is a finite probability of finding Cooper pairs in N, i.e. Cooper pairs are leaking into the normal metal region[132,133]. It is important to note that this conclusion is true, even if one does not assume a pairing potential in the N.
In the nonequilibrium theory of superconductivity, one defines a complex function of space and energy $\theta(x, E)$, which has to obey the Usadel equation given in Equation 2.27 for a model type N/S heterostructure[134,135]

$$\frac{\hbar\mathfrak{D}}{2}\frac{\partial^2\theta}{\partial x^2} + (iE - \hbar\gamma_{\mathrm{SF}}\cos(\theta))\sin(\theta) + \Delta(x)\cos(\theta) = 0 \tag{2.27}$$

where γ_{SF} is the spin-flip scattering rate and $\Delta(x)$ has to obey

$$\Delta(x) = N_{\mathrm{SC}}(E_{\mathrm{F}})V\int_0^{\hbar\omega_{\mathrm{D}}}\tanh(\frac{E}{2k_BT})\,\mathrm{Im}[sin(\theta)]dE. \tag{2.28}$$

For adequate boundary conditions one can determine $\theta(x, E)$, which gives access to the pair amplitude $F(x,\epsilon) = -i\sin(\theta(x,\epsilon))$ and to the density of states $n(x,\epsilon) = N_{\mathrm{SC}}(E_{\mathrm{F}})\,\mathrm{Re}(\cos(\theta(x,\epsilon)))$.
An example of the density of states obtained for various values of x ($x = 0$ corresponds to the N/S interface) and E, where $\mathfrak{D}$ and γ_{SF} are set to constant values is shown in Figure 2.4c. For positive values of x, deep in the SC region, we find that the gap reaches a value of 1.5 arb. units, which is set in the definition of Equation 2.27. Approaching the interface, the size of the superconducting gap decreases continuously and the gap is no longer fully pronounced, which manifests itself in the V-like shape of individual density of states spectra. The phenomenon that the superconducting gap is no longer fully pronounced close to the N/S interface in the SC region is referred to as the inverse proximity effect.
As we will discuss in Chapter 4, we are dealing with ultrathin films of normal metals on superconductors in this thesis, where the superconducting gap is typically still fully pronounced and the size of the gap is

either similar as for the bulk superconducting substrate or close to it. The theory of non-equilibrium superconductivity is applicable when the film thickness is on the same order of magnitude as the diffusion length, i.e. typically around several hundred nanometers for metallic films[135]. Recently powerful novel first principle methods were introduced to describe N/S systems in the limit of few atomic layers, which further demonstrate the connection of Andreev reflections and the proximity effect[138–140].

2.2.4. Yu-Shiba-Rusinov states

As we have learned in Subsection 2.2.1, magnetic fields destroy superconducting phases if they exceed a certain threshold. Yu, Shiba and Rusinov separately investigated this effect in the atomic limit, following the interesting question how a single magnetic impurity interacts with a SC host[141–143]. Magnetic atoms or molecules placed on or in a superconducting substrate are associated with a pair-breaking potential. As a result, magnetic scattering centers lead to locally bound quasiparticle states, which we refer to as YSR states in the following.
It should be noted that non-magnetic potential scattering can be pair-breaking as well. However, it is only considered for p-wave, d-wave etc. pairing mechanisms in common literature. This is motivated by the fact that the low-energy states of a potential scattering impurity that act on a s-wave SC have a finite width due to the hybridization with the substrate's conduction band. Since this width is commonly much larger than the superconducting gap Δ, the resulting bound states are typically merged with the coherence peaks. Therefore, it is commonly assumed that an important distinction of s-wave SCs is that non-magnetic potential scattering is not Cooper pair-breaking[144].
In the quasi-classical description of Shiba[142], the origin of YSR states for $3d$ transition metal atoms lies in the $s-d$ exchange interaction of a paramagnetic impurity spin with the conduction electrons, which can

be treated like a local magnetic field. This is typically valid for a large $|\mathbf{S}| >> 1$. Assuming a low J, to obtain a finite value for $J\mathbf{S}$, one can add

$$\hat{H}_{\mathrm{SD}} = -\frac{J}{2N} \sum_{\mathbf{k},\mathbf{k}'} \hat{c}^{\dagger}_{\mathbf{k}} \hat{\boldsymbol{\sigma}} \hat{c}_{\mathbf{k}'} \cdot \mathbf{S} \tag{2.29}$$

to the BCS Hamiltonian to account for the *s-d* interactions. Using the Greens function formalism and evaluating the poles of the T-matrix one obtains solutions for a pair of localized excited quasiparticle states inside the superconducting gap Δ[142], which are the aforementioned YSR states. Their energy is given by

$$\epsilon = \Delta \cdot \frac{1 - a^2}{1 + a^2} \tag{2.30}$$

where $a = J \cdot S \cdot \pi \cdot N_{\mathrm{N}}(E_{\mathrm{F}})$. This model neglects that the impurity may also acts as a potential scattering site, which can be implemented by adding a non-magnetic scattering potential U to the exchange term described in Equation 2.29. However, as discussed above, the potential scattering term does not influence the energy of the YSR states, it may only cause an asymmetry in their particle-hole weight, which manifests itself in an asymmetry of the $\mathrm{d}I/\mathrm{d}V$ intensity of the YSR states in STS experiments[145]. A plot comparing the DOS of a bare SC with the DOS of a magnetic impurity on a SC, which gives rise to YSR states is shown in Figure 2.5b. Therein, it is illustrated that the YSR states are particle-hole symmetric in energy, but not in their particle-hole weight. An additional plot displaying how the energy of the YSR states ϵ depends on a (a depends on the impurity spin and the coupling strength) is shown in Figure 2.5c. For a fixed impurity spin S, the coupling strength J is the remaining free parameter, determining the energy of the YSR states. In a regime of very low or very high coupling, the YSR states have an energy of $\pm\Delta$, i.e. in STS experiments they are merged with the coherence peaks. In a certain range of J, the YSR states split off the coherence peaks and are located inside the superconducting gap. At a critical coupling strength

J_{crit} a level crossing occurs and the ground state is switched, i.e. a quantum phase transition occurs. This behavior was also demonstrated in clever experiments, where the coupling strength J was tuneable[146–149].
Another way to physically describe the origin of YSR states is the quantum spin model, where the spin and the $s-d$ exchange are treated quantum mechanically and include Kondo correlations in the conduction electron system. In the simplest case, one can consider a $S = 1/2$ spin. The magnetic impurity can either be screened by conduction electrons resulting in a ground state with $S = 0$, which can be excited to $S = 1/2$ by tunneling electrons, or — in the low coupling regime— screening is weak and therefore a finite spin $S > 0$ makes up the ground state, which can be excited to $S = 0$ by a tunneling electron. The two possible ground states and their excitations are shown in Figure 2.5a.
The descriptions above were performed for a single orbital (i.e. $S = 1/2$) for the sake of simplicity. However, from the theory of single atom magnetism, which I introduced in Section 2.1, we know that real systems usually have multiple orbitals resulting in a higher spin. Additionally, the spin-carrying orbitals of an adsorbed magnetic adatom are typically non-degenerate due to the crystal field splitting. Therefore, single adatoms can host multiple scattering channels of different orbital origins, leading to multiple observable YSR states[150–152].
Finally, one can show that the quasiparticle amplitudes of the YSR states $|u_\mu(\mathbf{r})|^2$ and $|v_\mu(\mathbf{r})|^2$ are probed at positive and negative biases in the low conductance regime of STM measurements, respectively[144,153]. Here, μ indicates the respective scattering channel. The spatial distributions of the quasiparticle amplitudes resemble the shapes of the d-orbitals associated with the scattering channel[152] and they spatially decay with the term[143,145]

$$u_{\mathbf{r}}, v_{\mathbf{r}} \propto \frac{\sin(k_{\mathrm{F}} r + \delta^{\pm})}{k_{\mathrm{F}} r} \exp(\frac{-r}{\xi_0}), \tag{2.31}$$

where $\delta^{\pm}$ is a scattering phase shift and ξ_0 is the coherence length of the SC. This description seems to be reproducible in STM experiments[154].

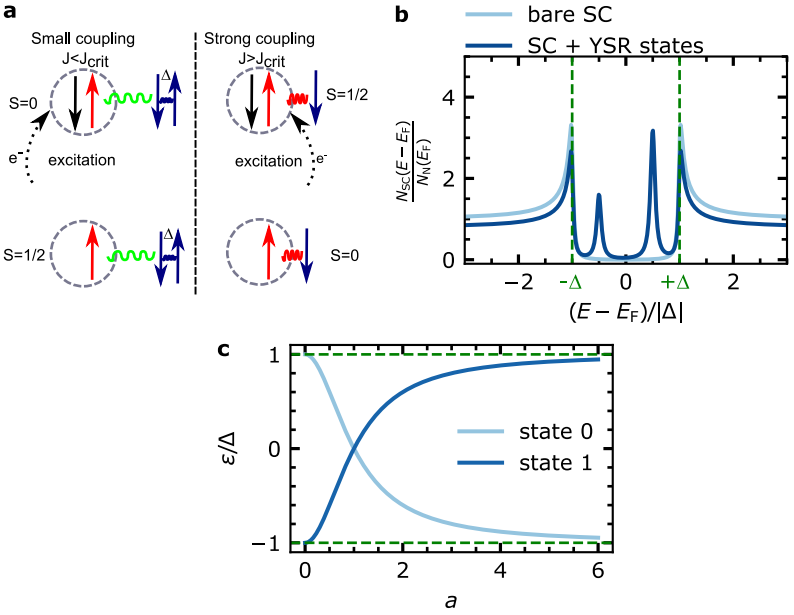

Figure 2.5.: a Illustration of the two processes leading to Shiba states in case of a $S = 1/2$ impurity. The left panel shows the low coupling regime, where the spin is largely unscreened by the conduction electrons, leading to a $S = 1/2$ ground state, which can be excited by a tunneling electron resulting in a singlet excited state. The right panel illustrates the strong coupling regime, where the ground state is a completely screened spin ($S = 0$) and the excited case has $S = 1/2$. Inspired by Ref. [145]. **b** Illustration of the particle component of the DOS for a bare SC and a magnetic impurity placed on a SC, giving rise to YSR states. **c** Plot of the YSR states' energy-dependence on the parameter a according to Equation 2.30. Black arrows mark the energetic position of the YSR states in **b** and **c**.

However, there are recent reports on two-dimensional systems displaying long-range decays, which strongly depend on the Fermi surface of the superconducting substrate[155–157].

2.2.5. Insert: Majorana bound states

As described in Chapter 1, the ultimate goal of a large part of the experimental effort presented in this thesis is dedicated to the realization of MBS . The previous Subsections 2.1.3, 2.2.2, 2.2.3 and 2.2.4 enable us to develop an intuitive approach to identify potentially interesting material properties for the realization of MBS in condensed matter systems.
Originally, the theoretical description of fermions which are their own antiparticles was developed by Ettore Majorana[158] in 1937 and was well received in the field of particle physics. Only this century, the idea of realizing a quasiparticle excitation, where the creation operator equals the annihilation operator (similar to the expression that a particle is its own antiparticle)

$$\hat{\gamma} = \hat{\gamma}^{\dagger}, \tag{2.32}$$

became widely popular in condensed matter systems. The reason lies in two striking properties of this quasiparticle excitation, called MBS:

- to fulfill Equation 2.32, localized MBS have zero excitation energy and they appear in spatially isolated pairs
- MBS obey nonabelian exchange statistics.

A popular theoretical idea proposes to exploit these properties in topological quantum computation[8,159], where information is processed by exchanging MBS (braiding), which is robust against some extent of perturbations from the environment (electric and/or magnetic fields), as long as their effect is smaller than the energy gap which separates MBS from the quasiparticle continuum.

To identify the necessary physical properties to host MBS in a condensed matter system, we can derive some arguments from Equation 2.32: The solid state analogue to particles and antiparticles are electrons and holes, i.e. we are looking for a quasiparticle with equal electron and hole character. From Subsection 2.2.2, we know that quasiparticles in a BCS superconductor are described by the amplitudes $u_{\mathbf{k}}$ and $v_{\mathbf{k}}$, whose absolute squares are equal at the Fermi level $|u_{\mathbf{k}}|^2 = |u_{\mathbf{k}}|^2 = 0.5$ (Figure 2.3a). However, we have neglected the spin of the Bogoliubov-de-Gennes (BdG) quasiparticles in this treatment. If we drop the spin, by assuming that we are treating spinless fermions, the conclusion that BdG quasiparticles at the Fermi level could be MBS remains intact. This leads us to an issue with the *s*-wave pairing mechanism of SC, though. Usually, the spin wavefunction would have to be antisymmetric for this pairing mechanism (Subsection 2.2.2), which is not possible in a spinless system. The simplest pairing mechanism with an antisymmetric orbital wavefunction and a symmetric spin wave function is *p*-wave pairing. We can conclude that zero-energy excitations in spinless *p*-wave superconductors could be MBS[15,16,160].

As candidates of naturally occurring *p*-wave SCs are sparse, and even promising material systems like Sr_2RuO_4[161–163] are still under debate[164], an alternative route to engineer spinless *p*-wave superconductors including the following physical properties were proposed[17,18]:

- a 1D or 2D system proximity coupled to a *s*-wave superconductor
- spin-polarization in order to achieve an essentially spin-less system and break the spin degeneracy
- SOC to enable the *s*-wave SC to still induce pairing in the spin-polarized system.

A variety of experimentally accessible systems were predicted to host MBS, including vortices in a strong topological insulator coupled to a *s*-wave SC[17,19,20], materials with a Dirac-like surface state being intrinsi-

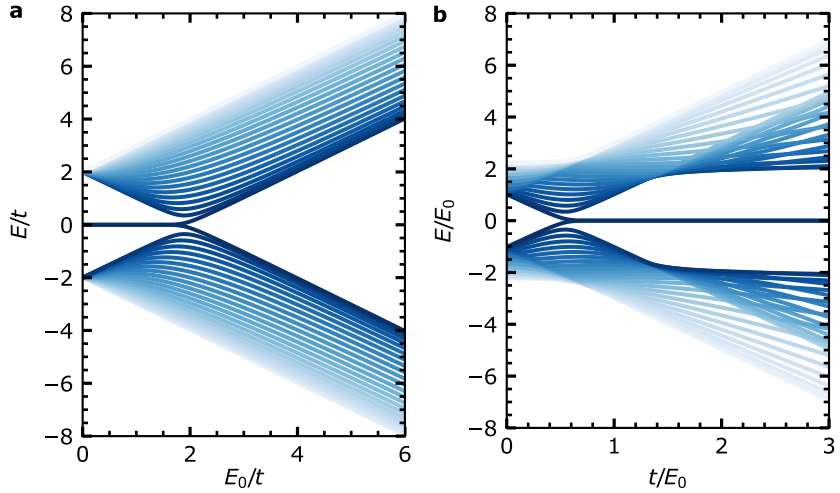

Figure 2.6.: a and **b** Development of the eigenstate energies depending on E_0/t and t/E_0 for a finite chain. Δ is set to constant value equal to $1t$ and $1E_0$, respectively. The eigenstates are color-coded in such a fashion that the lowest energy one is dark blue and the highest energy one is light blue.

cally superconducting[21–24], semiconductor nanowires with strong SOC which are proximity coupled to a *s*-wave superconductor and exposed to an external B- field[25–31] and spin-orbit coupled magnetic chains on *s*-wave superconductors[32–39]. In this thesis we focus on the latter approach, which is discussed in more detail in Subsection 2.2.6. Reviews of other platforms are given in Refs. [165, 166].

2.2.6. Dilute chains of Yu-Shiba-Rusinov states

In this subsection, I will discuss the seminal Kitaev chain model and I apply it to dilute chains of magnetic adatoms on SCs, which enables a surprisingly good initial understanding of what is necessary to obtain

topological superconducting phases and MBS. Afterwards, I will focus on the role of SOC in more advanced models describing YSR chains.

The Kitaev chain

The general idea of hosting topological superconductivity and MBS in chains of magnetic adatoms lies in the band formation of their YSR states, in which topologically non-trivial band openings may occur under certain circumstances. For one, a necessary condition is a finite overlap of the individual YSR states of the multiple impurities in the chain, such that they hybridize and split into linear combinations of the individual states, which leads to a finite band width. This splitting was predicted already by Rusinov in his original paper[167] and was further investigated theoretically[168–170] and experimentally[60,171–175], recently.
Building upon these findings, we can set up a tight-binding model (TBM), which describes the relevant physics under the assumptions that only YSR states form bands wide enough to cross the Fermi level (i.e. all other bands are excluded from the description). Two additional assumptions are that only a single YSR state exists (one-band model) and that the chain is perfectly spin-polarized. Alternatively, if there are multiple YSR states in a given system, only one should be in the vicinity of E_F, while the other YSR states are far enough from the Fermi level to prevent them from forming a band which overlaps with E_F. In the nearest-neighbor model (only nearest neighbor interactions are considered), we may describe such a system with the following Hamiltonian[16,176]

$$\hat{H} = E_0 \sum_n \hat{c}_n^\dagger \hat{c}_n - t \sum_n (\hat{c}_{n+1}^\dagger \hat{c}_n + \mathrm{h.c.}) + \Delta \sum_n (\hat{c}_n \hat{c}_{n+1} + \mathrm{h.c.}), \qquad (2.33)$$

where E_0 is the single atom YSR state energy, t is the hopping term, quantifying the hybridization between neighboring YSR states (discussed in Subsection 2.1.2), and Δ is the pairing strength between neighboring sites.

The latter parameter Δ is crucial, since it induces pairing interactions between different sites even though the system is perfectly spin-polarized and can, therefore, be interpreted as the effect of SOC. It should not be mistaken with the gap of the superconducting substrate. We can write the Hamiltonian in the BdG formalism and then solve it numerically (the results shown here are calculated along the lines of Ref. [177] and the numerical calculations were performed using the Kwant code[178]).
The energies of the eigenstates depending on E_0 and t are shown in Figures 2.6a and b. Starting with a hopping of $t = 0$ in Figure 2.6b we find trivial quasiparticles at $E = E_0$. With an increasing hopping t, the band broadens until it eventually crosses the Fermi level $E = 0$ at $t = 0.5E_0$. Afterwards we find that the lowest-energy eigenstate is pinned at zero energy, and is separated from the quasiparticle continuum by a gap.
We can evaluate the band structure of an infinite chain and the LDOS line profiles of a finite chain for these three limits, as shown in Figure 2.7. In the limit of low hopping $t = 1/4E_0$ (Figures 2.7c and f), we find two narrow bands at positive and negative energies, which do not overlap. The LDOS profiles of selected eigenstates resemble regular standing waves of a confined electron systems. At $t = 1/2E_0$ (Figures 2.7b and e), the bands are ungapped and just touch at $k = \pi/a$. Increasing the hopping further, we find that a gap reopens as shown in Figure 2.7a for $t = 1E_0$. Further we observe that the lowest energy state at $E = 0$ is now localized on the first and the last site of the chain (Figure 2.7d). From the Hamiltonian, we can further calculate the topological invariant of the system[179] $Q = \mathrm{sign}(\mathrm{Pf}[\mathrm{iH}(0)]\mathrm{Pf}[\mathrm{iH}(\pi)])$[177], which is $Q = -1$ for Figure 2.7a and $Q = 1$ for Figure 2.7c. Therefore, we conclude that both band structures are topologically distinct, i.e. they can not be transformed continuously into one another without closing the gap, as seen in Figure 2.7b.
Taking all the arguments above into account, we can conclude that the observed pinned zero energy states are MBS. Further, we have gained an initial understanding, that in order to realize MBS in YSR chains, we have to tailor bands which cross the Fermi level. In particular an odd

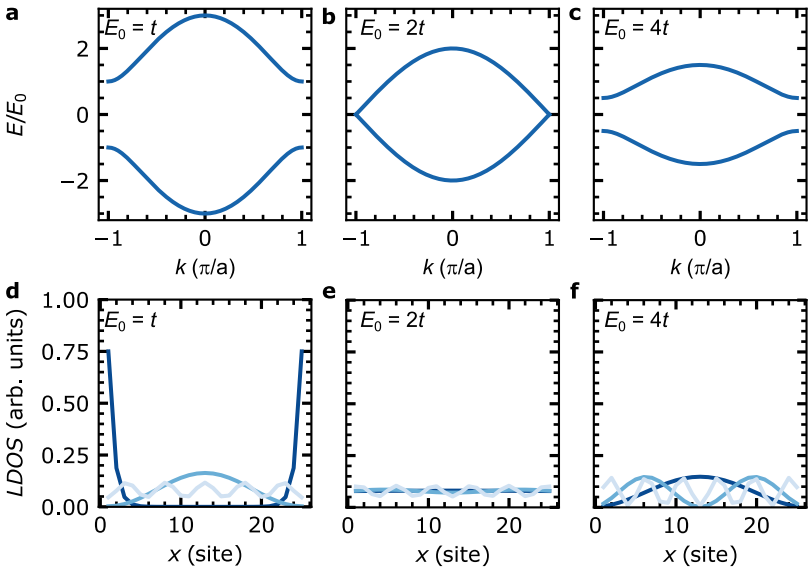

Figure 2.7.: a-c Plots of the band structures of an infinite Kitaev chain with parameters $t = 1$, $\Delta = 1$ and $E_0 = 1t$, $E_0 = 2t$ and $E_0 = 4t$, as indicated in the top left corner of each panel. **d-f** Plots of the LDOS for a finite Kitaev chain with $L = 25$, showing the lowest energy eigenstate, the first and the fifth excited state. The same parameters as for panels **a-c** were used.

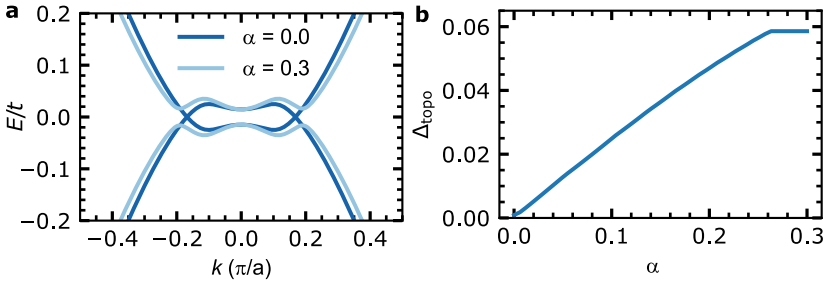

Figure 2.8.: a and **b** Influence of the SOC parameter α on the band structure and the opening of a topological gap Δ_{topo}.

number of band crossing should be present between $k = 0$ and $k = \pi/a$.

The influence of spin-orbit coupling

Initially, I discussed that SOC has to be present in fully spin-polarized systems in order to be able to induce superconductivity by proximity, as illustrated in the context of the paring parameter Δ in Equation 2.33. However, it plays a larger role in reality. To investigate the dependence of a particular system on SOC, we can add a simplified Rashba term $\alpha\hat{\sigma}_y k_x$ (see Subsection 2.1.3) and a Zeeman term $B_z\hat{\sigma}_z$ to the Hamiltonian shown in Equation 2.33. In fact, this Hamiltonian then describes the semiconductor nanowire platform[32]. However, we can still draw conclusions on the role of SOC for the spin chain platform.
Dispersions of the two energetically lowest bands in such a system are shown in Figure 2.8a for a SOC parameter of $\alpha = 0$ and $\alpha = 0.3$. In the case without SOC the bands are ungapped and cross the Fermi level continuously such that they intersect each other. If we keep all other parameters fixed (t, Δ and E_0) , but assume a finite SOC parameter, a gap opens around the Fermi level which is of p-wave nature and is often referred to as the topological gap. An evaluation of this gap depending on

the Rashba parameter is shown in Figure 2.8b. For this set of parameters, the gap increases up to a value of $\alpha \sim 0.27$ and saturates there.
It should be noted, that the relationship of SOC and the band structure is more complex in real systems. However, from the discussion above we can still take away that no (very low) SOC prevents the opening of a topological gap (or only opens a very small gap). Additionally, one should mention that SOC and a spin helix ground state are often mapped on one another in theoretical descriptions[34,180] of the adatom chain platform. Therefore, if we consider a chain which fulfills all the criteria of the band structure discussed above, it should be sufficient to either have a spin helix ground state or to expose the chain to high SOC, in order to host MBS.

2.3. Dynamics of spin chains

Atomic-scale spin systems, that are effectively described by a spin Hamiltonian that includes magnetic anisotropy (Equations 2.3 and 2.4), Heisenberg exchange (Equation 2.10) and a Zeeman term are described by the following Hamiltonian

$$\hat{H} = \sum_{i=1}^{N-1} (J\hat{\mathbf{S}}_i \cdot \hat{\mathbf{S}}_{i+1} + g\mu_B \hat{\mathbf{S}}_i \cdot \mathbf{B} + D\hat{S}_{z,i}^2 + E(\hat{S}_{x,i}^2 - \hat{S}_{y,i}^2)). \tag{2.34}$$

Furthermore, spin chains can be separated into two categories concerning the description of their dynamics. To begin with, e.g. chains of coupled Ising-type $S = 1/2$ spins with two degenerate ground states can be described by two oppositely FM-aligned out-of-plane states $|\uparrow ... \uparrow\rangle$ and $|\downarrow ... \downarrow\rangle$, which can generally be distinguished in a measurement[65]. An additional example are AFM coupled spin chains which are coupled to the substrate's electron bath (see Figure 2.9a). As discussed below, the scattering of substrate electrons with the chain's atoms can lead to a

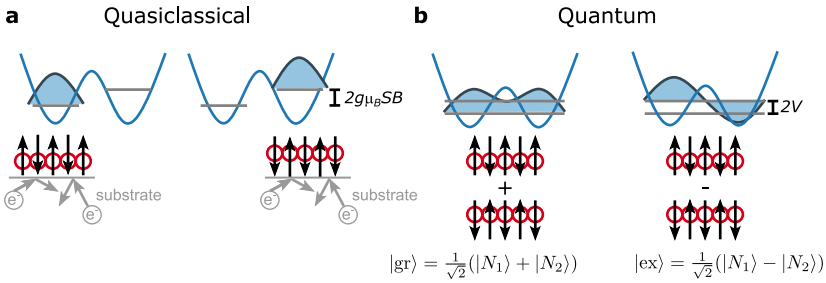

Figure 2.9.: a and **b** Illustrations of the two types of spin systems which can generally be distinguished from one another by the overall spin and properties as the magnetic anisotropy or by the scattering rate of substrate electrons with the chain's atoms. **a** Depicts the quasiclassical case of two degenerate ground states with opposite magnetization. The degeneracy is lifted by an external B-field in this illustration. Gray circles and arrows illustrate scattering substrate electrons which increase the lifetimes of the quasiclassical spin states. **b** Illustration of a spin system with non-degenerate ground states. Quantum spin tunneling leads to the coupling of both states and results in a ground state ($|\mathrm{gr}\rangle$) and a first excited state ($|\mathrm{ex}\rangle$), which are linear combinations of the two Néel states with opposite magnetization. They are separated by the coupling V between the two Néel states. Here, the influence of substrate electrons is neglected, which can be realized experimentally by investigating spin chains on an insulator or a SC. Inspired by Ref. [65].

decoherence of the quantum mechanical ground state of the system, such that there are two bistable Néel states.
On the other hand, there is the case of quantum spin chains. In Ref. [181] it is shown that for an integer total spin and an antiferromagnetic spin chain that is nearly described by an Ising model, there are no degenerate ground states but a single one $|\mathrm{gr}\rangle$ and a first excited state $|\mathrm{ex}\rangle$. The ground state and the first excited state are both a superposition of many states of the local spins, but are dominated by the semiclassical Néel states with equal weight. Therefore, the ground- and first excited state can be described as a linear combination of both Néel states (see Figure 2.9b). The ground state and the excited state are split by $\Delta E = 2V$ due to quantum spin tunneling[182] (V is the coupling between both Néel states). It was shown, that this description can be valid for even- and odd chain lengths as well as for integer- and half-integer spins.
If one were to initialize the spin chain in one of the Néel states, in a situation where it is completely isolated from its environment, Rabi oscillations would occur between the two Néel states with a period of $T_{\mathrm{Rabi}} = \hbar\pi/V$. Therefore, in this fully decoupled case, the spin chain would oscillate between both states with a very short period $< 1 \cdot 10^{-6}\,\mathrm{s}$ (assuming a value of $V \approx 2\,\mathrm{neV}$, which was determined for short Fe chains on $Cu_2N/Cu(100)$[64]). If substrate electrons, which contribute to a decoherence of the quantum states, are taken into account and the spin chain is again initialized in one of the Néel states, the system evolves to an equal population of both Néel states. The time scale at which this process takes place is given by $\Gamma = \hbar/T_2^*$ where Γ is the decoherence rate of a Néel state and T_2^* is the inverse dephasing time[64].
If we assume the realistic case, that the decoherence rate is very fast compared to the Rabi evolution, the switching rate between the two Néel states can be approximated by

$$\frac{1}{\tau_{0\to1}} = \frac{2V^2}{\hbar\Gamma}, \tag{2.35}$$

which shows that a high dephasing rate and a small coupling between the Néel states favors long switching lifetimes.
As a rough assumption, we can approximate the dephasing rate as the electron collision rate[183]

$$\Gamma = N \cdot T_{\mathrm{atom}}(E_{\mathrm{F}}) \frac{k_{\mathrm{B}} T}{2\pi} P_{\mathrm{Spin}}(N_1 \rightarrow N_1) \tag{2.36}$$

where N is the chain length in numbers of atoms, $T_{\mathrm{atom}}(E_{\mathrm{F}})$ is the transmission of electrons at the Fermi level to an atom of the chain and $P_{\mathrm{Spin}}(N_1 \rightarrow N_1)$ is the elastic scattering probability that an electron is scattered at a chain site. Therefore, Equation 2.36 highlights that the dephasing rate can be drastically reduced if there are no substrate electrons at the Fermi level, which would result in a situation where the spin chain is largely decoupled with a strongly increased switching rate and eventually should display the aforementioned superposition of the two Néel states[64]. Should the dephasing rate, however, be finite, as it would be the case if the spin chain is positioned on a normal metal, a switching between the two Néel states would be expected at a time scale ~ 0.01 s (assuming a decoherence rate of 20 ps[64]) and is therefore accessible in STM measurements[50,184]. In the latter limit, the switching dynamics between the two Néel states are then governed by direct tunnel electron-induced transitions and by spin-waves[181,185–187].

3 Experimental methods and setups

In this chapter I will introduce the basic working principle of the STM, including a theoretical description of the quantum tunneling effect, spin-polarized tunneling and the different measurement modes, that are employed throughout this thesis (Section 3.1). The experimental UHV setups used for ultra-low temperature measurements and for growth studies as well as the design of an STM head are presented in Section 3.2. Last, preparation methods for clean Nb(110) & Ta(110) single crystals, the methods used for atom manipulation and procedures to obtain spin-polarized tips are introduced in Section 3.3.

3.1. Scanning tunneling microscopy

As already indicated by the name of the method — scanning tunneling microscopy (STM) — it relies on two major concepts, one being the quantum tunneling effect and the other being the real-space scanning of a given sample. The former is a well known effect that was predicted and observed in the last century and is part of the success story of quantum mechanical effects. Apart from its great use in the description of physical effects as e.g., the α decay[188], it is also employed as a method to characterize solid-state materials in planar tunnel junctions, where the material of interest is typically separated from a metallic contact by an insulating barrier.
Using this concept as a basis, G. Binnig and H. Rohrer introduced the concept of an STM in 1982[45,46] where they replaced the metallic contact with a metallic tip, the insulating layer with a vacuum barrier and additionally

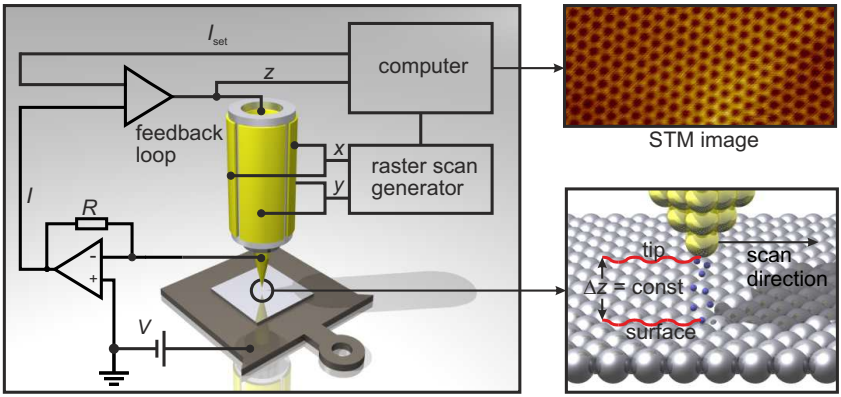

Figure 3.1.: Rendered illustration of an STMs working principle. The tip and the piezo tube are colored yellow, the sample is the reflective square-shaped foil on a gray sample holder. The electric circuit and the feedback loop are sketched by black lines and labels. A rendered image of an atomically sharp tip and a surface is shown in the bottom right panel and illustrates the actual measurement process. An exemplary output image is shown in the top right panel. Figure taken from Ref. [189].

introduced scanning with a piezoelectric motor. As I will demonstrate in Subsection 3.1.1, the tunneling current between the metallic tip and the surface of a given sample depends — among other parameters — most strongly on the tip-sample distance. Therefore, one can relate the tip-sample distance to a certain current. By actively controlling this distance with a feedback loop, which regulates the tip-position Z such that a constant current is measured, one can obtain an image which, to first order, is given by the topography of the sample's surface. The actual process of the image generation using an STM is illustrated in Figure 3.1. To begin with, the tip can be positioned in-plane (x,y) and perpendicular to the sample surface (Z) using a piezoelectric tube (yellow). Furthermore, one applies a constant bias voltage V_{bias} between the tip and the sample, such that a tunneling current I(pA-nA) flows between both electrodes.

As described above, one can now regulate the tip-sample distance such that this current is kept constant (bottom right panel of Figure 3.1). If one now scans the tip in the $x-y$-plane and links every spatial position to a certain Z-value, which was required to maintain the constant current, one obtains a topographic image of the surface (top right panel of Figure 3.1). Under good experimental conditions, i.e. with an atomically sharp tip, a clean surface and a noise-free environment etc. this method is so precise and accurate, that it's possible to obtain images of surfaces with atomic resolution. In 1986 Binnig and Rohrer were awarded with the Nobel prize in physics for designing the STM[190].

3.1.1. Quantum tunneling

An instructive approach to quantum tunneling is obtained by discussing the 1D problem of a square-shaped potential barrier, which is performed along the lines of Ref. [191] here. An illustration of the physical problem is shown in Figure 3.2. The potential $\mathrm{V}(\mathrm{x})$ is defined as zero everywhere, except for the barrier region which extends from $0 \leq x \leq a$, where the potential is set to V_0. In classical mechanics, a particle with an energy lower than the barrier $E < V_0$ can't cross the potential barrier. This assumption does not hold true if we treat the problem quantum mechanically:
To begin with, we separate the problem into three regions, as indicated by roman numericals in Figure 3.2. We then assume that each of the regions has a wave function of the form:

$$\psi(x) = \begin{cases} \mathrm{e}^{ikx} + A \cdot \mathrm{e}^{-ikx} & x < 0 \\ B \cdot \mathrm{e}^{-k'x} + C \cdot \mathrm{e}^{k'x} & 0 \leq x \leq a \\ D \cdot \mathrm{e}^{ikx} & a < x \end{cases} \tag{3.1}$$

with $k = \sqrt{2mE}/\hbar$ being the wave vector and $k' = \sqrt{2m(V_0 - E)}/\hbar$. Since the wave functions above must obey the continuity conditions, one

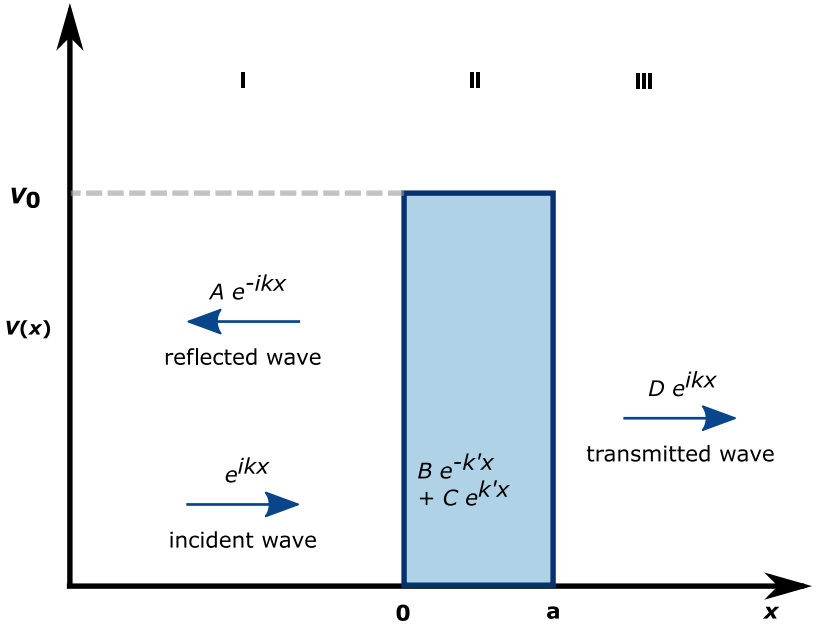

Figure 3.2.: Illustration of a 1D rectangular potential barrier with a height of V_0 and a width of a. Roman numerals indicate the areas into which the problem is separated. Blue arrows and black labels indicate the regional solutions of the Schrödinger equations.

can solve this equation system for the four coefficients A, B, C and D. The absolute square of D is equal to the transmission, i.e. the probability of a particle crossing the barrier. In the limit of $k^{'}a >> 1$ one can derive the following equation for the transmission

$$|D|^2 \simeq \frac{16k^2k'^2}{(k^2+k'^2)^2} \cdot \mathrm{e}^{-2k'a}. \tag{3.2}$$

From Equation 3.2, it is apparent that there is a nonzero probability that a particle crosses the barrier, even for $E < V_0$. The strong dependence of the tunneling current on the tip-sample distance (a in this model) is apparent from the exponential factor in Equation 3.2.
If we translate this simplified picture to the STM setup, the vacuum between tip and sample can be seen as the tunnel barrier of width a and the regions I and III are considered as the sample and the STM tip. This results in an exponential dependence of the measured current on the width a of the barrier, i.e. the spacing between the STM tip and the sample, which was mentioned in the previous section[191,192].

Bardeen Ansatz

A better understanding of the tunneling effect in STM and STS measurements, which takes the electronic structure of a given sample and tip into account, is the transfer Hamiltonian approach by Bardeen. It has proven to be a good approximation of the exact solution as long as the DOS in the tunneling barrier is low[193].
As a foundation, let us assume that the tip and sample are both metals (referred to as electrodes in the following) which are separated by a tunneling barrier extending from x_a to x_b and let us define two many-particle states Ψ_0 and Ψ_mn, where the latter describes the state after one electron from metal a in state m was transferred to metal b in state n. The quasiparticle wave function Ψ_0 is a good solution for $x < x_\mathrm{a}$ and drops to zero for $x > x_\mathrm{b}$, the opposite is valid for Ψ_mn, meaning that it is a solution for $x > x_\mathrm{b}$ but not for $x < x_\mathrm{a}$.
We can describe the system by a Hamiltonian of the form

$$\hat{H} = \hat{H}_0 + \hat{H}_\mathrm{T} \tag{3.3}$$

where $\hat{H}_\mathrm{T}$ is the transfer Hamiltonian describing the tunneling process from one electrode to the other and $\hat{H}_0$ is the sum of the Hamiltonians

that describe the left and right electrode. After applying first order time-dependent perturbation theory we derive transition matrix elements of the form

$$M_{\mathrm{mn}} = \int \Psi_0^* \hat{H}_{\mathrm{T}} \Psi_{\mathrm{mn}} d\tau, \tag{3.4}$$

which results in a transition probability from the left electrode to the right electrode that is given by

$$j = \frac{2\pi}{\hbar} |M_{\mathrm{mn}}|^2 \frac{\mathrm{d}n_{\mathrm{r}}}{\mathrm{d}E_{\mathrm{r}}}. \tag{3.5}$$

Here, $\frac{\mathrm{d}n_{\mathrm{r}}}{\mathrm{d}E_{\mathrm{r}}}$ is the right electrode's DOS[192,194].
For the calculation of the tunneling current the transition rates (Equation 3.5) have to be multiplied by the electron charge e and the Fermi-Dirac distributions of the electrodes, which determine the occupation of fermionic states in both electrodes at finite temperatures T $>$ 0 K:

$$f_{\mathrm{l,r}}(E - E_{\mathrm{F}}) = \frac{1}{\mathrm{e}^{\frac{E-E_{\mathrm{F}}}{k_{\mathrm{B}}T}} + 1}. \tag{3.6}$$

The net current is then given by

$$\begin{aligned} I = I_{\mathrm{rl}} - I_{\mathrm{lr}} = \frac{4\pi e}{\hbar} \cdot \int |M|^2 N_{\mathrm{l}}(E - E_{\mathrm{F}}) N_{\mathrm{r}}(E - E_{\mathrm{F}} + eV) \\ [f_{\mathrm{l}}(E - E_{\mathrm{F}}) - f_{\mathrm{r}}(E - E_{\mathrm{F}} + eV)] \mathrm{d}E \end{aligned} \tag{3.7}$$

where we assume that the transition matrix elements M_{lr} and M_{rl} are equal (independent of the direction) and are summarized to M. Furthermore, the DOS of the left and right electrode are now labeled $N_{\mathrm{r,l}}(E - E_{\mathrm{F}} + eV)$ and V indicates the applied bias voltage between both electrodes.
If we consider the case of temperatures close to 0 K, the Fermi-Dirac distributions (Equation 3.6) are approximated by step functions. The

tunneling current then only depends on the integral of the DOS and the transition matrix. Differentiating Equation 3.7 with respect to V and assuming a constant DOS of the tip (good approximation for metals), we find that the differential conductance is proportional only to the DOS of the sample and the transition matrix. Therefore, $\mathrm{d}I/\mathrm{d}V$-spectra are often considered as a probe for the LDOS of the sample. However, this is a drastic oversimplification of the tunneling processes, as the tip DOS is not necessarily constant. Therefore, a calculation of the sample's DOS from a $\mathrm{d}I/\mathrm{d}V$-spectrum requires an appropriate model for the tip[192].

3.1.2. Superconductor-Insulator-Superconductor junctions

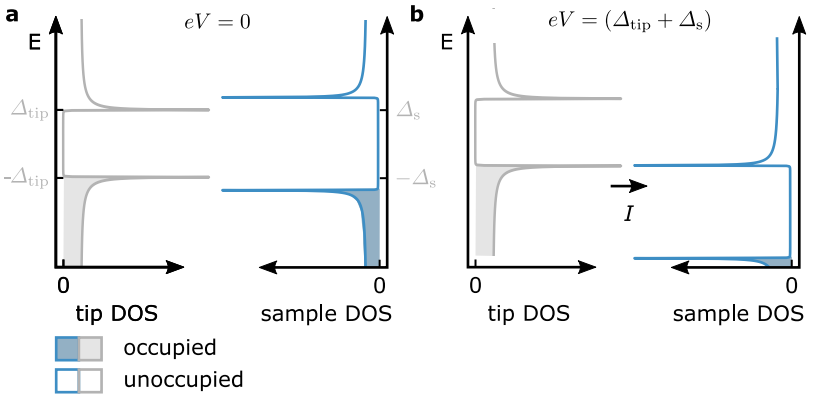

Figure 3.3.: a and **b** Illustration of a SIS tunnel junction at $eV = 0$ (**a**) and $eV = (\Delta_{tip} + \Delta_s)$ (**b**). Single particle tunneling processes are only possible in scenario **b**, where electrons may tunnel from the occupied coherence peak of the tip's DOS to the unoccupied states of the sample's DOS.

Superconducting STM tips are used throughout this thesis for all measurements where a high energy resolution is required. As we have seen in the previous section, the use of a metallic tip results in a probing of the

sample's DOS with a constant tip DOS around the Fermi level, which is smeared out by the Fermi-Dirac distribution (Equation 3.6). Therefore, spectroscopic features in $\mathrm{d}I/\mathrm{d}V$-spectra would be considerably broadened due to the finite measurement temperature. We overcome this limit by employing superconducting tips, which do not have a constant DOS around the Fermi level, but are rather gapped out (see Figure 2.3 and Figure 3.3). In this case, one probes the sample's DOS with the extremely sharp coherence peaks of the tip's DOS, resulting in very sharp in-gap features in $\mathrm{d}I/\mathrm{d}V$-spectra.

However, this method has the downside that all in-gap features are shifted to higher biases by Δ_{tip} in $\mathrm{d}I/\mathrm{d}V$-spectra. This is illustrated by the sketches in Figure 3.3. At a bias of $eV = 0$, no single particle tunneling processes are allowed (Figure 3.3a). If a bias of $eV = (\Delta_{\mathrm{tip}} + \Delta_{\mathrm{s}})$ is applied to the sample, electrons in the occupied states of the tip's coherence peak can tunnel into the unoccupied states of the sample's coherence peak (Figure 3.3b). Therefore, the coherence peaks of a sample with Δ_{s} appear at a bias voltage of approximately $eV = (\Delta_{\mathrm{tip}} + \Delta_{\mathrm{s}})$ in $\mathrm{d}I/\mathrm{d}V$-spectra.

It is easily seen that this conclusion is true for all in-gap states of the sample. To obtain the actual energies of the features observed in a $\mathrm{d}I/\mathrm{d}V$-spectrum, one can simply subtract the tip gap Δ_{tip} from the bias voltages at which this feature is observed. A more accurate method that is employed to display all features at their actual energy in this thesis is the post-processing of raw data by numerical deconvolution as described in Ref. [195]. As an input for this method we describe the tip's DOS using a Dynes function (see Equation 2.25), which in return requires knowledge about the superconducting gap of the tip. We typically obtain accurate values of Δ_{tip} for a given microtip by analyzing multiple Andreev reflections[196] in $\mathrm{d}I/\mathrm{d}V$-spectra obtained with a small tip-sample distance. Since we acquire them prior to most measurements, we have an accurate value of Δ_{tip} and can precisely deconvolute $\mathrm{d}I/\mathrm{d}V$-spectra. As apparent from Equation 2.25, we require further input parameters, one

being the quasiparticle lifetime, which leads to a broadening and is typically found to be $\gamma = 1 \cdot 10^{-6}$ eV in our setup[61], and the measurement temperature of $T = 320$ mK[197].

3.1.3. Spin-polarized tunneling

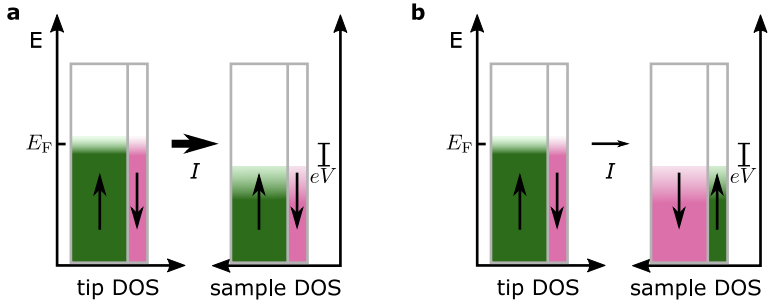

Figure 3.4.: a and **b** Illustration of the spin-resolved DOS of a tip and a sample. The electrodes are in a configuration where the majority of electrons are spin up in both cases (**a**) or spin up in the tip and spin down in the sample (**b**). The contributions to the tunnel current are indicated by the thickness of the gray arrow, which is thicker in the case of aligned majority spins and thinner in the case of anti-parallel aligned majority spins.

In order to obtain information on the magnetic state of a given sample, one can employ magnetic tips and exploit the tunnel magnetoresistance (TMR) effect, which was first discovered by M. Julliere in 1975[198] in planar tunnel junctions of FM films. The effect of TMR is schematically shown in Figure 3.4. Let us assume a FM electrode that has an energy-independent spin polarization, as illustrated in Figure 3.4a, where the spin up electrons are the majority charge carriers. In a situation where the second electrode is similarly spin-polarized (spin up electrons are the majority spin channel) and if one applies a finite bias voltage V, a large tunnel current flows between the electrodes, which does not require

spin-flips of the majority charge carriers in the tunnel junctions.
If the spin-polarization of the second electrode is inverted, as illustrated in Figure 3.4b, the situation is altered and a lower net tunneling current flows between the two electrodes. In a simplified model, the TMR is described by[199]

$$I = I_0(1 + P_{\text{tip}} P_{\text{s}} \cos(\theta)), \tag{3.8}$$

where I_0 is the net spin-averaged current, P_{tip} and P_{s} are the spin polarizations of the tip and the sample, and θ is the relative angle between the two electrodes' magnetizations, i.e. $\theta = 0$ (π) in Figure 3.4a (b).
The realization of the TMR effect in combination with an STM, which was demonstrated by R. Wiesendanger in 1990[47], enabled the route to a uniquely powerful method (SP-STM). It is capable of spin-resolved measurements with atomic resolution. For a detailed review on SP-STM see Ref. [48].

3.1.4. Measurement modes

In the following, I proceed to link the measurement modes, which were used throughout this thesis, to their respective names. Furthermore, I explain the general experimental procedure of obtaining STM images in the given modes.

STM images

Images obtained in the mode commonly called constant-current mode in the literature, are referred to as STM images in the following chapters. The measurement procedure is the following: We apply a bias voltage V_{bias} to the sample upon which the tip-sample distance is controlled by a feedback loop such that a constant current I is achieved. Combining this procedure with the scanning of the tip over a predefined spatial extent

with a given scanning speed and pixel density, we obtain an STM image.

$\mathrm{d}I/\mathrm{d}V$-spectra

$\mathrm{d}I/\mathrm{d}V$-spectra are obtained using a standard lock-in technique. A modulation with an amplitude (root mean square (rms) value) V_{mod} is added to the bias voltage V_{bias} with a modulation frequency of $f_{\mathrm{mod}} = 4142\,\mathrm{Hz}$. Before performing a $\mathrm{d}I/\mathrm{d}V$-spectrum, the STM's tip is stabilized at a certain bias voltage V_{stab} and tunneling current I_{stab}. After an initial settling time at those parameters has passed, the feedback loop is turned off. The bias voltage is then swept in a defined range V_{sweep} and the frequency components of the current signal that are modulated by V_{mod} are recorded, resulting in a $\mathrm{d}I/\mathrm{d}V$-curve.

$\mathrm{d}I/\mathrm{d}V$-grids, -maps and -line profiles

$\mathrm{d}I/\mathrm{d}V$-grids and $\mathrm{d}I/\mathrm{d}V$-line profiles are obtained by recording $\mathrm{d}I/\mathrm{d}V$-spectra on a predefined spatial grid. Thereby, one obtains a map of the $\mathrm{d}I/\mathrm{d}V$-signal at every bias in the predefined sweep range $V \in V_{\mathrm{sweep}}$. $\mathrm{d}I/\mathrm{d}V$-maps are the 2D maps of an energy-slice of such a grid evaluated at a given bias voltage. $\mathrm{d}I/\mathrm{d}V$-line profiles are measured similarly to $\mathrm{d}I/\mathrm{d}V$-grids. The only difference is that the spatial grid which is positioned over the structure of interest is 1D in the case of $\mathrm{d}I/\mathrm{d}V$-line profiles.

Constant-contour maps

Constant-contour maps are measured by repeated scanning of individual lines of STM images. In a first sweep, a line is measured as it would be the case in a regular STM image. The Z-signal of this sweep is saved.

In the next sweep, the bias voltage V_{bias} is set to a previously specified value, for which one wants to obtain a $\mathrm{d}I/\mathrm{d}V$-map. The feedback loop is turned off and the previously recorded Z-signal is retraced. The current signal and the $\mathrm{d}I/\mathrm{d}V$-signal are recorded throughout this retracing. This procedure enables the measurement of $\mathrm{d}I/\mathrm{d}V$-maps at biases located in the superconducting gap of the sample, which would not be possible using conventional STM images. The advantage of this method over a $\mathrm{d}I/\mathrm{d}V$-grid, is the fast acquisition time and, therefore, the much higher achievable pixel density. On the downside, one has to select the bias voltages of interest prior to the measurement, while the measurement of a $\mathrm{d}I/\mathrm{d}V$-grid yields $\mathrm{d}I/\mathrm{d}V$-maps at all bias values in V_{sweep}.

Random telegraph noise measurements

Neglecting pump-probe schemes, the best temporal resolution achievable with an STM is obtained by moving the STM tip into a stationary position over a subject of interest and by recording the current signal as a function of time. Thereby, one avoids two limiting factors that STM images or $\mathrm{d}I/\mathrm{d}V$-maps have: Firstly the actual scanning is avoided, which would cause a large time delay between two measurement points. Secondly, by recording the I-signal instead of the $\mathrm{d}I/\mathrm{d}V$-signal one avoids the additional time constraints that a lock-in would impose. However, the current-to-voltage conversion of the tunneling current which is performed by a transimpedance amplifier with a limited bandwidth, as well as the resonance frequencies of a given experimental setup in the kHz regime limit the sampling rate to approximately 1 kHz, corresponding to a time resolution of 1 ms.
To study the spin dynamics of artificial chains in this thesis, we employ the random telegraph noise method. The raw data (a time trace) is obtained by stabilizing a spin-sensitive STM tip over a particular atom of a given artificial structure at parameters V_{stab} and I_{stab}. Afterwards, we

turn off the feedback loop and record a time trace of the current signal. If the spin chain has a bistable magnetic ground state, and assuming that the STM tip is magnetically sensitive to those states, we observe a current signal which abruptly switches between two current states. The switching in the I-signal corresponds to a switching between the bistable magnetic states of the chain, which we are able to observe due to TMR. After a statistically relevant amount of switching events have occurred in a given time trace (typically ~ 1000), we stop the measurement and turn the feedback loop back on again.
The time traces are then analyzed in order to extract three characteristic parameters of the dynamics. To begin with, one can determine the arithmetic averages τ_1 and τ_0 of the randomly distributed lifetimes of the high current state τ_1^i and the low current state τ_0^i

$$\tau_{0,1} = \frac{1}{N} \sum_i \tau_{0,1}^i \tag{3.9}$$

where N is the total number of switching events. From τ_0 and τ_1 one can then calculate the average lifetime τ or switching frequency ν by taking the arithmetic average

$$\frac{1}{\nu} = \tau = \frac{\tau_0 + \tau_1}{2}. \tag{3.10}$$

Last, we may determine the lifetime asymmetry A, which describes the asymmetry in the temporal population of the two spin states by

$$A = \frac{\tau_1}{\tau_0 + \tau_1}. \tag{3.11}$$

3.2. Experimental setups

The experimental results presented in this thesis were obtained in two distinct UHV chamber systems, which generally serve different purposes.

To begin with, all measurements characterizing transition metal adatoms on superconducting surfaces were performed in an ultra-low temperature setup, which is described in Subsection 3.2.1. On the other hand, measurements which served the purpose of surface characterization and growth optimization were performed in a distinct UHV chamber system hosting a variable-temperature scanning tunneling microscope (VT-STM), which is described in Subsection 3.2.2.

3.2.1. The ultra-low temperature STM setup

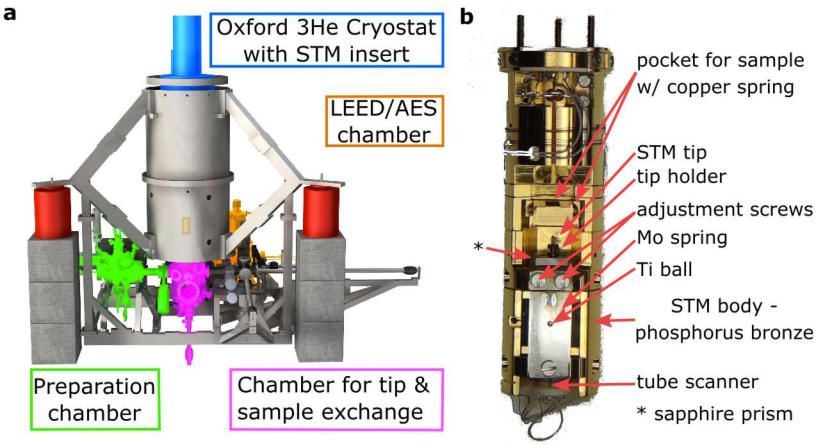

Figure 3.5.: a Schematic of the UHV setup that is used for ultra-low temperature and B-field dependent measurements. The three UHV chambers and the ^{3}He cryostat are color-coded and labeled. The yellow square marks the position of the STM head in the measurement mode. Taken from Ref. [200]. **b** Image of the STM head, where red arrows and labels indicate the main components.

A detailed description of the ultra-low temperature setup that was used throughout this thesis is presented in Refs. [201, 202] by J. Wiebe and A. Wachowiak, who designed and constructed the STM and the UHV

chambers. A rendered image of the three UHV chambers and the ^{3}He cryostat is shown in Figure 3.5a. To begin with, the setup features a UHV chamber that is devoted to the cleaning of samples and the focused evaporation of metallic films onto sample surfaces. This so-called preparation chamber includes a sputter gun that can bombard a sample's surface with Ar ions. To do so, Ar atoms are dosed into the vacuum using a needle valve located in close proximity to the gun, where they are then ionized. The positively charged Ar ions are then accelerated towards the grounded sample using a high voltage. The bombardment of a given sample with an unreactive noble gas species of high mass enables the removal of the topmost surface layers of the sample.
To enable the healing of freshly sputtered samples and to flash samples to high temperatures, the preparation chamber is equipped with a home built e-beam heating stage. A fine tungsten filament is heated up until it glows by passing a large current through it, which causes it to thermally emit electrons. By applying a high voltage to the sample, which is held close to the filament by a tungsten plate (or tungsten rods in the UHV chamber system described in Subsection 3.2.2), the electrons are accelerated onto the sample. Thereby, one can heat samples up to a temperature of $T > 2800\,^\circ$C. At low heating powers/temperatures, the sample temperature can be estimated with a pyrometer. However, as the preparation of Nb(110) and Ta(110) both require temperatures well above $2000\,^\circ$C and since the repeated preparation of both sample types results in the deposition of thin reflective layers on the inside of window flanges, we typically don't measure the temperature but achieve reproducible heating cycles by controlling the heating power.
The preparation chamber is equipped with commercially available EFM3 e-beam evaporators of *Focus*. A long rod that is mounted on a high voltage feedthrough is located in the very center of these evaporators. Depending on the particular evaporant, the evaporator material is attached to the tip of this rod in the form of small pieces that are loaded into a tungsten crucible or as a rod made form the evaporant, which is fixed by

a molybdenum barrel connector. In a process that is similar to the one described above for the heating stage, the evaporant can be heated by a filament and by applying a high voltage to it.
Finally, the preparation chamber is equipped with a mass spectrometer, which enables the analysis of the residual gas inside the chamber.
The low-energy electron diffraction (LEED) chamber is highlighted in orange in Figure 3.5a. Its main feature is a LEED setup that was bought from *Omicron*. It consists of an electron gun (uses a LaB_6 filament), a fluorescent screen and 4-grid optics. Additionally, the chamber is equipped with a manipulator capable of resistive heating, dc heating and reading out currents.
The centered UHV chamber is connected to the ^{3}He cryostat (blue) and can be used to exchange samples and STM tips (purple). In the measurement mode, the STM head is located inside the ^{3}He cryostat as indicated by the yellow rectangle in Figure 3.5a. For the purpose of sample and tip exchanges, the STM head has to be moved down from the cryostat using an electrical motor. Additionally, a triple e-beam evaporator (three different cells which can be equipped by three different evaporants) is positioned in such a way, that it can be directed onto the STM head, if it is moved down into the transfer chamber, while the sample maintains a temperature below ~ 10 K because of a radiation shield mounted around the STM head.
An image of the STM head, which was taken while it was removed from the UHV setup, is shown in Figure 3.5b. Red arrows indicate the crucial parts of the STM head. STM images are obtained as described in Section 3.1 (fine movement in the (x, y)-plane and the Z-direction relies on the piezo tube). The coarse motor, which enables an approach of the tip towards the sample until the travel of the piezo tube is large enough to maintain a tunnel current, is achieved by the slip-stick movement, similar to the walker principle introduced by Pan[203]. Unfortunately, the shear piezos, which are in contact with the STM body and the sapphire, can not be seen in Figure 3.5b. Four of them are hidden behind the sapphire

and two additional ones are glued to the bridge, which is located behind the Mo spring plate and the Ti ball. The screws pressing the Mo spring onto the Ti ball can be used to change the pressure of the shear piezos onto the sapphire *in situ*.
The ^{3}He evaporation refrigerator can cool the STM down to 320 mK in a single-shot mode, where the system retains the base temperature for approx. 27 h. Afterwards, the ^{3}He has to be reliquified, in order to cool the STM down to base temperature again. This period of 27 h imposes some constraints on the possible measurements, e.g. for the B-field dependent measurement series of spin lifetimes in Chapter 5 where the time limit set by the cryostat prevents the measurement of statistically relevant spin lifetimes with $\tau > 20$ s.
The ^{3}He system is located in the UHV part of the cryostat, which is surrounded by a ^{4}He bath including a superconducting magnet with $B \leq 12$ T applicable in Z-direction (perpendicular to the sample surface), a shield filled with liquid N_2 and an outer vacuum chamber, which decouples all components from one another as good as possible.
All UHV chambers are pumped down to typical base pressures of $\sim 1 \cdot 10^{-10}$ mbar where turbomolecular pumps and pre-vacuum pumps are used to reach a rough vacuum. Additionally, ion getter pumps, non-evaporable getter pumps, titanium sublimation pumps and the cryogenic pumping effect of the ultra-cold components of the insert lead to very good UHV conditions during measurements and sample/tip transfers.

3.2.2. The variable temperature STM setup

The second UHV setup used in this thesis is a commercial Omicron UHV chamber setup, in which we typically achieve a base pressure of $1 \cdot 10^{-11}$ mbar. Apart from an overall more compact design, the system is equipped with similar preparation tools as the ultra-low temperature system described in Subsection 3.2.1. The major difference between both

setups is the STM instrument and the cryostat. The home-built VT-STM (similar to the one described in[204]) is cooled to 30 K using a flow-cryostat operated with liquid helium throughout this work. The main advantage of this system compared to the ultra-low temperature setup is the fact that the STM head is not moved into a cryostat, but it is mounted on an eddy current damping stage on a flange of the UHV chamber. Therefore, sample transfers are easy and quick which is ideal to study the growth and preparation of novel sample systems, where multiple preparation attempts a day are desirable.

3.3. Preparation of samples and tips

Two single crystal substrates are used in the course of this thesis. In particular, I investigate the following sample systems: Nb(110), Ta(110) and thin films of high-Z materials grown on Nb(110). As single crystals of niobium and tantalum with a (110)-cut are prepared similarly (except for the exact temperature necessary during flashes), I will only introduce the preparation of Ta(110) in Subsection 3.3.1. Interested readers are referred to the detailed descriptions in Refs. [200, 205, 206] regarding the preparation and the properties of clean Nb(110). As the growth of iridium and gold on clean Nb(110) are fundamental results of my thesis, they are presented in the *Results* chapter in Section 4.5. In Subsection 3.3.2, I will introduce some important details regarding STM tip-induced atom manipulation and its reproducibility using the example of Mn on Ta(110). Parts of the following experimental results, text and figures are published in Ref. [197].

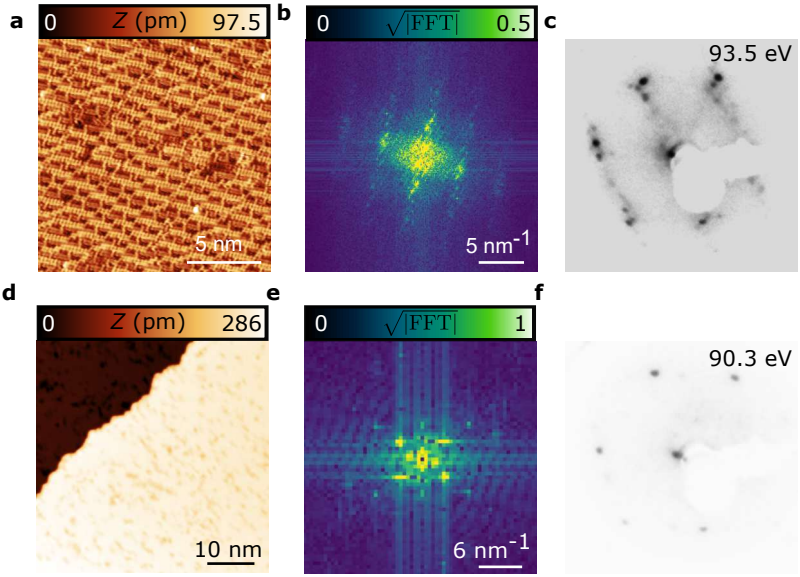

Figure 3.6.: **a-c** Ta(110) surface covered by an oxygen-induced reconstruction, which was obtained by flashing the sample with a power of 250 W. The sample is characterized using an overview STM image displaying the atomic Ta rows of the oxygen-induced reconstruction (**a**), the 2D-fast Fourier transformation (FFT) of an STM image with atomic resolution of the oxygen-induced reconstruction (**b**) and a LEED pattern obtained at 93.5 eV (**c**). **d-f** Characterization of clean Ta(110), which was prepared by flashing the sample with a power of 360 W. It is characterized by an overview STM image (**d**), the 2D-FFT of an atomically resolved STM image (**e**) and a LEED pattern measured with a beam energy of 90.3 eV (**f**). Measurement parameters: **a** and **b** $V_{\text{bias}} = -20\,\text{mV}$, $I = 2\,\text{nA}$, **d** $V_{\text{bias}} = 5\,\text{mV}$, $I = 1\,\text{nA}$, **e** $V_{\text{bias}} = 10\,\text{mV}$, $I = 1\,\text{nA}$.

3.3.1. Preparation of clean Ta(110)

Along with the renewed interest in superconducting surfaces, which was spiked by promising theoretical predictions as the realization of MBS in adatom chains or topological insulator-superconductor heterostructures, new attempts to prepare clean surfaces of long-thought uncleanable elements were initiated. Two particularly intriguing candidates are Ta(110)[207] and Nb(110)[206]. Here I present a novel method to clean Ta(110), which in contrast to the previously reported ones does not include high temperature annealing cycles at 2500 K for multiple hours[207] or annealing in oxygen atmosphere[208], where the latter seems counterproductive given that oxygen is the main contaminant of tantalum. In the following, I demonstrate that a surface quality similar or even better than previously reported is achievable by consecutive 30 s long flashes. The only downside using this method is that the sample is flashed to higher temperatures, which increases the risk of accidentally melting the single crystal. In the following, flashes are carried out by positioning the sample in such a way, that the polished side of the single crystal is oriented towards the filament.
It is crucial that the sample quality is checked after each preparation, in order to determine whether a higher flashing power/temperature is needed. An STM image, a 2D-FFT of an atomic resolution STM image and a LEED pattern of a preparation cycle where the Ta(110) single crystal was flashed with a power of 250 W are shown in Figures 3.6a-c. The well-known oxygen-induced reconstruction of Ta(110) is clearly visibile in the atomically resolved overview STM image and the 2D-FFT (cf. Ref. [207]). Stripe-like features consisting of 9-11 atoms are quasi-periodically arranged on top of the surface which looks very similar to the well-known oxygen-induced reconstruction of Nb(110)[209]. Additionally, the similarity of the LEED pattern measured on Ta(110) (Figure 3.6c) in comparison with LEED measurements of reconstructed Nb(110) (cf. Ref. [210]) suggests a similar structure of the oxygen-induced reconstruction, which

is described in the following. The reconstruction is composed of two distinct crystallographic layers: One being the Nb(110) substrate and the other is a slightly distorted face-centered cubic (fcc) layer of NbO on top of this substrate. Nb atoms form the quasiperiodic chains on top of this NbO layer, which are clearly visible in Figure 3.6a[211].
After having characterized the surface structure of oxygen-reconstructed Ta(110) and finding that it is useless for experiments with single atoms, we proceed to increase the flashing power. Furthermore, we only characterize freshly prepared samples by LEED as long as we observe a pattern similar to Figure 3.6c. Once a change in the LEED pattern is observed, we return to investigate the given sample by STM.
This procedure leads to a gradual increase of the flashing power to 360 W, where we observe a first change in the LEED pattern (see Figure 3.6f). An overview STM image and a 2D-FFT of an atomically resolved STM image are shown in Figures 3.6d and e. The overview STM image displays largely flat terraces that are covered by some residual defects that appear as dark spots, which we interpret as oxygen impurities. They cover 15 % of the clean Ta(110) regions. The 2D-FFT shown in Figure 3.6e confirms that the flat areas of Figure 3.6d are indeed clean Ta(110) and display an unreconstructed (1x1) bcc(110) surface. The LEED pattern further supports the large-scale cleanliness and absence of oxygen reconstructions on the sample surface, as it only displays sharp diffraction spots of the bcc(110) surface, which is in stark contrast to the LEED pattern of reconstructed Ta(110) in Figure 3.6c.
From our experience with the cleaning procedure of Nb(110) we expect that a cleaner Ta(110) surface with less residual oxygen atoms can be obtained by slightly increasing the flashing power. It is crucial to have an extremely low defect density in order to obtain reproducible $\mathrm{d}I/\mathrm{d}V$-spectra, since the local environment of magnetic adatoms strongly influences the YSR states as recently shown in Ref. [212].
Therefore, we increase the flashing power by 20 W to 380 W. We obtain a clean Ta(110) surface that is merely covered by 6 % of oxygen atoms (see

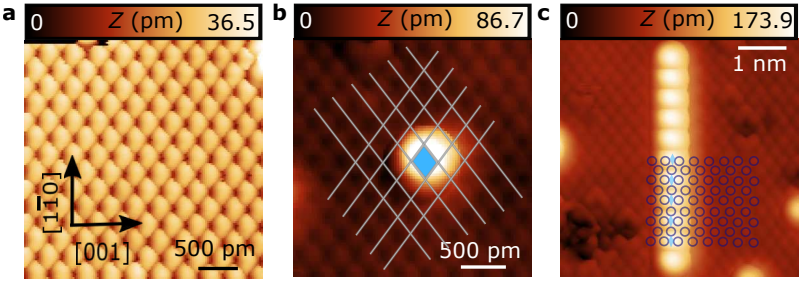

Figure 3.7.: **a** Manipulated atom image which is obtained by stabilizing the STM tip at a low bias voltage and high tunnel current (low tip-sample distance) and by approaching a single Mn atom on the Ta(110) surface, which is then loosely bound by the tip-potential. This configuration is then used to perform a regular STM image. Black arrows and labels indicate crystallographic directions, which are valid for all three panels. **b** Atomically resolved STM image displaying a single Mn atom on clean Ta(110). White lines in **b** highlight the $[1\bar{1}1]$-oriented atomic rows of Ta atoms and reveal the position of the four-fold coordinated hollow site. The adsorption site of the single Mn atom is highlighted by a blue diamond. **c** Atomically resolved STM image displaying an artificially constructed close-packed Mn chain in $[1\bar{1}0]$-direction, where dark blue circles highlight the atoms of the Ta(110) surface. Blue diamonds mark the fourfold-coordinated adsorption sites in which Mn adatoms of the chain are positioned. Measurement parameters: **a** $V_{\text{bias}} = -2.2\,\text{mV}$, $I = 121\,\text{nA}$, **b** and **c** $V_{\text{bias}} = 10\,\text{mV}$, $I = 1\,\text{nA}$.

Figures 4.16a and b). This sample is used for all experiments with Mn and Fe adatoms and their artificial structures in this thesis. We find that it is of sufficient quality to prepare defect-free structures in state-of-the-art length. Last, one should note that the required flashing power can vary between different e-beam stages and samples[197].

3.3.2. Atom manipulation of Mn adatoms on Ta(110)

After the preparation of Ta(110), which is described in Subsection 3.3.1, we deposit Mn and Fe to the sample surface. Since the sample remains in

the STM head throughout this procedure and since it is cooled below 7 K we obtain statistically distributed single Mn and Fe adatoms, which can not overcome the diffusion barrier at such low temperatures and, therefore, remain in place. The deposition is carried out in two steps: To begin with we deposit Mn atoms and subsequently carry out all investigations of single Mn atoms and artificial structures. Afterwards, we proceed to evaporate Fe atoms onto the same sample. The strict separation of the two deposition procedures allows us to unambiguously distinguish both adatom species and their physical characteristics.

STM tip-induced lateral atom manipulation[52] at typical tunneling resistances of $\sim 30\,\mathrm{k}\Omega$ (exact values depend on the specific microtip), enables us to laterally position Mn atoms with atomic precision in a highly reliable process. Upon approaching a single Mn atom at manipulation parameters (low tip-sample distance) such that it is loosely bound to the tip and by subsequently scanning a clean area of Ta(110) we obtain a so-called manipulated atom image[213] which is shown in Figure 3.7a. The image displays the geometric order of possible adsorption sites and matches an atomic resolution image of the clean Ta(110) surface in this case, i.e. the adsorption sites have the same lattice symmetry and spacing of equal sites. Therefore, we conclude that there is only a single stable adsorption site for Mn adatoms on Ta(110). Additionally, an atomically resolved STM image including an adsorbed Mn atom is shown in Figure 3.7b. White lines highlight the $[1\bar{1}1]$-directions of atomic rows of the atoms located in the topmost substrate layer. From an evaluation of the Mn atom's position in relation to this grid, we can unambiguously conclude that the only stable adsorption site of Mn atoms on Ta(110) is the fourfold-coordinated hollow site.

By employing the manipulated atom image shown in Figure 3.7a as an overlay of all regular STM images, we are able to build nanostructures composed of atomically precise positioned Mn atoms in an atom-by-atom fashion even without having an ultra-sharp STM tip. An example of such an artificial structure is shown in the atomically resolved

STM image of Figure 3.7c, which displays a close-packed ($d = \sqrt{2}a$ and $a = a_{\mathrm{Ta}(110)} = 331\,\mathrm{pm}$)[214] Mn chain consisting of eleven atoms oriented in the $[1\bar{1}0]$-direction. Dark blue circles highlight the Ta atoms located in the topmost layer of the surface and blue diamonds mark the positions of the fourfold-coordinated hollow sites, in which one would expect the Mn atoms of the chain to be positioned, based on a continuation of the Ta lattice. Since we find an excellent agreement between the Mn atoms' positions and the fourfold-coordinated hollow sites, we can unambiguously determine that the fabricated chain is indeed a close-packed chain in $[1\bar{1}0]$-direction. In particular, we find that the interatomic spacing is homogeneous along the chain and exactly matches the distance directed from the substrate. This conclusion concerning the perfect geometry of our artificially constructed chains is crucial, since if all Mn atoms in the bulk of the chain are adsorbed/coordinated equally, we can conclude that they experience similar interactions with the physical environment, e.g. the coupling strength to the Ta(110) substrate electrons or the overlap of the YSR states with neighboring Mn atoms is homogeneous throughout the chain.
While it is not necessarily possible to manipulate dimers or chains in all crystallographic directions or distances for all adatom-substrate combinations, we find that this is reliably possible for Mn on Ta(110) in all three symmetric directions $[001]$, $[1\bar{1}0]$ and $[1\bar{1}1]$ in every spacing down to the close-packed distances a, $\sqrt{2}a$ and $(\sqrt{3}/2)a$, respectively. On the other hand it is tremendously difficult to manipulate Fe atoms while maintaining a stable tip, which renders it impossible to create artificial structures. Therefore, we only study single Fe atoms with regards to their YSR states, but do not investigate artificial Fe dimers or chains throughout the course of this thesis.

3.3.3. Preparation of STM tips

For most of the measurement series in Chapters 4 and 5, where the energy resolution of YSR states and Shiba bands is decisive, we employ superconducting Nb tips (see Subsection 3.1.2). For the *ex situ* preparation of Nb tips we mechanically sharpen short pieces of Nb wire using non-magnetic wire cutters. An appropriate piece is then mechanically wedged into the tip holder. Upon moving the tip into the UHV chamber, we flash it to 50 W in order to remove contaminants. To sharpen the tip *in situ*, we apply bias pulses and/or dip the tip into the sample's surface. To magnetically functionalize the Nb tips, we pick up Mn and Fe atoms by lowering the tip-sample distance over such an adatom and by applying a slight bias pulse ($\approx 200\,\mathrm{mV}$). Afterwards, we measure a $\mathrm{d}I/\mathrm{d}V$-spectrum to check if there are YSR states at the tip.
Sections 4.1 and 4.2 are an exception with regard to the used tip. Here, we use an electrochemically etched W wire, that was flashed to 1850 K in order to remove contaminants *in situ*. Afterwards, the tip is dipped into a clean Nb(110) sample to obtain a superconducting tip.
For some of the measurements in Chapter 5 (indicated in the figure captions) we use a bulk Cr tip. This tip is prepared by glueing Cr splinters to a tip holder using conductive H20E glue. We heat the tip up to 700 K *in situ* in order to remove contaminants. Additionally, the tip is sharpened by voltage pulses once it is approached to a given sample. In order to obtain magnetically sensitive tips, we pick up magnetic adatoms until magnetic contrast is obtained on a reference chain where the spins are AFM aligned.

4 The influence of spin-orbit coupling on Shiba bands

In this chapter I discuss the experimental signatures of the influence that SOC has on MSH structures and how it manifests itself in the physics of in-gap states. The chapter is divided into five sections, each discusses a different experimental approach and/or measurable effect. The observation of a lifted degeneracy of hybridized YSR states in AFM coupled dimers of Mn atoms on Nb(110), which is shown to be a manifestation of SOC, is presented in Section 4.1. I move on to present the formation of Shiba bands and the intriguing properties of precursors of Majorana modes (PMMs) in FM coupled chains of Mn on Nb(110), focusing on the role of SOC. Furthermore, I demonstrate the need of novel ideas to increase SOC in Shiba chains to realize MBS in a hard topological gap in Section 4.2. Novel ideas to do so, which rely on the construction of tailored chain geometries of Mn adatoms on Nb(110) are presented in Section 4.3. Afterwards, I demonstrate the need to move to other substrates in order to increase SOC by a comparative study of Mn/Ta(110) and Mn/Nb(110) in Section 4.4. Last I present the approach of using proximitized high-Z materials as substrates for Shiba chains in Section 4.5.

4.1. SOC induced splitting of hybridized YSR states in AFM dimers

While the experimental results shown in this section are already part of my Master thesis[205], their interpretation and the physics discussed here

are a result of my PhD work. The experimental data, the figures and parts of the following text are published in the article

> Philip Beck, Lucas Schneider, Levente Rózsa, Krisztián Palotás, András Lászlóffy, László Szunyogh, Jens Wiebe and Roland Wiesendanger
>
> *Spin-orbit coupling induced splitting of Yu-Shiba-Rusinov states in antiferromagnetic dimers*
>
> Nature Communications, **12**:2040 (2021).

The measurements presented in the following section were obtained with a bulk W tip, which was indented into the clean Nb(110) sample multiple times in order to pick up a superconducting cluster to the tip (see Subsection 3.3.3).

Contributions from experiment and theory

The STM and STS data presented in this section were measured by Dr. Lucas Schneider an myself. We both analyzed the spectroscopic data using self-written Python and Mathematica code. Dr. Krisztián Palotás performed calculations using the Vienna Ab-initio Simulation Package (VASP). Dr. András Lászlóffy performed Korringa-Kohn-Rostoker (KKR) calculations. Dr. Levente Rózsa performed model calculations for single Mn adatoms and dimers on Nb(110).

Introduction

Roughly a decade before proposals to realize MBS in 1D chains of magnetic adatoms on *s*-wave superconductors[33,34,36,37] attracted growing interest, the interactions of YSR states in coupled magnetic impurities on superconductors were studied theoretically[168–170]. These works con-

clude, that in the case of a small-enough spacing between two coupled adatoms — smaller than the lateral extent of the YSR states of single impurities — the YSR states hybridize and form symmetric and antisymmetric combinations of the single impurity states. In the case of FM aligned adatom spins the YSR states can shift in energy compared to the single atom case, due to the Zeeman field of the second impurity. Further, the hybridized symmetric and antisymmetric states are expected to split up in energy. This behavior was observed experimentally for Fe dimers on Pb(001)[171], Cr dimers on $\beta - Bi_2Pd$[172] and for phthalocyanine molecules with a Co center on $NbSe_2$[173].
In the case of AFM coupled dimers, the theories conclude that the hybridization is weaker, since quasiparticles of antiparallel spin are preferably scattered, leading to a smaller shift in the energy of YSR states in such a dimer. However, the most striking conclusion is that the hybridized YSR states remain energetically degenerate, i.e. there is no splitting of the symmetric and antisymmetric states. This is explainable by the symmetry of an AFM coupled dimer, which is invariant under exchanging the two atoms of the dimer and flipping both spins[168,169].
A symmetry governed absence of the splitting of hybridized YSR states in AFM coupled dimers and chains would have drastic consequences on the band formation in such structures. In particular, it would mean that the nearest-neighbor hopping parameter, discussed in Subsection 2.2.6, is $t = 0$ in the case of symmetry-protected AFM coupled dimers. Since the nearest-neighbor hopping parameters are typically dominant in close-packed Shiba chains on 3D substrates, one would expect a non-dispersive or very flat Shiba band for AFM coupled chains. Recent work indicates that the next nearest-neighbor hopping of Mn adatoms on Nb(110) are already significantly reduced compared to the nearest-neighbor hopping. Therefore, one would expect a narrow band in AFM coupled chains, even if one takes the next-nearest neighbor hopping into account[60,197]. Hence, AFM coupled chains would hardly be interesting from the standpoint of tailoring TSC and MBS .

However, the absence of this splitting in AFM coupled dimers is not unambiguously confirmed, so far. While there is a study on dimers of Cr atoms on $\beta - Bi_2Pd$ with different magnetic couplings, which attempts to support these predictions, the work concludes on the magnetic interactions by only considering density functional theory (DFT) calculations[172]. Here, I present a study of artificial Mn dimers on Nb(110) where we investigate their YSR states using STS. In contrast to the previous work on AFM coupled dimers, we investigate artificial chains with similar lattice orientation and interatomic spacing as the respective dimers by SP-STM[59] to determine the magnetic coupling and support those findings by calculations applying the screened KKR method[60,215,216]. As opposed to the theoretical predictions and prior experimental publications, we find an unambiguous splitting of multi-orbital YSR states in FM- and AFM coupled dimers. These findings are explained by taking into account inversion-symmetry breaking and SOC, which are ubiquitous effects at surfaces. So far, only little theoretical work has been done including these effects in the description of YSR states[217,218].

4.1.1. Single Mn adatoms on Nb(110)

The starting point of this investigation are the in-gap states of a single Mn adatom on Nb(110), which are presented in Figure 4.1. The good sample quality of the Nb(110) substrate is apparent from the overview STM image shown in Figure 4.1c. Only few oxygen impurities (depressions) are found in this image, leaving enough room to study single Mn atoms and dimers without the influence of impurities or contaminants. A $\mathrm{d}I/\mathrm{d}V$-spectrum measured on bare Nb (black curve) and on a Mn adatom (blue curve) which is several nanometers apart from any contaminants, are shown in Figure 4.1a. The spectrum on bare Nb resembles a typical curve of a superconductor-insulator-superconductor tunnel junction at

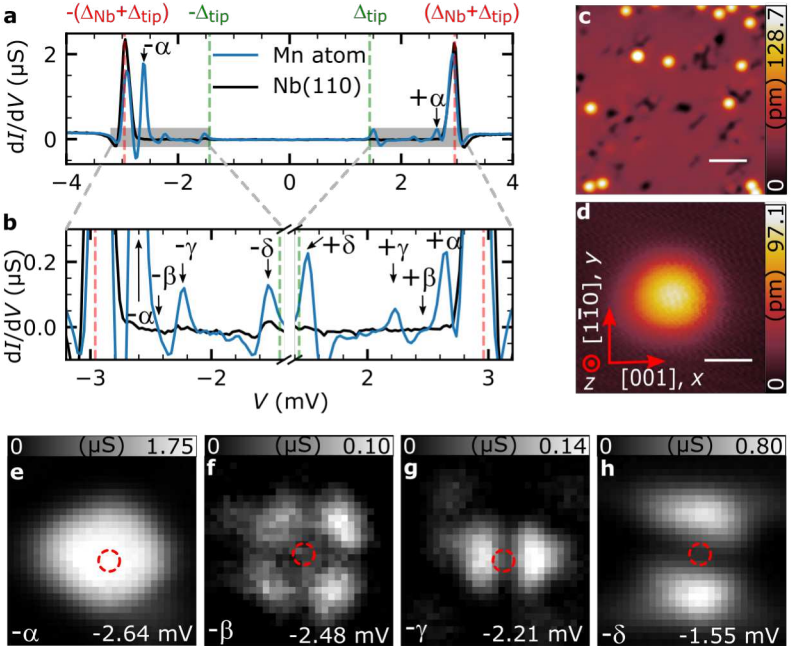

Figure 4.1.: a and **b** Raw $\mathrm{d}I/\mathrm{d}V$-spectra measured on bare Nb(110) and centered on a Mn adatom. The coherence peaks $\pm(\Delta_{\mathrm{Nb}} + \Delta_{\mathrm{tip}})$ and the tip gap $\pm\Delta_{\mathrm{tip}}$ are marked by red and green dashed lines, respectively. Black arrows and labels indicate the energetic positions of the YSR states . **b** is a magnification of **a**, to increase the visibility of the YSR states with a low $\mathrm{d}I/\mathrm{d}V$-intensity. **c** STM image of the Mn/Nb(110) sample. The white scale bar represents a length of 3 nm ($V_{\mathrm{bias}} = 100\,\mathrm{mV}$ and $I = 200\,\mathrm{pA}$). **d** STM image of a single Mn adatom, isolated from any defects and impurities. **e-h** Energy slices of a $\mathrm{d}I/\mathrm{d}V$-grid, evaluated at all biases where YSR states are observed. The white scale bar in **d** represents a length of 500 pm and is valid for panels **e-h** as well. Measurement parameters of $\mathrm{d}I/\mathrm{d}V$-spectra: $V_{\mathrm{stab}} = 6\,\mathrm{mV}$, $I_{\mathrm{stab}} = 1\,\mathrm{nA}$ and $V_{\mathrm{mod}} = 20\,\mu\mathrm{V}$.

low temperatures (see Subsection 3.1.2): Inside the superconducting gap, which is confined by the coherence peaks $\pm(\Delta_{\mathrm{Nb}} + \Delta_{\mathrm{tip}})$, the spectrum is featureless. On the other hand, the $\mathrm{d}I/\mathrm{d}V$-spectrum measured on a Mn adatom displays four pairs of in-gap states. The ones highest in intensity ($\pm\alpha$) are easily visible in Figure 4.1a, while the other states are better seen in the magnification (Figure 4.1b). We label the pairs of peaks with greek letters ranging from $\pm\alpha$ to $\pm\delta$ according to their energetic order, starting with the highest energy one.
Together with the spatial distributions of the YSR states shown in Figures 4.1e-h, we determine their multiorbital origin in the d-states of the Mn adatom (see the orientation of the $x-$ and $y-$axis in panel Figure 4.1d): $\pm\alpha$ resembles a d_{z^2}-orbital with an admixture of a $d_{x^2-y^2}$-orbital, $\pm\beta$ resembles a d_{xy}-orbital, $\pm\gamma$ resembles a d_{xz}-orbital and $\pm\delta$ resembles a d_{yz}-orbital. We explain these results by symmetry considerations: The five 3d-orbitals in a freestanding Mn impurity are all singly occupied, resulting in a spin of $S = 5/2$. Upon the adsorption on the Nb(110) surface, the adatom relaxes into a fourfold-coordinated hollow site, as revealed by the STM images in Figure 4.2, which unambiguously determine it to be the only adsorption site. For one, the atomically resolved STM image in Figure 4.2a directly reveals the adsorption geometry as apparent from the white lines, which are extrapolations of the atomic rows of Nb atoms in the substrate, and their intersection with a Mn adatom. Further, the manipulated-atom image shown in Figure 4.2b reveals that there is only one adsorption site for Mn adatoms on Nb(110), which has precisely the same symmetry and lattice constants as the substrate. This leaves only the conclusion, that Mn adatoms are adsorbed in the fourfold-coordinated hollow site, as illustrated in Figure 4.2c.
Knowing the adsorption site, we can determine the point group of such an impurity to be C_{2v}, as we find a $C2$-rotational axis perpendicular to the surface in the center of the impurity (green axis in Figure 4.2c) and two mirror planes (green σ_{xz} and red σ_{yz}) including the rotational axis. As the d_{z^2}- and $d_{x^2-y^2}$-orbitals belong to the same irreducible representation,

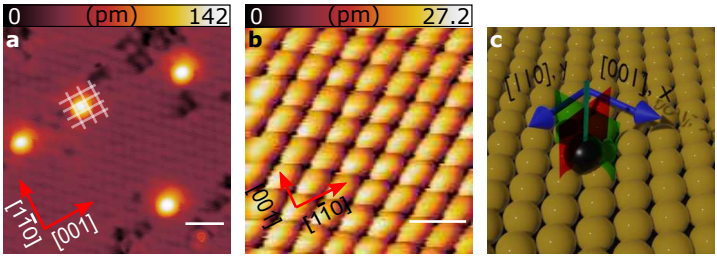

Figure 4.2.: a Atomically resolved STM image of the Nb(110) surface and Mn adatoms randomly distributed on it. Red arrows and white labels mark the crystallographic directions. White lines indicate rows of Nb atoms in the topmost substrate layer in the [001]- and [1$\bar{1}$0]-directions. The white scale bar represents a length of 2 nm ($V_{\mathrm{bias}} = 6\,\mathrm{mV}$ and $I = 1\,\mathrm{nA}$). **b** Manipulated-atom image obtained by dragging/pushing a Mn atom across the substrate and measuring an STM image at manipulation parameters ($V_{\mathrm{bias}} = -3\,\mathrm{mV}$ and $I = 50\,\mathrm{nA}$). **c** 3D rendered illustration showing the adsorption geometry of a Mn adatom (black sphere) on Nb(110) (yellow spheres). Green and red planes/axis penetrating the Mn adatom represent symmetry elements, which are described in the main text.

they may hybridize, while all other d-orbitals have distinct irreducible representations and result in a single scattering channel each. We only observe a single YSR state of the orbital origin d_{z^2}- and $d_{x^2-y^2}$ in the $\mathrm{d}I/\mathrm{d}V$-spectra of Figure 4.1, though. We speculate that the second YSR state of this symmetry is located in the coherence peak.

4.1.2. Hybridized YSR states in FM coupled dimers

To illustrate the expected physical behavior of sufficiently close-spaced adatoms hosting YSR states I proceed to discuss FM coupled $\sqrt{2}a - [1\bar{1}0]$ Mn dimers in the following. To begin with, the coupling of magnetic nanostructures in this crystallographic direction is known from SP-STM measurements[62] and *ab initio* based KKR calculations[60]. An overview of the spectroscopic results is given in Figure 4.3. A comparison of $\mathrm{d}I/\mathrm{d}V$-

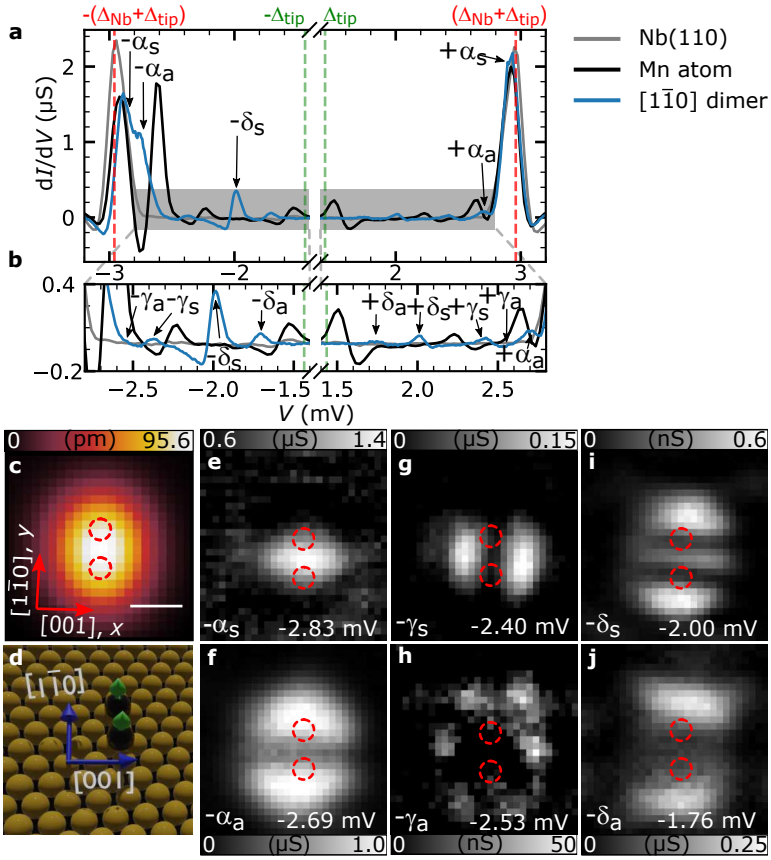

Figure 4.3.: a and **b** Raw dI/dV-spectra measured on bare Nb(110), centered on a Mn adatom and taken in the center of a $\sqrt{2}a - [1\bar{1}0]$ Mn dimer. Black arrows and labels indicate the energetic positions of the YSR states . **b** is a magnification of **a**. **c** STM image of the $\sqrt{2}a - [1\bar{1}0]$ Mn dimer used for the dI/dV-grid of panels **e-j**, which show all biases for which YSR states are found. The white scale bar represents a length of 500 pm. Red arrows indicate the crystallographic directions of the Nb(110) substrate and red circles mark the locations of the atoms composing the dimer ($V_{\text{stab}} = 6\,\text{mV}$, $I_{\text{stab}} = 1\,\text{nA}$ and $V_{\text{mod}} = 20\,\mu\text{V}$). **d** 3D rendered illustration of the $\sqrt{2}a - [1\bar{1}0]$ Mn dimer (black spheres) on the Nb(110) substrate (yellow spheres), including the spin structures (green arrows) and crystallographic directions (blue arrows).

spectra taken on the substrate, a single Mn atom and in the center of the $\sqrt{2}a - [1\bar{1}0]$ Mn dimer is shown in Figures 4.3a and b. In contrast to the four pairs of peaks, that we observe for the single impurity (black curve), we find six pairs of peaks for the dimer (blue curve). Each peak that we identify in the $\mathrm{d}I/\mathrm{d}V$-spectrum is marked by a black arrow and a label. An evaluation of the spatial distributions of all these states, which are shown in the $\mathrm{d}I/\mathrm{d}V$-grids of Figures 4.3e-j, reveals that the YSR states of the single Mn impurity (Figure 4.1) have hybridized and split into three pairs of linear combinations of the single Mn adatom's $\pm\alpha$, $\pm\gamma$ and $\pm\delta$ YSR states.

In particular, we find that one state of each pair has a nodal line in the $x-z-$plane in the center between both Mn atoms making up the dimer (Figures 4.3f, h and j), while the corresponding other state has a maximum of the $\mathrm{d}I/\mathrm{d}V$-intensity at precisely this location (Figures 4.3e, g and i). Therefore, we can unambiguously determine those states to be antisymmetric and symmetric combinations of the single atom's α, γ and δ states, respectively.

It should be noted that no YSR states resembling the single impurity β state are observed in this dimer, which we ascribe to its low $\mathrm{d}I/\mathrm{d}V$-intensity, that is already observed for the single atom in Figure 4.1. Further, one should note that the symmetry constraints on the hybridization of d-orbitals are altered, in comparison to the single atom: The d-orbitals are now distinguished by their transformation under mirroring on the σ_{yz}-plane. While the wave functions change sign for the d_{xy} and d_{xz} orbitals, they don't do so for the $d_{x^2-y^2}$, d_{z^2} and d_{yz} orbitals. As a consequence, wave functions of the first irreducible representation may hybridize with one another and the wave functions of the second irreducible representation may hybridize with one another in $\sqrt{2}a - [1\bar{1}0]$ dimers. Therefore, hanging on to the old labels of the single adatom states is not entirely correct. However, we proceed to do so for this dimer, as we do not observe any signatures of a hybridization of different YSR states.

4.1.3. Hybridized YSR states in AFM coupled dimers

Now, we move on to study the influence of the spin configuration on the YSR states states of a dimer. We recall that the absence of split YSR states is expected for AFM coupled dimers[168,169], as described in the beginning of Section 4.1. A report on short chains of close-packed Mn atoms in $[1\bar{1}1]$-direction on Nb(110) reveals that the exchange interaction is AFM by using SP-STM[59]. Furthermore, calculations based on the fully relativistic screened KKR method support this conclusion[60]. Therefore, we conclude that dimers in this geometry are AFM coupled as well.
The results obtained on a $\sqrt{3}/2a - [1\bar{1}1]$ Mn dimer are presented in Figure 4.4. Surprisingly, we find six pairs of peaks in the $\mathrm{d}I/\mathrm{d}V$-spectrum, shown in Figure 4.4a. This implies that there is a hybridization and a splitting of YSR states, since the total number of states is increased in comparison to a single Mn adatom (four peaks). A similar analysis of the spatial distributions of all states, which are shown in Figures 4.4d-i, reveals that we observe linear combinations of the single adatom's YSR states. For the single impurities α and δ states, we can straightforwardly determine symmetric combinations (Figures 4.4d and h) and antisymmetric combinations (Figures 4.4e and i) following a similar argumentation as in Subsection 4.1.2. We refer to these YSR states as $\pm\alpha_{1,2}$ and $\pm\delta_{1,2}$, respectively. The splitting is a bit more unclear for γ, where the nodal line or the $\mathrm{d}I/\mathrm{d}V$-intensity maximum in the center of the dimer is not that apparent. As it was already the case for the $\sqrt{2}a - [1\bar{1}0]$ dimer, we find no signatures of the β state, presumably due to its low intensity in $\mathrm{d}I/\mathrm{d}V$-spectra.
Overall, the assignment of the orbital origin of a particular YSR state is more difficult in the $\sqrt{3}/2a - [1\bar{1}1]$ Mn dimer, which can be explained by an extension of the symmetry considerations performed for the $\sqrt{2}a - [1\bar{1}0]$ dimer. As opposed to this geometry, the symmetry is reduced from the C_{2v} point group to a single C_2 twofold rotation around the center of the dimer. As all orbitals reduce to the same pair of irreducible rep-

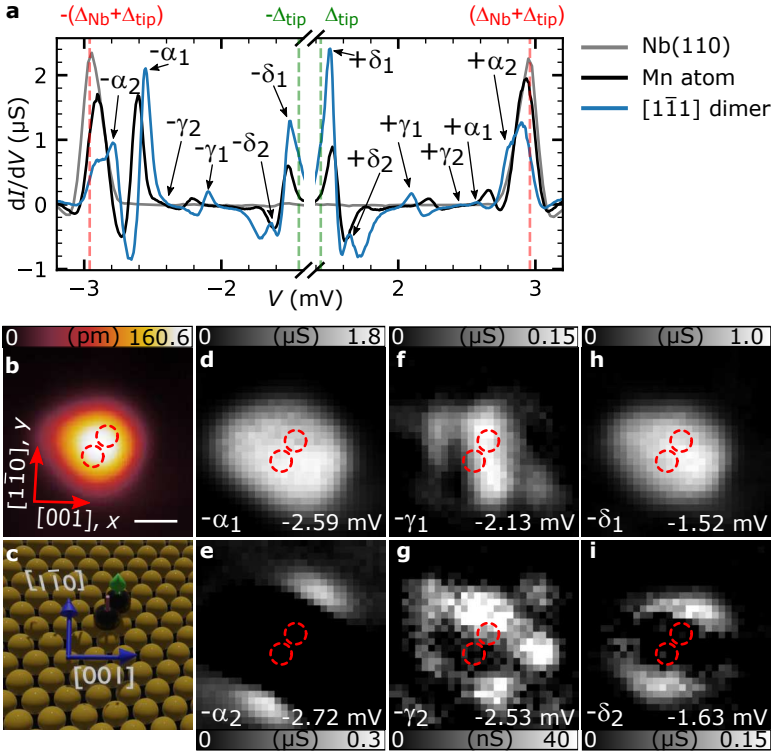

Figure 4.4.: a Raw $\mathrm{d}I/\mathrm{d}V$-spectra measured on bare Nb(110), centered on a Mn adatom and taken in the center of a $\sqrt{3}/2a - [1\bar{1}1]$ Mn dimer. The coherence peaks $\pm(\Delta_{\mathrm{Nb}} + \Delta_{\mathrm{tip}})$ and the tip gap $\pm\Delta_{\mathrm{tip}}$are marked by red and green dashed lines, respectively. Black arrows and labels indicate the energetic positions of the YSR states. **b** STM image of the $\sqrt{3}/2a - [1\bar{1}1]$ Mn dimer used for the $\mathrm{d}I/\mathrm{d}V$-grids of panels **d-i**, which show all biases for which YSR states are found. The white scale bar represents a length of 500 pm. Red arrows indicate the crystallographic directions of the Nb(110) substrate and red circles mark the locations of the atoms composing the dimer ($V_{\mathrm{stab}} = 6\,\mathrm{mV}$, $I_{\mathrm{stab}} = 1\,\mathrm{nA}$ and $V_{\mathrm{mod}} = 20\,\mu\mathrm{V}$). **c** 3D rendered illustration of the $\sqrt{3}/2a - [1\bar{1}1]$ Mn dimer (black spheres) on the Nb(110) substrate (yellow spheres), including the spin structures (green and pink arrows) and crystallographic directions (blue arrows).

resentations, any orbitals may hybridize in this dimer. Therefore, it is no longer possible to clearly assign any of the observed states a label according to their single adatom origin, in principle. The labels expressed above should be understood as an indication, which is derived from the shapes and the energetic positions of the YSR states compared to those of a single Mn atom.

4.1.4. On the role of SOC in the splitting of YSR states in AFM coupled dimers

Overall, from the experimental results in Subsections 4.1.2 and 4.1.3 we find that there is a hybridization and splitting of YSR states in both FM and AFM coupled dimers. A summary of the shifts and splittings of the $\sqrt{2}a - [1\bar{1}0]$ and the $\sqrt{3}/2a - [1\bar{1}1]$ Mn dimer is given in Table 4.1. While one should not overstress the comparison of both dimers, as the spin configuration is not the only physical difference (i.e. they additionally have a different spacing and the interaction strength can differ due to the direction-dependence of the Fermi surface), we can still conclude that the splittings and shifts are of similar size. As expected from the early theoretical treatments of AFM coupled dimers[168,169], we find that the shifts show a tendency to be lower for the AFM coupled dimer than for the FM coupled dimer. On the other hand, the splittings are comparable in size for both dimers, which is in stark contrast to these theories.
In order to explain this phenomenon it is instructive to start the theoretical treatment with some thoughts on the reason of the forced degeneracy of hybridized YSR states in AFM coupled dimers. Initially, if one assumes non-magnetic impurities for the dimer, the according Hamiltonian is invariant under time reversal. One can show that the antiunitary time reversal operator T is given by $T = i\sigma_y K$, where σ_k are the Pauli matrices

Table 4.1.: Comparison of the energetic shifts and splittings of hybridized YSR states in FM and AFM coupled Mn dimers. The shifts were calculated from the experimental results by $1/2(|E_{n,2}| - |E_{n,1}|) - |E_n|$, where E_n is the energetic position of the single atom's YSR state with $n \in (\alpha, \gamma, \delta)$ and $E_{n,2}$, $E_{n,1}$ are the energies of the respective hybridized and split YSR states in the dimer. The splittings are calculated by $|E_{n,1}| - |E_{n,2}|$.

	$\sqrt{2}a - [1\bar{1}0]$ dimer (FM)		$\sqrt{3}/2a - [1\bar{1}1]$ dimer (AFM)	
YSR state	Shift (µeV)	Splitting (µeV)	Shift (µeV)	Splitting (µeV)
α	+120	+140	+15	-130
γ	+260	+130	+120	-400
δ	+330	+240	+25	-110

with $k \in (x,y,z)$:

$$\sigma_x = \begin{pmatrix} 0 & 1 \\ 1 & 0 \end{pmatrix}, \tag{4.1}$$

$$\sigma_y = \begin{pmatrix} 0 & -i \\ i & 0 \end{pmatrix} \tag{4.2}$$

and

$$\sigma_z = \begin{pmatrix} 1 & 0 \\ 0 & -1 \end{pmatrix}. \tag{4.3}$$

As $T^2 = -1$ is valid, Kramers' theorem dictates that all eigenstates of the Hamiltonian are pairwise degenerate, which is known as Kramers' degeneracy. If one takes the AFM ground state of the dimer into account, time reversal symmetry is broken in principle. However, one can define a new operation under which the Hamiltonian of the dimer remains invariant $T_r = TC_2$, where T is the previously defined time reversal operator and C_2 describes the rotation by π around the out-of-plane rotation-axis in the center of the dimer. As $T_r^2 = -1$ is valid there is an effective time reversal symmetry and Kramers' theorem is still valid. This argumentation leads to the conclusion that hybridized YSR states remain degenerate in AFM

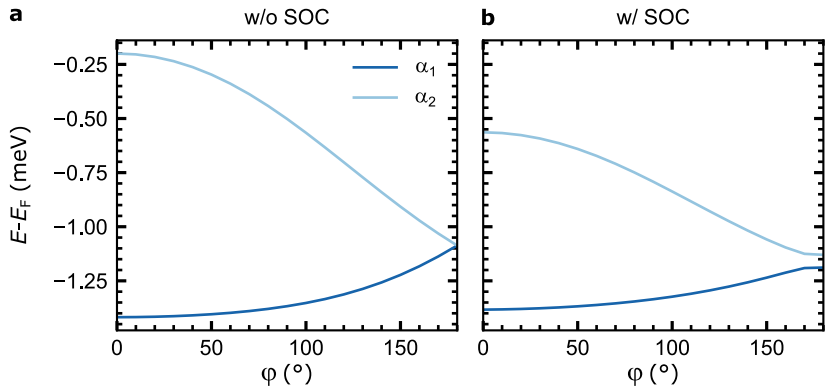

Figure 4.5.: a and **b** Calculated energies of the hybridized α states α_1 and α_2 in a $\sqrt{3}/2a - [1\bar{1}1]$ dimer depending on the orientation of the adatom spins making up the dimer $\mathbf{S}_1 = (0,0,1)$ and $\mathbf{S}_2 = (\sin\varphi, 0, \cos\varphi)$. The calculation shown in **a** is performed without SOC, and the one in **b** with SOC.

coupled dimers. In contrast, there is no such an effective time reversal operator for FM coupled dimers and, therefore, Kramers' theorem does not hold and one expects split YSR states if the interatomic spacing is low enough.

However, the situation is altered if we take SOC into account: T_r has to be adjusted as the Hamiltonian is no longer invariant under spin flip and the rotation around the C_2 axis. Now, not only the spin degree of freedom has to rotate, but also the orbital one, which results in an effective operator of $T_{r'} = TC_2\sigma_z$ for out-of-plane spins. For this operator we obtain $T_{r'}^2 = 1$. Therefore, Kramers' theorem no longer holds and does not force the degeneracy of hybridized YSR states any longer.

As the symmetry considerations above apply for the $\sqrt{3}/2a - [1\bar{1}1]$ Mn dimer, we conclude that SOC enables the experimentally observed splitting of the YSR states. Model calculations shown in Figure 4.5 further support these findings. The model is a Green's function-based method[167,172,219]. Among others, there are two crucial input parameters

determining the energy and the intensity asymmetry of the calculated YSR states, being the non-magnetic K^{μ} and the magnetic $J^{\mu}S/2$ scattering parameters, which are different for every of the four scattering channels (four different irreducible representations of d-orbitals for C_{2v} point group) and can be adjusted in such a way, that they match the experimental results of Figure 4.1.
Using these parameters, which have to be determined separately if SOC is set on or off, we calculate the energies of the hybridized YSR states of the α channel, called $\alpha_{1,2}$, as a function of the orientations of the adatom spins in a $\sqrt{3}/2a - [1\bar{1}1]$ Mn dimer for the case without SOC in Figure 4.5a and with SOC in Figure 4.5b. Here, $\varphi = 0°$ ($\varphi = 180°$) corresponds to FM (AFM) coupled spins. As expected from the model excluding SOC (Figure 4.5a), we observe a large splitting of α_1 and α_2 for $\varphi = 0°$, which decreases with an increasing angle between the impurity spins. At $\varphi = 180°$, we observe the degeneracy of α_1 and α_2 enforced by Kramers' theorem, as discussed above. If we include SOC (Figure 4.5b), we observe an overall similar behavior of the $\alpha_{1,2}$ states at low values of φ. However, moving closer to the AFM ordered spin structure, α_1 and α_2 no longer approach but remain energetically separated by a finite energy value of $\sim 100\,\mu$eV, which is comparable to the experimentally observed values shown in Table 4.1. While it can be shown that realistic non-collinearities in the spin orientations of the dimer can induce splittings of the YSR states in AFM coupled dimers as well, it is also found that those splittings are too low to explain the experimentally observed ones[60]. This indicates that SOC is indeed the key component leading to the splitting of YSR states in AFM coupled dimers.
Similar curves as the ones shown in Figure 4.5 can be calculated for the other YSR states and are shown in Ref. [60]. Overall, they display a similar behavior as what I have discussed for $\alpha_{1,2}$ in Figure 4.5.

4.1.5. Conclusion

The experimental observation that YSR states hybridize and split in dimers with considerable overlap — irrespective of the spin configuration and in a similar order of magnitude — have far-reaching implications for AFM coupled chains or self-organized islands[220,221]. If sufficiently strong SOC is present in a non-centrosymmetric system, our results imply that the hybridization and splitting of YSR states as well as the Shiba band formation in AFM coupled chains can yield band widths of similar magnitude as for FM coupled systems. In fact, $\sqrt{3}/2a$-$[1\bar{1}1]$ Mn chains on Nb(110) and Ta(110), which are AFM coupled, were recently studied in Refs. [200, 222]. Indeed, it is found that Shiba bands with a considerable width form, making them interesting for tailoring TSC and MBS as well. For completeness, it should be noted that single Mn adatoms and artificial dimers in $[1\bar{1}0]$- and $[1\bar{1}1]$-direction on Nb(110) were studied using fully relativistic first-principles based calculations by B. Nyári *et al.* in Ref. [223], which partly results in very good agreement with experiments. While the general effect of SOC on the YSR states of Mn adatoms on Nb(110) and on the AFM coupled $\sqrt{3}/2a$-$[1\bar{1}1]$ dimers is reproduced, it is also found that the effect is small according to this framework and does not result in a large splitting of the YSR states in AFM coupled dimers. Furthermore, it should be noted that realistic changes in the relative angle between both impurity spins yield splittings that are one order of magnitude below the experimentally obtained values. Therefore, a satisfactory explanation of the experimental observations is not fully achieved yet within this very promising framework.
Additionally, YSR dimers were studied by treating spins in the quantum limit in a recent publication by H. Schmid *et al.* in Ref. [224]. This treatment of AFM coupled dimers could shine light on the splitting of YSR states as well.

4.2. Spin chains exposed to low SOC

Building upon the findings obtained from the in-depth investigation of the Mn dimers in Section 4.1, I proceed to discuss two STS studies on artificial chains of Mn atoms on Nb(110), which are constructed by STM tip-induced atom manipulation. In particular, I will present results on close-packed chains in [001]- and $[1\bar{1}0]$-direction. While both studies can be seen as crucial developments in the field of Shiba chains, I will focus on highlighting the problem of small SOC in both chain types. A more general discussion of these chains is available in Ref. [200].
The results on $1a - [001]$ Mn chains are published in two articles. A first publication discusses the direct observation of multi-orbital Shiba band formation, which is resolved in k-space by analyzing the quasiparticle interference (QPI) of BdG states. Furthermore, a topological gap is identified in one of the two Shiba bands. The experimental data, the figures and parts of the text presented in Subsection 4.2.1 are based on the following publication:

> Lucas Schneider, Philip Beck, Thore Posske, Daniel Crawford, Eric Mascot, Stephan Rachel, Roland Wiesendanger and Jens Wiebe
>
> *Topological Shiba bands in artificial spin chains on superconductors*
>
> Nature Physics, **17**, 943-948 (2021).

A second publication focuses on the spatial distribution of possible MBS and the observed in-gap states with side features in this type of chains:

> Daniel Crawford, Eric Mascot, Makoto Shimizu, Lucas Schneider, Philip Beck, Jens Wiebe, Roland Wiesendanger, Harald O. Jeschke, Dirk K. Morr and Stephan Rachel
>
> *Majorana modes with side features in magnet-superconductor hybrid systems*

arXiv:2109.06894 [cond-mat.supr-con] (2021).

The tailoring of an effective one Shiba band system by constructing $\sqrt{2}a - [1\bar{1}0]$ Mn chains and the length-dependent observation of end states that are identified as PMMs is described in yet another publication. The experimental data, the figures and parts of the text presented in Subsection 4.2.2 are based on the following publication:

> Lucas Schneider, Philip Beck, Jannis Neuhaus-Steinmetz, Levente Rózsa, Thore Posske, Jens Wiebe and Roland Wiesendanger
>
> *Precursors of Majorana modes and their length-dependent energy oscillations probed at both ends of atomic Shiba chains*
>
> Nature Nanotechnology, **17**, 384-389 (2022).

All measurements presented in this section were obtained with an electrochemically etched W tip with a superconducting apex, which was realized by repeated indenting of the tip into the Nb sample. Furthermore, the studies were performed on the same Mn/Nb(110) sample that is presented in Section 4.1. All $\mathrm{d}I/\mathrm{d}V$-spectra were processed by numerical deconvolution as described in Subsection 3.1.2. Unless indicated otherwise, STS measurements were performed using the following measurement parameters: $V_{\mathrm{stab}} = -6\,\mathrm{mV}$, $I_{\mathrm{stab}} = 1\,\mathrm{nA}$ and $V_{\mathrm{mod}} = 20\,\mu\mathrm{V}$.

Contributions from experiment and theory

The STM and STS data presented in this section were measured by Dr. Lucas Schneider an myself. We both analyzed the spectroscopic data using self-written Python and Mathematica code. TBM calculations reproducing the results by experimentally motivated parameters were performed by Dr. Lucas Schneider and Dr. Thore Posske for $1a - [001]$ chains and by Dr. Lucas Schneider and Jannis Neuhaus-Steinmetz (University of

Hamburg) for $\sqrt{2}a - [1\bar{1}0]$ chains. Dr. Daniel Crawford (University of Melbourne, group of Prof. Dr. Stephan Rachel) and Dr. Eric Mascot (University of Illinois at Chicago, group of Prof. Dr. Dirk Morr) contributed TBM calculations using input parameters obtained from *ab initio* DFT calculations, that were performed by Dr. Makoto Shimizu (Okayama University, group of Prof. Dr. Harald Jeschke).

Introduction

Since we have demonstrated that artificially constructed Mn dimers on Nb(110) are at least subject to some degree of SOC in Section 4.1, let us recall the ingredients for TSC in magnetic chains coupled to *s*-wave superconductors. Topological phases are predicted if an odd number of spin-polarized bands cross the Fermi level (in the absence of superconducting pairing)[37], which is linked to a fine tuning of the single adatom's YSR energy E_0 and the hopping parameter t (see Subsection 2.2.6). As an effect of Rashba SOC and superconducting pairing, these bands may be gapped around E_F by *p*-wave contributions to the pairing, which can result in a minigap Δ_{ind}[32].
Up to this point, the search for TSC phases in magnetic chains on *s*-wave superconductors focused on the observation of zero-energy edge modes and tried to pin-point them as MBS[53–57,225]. However, it is difficult to unambiguously determine the origin of such edge states, as they may also exist in topologically trivial structures[58,63]. Therefore, it seems as if the problem was so far tackled from the wrong side, focusing on the consequences of TSC — MBS — rather than on its origin , the Shiba band structure. The difficulty lies in the experimental access to this quantity, since typical momentum resolved methods of solid state physics as ARPES are limited by their spatial averaging[226], which renders them useless in measuring single sparsely distributed nanostructures. Approaches to narrow the X-ray beam size down to the nanometer range

are still under development[227,228].
However, for certain systems there are possibilities to extract parts of the band structure using STM-based methods. In confined electronic systems of a good crystallographic quality one can obtain energy-dependent $\mathrm{d}I/\mathrm{d}V$-maps of interfering quasiparticles, which are scattered from defects or step-edges[229–231] — commonly referred to as QPI. A Fourier analysis of these QPI patterns enables the determination of the dispersion relation of some electronic states. This method was already successfully used to gain new insights in high-T_C superconductors[232,233] and topological surface- and edge states[234–237]. Here, we are able to apply the method to BdG quasiparticles, which are confined to the spatial extent of a 1D magnetic structure. In the case of $1a - [001]$ Mn chains, we extract the dispersion of two Shiba bands with distinct orbital origin and identify a topological gap in one of those bands (Subsection 4.2.1).
Building upon the knowledge of the multi-orbital band structure obtained for $1a - [001]$ Mn chains, we tailor a chain geometry in which we only expect a single band to cross the Fermi level. In particular, we construct chains along the $[1\bar{1}0]$-direction with an interatomic spacing of $\sqrt{2}a$. A length-dependent analysis of the BdG QPI reveals that we have indeed obtained a system with a single Shiba band crossing the Fermi level. Furthermore, our STS study shows the occurrence of low-energy end states.
Similar to other material platforms of atomic spin chains on *s*-wave superconductors, the experimentally accessible chain lengths constructed by STM tip-induced atom manipulation lie on the order of a dozen nanometers[55,58,61,63,238]. Therefore, if one were to realize MBS on both ends of such a chain, they might still interact and split away from zero energy. This splitting should oscillate as function of the chain length. Topological end states showing this feature are so-called PMMs, since they are expected to be pinned to zero energy if the chain length is increased sufficiently[30,239,240], making them adiabatically connected to MBS. So far, length-dependent measurements were performed for the

semiconductor nanowire platform[30], however the amount of data points is very low, as a new device has to be designed for every length. Using STM tip-induced atom manipulation, we are not limited in this regard and can perform length-dependent studies with atomic precision.
Another upside of our method is the possibility to straightforwardly perform measurements on both ends of a 1D structure. The observation of signatures of MBS must be performed on both ends of a given chain to be significant at all. This issue has recently been addressed for self-organized magnetic chains[53,54,225] and semiconducting nanowires[42] and it was found that signatures of MBS were neither observed for all of the investigated chains or nanowires nor on both ends of the same chain or nanowire, proving that the observed end states can't be MBS.
Our length-dependent STS study on $\sqrt{2}a - [1\bar{1}10]$ Mn chains on Nb(110) in Subsection 4.2.2 shows exactly these two characteristics discussed above. We observe end states on both ends of a chain, which oscillate as a function of the chain length, which we increase atom-by-atom. We interpret them as PMMs and predict that they will evolve into topologically protected MBS for chains longer than 70 sites[62].

4.2.1. Multi-orbital Shiba band structure

Let us recall, that a single Mn adatom has four pairs of YSR states:

- α is the one highest in energy and $\mathrm{d}I/\mathrm{d}V$-intensity (for negative bias) and resembles a mixed d_{z^2}- and $d_{x^2-y^2}$-orbital
- β resembles a d_{xy}-orbital and is barely visible in $\mathrm{d}I/\mathrm{d}V$-spectra
- γ resembles a d_{xz}-orbital
- δ, which is closest to E_F , resembles a d_{yz}-orbital

Additionally, it is worthwhile to consider similar symmetry arguments as in Subsection 4.1.4 for chains in $[001]$-direction (i.e. along the x-axis) with

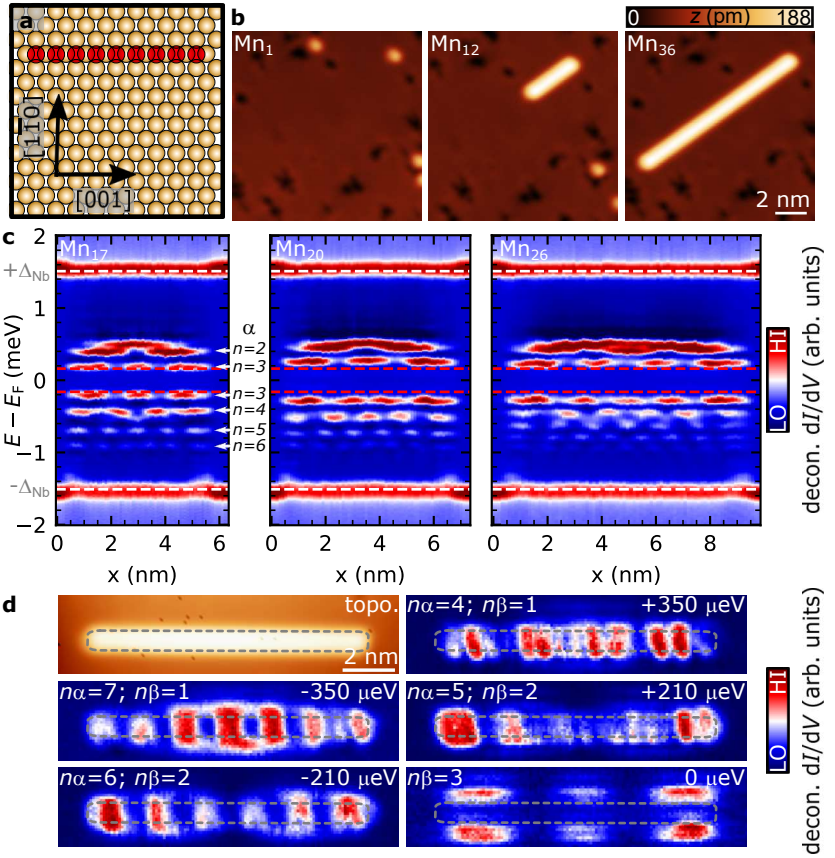

Figure 4.6.: a Illustration of a 1a-[001] Mn chain (red spheres) on Nb(110) (yellow spheres). Black arrows and labels indicate crystallographic directions, which are valid for panel **d** as well. **b** STM images displaying the construction of $1a - [001]$ chains with lengths 1, 12 and 36, which is indicated in the top left corner. **c** Three exemplary dI/dV-line profiles of lengths 17, 20 and 26. White arrows and black labels mark standing waves with a well-defined number of maxima n, that originate from the α band. **d** STM image and energy slices of a dI/dV-grid measured over a Mn_{34} chain. Labels in the top left corner indicate the number of maxima located on the chain (α) and on the side of the chain (β). Measurement parameters as indicated above.

a spacing of $1a = 329.4\,\mathrm{pm}$, which we will investigate in the following. An illustration of such a chain is shown in Figure 4.6a. There are two distinct irreducible representations for this chain type, which differ from one another by being symmetric or antisymmetric with respect to the xz-mirror plane, that cuts the chain in half along its long axis. The d_{z^2}- , $d_{x^2-y^2}$- and d_{xy}-orbitals are symmetric with respect to the mirror plane and the d_{xy}- and d_{yz}-orbitals are antisymmetric. Therefore, the former YSR states may hybridize and form Shiba bands which are symmetric with respect to the $x-z-$plane, while the latter two may hybridize and form bands which are antisymmetric with respect to the $x-z-$plane.
As demonstrated in Section 3.3 and Figure 4.2, the Nb(110) surface allows the precise and reproducible STM tip-induced manipulation of Mn atoms, which is further highlighted by the construction of defect-free $1a-[001]$ Mn_{12} and Mn_{36} chains starting from a single atom in Figure 4.6b. The individual magnetic moments in such chains are aligned FM, which was recently demonstrated by SP-STM measurements[59] and DFT calculations[216]. To study the formation of Shiba bands, we performed $\mathrm{d}I/\mathrm{d}V$-line profiles in a length-dependent fashion, starting with a single atom ($N = 1$, left panel in Figure 4.6b) and increasing it atom-by-atom up to a Mn_{36} chain ($N = 36$, right panel in Figure 4.6b). Three examples of these $\mathrm{d}I/\mathrm{d}V$-line profiles for chains with $N = 17, 20$ and 26 are shown in Figure 4.6c. We observe energetically sharp states with a well-defined number of maxima along the chains, which resemble standing waves. White arrows and black labels on the side of the leftmost panel mark some of these states. Starting with the state that has one maximum along the chain and an energy of $\approx 500\,\mu\mathrm{eV}$, we find that the number of maxima $n\alpha$ increases with decreasing energy. Additionally, the relation $E(n\alpha)$ depends on the chain length N, as visible by the shift of these states with defined numbers of maxima for the two longer chains in Figure 4.6c.
Energy slices of a $\mathrm{d}I/\mathrm{d}V$-grid, which are evaluated at exemplary energies where standing waves are observed, are shown in Figure 4.6d. We find

that the states with maxima $n\alpha = 4$, 5, 6 and 7 are localized dominantly on top of the chain, whose perimeter is indicated by a gray dashed line. Taking the length-dependent evolution of the energies of these $n\alpha$ states into account, which are shown in Figure 4.7a by chain-length dependent spectra being averaged over the whole chain length, we find that the previously mentioned state with one maximum $n\alpha = 1$ at $+500\,\mu\text{eV}$ emerges from the single Mn adatom ($N = 1$) α YSR state. Combining the spatial distributions, the dominant $\mathrm{d}I/\mathrm{d}V$-intensity of these states, and the evolution form the α state, we unambiguously conclude that this state has its origin in the single atom α YSR state and, therefore, we refer to it as the α band. The states with different numbers of maxima have their origin in the confinement of the BdG quasiparticles residing in this α Shiba band by backscattering at the ends of the chain with a scattering vector of length q.

Therefore, we can extract the Shiba band structure by performing an energy-wise 1D-FFT of the $\mathrm{d}I/\mathrm{d}V$-line profiles with lengths $N = 14$ to $N = 36$. To match all FFTs to the same k-points, we interpolate all arrays to the same axis. Subsequently, we average all of the 1D-FFTs. This averaging has the purpose of not only considering the standing waves given by the boundary condition $q = \pm 2n\pi/Na$ of one particular length, but we include those of all chains over a certain length threshold ($N = 14$). The plot of this averaged 1D-FFTs is shown in Figure 4.6b. We find a parabolic band of dominant intensity, which has its band maximum at $+500\,\mu\text{eV}$ and a negative curvature. The particle-hole partner of this band with a minimum at $-500\,\mu\text{eV}$ is visible as well. However, it has a much lower intensity, which is reminiscent of the single atom α state for which a strong particle-hole asymmetry was observed as well. A comparison of the dispersion with the previously identified standing waves in the $\mathrm{d}I/\mathrm{d}V$-line profiles results in the conclusion that this must be the α band. The most striking feature of this band is its minigap around the Fermi level. A cut through the 1D-FFT at the k-value of the expected α band crossing (if there was no minigap), is shown in Figure 4.7c. We find a

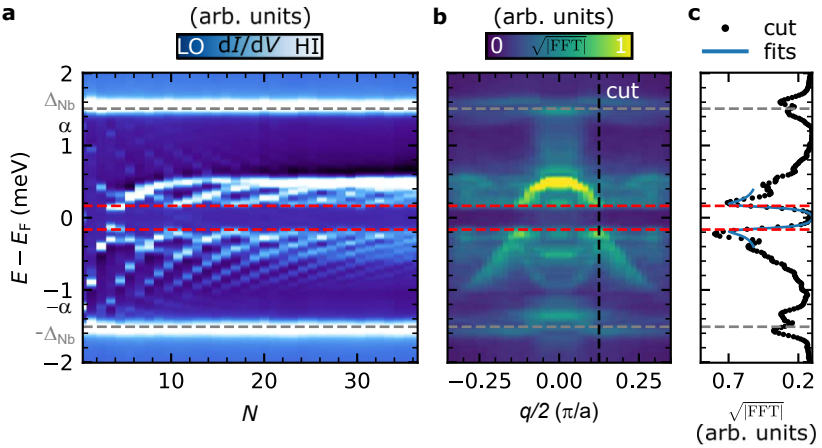

Figure 4.7.: a $\mathrm{d}I/\mathrm{d}V$-spectra averaged over the whole chain length, plotted as a function of the chain length N. Gray and red dashed horizontal lines mark the superconducting gap of Nb and the minigap induced in the α band in all panels. **b** Absolute square of the energy-wise averaged 1D FFT of the $\mathrm{d}I/\mathrm{d}V$-line profiles of all chains from $N = 14$ to $N = 36$. The black dashed vertical line is a cut through the 1D FFT approximately at the k-value, where the α band would cross the Fermi level in the absence of a minigap. The spectral function extracted along the cut is plotted in panel **c** and includes the fit of a Dynes function to the minigap resulting in the following parameters: $\Delta_{\mathrm{ind}} = (164 \pm 4)\,\mu\mathrm{eV}$, $\gamma = (35 \pm 4)\,\mu\mathrm{eV}$ and $A = (476 \pm 11)$ arb. units. Here, A is a dimensionless prefactor of the Dynes functions to account for the unnormalized $\mathrm{d}I/\mathrm{d}V$-intensities. Measurement parameters as indicated above.

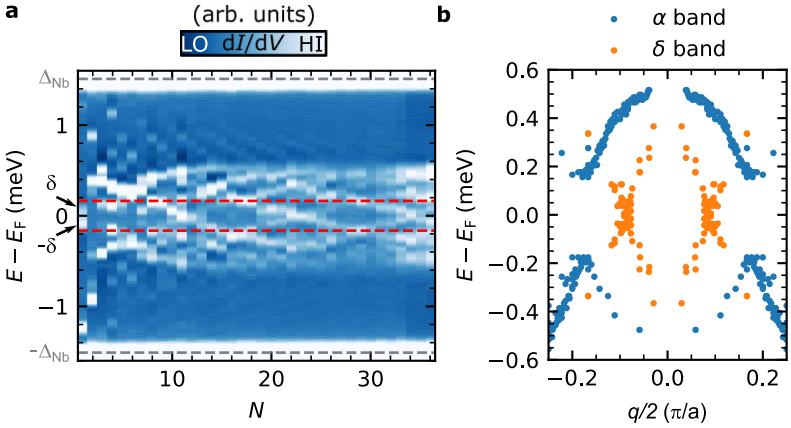

Figure 4.8.: a Length-dependent $\mathrm{d}I/\mathrm{d}V$-spectra obtained at the end and on the side of each chain, i.e. at a location where δ states are observable in Figure 4.6d. Gray and red dashed horizontal lines mark the superconducting gap of Nb and the minigap induced in the α band. **b** Shiba band dispersions of the α (blue) and the δ (orange) bands, evaluated manually by linking a calculated scattering vector $q = \pm 2n\pi/Na$ to its respective energy. Measurement parameters as indicated above.

quite sharp cut-off of the spectra intensity in a range from $-180\,\mu\mathrm{eV}$ to $+180\,\mu\mathrm{eV}$, which somewhat resembles a superconducting gap. To obtain a good estimate for the minigap size we fit the respective energy range using a Dynes function[125] and obtain $\Delta_{\mathrm{ind}} = (164 \pm 4)\,\mu\mathrm{eV}$.
To discuss the origin of the gap, we have to consider that this band originates form the single impurity α YSR state, which is non-degenerate. This remains valid even if we take the spin degree of freedom into account, since we are dealing with Shiba bands in the gap of a superconductor, where the particle-hole partners of these bands carry opposite spin polarization (Subsection 2.2.6). Therefore, we can conclude that bands may only be gapped by p-wave contributions to the pairing mechanism. If we imagine this band structure but assuming zero SOC, we would find that

there is a single band-crossing of the α band with the Fermi level. As this is an odd number of band-crossings, we can determine the topological invariant to be $M = -1$, making it topologically non-trivial[176].
Taking a closer look at the $\mathrm{d}I/\mathrm{d}V$-grids in Figure 4.6d, we find that there are additional in-gap states. Besides the ones located on top of the chain (identified as the α band), there are states with a distinct symmetry, which are located on the side of the chain. These states appear as dumbbells along the $[1\bar{1}0]$-direction, but have a well defined number of maxima on both sides along the chain. Their nodal line makes them difficult to be observed in $\mathrm{d}I/\mathrm{d}V$-line profiles, especially since the α band has a very dominant intensity. Additionally to the $\mathrm{d}I/\mathrm{d}V$-line profiles measured on each chain, we also took a $\mathrm{d}I/\mathrm{d}V$-spectrum on the side of every chain with a length ranging from $N = 1$ to $N = 36$. A corresponding plot of these length-dependent $\mathrm{d}I/\mathrm{d}V$-spectra, similar to Figure 4.7a, is shown in Figure 4.8a. We find that the states besides the chain emerge from the single atom's δ YSR state and, therefore, attribute these states to the δ band. In contrast to Figure 4.7a, where we dominantly investigated the α band, we find that there are dispersive states shifting continuously across the Fermi level for the δ band without an obvious minigap.
Since it is difficult to extract the dispersion of the δ band from the 1D FFT — due to it's low intensity, caused by the nodal line— we evaluate the band by performing the QPI analysis manually. We link each state located on the side of the chain with a wave vector $q = \pm 2n\pi/Na$ to the δ band. Then, by linking these scattering vectors to their respective energy we obtain the dispersion relation shown in Figure 4.8b by orange dots. The δ band obviously has a Dirac-like dispersion, which crosses the Fermi level at $0.1\ \pi/\mathrm{a}$. Evidently, the δ band is not gapped but appears to cross the Fermi level continuously.
If there were an odd-numbered amount of topological bands for chains of this type, which would imply that they are gapped by p-wave correlations and that the chain length is long compared to the localization length of MBS[37,241], we would expect the emergence of MBS. However, we do

not observe clear indications of MBS in our measurements. In principle, states similar to the one at $E = 0\,\mu\text{eV}$ in Figure 4.6d have end-state character and could be interpreted as MBS, as it was done in a previous study on Fe/Pb(110) where a zero energy state with a comparable spatial distribution was observed[57]. However, the novel methods demonstrated here allow us to disprove this idea: MBS that originate from the α band would have an imprinted modulation of $q_{F,\alpha}/2 \approx 0.2\pi/a$, as governed by the k-vector at the topological gap's minimum[241,242]. Since this doesn't agree with the scattering vectors of the states with dominant side weight (cf. blue and orange dots in Figure 4.8b), we conclude that those end states can't be MBS related to the topological gap of the α band.
Additionally to the two observed bands, it could be that there are up to three more Shiba bands originating from the $d_{x^2-y^2}$-, d_{xy}- and d_{xz}-like YSR states that might be difficult to observe experimentally due to their low $\mathrm{d}I/\mathrm{d}V$-intensity (Figure 4.1). Therefore, we conclude that the multi-orbital character of this chain may cause an overall topological trivial invariant for the entire system, preventing the emergence of MBS . This highlights the need to engineer chain geometries where only a single band crosses the Fermi level (see Subsection 4.2.2).
The absence of a measurable topological minigap in the δ band is a remaining interesting question. Apart form the explanation, that the superconducting order parameter is k-dependent in Shiba chains exposed to SOC[61,62] and could therefore vanish at the k-point where the δ band crosses E_F, a difference in SOC between the two observed bands could be the origin as well. In Subsection 2.1.3 we found that the SOC strength in metallic systems depends on the atomic contribution (related to Z and probably similar for both bands) and on the asymmetry of the wavefunctions, which are expected to vary heavily for both orbitals. The d_{z^2}-orbitals (where the α band stems from) mainly extends perpendicular to the surface, while the d_{xz}-orbitals (where the δ band stems from) lie in-plane. Therefore, the former could be exposed to a larger asymmetry and higher SOC naturally[243]. Furthermore, both orbitals hybridize dif-

ferently with the substrate bands, which may cause a difference in SOC strength as well.
It should be noted that the band structure of Mn $1a - [001]$ chains on Nb(110) has recently been calculated using parameters that were extracted from the DFT-determined band structure in the normal metallic state as an input for a multi-band TBM, where superconducting onsite pairing is introduced in the niobium substrate[244]. While these calculations were not able to reproduce the measured dispersion of the scattering vectors shown in Figures 4.7 and 4.8, they resulted in an overall topological gap with a very small size connected with PMMs that have a quite similar appearance as the δ states shown in Figure 4.6d. This suggests, that the chains are indeed in an overall topologically non-trivial phase, but the minigap is beyond the experimental resolution, and the connected MBS of δ-character are still strongly hybridized such that they are not protected by the tiny topological minigap.

4.2.2. Precursors of Majorana modes

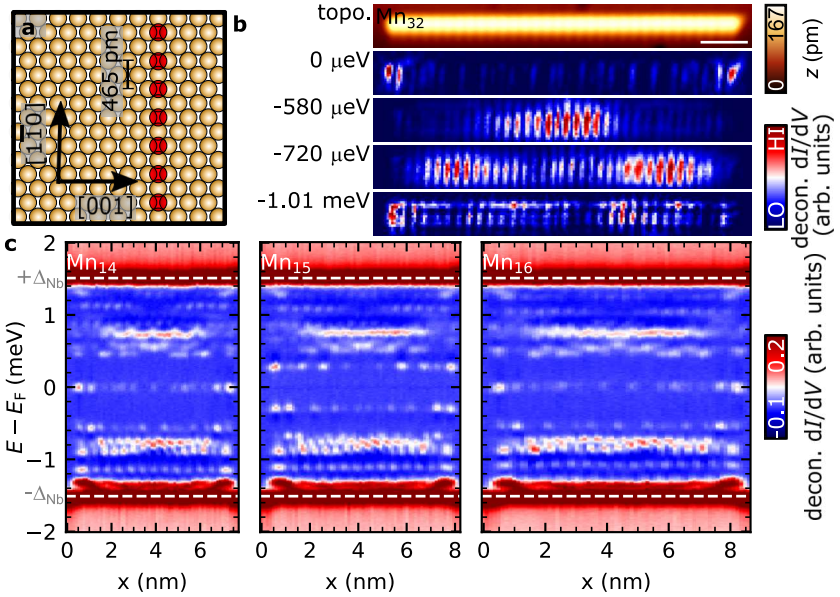

Figure 4.9.: a Illustration of a $[1\bar{1}0]$ Mn chain (red spheres) on Nb(110) (yellow spheres). Black arrows and labels indicate crystallographic directions. **b** STM image and energy slices of a dI/dV-grid measured over a Mn$_{32}$ $\sqrt{2}a$-$[1\bar{1}0]$ chain. The white scale bar represents a length of 2 nm. The crystallographic directions are rotated by 90° with respect to the illustration in **a**. **c** Three exemplary dI/dV-line profiles of lengths N =14,15 and 16, as indicated in the top left corner of each panel. White dashed lines mark the superconducting gap of Nb Δ_{Nb}. Measurement parameters as indicated above.

As we have seen in Subsection 4.2.1, the multi-orbital character of close-packed Shiba chains in [001]-direction makes a clear identification of the topological invariant of the entire system difficult. Therefore, we now attempt to realize a Shiba chain in which only a single band crosses the Fermi level. The spatial anisotropy of the YSR states of Mn adatoms

on Nb(110) allows us to tune the hybridization of YSR states in dimers and chains by varying the crystallographic direction[60,174,175]. If we reconsider the YSR states of an individual impurity (see Subsection 4.1.1), we find that the δ states lie very close to the Fermi level ($\pm 80\,\mu$eV) and that they spatially extend mainly along the $[1\bar{1}0]$-direction. Thus, if we construct a chain in $[1\bar{1}0]$-direction with an interatomic spacing of $d = \sqrt{2}a = 465\,$pm (see Figure 4.9a), we expect that the δ states form a Shiba band which should be wide enough to cross E_F. Furthermore, the interatomic spacing d, which is considerably increased with respect to the $1a - [001]$ case studies above, should prevent a strong hybridization of the other YSR states —in particular that of the α YSR states— which are not extended in $[1\bar{1}0]$-direction.

We perform a length-dependent STS study on $\sqrt{2}a - [1\bar{1}0]$ Mn chains, proceeding similar to the study discussed in Subsection 4.2.1. A $\mathrm{d}I/\mathrm{d}V$-grid and three exemplary $\mathrm{d}I/\mathrm{d}V$-line profiles are shown in Figures 4.9b and c. We find two important experimental signatures in these STS measurements. First, we observe in-gap states which are spatially distributed over the entire length of the chains in an energy range from $0.5\,\mathrm{meV} < |E| < 1.5\,\mathrm{meV}$. Since these states are located on top of the chain, we conclude that they stem from the single atom α YSR state. Second, by looking at the Mn_{32} chain (Figure 4.9b), the Mn_{14} and the Mn_{16} (Figure 4.9c) chain we find zero energy end states, which have an oscillatory decay into the bulk of the chain. Those end states are separated from the bulk α Shiba states by a gap of $\Delta_\mathrm{fs} \approx 400\,\mu$eV. Therefore, the states show all characteristics that have previously been ascribed to MBS.

The atom-by-atom construction of the Mn chains allows us to perform a length-dependent study of the end states. Strikingly, if we vary the chain length by only one atom from $N = 14$ or 16 to $N = 15$, we find that the end states shift to $\pm 300\,\mu$eV, as shown in the middle panel of Figure 4.9c. While this observation is not compatible with spatially isolated MBS, the fact that the energy shift occurs symmetrically on both ends of the chain indicates that the end states are a single quantum state of the chain.

To further investigate the length-dependent energy of the end states, a series of $\mathrm{d}I/\mathrm{d}V$-spectra obtained on the end of chains with lengths $1 \leq N \leq 39$ is shown in Figure 4.10a. To begin with, we find that the states of the α band appear to shift continuously from $\pm 1.5\,\mathrm{meV}$ to $\pm 0.8\,\mathrm{meV}$. The α band is also visible in the averaged 1D-FFT of the $\mathrm{d}I/\mathrm{d}V$-line profiles, which is shown in Figure 4.10d. In contrast to those states, the energy of the end states doesn't seem to evolve continuously with the chain length N but it appears to be modulated by $\Delta N = 2$. To clearly illustrate this effect, the $\mathrm{d}I/\mathrm{d}V$-spectra of chains with even and odd lengths are plotted separately in Figures 4.10b and c. Only this presentation of the data shows a continuous evolution of the in-gap states. From these two plots we find that the end states continuously evolve from the single atom's ($N = 1$) δ YSR state (see the states marked in Figure 4.10c). For lengths of $N = 12, 19$ and 32 the end states are tuned to zero energy within our energy resolution of $\approx 50\,\mu\mathrm{eV}$.
Using a TBM for the Shiba bands[34], theoretical calculations in Ref. [62] with experimentally motivated inputs are able to accurately reproduce the observed findings for finite values of SOC. The calculations result in a band structure of the δ band which is similar to the one shown in Figure 4.10d. The resulting Shiba band would have a band-crossing with E_F at $k_\mathrm{F} \approx \pi/2d$ in the ungapped phase. This band-crossing with $\lambda_\mathrm{F} \approx 2\pi/k_F \approx 4d$, which is an approximate multiple of the lattice constant, appears to lead to the modulation of the end states with $\Delta N \approx 2$. Similar beating effects have been observed for other platforms as well[245–247]. One may also understand the even-odd effect by considering the fact that MBS are modulated with $\lambda_F/2$[242] which equals $2d$ in our case, causing the overlap and interactions of the MBS to alternate with $\Delta N = 2$.
Since there is no minigap observable in the δ band within our experimental resolution, first-principles based simulations were performed[60,62] to determine a gap of $\Delta_p = 50\,\mu\mathrm{eV}$, which is just at the limit of the experimental energy resolution ($\Delta E = 50\,\mu\mathrm{eV}$) and considerably smaller than the observed finite-size gap (caused by the steep δ band in Figure 4.10d)

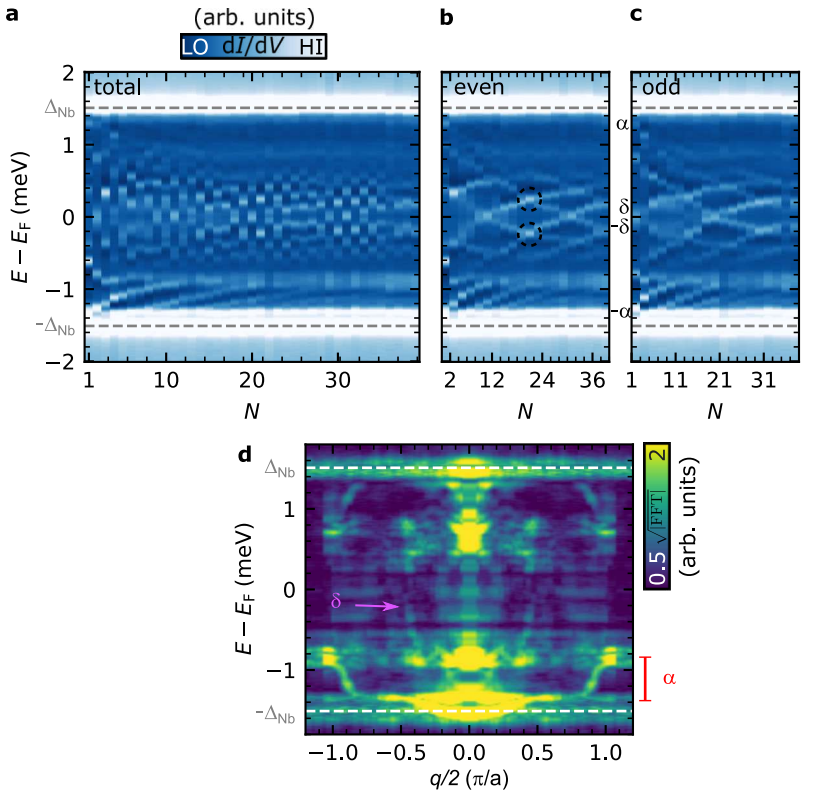

Figure 4.10.: **a** Length-dependent $\mathrm{d}I/\mathrm{d}V$-spectra obtained on the end of $\sqrt{2}a$-$[1\bar{1}0]$ Mn chains plotted sequentially. Gray dashed horizontal lines mark the superconducting gap of Nb. The same data set as in **a** is separated into even (**b**) and odd (**c**) lengths and is plotted separately. Black circles in **b** mark the locations, where an avoided crossing is expected. Arrows and greek labels in **c** indicate the energetic positions of the single Mn atom's α and δ states. **d** Absolute square of the energy-wise averaged 1D FFT of all chains from $N = 10$ to $N = 32$. White dashed horizontal lines mark the superconducting gap of Nb(110). The red scale indicates the band width of the in-gap states which we attribute to the α Shiba band. The pink arrow indicates the band crossing of the δ Shiba band with the Fermi level at $k_F \approx -\pi/2a$. Measurement parameters as indicated above.

and the hybridization of the PMMs (e.g. middle panel in Figure 4.9c). These unfavorable orders of magnitude make the detection of a topological gap difficult within our energy resolution. For the finite size limit investigated here, it is expected that the p-wave pairing manifests itself as an avoided crossing of the two energetically lowest states (see circles in Figure 4.10b)[62]. However, this effect is too small to be observed within our energy-resolution. The model calculations show that the end modes converge to energies below Δ_p for chains longer than $N > 70$ sites. Since it is not possible to construct defect free chains of this length ($\sim 33\,\mathrm{nm}$), due to the remaining oxygen impurities on Nb(110), we have to develop other ideas to improve the localization of the PMMs, such that they converge to zero energy for shorter chains.

4.2.3. Conclusion

In conclusion, the absence of topologically protected MBS in both types of Mn chains on Nb(110) is linked to a low SOC in some of the Shiba bands. In the case of close-packed $1a-[001]$ chains, we find that the multi-orbital character of the Shiba band structure is problematic for the realization of an overall topological system: Besides the α band with a sizable p-wave gap we observed a second band (δ band), which crosses the Fermi level continuously. We speculate that a low SOC might be the origin for the absence of a measurable p-wave gap in this band[244].
We were able to address the problem of having multiple Shiba bands by exploiting the spatial anisotropy of the single adatom's YSR states and by constructing close-packed chains in $[1\bar{1}0]$-direction. Indeed, we observe a single Shiba band that crosses the Fermi level. However, we can not resolve a gap within our experimental resolution and rely on model calculations to determine a gap size of $\Delta_p \approx 50\,\mu\mathrm{eV}$. Furthermore, we observe low-energy end states, which oscillate in energy with increasing chain lengths and we identify these end states as PMMs. Unfortunately,

the PMMs do not converge to zero energy within the accessible chain lengths. Since the localization of MBS is related inversely to $\Delta_p{}^{(241)}$, which is linked directly — but not exclusively — to the SOC strength (see Subsection 2.1.3), we expect that an increase in SOC might result in MBS that are protected by a sizable topological gap and that converge to zero energy for shorter chains than it is the case for $\sqrt{2}a-[1\bar{1}0]$ Mn chains on Nb(110).
Approaches and ideas to increase the SOC in Shiba chains are discussed in Sections 4.3, 4.4 and 4.5 .

4.3. Complex chain geometries of Mn on Nb(110)

The results of Section 4.2 were obtained at an early stage of my PhD work. Due to the link of these results to a small SOC strength in the investigated Shiba chains, novel ideas how to increase SOC were required. One particular set of ideas and first experimental approaches to realize it are presented in this section.
All measurements presented in this section were obtained with a mechanically sharpened and *in-situ* flashed Nb tip (see Subsection 3.3.3). All $\mathrm{d}I/\mathrm{d}V$-spectra were processed by numerical deconvolution as described in Subsection 3.1.2. Unless indicated otherwise, STS measurements were performed using the following measurement parameters: $V_{\mathrm{stab}} = -6\,\mathrm{mV}$, $I_{\mathrm{stab}} = 1\,\mathrm{nA}$ and $V_{\mathrm{mod}} = 20\,\mu\mathrm{V}$.

Contributions

The ideas and experimental results shown herein were obtained together with Dr. Lucas Schneider. They remain unpublished up to this date. Self-written Python code and Gwyddion[248] were used for the data analysis and for the presentation of data in figures.

Introduction

The experimental results of Sections 4.1 and 4.2 lead to the conclusion that the YSR states and Shiba bands of the Mn/Nb(110) system are at least exposed to some degree of SOC[60]. However, it is too low to gap out all observed Shiba bands in $1a - [001]$ Mn chains[61] and its low strength in $\sqrt{2}a - [1\bar{1}0]$ Mn chains hinders the clear separation of the observed PMMs into topologically protected Majorana modes (MMs) at accessible chain lengths[62]. Furthermore, the comparatively small SOC is most

probably also the reason for the predominant collinear magnetic spin-alignment of most linear chain geometries as shown experimentally by employing SP-STM[59] and as calculated theoretically using the Vienna *ab initio* simulation package and the KKR multiple scattering theory[216]. Therefore, I am devoting this section to the identification of new routes to increase SOC artificially, i.e. without changing our material system entirely to a high-Z superconductor (Section 4.4) or choosing another transition metal adatom species.

We restrict ourselves to ideas which increase SOC in the Shiba chains, but allow the use of Nb as the superconducting host, which contributes the s-wave pairing. This choice is experimentally motivated by the high T_C (large Δ) of niobium, which enables an unprecedented energy resolution in STS experiments on Shiba chains and is crucial for the resolution of in-gap bands as well as for the distinction of topological states from trivial ones.

The basic principle behind the herein presented ideas lies in the analogy of SOC and a spin spiral magnetic configuration, which I briefly touched in Subsection 2.2.6. I will proceed to describe it in more detail, following the argumentation presented in Ref. [180]. If one treats a 1D electron system, such as a semiconductor nanowire, in a similar fashion as in Subsection 2.2.6, but neglecting SC, it may be described by a Hamiltonian consisting of three terms:

- $\hat{H}_{\mathrm{el}}$, which includes the kinetic energy terms
- $\hat{H}_{\mathrm{so}}$, the well known 1D spin-orbit term (see Subsection 2.1.3)
- $\hat{H}_{\mathrm{Z}}$, a Zeeman term of a uniform externally applied magnetic field.

In the following, I define the coordinate system in such a way, that the chain and the **B**-field, which aligns the spins, are both oriented in x-direction. Then, the one-dimensional SOC term is given by $\hat{\sigma}_y k_x$. One can show, that a spin-dependent gauge transformation can be defined in such a way, that the spin-orbit term is eliminated. However,

thereby, the previously uniform **B**-field is turned into a non-uniform one: $B(r) = {}^{B_x g \mu_B}/_2(\cos(2k_{SO}r)\mathbf{x} - \sin(2k_{SO}r)\mathbf{y})$, where k_{SO} is the shift of the spin-up and the spin-down bands caused by SOC in **k**-space (see Figure 2.2) and **x**, **y** are the unit vectors in x- and y-direction, respectively. Therefore, the Hamiltonian now describes a system without an explicit SOC term, but the electrons are now exposed to a non-uniform spiral magnetic field in the $x-y$-plane.
Most of the following ideas rely on this conclusion. While it's not possible to apply such a spiral magnetic field using an external magnet, we can employ on-sample nanofabrication to realize stray fields resembling a spiral magnetic field[249]. In the following, I will refer to an increase of SOC by such a field as synthetic SOC. If one could organize an array of nanomagnets parallel to an out-of-plane spin-polarized Shiba chain, where the nanomagnets are magnetized in such a way that they have alternating in-plane fields, the physical system would be equivalent to the one described above and the 1D electron system should be exposed to a higher SOC than in the case without nanomagnets. In order for the spatially varying magnetic field to act as synthetic SOC, it must have Fourier components similar to k_F[250,251].
One example for the realization of synthetic SOC is the study of a carbon nanotube positioned over an Al_2O_3-capped multi layer sandwich of Pt and Co. In this system, the synthetic SOC is induced by spatially-varying out-of-plane polarized magnetic domains[252]. An equally elegant experimental realization could be obtained for Shiba chains, if one were to construct them parallel to quasi 1D structures with domain walls as e.g. Fe on W(110)[80,253] or other self-organized islands with in-plane magnetization. However, Fe[254] and Mn[221] islands, which were experimentally studied on Nb(110), show out-of-plane FM and AFM ground states without domain formation, respectively. Furthermore, while there are material systems with domain widths in the single nanometer range[48], it would be another challenge to tune the domain size of a given system into the range of λ_F. Furthermore, it is an open question whether the

dominant interaction mechanism between such an island and a Shiba chain would be the stray field of the island, or if RKKY interactions and the coupling of YSR states would dominate. An experimental attempt addressing this question is presented in Subsection 4.3.1.
In contrast to applying the spiral magnetic field synthetically, a more obvious approach to increase the SOC is to design an artificial chain that is in a spin-spiral magnetic ground state (see Refs. [55, 93]), as it was already proposed in early theoretical work[34,36]. As shown above, linear Mn chains in high-symmetry directions on Nb(110) are in collinear magnetic ground states due to a low DM interaction. However, exploiting the frustration of isotropic interactions and constructing zigzag or double chain structures may lead to spin spirals[255–257]. An attempt to construct a magnetically frustrated Shiba chain is presented in Subsection 4.3.2

4.3.1. Coupled Shiba chains

Due to the lack of an experimentally realizable self-organized magnetic 2D system that is in an in-plane FM state and that forms domains, I proceed to discuss an experiment where two chains of distinct geometries and magnetic ground states are coupled to one another. As a starting point, I choose to investigate a $\sqrt{2}a - [1\bar{1}0]$ Mn_{29} chain, which is well known from Section 4.2. As a reminder about the spectroscopic properties of such chains and to enable an easy comparison with the new geometry, STS results of a $\sqrt{2}a - [1\bar{1}0]$ Mn_{29} chain are shown in Figure 4.11, where panel a is a $\mathrm{d}I/\mathrm{d}V$-line profile, panel b is an STM image of the chain and panel c are slices of a $\mathrm{d}I/\mathrm{d}V$-grid at energies where clear in-gap states are observed.
As discussed in Section 4.2, we find dispersive states in an energy region from $\pm 1.30\,\mathrm{meV}$ to $\pm 0.5\,\mathrm{meV}$. Additionally, we observe another dispersive state at about $\pm 380\,\mu\mathrm{eV}$ and end states at $\pm 60\,\mu\mathrm{eV}$. The latter states are separated form the continuum of in-gap states by a finite-size gap

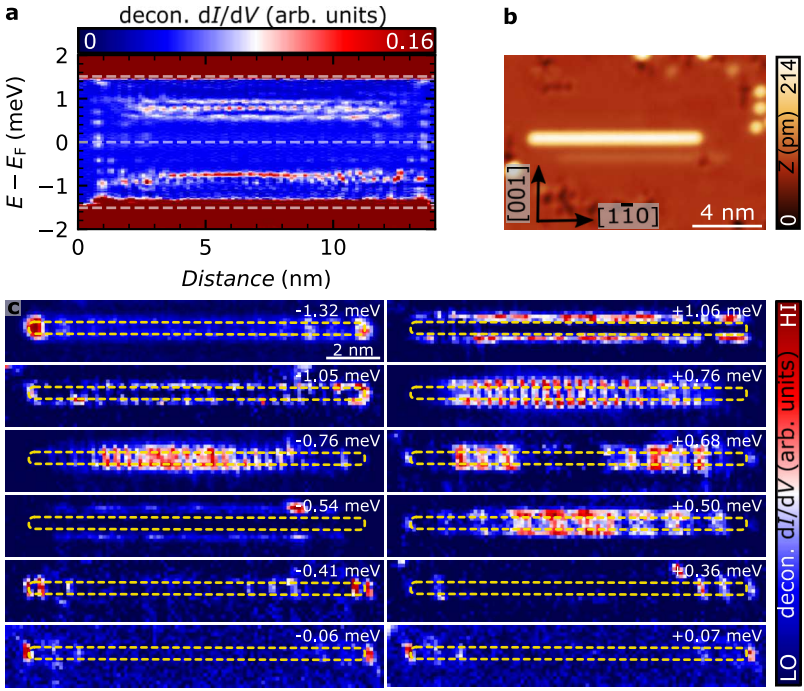

Figure 4.11.: **a** Deconvoluted $\mathrm{d}I/\mathrm{d}V$-line profile of a Mn_{29} $\sqrt{2}a - [1\bar{1}0]$ chain. White dashed horizontal lines mark the coherence peaks Δ_{Nb} and the Fermi level. **b** STM image of the chain shown in **a**. Black arrows and labels indicate crystallographic directions and are valid for panel **c** as well. **c** Energy slices of a $\mathrm{d}I/\mathrm{d}V$-grid, where in-gap states are observed in **a**. White labels in the top right corner of each panel indicate the energy. Yellow dashed lines mark the perimeter of the Mn_{29} $\sqrt{2}a - [1\bar{1}0]$ chain. Measurement parameters as indicated above.

and are identified as PMMs in Section 4.2 and Ref. [62]. If we were to increase the SOC in such a chain, we would expect that the localization of these modes improves and, thereby, the interactions of the MMs would be reduced. Therefore, MMs would already be pinned to zero energy at smaller chain lengths and a topological gap Δ_p should be observable in STS measurements.

We now attempt to increase SOC by constructing a chain in parallel and in proximity to the Mn_{29} $\sqrt{2}a - [1\bar{1}0]$ (original) chain by perturbing it with additional RKKY exchange-couplings. Ideally, the Shiba band structure of the original chain should only be altered by the additional SOC but not by a hybridization with the perturbing chain. In particular we attempt to do so by constructing an AFM-coupled $2\sqrt{2}a - [1\bar{1}0]$ (perturbing) chain$^{(216)}$ on one side of the close-packed FM coupled $\sqrt{2}a - [1\bar{1}0]$ chain$^{(62)}$ with a separation of $2a$ in $[001]$-direction, as illustrated in Figure 4.12a.

Comparing the $\mathrm{d}I/\mathrm{d}V$-line profile of the unperturbed Mn_{29} $\sqrt{2}a - [1\bar{1}0]$ chain in Figure 4.11a and the perturbed one in Figure 4.12b, we find that the in-gap states are drastically altered. While we still observe dispersive states, they are now located at almost all energies and we no longer observe a finite size gap. Furthermore, there are no clear signatures of PMMs localized at the ends of the original chain. While there are still end states, they are now shifted to higher energies. Furthermore, these end states are not symmetric in $\mathrm{d}I/\mathrm{d}V$-intensity for positive- and negative bias voltages as well as for the left and right edges.

Taking the spatial distributions of the new in-gap states into account, which are shown in Figure 4.12c, we find that most of the in-gap states are located on the perturbing chain. Furthermore, the states that have considerable $\mathrm{d}I/\mathrm{d}V$-intensity located on the original chain or to the side of the original chain that faces away from the perturbing chain (e.g. at $-1.39\,\mathrm{meV}$, $-0.96\,\mathrm{meV}$,$\pm 0.72\,\mathrm{meV}$ and $1.09\,\mathrm{meV}$ in Figure 4.12c) seem to be intimately connected to the states of the perturbing chain, i.e. we observe maxima in the $\mathrm{d}I/\mathrm{d}V$-intensity which have the same spatial distri-

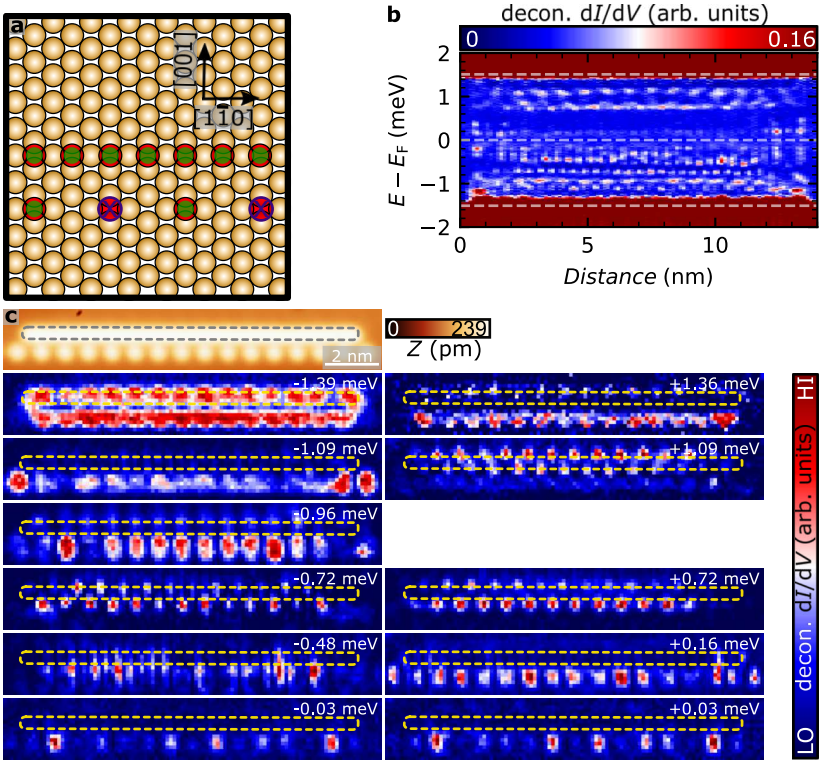

Figure 4.12.: a Illustration of the attempt to increase SOC in the Mn_{29} $\sqrt{2}a - [1\bar{1}0]$ chain on Nb(110), by constructing an AFM coupled $2\sqrt{2}a - [1\bar{1}0]$ chain in parallel to the FM coupled Mn_{29} $\sqrt{2}a - [1\bar{1}0]$ chain. Yellow and red spheres represent Nb and Mn atoms, respectively. Green spheres indicate spins that point out-of the paper plane and purple crosses point through the paper plane. Black arrows and labels indicate crystallographic directions and are valid for panel **c** as well. **b** Deconvoluted dI/dV-line profile of the Mn_{29} $\sqrt{2}a - [1\bar{1}0]$ chain located next to a Mn_{16} $2\sqrt{2}a - [1\bar{1}0]$ chain shown in the STM image in **c**. White dashed horizontal lines mark the coherence peaks Δ_{Nb} and the Fermi level. **c** STM image and energy slices of a dI/dV-grid, where in-gap states of the structure described in **a** are observed. White labels in the top right corner of each panel indicate the energy. Gray and yellow dashed lines mark the perimeter of the Mn_{29} $\sqrt{2}a - [1\bar{1}0]$ chain. Measurement parameters as indicated above.

bution on the perturbing chain and on the original chain (-1.39 meV and -0.96 meV) or are only spatially shifted by half a period (± 0.72 meV). Therefore, we conclude that the side chain is not a small perturbation in the present case but rather substantially hybridizes with the Shiba states/bands of the Mn_{29} $\sqrt{2}a - [1\bar{1}0]$ chain. This hybridization is one of the limiting factors in attempts to perturb Shiba chains by other magnetic structures, be it by 2D islands or by other chains. Ideally, one wants to avoid a change of the Shiba band structure and only aims at exposing the chain to a spiral magnetic field or to additional magnetic couplings which could lead to an exchange frustration in the original chain. Therefore, the herein presented attempt does not appear to work out in the planned way. However, it should be noted that the magnetic state which we expect from the perturbing chain — according to calculations — is not as ideal as described in the introduction (in-plane AFM coupled chain). Furthermore, SP-STM measurements of the system shown in Figure 4.12c are not available, so we can't be sure about the spin order in the coupled chains. Therefore, the observed physics might be altered for other material platforms.

4.3.2. Mn zigzag chains on Nb(110)

In this subsection we attempt to construct a Mn chain on Nb(110) with frustrated magnetic interactions, which could lead to the emergence of a spin spiral ground state. The magnetic couplings of Mn adatoms on Nb(110) are well-known from the SP-STM measurements of Ref. [59] and from *ab-initio* calculations of Refs. [60, 216]. Frustrated magnetic couplings may occur for example by tailoring a system in which the nearest-neighbors and the next nearest-neighbors of a given chain atom are both AFM-coupled.
The strongest AFM coupling of Mn atoms on Nb(110) is found for close-packed structures in $[1\bar{1}1]$-direction, for which an exchange interaction

of $J_{12} = -33\,\mathrm{meV}$ was calculated. The sign of this magnetic coupling is supported by SP-STM measurements on chains in this direction. Furthermore, an AFM coupling of $J_{12} = -7\,\mathrm{meV}$ is calculated for close-packed structures in $[1\bar{1}0]$-direction. However, SP-STM measurements indicate FM aligned moments in chains along the $[1\bar{1}0]$-direction with the close-packed spacing of $\sqrt{2}a^{(62)}$. This discrepancy makes a clear allocation of the sign of the exchange coupling in the $[1\bar{1}0]$-direction difficult.
If we assume an AFM coupling in the $[1\bar{1}0]$-direction we would be able to tailor a magnetically frustrated system by building a zigzag chain in the $[1\bar{1}0]$-direction, which is illustrated in Figure 4.13a (I will refer to this chain geometry as zigzag chain in the following). For a certain parameter range of the magnetic couplings in $[1\bar{1}0]$- and $[1\bar{1}1]$-direction, a spin spiral may occur, even if contributions of the DM interaction are negligible. In the following, we perform a STS and SP-STM study of such chains.
To begin with, we perform a length-dependent STS study where we construct zigzag chains in an atom-by-atom fashion and measure a $\mathrm{d}I/\mathrm{d}V$-line profile for each length up to a size of $N = 40$. This procedure enables us to perform a data analysis along the lines of the close-packed chains in [001]- and $[1\bar{1}0]$-direction which was presented in Section 4.2 and gave great insight into the Shiba band properties. Three exemplary $\mathrm{d}I/\mathrm{d}V$-line profiles of chains with lengths $N = 34, 35$ and 36 are shown in Figure 4.13b. We observe clear signatures of BdG QPI, indicating a good crystallographic quality and the absence of defects. Additionally, we measured a $\mathrm{d}I/\mathrm{d}V$-grid over a Mn_{34} zigzag chain, where the energy slices of Shiba states are shown in Figure 4.13c.
The $\mathrm{d}I/\mathrm{d}V$-line profiles in Figure 4.13b reveal three distinct energy-sections with strongly varying in-gap states. In the range of $-1\,\mathrm{meV} \geq E \geq -1.5\,\mathrm{meV}$, we find a single end state that is primarily located on the main axis of the chain. From the length-dependent data of the end states, we find that this state is constant in energy starting from a length of $N \sim 10$, as shown in the length-dependent data of Figure 4.14c (see

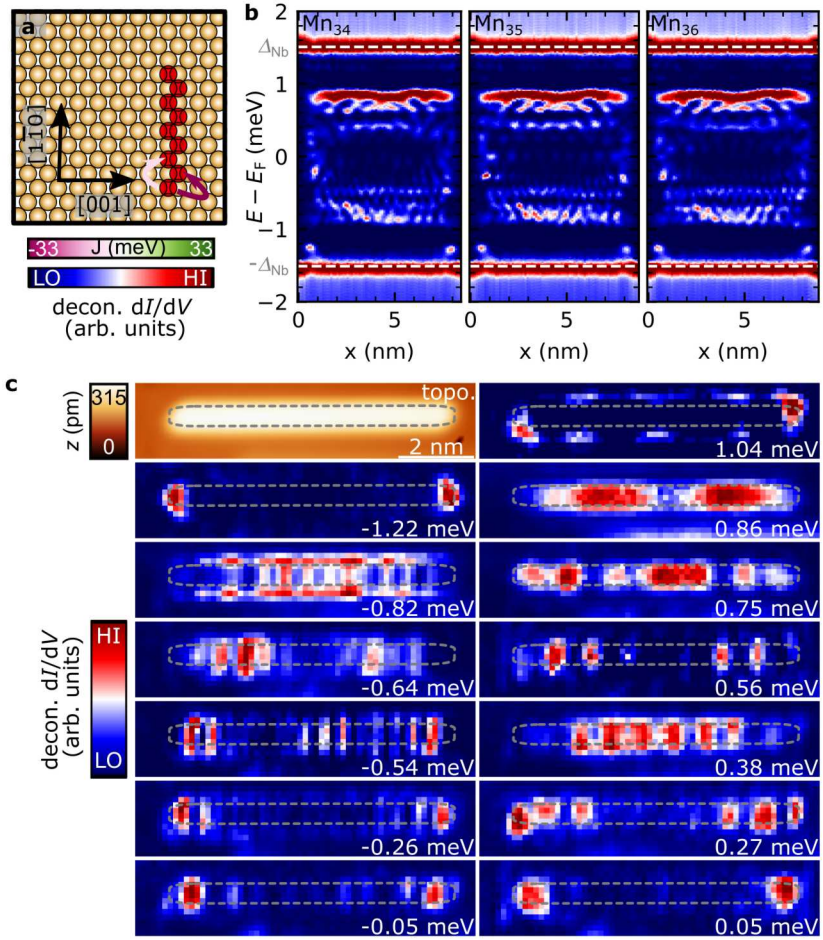

Figure 4.13.: a Illustration of a close-packed zigzag chain in $[1\bar{1}0]$-direction (red spheres) on Nb(110) (yellow spheres). Black arrows and labels indicate crystallographic directions. Color-coded arrows between red spheres indicate the magnetic couplings according to the scale underneath the panel, as calculated in Ref. [216]. **b** Three exemplary $\mathrm{d}I/\mathrm{d}V$-line profiles for zigzag chains of lengths 34, 35 and 36. White dashed horizontal lines mark the superconducting gap Δ_{Nb} of Nb. **c** STM image and energy slices of a $\mathrm{d}I/\mathrm{d}V$-grid measured over a Mn_{34} zigzag chain. Labels in the bottom right corner indicate the energy of the respective slice. Measurement parameters as indicated above.

description of the other panels of Figure 4.14 below). A comparable end state with an energy well above the Fermi level was observed for linear Mn chains in $[1\bar{1}0]$-direction (cf. Figure 4.11) as well.
In contrast, for positive energies in the range given above, we observe states that resemble standing waves along the chain that are located on the side of it (similar to the β states in Figure 4.6d) and have a nodal line in the center, i.e. they have a dumbbell-like shape in $[001]$-direction (see slice of the $\mathrm{d}I/\mathrm{d}V$-grid with $E = 1.04\,\mathrm{meV}$ in Figure 4.13c). The nodal line in the center of the zigzag chains causes a low $\mathrm{d}I/\mathrm{d}V$-intensity of these states in $\mathrm{d}I/\mathrm{d}V$-line profiles of Figure 4.13b. Nevertheless, we find that the states are dispersive and continuously shift from 0.8 meV to 1.4 meV, as seen in Figures 4.14a-c.
The in-gap states with the highest $\mathrm{d}I/\mathrm{d}V$-intensity are observed in the energy range from $0.4\,\mathrm{meV} \leq |E| \leq 0.9\,\mathrm{meV}$. These states clearly resemble standing waves, which have an increasing amount of maxima with decreasing energy. In the $\mathrm{d}I/\mathrm{d}V$-line profiles of Figure 4.13b and the length-dependent $\mathrm{d}I/\mathrm{d}V$-spectra obtained in the bulk of the chain (Figure 4.14b), it appears as if these states are cut-off from the energy range of$+400\,\mu\mathrm{eV}$ to $-400\,\mu\mathrm{eV}$. Furthermore, from the $\mathrm{d}I/\mathrm{d}V$-grid in Figure 4.13c we find that the states are localized primarily in the area given by the dashed ellipse, i.e. inside the chain.
The third distinct energy range extends from $+400\,\mu\mathrm{eV}$ to $-400\,\mu\mathrm{eV}$. Interestingly, we do not find any in-gap states in the bulk of the zigzag chains in this energy range, as shown in Figure 4.13b. We observe the absence of bulk states starting at a length of $N \sim 20$, as apparent from Figure 4.14b.
However, in contrast to the bulk of the chain, we observe a plethora of end states in this energy range. We find that the exact energies of the end states depend strongly on the particular chain length. This is easily visible in Figure 4.14c, where $\mathrm{d}I/\mathrm{d}V$-spectra obtained at the ends of the zigzag chain are plotted sequentially. It appears as if the end states are continuously shifting from $-300\,\mu\mathrm{eV}$ to $+300\,\mu\mathrm{eV}$ with increasing chain

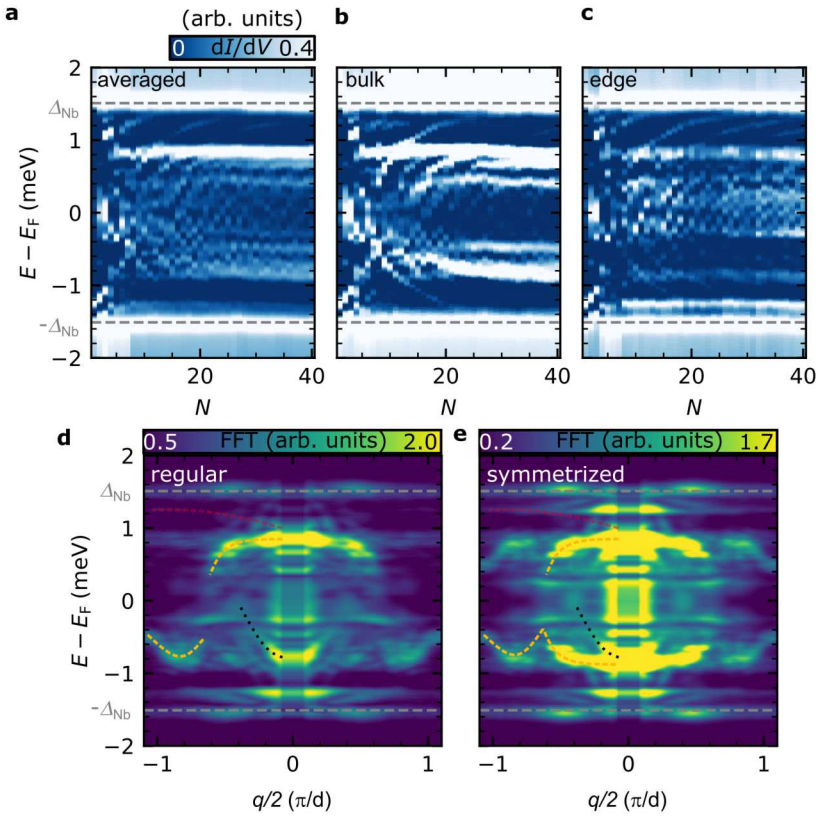

Figure 4.14.: a-c Length-dependent $\mathrm{d}I/\mathrm{d}V$-spectra obtained for zigzag Mn chains in $[1\bar{1}0]$-direction on Nb(110) by averaging over an entire $\mathrm{d}I/\mathrm{d}V$-line profile (**a**), by plotting only the $\mathrm{d}I/\mathrm{d}V$-spectra obtained in the bulk of the chain (**b**) and at the ends of the chains (**c**). Gray dashed horizontal lines mark the superconducting gap of Nb. **d** 1D-FFT of all investigated zigzag chains with lengths of $N = 16$ to $N = 40$. Gray dashed horizontal lines mark the superconducting gap of Nb(110). **e** Symmetrized 1D-FFT obtained by flipping the array along the energy axis and averaging it with the original 1D-FFT of panel **d**. This illustrates how the scattering pattern would look like in the absence of particle-hole asymmetry. Colored dashed lines are guides to the eye. Measurement parameters as indicated above.

length and in periods of $\Delta N \approx 6$. From the $\mathrm{d}I/\mathrm{d}V$-grid in Figure 4.13c, we find that these end states are located on the main axis of the chain.
The analysis above indicates that there are at least three Shiba bands in Mn zigzag chains on Nb(110). To obtain information on their dispersion, we perform an energy-wise 1D-FFT of the $\mathrm{d}I/\mathrm{d}V$-line profiles of chains with lengths $N = 16$ to $N = 40$, which is shown in Figure 4.14d. Here, d in the x-axis label refers to the nearest-neighbor distance in $[1\bar{1}0]$-direction, which is $0.5 \cdot \sqrt{2}a$. Again, we can analyze the entire energy range in the three separate sections mentioned above. From $1\,\mathrm{meV} \leq E \leq 1.5\,\mathrm{meV}$ we find a Shiba band with positive curvature and very low $\mathrm{d}I/\mathrm{d}V$-intensity (red dashed line). From 0.9 meV and $q/2 = 0$ to 0.4 meV and $q/2 = \pm 0.5\pi/d$ we find a parabolic band with negative curvature (yellow dashed line). The band appears to be gapped from $+400\,\mu\mathrm{eV}$ to $-400\,\mu\mathrm{eV}$, since it seems as if the Shiba band continues at $-400\,\mu\mathrm{eV}$ and $q/2 = \pm 0.6\pi/d$. The fact that these two branches might belong to the same band, is highlighted in the 1D-FFT that is symmetrized around E_F (these particle-hole partners must exist, but are probably not visible in STM measurements due to a strong particle-hole asymmetry[61]), which is shown in Figure 4.14e. In this representation of the data, both yellow color-coded bands that I have previously described appear to be continuous at $q/2 = \pm 0.6\pi/d$.
Additionally to this gapped band, we find another Shiba band which might cross the Fermi level continuously. It has its band bottom at $\pm 700\,\mu\mathrm{eV}$ and $q/2 = 0$ and might proceed to cross E_F at $q/2 = \pm 0.4\pi/d$ (black dashed line). However, the low $\mathrm{d}I/\mathrm{d}V$-intensity makes it difficult to unambiguously determine if the band crosses the Fermi level, or whether there is a small gap.
To investigate the magnetic ground state of Mn zigzag chains in $[1\bar{1}0]$-direction, we perform SP-STM measurements using a bulk Cr tip. Prior to the measurements of the zigzag chain, we verify the magnetic sensitivity and the magnetic stability of the tip magnetization for the relevant field strengths ($-700\,\mathrm{mT}$ to $+700\,\mathrm{mT}$) by performing SP-STM measurements

on an AFM coupled chain in $[1\bar{1}1]$-direction, where magnetic contrast is clearly visible (not shown here). Additionally, it should be noted that a slight asymmetry of the tip can produce fake features in $\mathrm{d}I/\mathrm{d}V$-maps. A regular STM image, $\mathrm{d}I/\mathrm{d}V$-maps obtained at $+700\,\mathrm{mT}$ and at $-700\,\mathrm{mT}$, and the calculated asymmetry map are shown in Figure 4.15a. The latter was calculated by

$$A = \frac{\mathrm{d}I/\mathrm{d}V(6\,\mathrm{mV},\mathbf{r})|\uparrow\uparrow - \mathrm{d}I/\mathrm{d}V(6\,\mathrm{mV},\mathbf{r})|\uparrow\downarrow}{\mathrm{d}I/\mathrm{d}V(6\,\mathrm{mV},\mathbf{r})|\uparrow\uparrow + \mathrm{d}I/\mathrm{d}V(6\,\mathrm{mV},\mathbf{r})|\uparrow\downarrow}. \tag{4.4}$$

We find that there is no strong contrast modulation along the chain direction in the $\mathrm{d}I/\mathrm{d}V$-maps. While there is a contrast modulation in the direction perpendicular to the chain in $\mathrm{d}I/\mathrm{d}V$-maps, as it would be expected for a row-wise AFM coupled chain, we attribute those features to an asymmetry of the tip. This is motivated by the fact, that the contrast modulation is strongly reduced in the asymmetry map and that similar features are observed in simple linear chains (e.g. for $\sqrt{3}/2a$-$[1\bar{1}1]$ Mn chains, which is not shown here). Furthermore, the $\mathrm{d}I/\mathrm{d}V$-intensity is continuously higher at $-700\,\mathrm{mT}$ than at $+700\,\mathrm{mT}$, which is clearly visible in the asymmetry map. Here, almost the entire spatial extent of the chain (indicated by the gray dashed line) appears dark blue. Therefore, we conclude that an AFM ground state of this chain is unlikely. Due to the lack of any contrast modulation along the chain, it rather appears as if the chain is FM coupled. As we performed $\mathrm{d}I/\mathrm{d}V$-maps B-field-dependently, we can evaluate the $\mathrm{d}I/\mathrm{d}V$-intensity averaged over the chain as a function of the magnetic field. This is demonstrated in Figure 4.15b.
It should be noted that the $\mathrm{d}I/\mathrm{d}V$-intensities in the field range of $-400\,\mathrm{mT}$ and $+400\,\mathrm{mT}$ appear unreasonable, which is caused by the fact that the Nb substrate is superconducting in this B-field range, which may strongly alter the $\mathrm{d}I/\mathrm{d}V$-intensity at low biases as 6 mV. Nevertheless, a clear difference in $\mathrm{d}I/\mathrm{d}V$-intensities is observed for fields above $+400\,\mathrm{mT}$ and

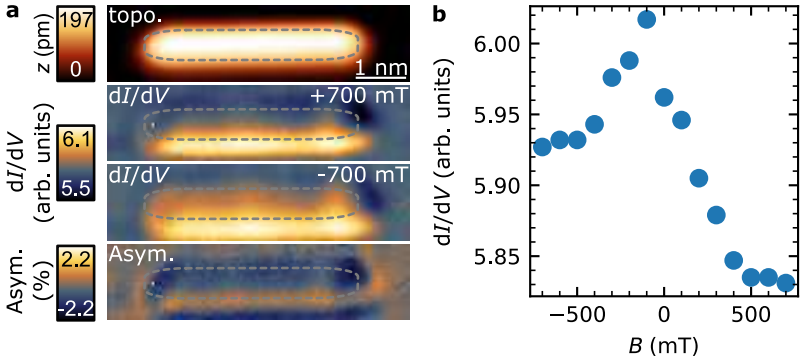

Figure 4.15.: a STM image and $\mathrm{d}I/\mathrm{d}V$-maps of a zigzag Mn chain in $[1\bar{1}0]$-direction, measured with a spin-polarized bulk Cr tip in an out-of-plane magnetic field of $\pm 700\,\mathrm{mT}$, as indicated in the top right corner of each panel. The bottom panel is the spin asymmetry map of the $\mathrm{d}I/\mathrm{d}V$-maps obtained at opposite magnetic fields. **b** Averaged $\mathrm{d}I/\mathrm{d}V$-intensity of the zigzag chain depending on the applied magnetic field. Measurement parameters: $V_{\mathrm{bias}} = 6\,\mathrm{mV}$, $I = 1\,\mathrm{nA}$, $V_{\mathrm{mod}} = 40\,\mu\mathrm{V}$.

below $-400\,\mathrm{mT}$, as it is larger in the latter case.
In any case, we did not observe any evidence for a spin spiral magnetic ground state. However, the chain doesn't appear to be in an AFM state either, which is interesting as the AFM exchange coupling in $[1\bar{1}1]$-direction is the strongest one of all that were calculated and should, therefore, dominate the overall magnetic interactions in the zigzag chains.

4.3.3. Conclusion

In conclusion, we have realized two artificially constructed systems in which we attempt to tailor magnetic frustration or expose a spin chain with a well-known Shiba band structure to a spiral magnetic field or alternate its magnetic couplings. On the upside, it was possible to construct such complex structures reliably and we observed well-defined Shiba bands in both cases. However, we found that a variation of the hybridization of the YSR states is the dominant effect in both structures. Considering the geometry with the perturbing chain in $[1\bar{1}0]$-direction, we observed that the in-gap states of the $\sqrt{2}a - [1\bar{1}0]$ chain were considerably altered. If one were to further pursue this approach, one would have to carefully study the influence of the distance between a well-known Shiba chain and 2D island or a perturbing chain.
In the second approach we attempt to construct a Mn chain in a more complex zigzag geometry, in order to achieve frustrated magnetic couplings. However, we do not observe indications for a non-collinear magnetic ground state, but we rather find indications of FM order. Due to the very low symmetry and interatomic distances in these particular zigzag chains we observe at least three Shiba bands in the length-dependent study of $\mathrm{d}I/\mathrm{d}V$-line profiles. The in-gap states lost their clear orbital character, which results in a scattering pattern of BdG quasiparticles that is very difficult to understand due to the plethora of in-gap states. Even after performing a QPI analysis it is difficult to unambiguously determine the

band properties without extensive theoretical model calculations. This result illustrates the advantage of linear chains along the high symmetry directions of the Nb(110) substrate over more complex chain geometries.

4.4. Effect of substrate SOC on the topological gap size of Shiba bands

In this section, I demonstrate that it is indeed possible to influence the Shiba band properties and the size of a minigap by placing a given spin chain on a substrate with higher SOC, namely Ta(110). I proceed to present two STS studies on artificial chains of Mn atoms on Ta(110), which are performed in analogy to Section 4.2. In particular, I discuss length-dependent STS measurements to reveal the Shiba band structures and I present spin-polarized scanning tunneling spectroscopy (SP-STS) results on the magnetic ground states of close-packed Mn chains in [001]- and $[1\bar{1}0]$-direction.
The experimental data, the figures and parts of the following text are largely based on two joint publications. One lays the foundation for the entire experimental results of this study:

> Philip Beck, Lucas Schneider, Roland Wiesendanger and Jens Wiebe
>
> *Systematic study of Mn atoms, artificial dimers and chains on superconducting Ta(110)*
>
> arXiv:2205.10073 [cond-mat.supr-con] (2022).

The preparation methods (see Section 3.3), the investigation of single Fe and Mn adatoms (see Subsection 4.4.1) and of close-packed chains in $[1\bar{1}0]$-direction (Subsection 4.4.3) are published in this manuscript. The investigation of artificial dimers in [001]- and $[1\bar{1}0]$-direction is not presented in this thesis for the sake of shortness.
A second publication focuses on the direct comparison of in-gap states and the Shiba band structure of $1a - [001]$ Mn chains on Ta(110) and Nb(110). In analogy to Subsection 4.2.1, we identify a topological minigap in one of the two Shiba bands. Due to a very similar Shiba band structure

of the $1a - [001]$ Mn chains on Ta(110) and Nb(110), we can link an increase of the minigap for the former substrate to the higher SOC of the substrate. The experimental results, the figures and parts of the text presented in the Introduction and Subsections 4.4.1 and 4.4.2 are largely based on this publication:

> Philip Beck, Lucas Schneider, Roland Wiesendanger and Jens Wiebe
>
> *Effect of substrate spin-orbit coupling on the topological gap size of Shiba chains*
>
> arXiv:2205.10062 [cond-mat.supr-con] (2022).

The following studies were performed on the Ta(110) sample, whose preparation is described in Subsection 3.3.1. The mechanically sharpened Nb bulk tip (described in Subsection 3.3.3) was used for all measurements, unless indicated otherwise. All $\mathrm{d}I/\mathrm{d}V$-spectra which were obtained with a superconducting STM tip were processed by numerical deconvolution as described in Subsection 3.1.2.

Contributions

The ideas and experimental results shown herein were obtained together with Dr. Lucas Schneider. Self-written Python code and Gwyddion[248] were used for the data analysis and for the presentation of data in figures.

Introduction

The shortcomings of the MSH structures investigated in the previous two sections regarding the strength of SOC in Shiba bands (Section 4.2) and the limits with regards to tailoring structures of Mn on Nb(110) exposed to artificial/synthetic SOC (Section 4.3) lead to a search for new supercon-

ducting platforms with the possibility to construct artificial chains which are exposed to higher SOC. However, even though SOC is considered to be a key ingredient for the realization of MBS and a large topological gap, there is no experimental study on the origin of SOC in Shiba bands so far. In particular, I propose an experimental comparison of the in-gap band structures of systems with strongly different SOC but otherwise very similar properties, which is lacking so far.

In this section, I present a STS study of Mn adatoms and artificial chains on clean Ta(110). This material platform enables an investigation on the effect of strong substrate SOC on Shiba bands, as elaborated in the following: By looking at the periodic table of elements it is apparent that tantalum is the element located one period below niobium. Therefore, they have a similar electronic configuration of the valence level which leads to almost indistinguishable physical properties. Both elements share the body-centered cubic (bcc) crystal structure and their lattice constants are only 0.3 % apart[258]. Additionally, they have very similar electronic properties, as indicated by their work functions which only differ by 1.5 %[259], their almost identical Fermi surfaces[260,261] and by the occupied d_{z^2}-like surface state with similar effective masses and binding energies that the (110)-surfaces of both elements display[206,207,262,263]. In fact, niobium and tantalum are so similar, that they were even named after father and daughter in greek mythology, and are commonly referred to as "geochemical twins"[264].

However, one major difference between both materials is the strength of SOC effects. According to theoretical simulations and experiments on the surface states of both elements, it was found that the SOC strength is increased by a factor of ~ 3 for Ta(110) compared to Nb(110)[262,263]. This enables us to directly compare the band properties of artificial Shiba chains constructed on Ta(110) with those prepared on Nb(110). As demonstrated in the previous sections (Sections 4.1 and 4.2) the latter substrate is particularly well-characterized in combination with Cr[63,265], Mn[59–62] and Fe[244] adatom structures. Since the Mn chains on Nb(110) show the

clearest indications of SOC effects, e.g. the observation of a topological minigap in a Shiba band and the length-dependent investigation of PMMs, we proceed to study similar chains on Ta(110).
In particular, I discuss single Mn and Fe adatoms on Ta(110) and their YSR states in order to further highlight the pronounced similarities of Ta(110) and Nb(110) in Subsection 4.4.1. Afterwards I will focus on the characterization of $1a - [001]$ Mn chains on Ta(110) using SP-STM to determine the magnetic ground state and length-dependent $\mathrm{d}I/\mathrm{d}V$-spectra to reveal the Shiba band structure and the existence of a topological gap. As physical quantities other than SOC are expected to play only a minor role in the differences of these Mn chains on Ta(110) and Nb(110), I will directly compare these two types of Shiba chains in Subsection 4.4.2. Employing the same tools as before, I proceed to investigate $\sqrt{2}a$-$[1\bar{1}0]$ Mn chains on Ta(110) in Subsection 4.4.3.

4.4.1. YSR states of Mn and Fe atoms on Ta(110)

A clean Ta(110) sample with statistically distributed Mn adatoms that is prepared according to the description given in Subsection 3.3.1 is shown in Figure 4.16a. Here, we identify bright protrusions as Mn adatoms and dark spots/depressions as residual oxygen. We performed the deposition of Mn and Fe adatoms in a two step process as described in Subsection 3.3.1. We start with the investigation of Mn atoms and artificial structures and only then evaporated additional Fe atoms, which enables a clear distinction of both species. However, it is more instructive to discuss the properties of both species jointly. An overview STM image of the same Ta(110) sample as in Figure 4.16a but featuring additional randomly distributed Fe atoms is shown in Figure 4.16b. A closer look at the adatoms reveals that there are two dominant species present: At the measurement parameters of Figure 4.16b, the slightly shallower ones are identified as Fe atoms ((58.0 ± 0.5) pm), whereas the ones with a slightly

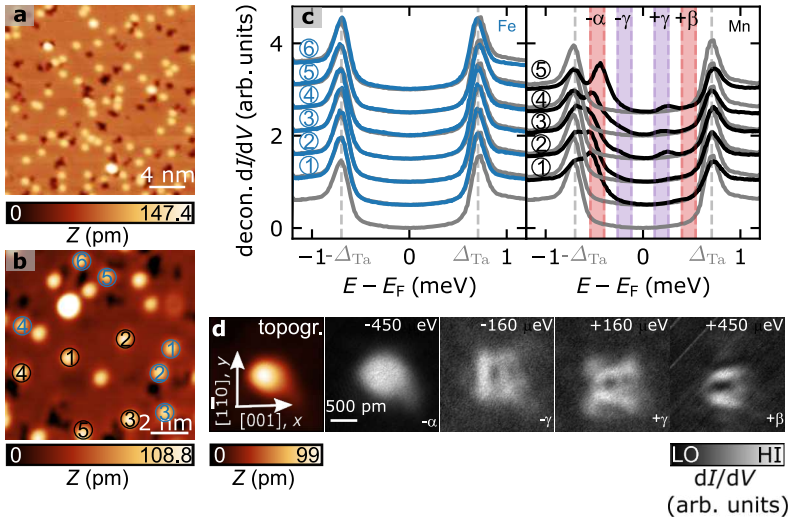

Figure 4.16.: a and **b** Overview STM images showing statistically distributed Mn atoms on clean Ta(110). Additionally, Fe atoms were deposited in panel **b**, where color-coded encircled numbers highlight the positions where $\mathrm{d}I/\mathrm{d}V$-spectra were measured. **c** Exemplary $\mathrm{d}I/\mathrm{d}V$-spectra measured on Fe atoms (blue), on Mn atoms (black), as well as on the Ta(110) substrate (gray). Color-coded encircled numbers link the spectra to a position in the overview image of panel **b**. A $\mathrm{d}I/\mathrm{d}V$-spectrum taken on the substrate is pasted behind every spectrum to enable an easy comparison. The spectra are offset by 0.5 arb. units for the sake of visibility. Gray vertical lines mark the coherence peaks of Ta at $\Delta_{\mathrm{Ta}} = \pm 690\,\mu\mathrm{eV}$. Red- and purple-colored lines enclose shaded energy areas where YSR states of randomly positioned Mn atoms are typically found. **d** STM image of a single Mn impurity and constant-contour $\mathrm{d}I/\mathrm{d}V$-maps taken at the bias indicated in the top right corner of each panel. The scale bar and the crystallographic directions displayed in the bottom left corner are valid for all panels of **d**. Measurement parameters: **a** $V_{\mathrm{bias}} = -1\,\mathrm{V}$, $I = 500\,\mathrm{pA}$, **b** $V_{\mathrm{bias}} = -20\,\mathrm{mV}$, $I = 200\,\mathrm{pA}$, **c** $V_{\mathrm{stab}} = -2.5\,\mathrm{mV}$, $I_{\mathrm{stab}} = 1\,\mathrm{nA}$, $V_{\mathrm{mod}} = 20\,\mu\mathrm{V}$ and **d** $V_{\mathrm{stab}} = -3\,\mathrm{mV}$, $I_{\mathrm{stab}} = 1\,\mathrm{nA}$ and $V_{\mathrm{mod}} = 40\,\mu\mathrm{V}$.

larger apparent height ((74.3 ± 0.6) pm) are identified as Mn atoms. An exemplary selection of each adatom species is marked by blue and black encircled numbers, respectively. Deconvoluted $\mathrm{d}I/\mathrm{d}V$-spectra, which were measured directly on top of each of the highlighted impurities are shown alongside the same color-coded numbers in Figure 4.16c. A deconvoluted $\mathrm{d}I/\mathrm{d}V$-spectrum measured on bare Ta(110) is pasted behind every spectrum of the impurities and is displayed in gray at the very bottom of both panels in Figure 4.16c. We observe sharp coherence peaks located at $\Delta_{\mathrm{Ta}} = \pm 690\,\mu\mathrm{eV}$, which exactly matches reference values[266]. At our measurement temperature of 320 mK the superconducting gap of bare Ta(110) is fully pronounced, i.e. the $\mathrm{d}I/\mathrm{d}V$-signal approaches the noise level at energies lower than Δ_{Ta}. It should be noted, that some of the used tips display a less sharp drop-off of the $\mathrm{d}I/\mathrm{d}V$-signal inside the gap, e.g., it is slightly visible in Figure 4.16c. This is most probably the result of a tip with a slightly reduced gap value or quasiparticle lifetime. A particularly good example of a very good tip displaying sharp Ta coherence peaks in $\mathrm{d}I/\mathrm{d}V$-spectra, which was obtained in the herein presented study, is shown in Ref. [267].

Comparing the six $\mathrm{d}I/\mathrm{d}V$-spectra of Fe atoms (blue) with the gray-colored substrate spectra, we find very little differences (Figure 4.16c). Most importantly, we do not observe any YSR states located between the coherence peaks of the Ta substrate. This changes clearly if we investigate Mn impurities. Here, we find that the $\mathrm{d}I/\mathrm{d}V$-spectra vary strongly in comparison to the substrate spectrum. In particular, the coherence peaks of tantalum are reduced in intensity and we additionally observe two pairs of YSR states inside the gap. Furthermore, all $\mathrm{d}I/\mathrm{d}V$-spectra measured on a Mn impurity show similar in-gap features: The most intense peaks are found at $(-470 \pm 70)\,\mu\mathrm{eV}$, as indicated by the red shaded region termed $-\alpha$. The corresponding states at positive bias termed $+\beta$ (as we will argue in the following, the states have distinct orbital origin) are very low in intensity and are not visible in the spectra shown in Figure 4.16c. Considering the 2D maps in Figure 4.16d, we will proceed

to show that this is partly caused by the spatial distribution of this particular state, which has a nodal line in the center of the atom. Nevertheless, even if one averages a spectrum over the adatom extent, the YSR state at $+(450 \pm 70)$ µeV only shows a low $\mathrm{d}I/\mathrm{d}V$-signal, which is most probably caused by a non-magnetic scattering contribution of the impurity[144,146]. The second pair of YSR states is located at $\pm(190 \pm 70)$ µeV as indicated by the energy range shaded in purple and termed $\pm\gamma$.
In the following, I proceed to discuss the absence and presence of YSR states inside the superconducting gap of Ta(110) for Fe and Mn adatoms, respectively. In a model for quasi-classical spins coupled to an *s*-wave superconducting host, which turns out to be a decent approximation for transition metal atoms having magnetic moments considerably larger than $1\mu_\mathrm{B}$, the energy of YSR states is given by

$$\epsilon = \Delta \frac{1 - (JS_\mathrm{imp}\pi N_\mathrm{N}(E_\mathrm{F}))^2}{1 + (JS_\mathrm{imp}\pi N_\mathrm{N}(E_\mathrm{F}))^2}, \tag{4.5}$$

which is derived from Equation 2.30[141–143,167]. Recent experiments and theoretical calculations have shown that J is subject to a systematic trend regarding the 3*d* transition metal series[265,268]. Starting with the atomic species of Mn, J is expected to increase for higher and lower atomic number elements. Exactly this trend has been shown to hold true for several 3*d* transition metal species on clean Nb(110)[60,63,212]. Therefore, we speculate that $JS_\mathrm{imp}\pi N_\mathrm{N}(E_\mathrm{F})$ is considerably increased for Fe with respect to Mn. According to Equation 4.5, an increase of this term eventually leads to YSR states that shift into the coherence peaks of the substrate.
Now, let us discuss the YSR states of Mn adatoms in detail. From Figure 4.16c one finds that the YSR states $+\alpha$ and $\pm\gamma$ vary slightly in energy for the different impurities investigated in Figure 4.16b. This is naturally explained by the random distribution of the Mn atoms investigated here, which were not moved to a defect free region of the surface prior to the measurement. It has been shown that one may influence the parameter

$JS_{\mathrm{imp}}\pi N_{\mathrm{N}}(E_{\mathrm{F}})$ in Equation 4.5 experimentally, i.e. by changing the tip-impurity distance and, thereby, modifying attractive/repulsive forces between tip and impurity[148,269], by having magnetic molecules forming a self-organized island with Moiré-like variations[270], or by bringing adatoms close to residual impurities[212]. The latter example is exactly what we are observing here, since some of the Mn adatoms are quite obviously positioned in proximity to residual oxygen (3–5) or might even be located on top of an oxygen patch (1–2). However, it is important to note that even though the energies of the YSR states vary slightly for randomly distributed Mn adatoms, the overall spectroscopic features appear to be quite similar, i.e. we always find two pairs of YSR states. Once an adatom is moved to a defect-free region, we find very reproducible energies of the YSR states ($\pm 450\,\mu\mathrm{eV}$ and $\pm 200\,\mu\mathrm{eV}$), which is crucial for the purpose of studying artificially assembled dimers and chains. Therefore, defect-free regions were chosen to perform the following experiments.

An example of a Mn atom that was moved to a defect free environment is shown in Figure 4.16d. A $\mathrm{d}I/\mathrm{d}V$-spectrum measured on this atom is shown in Ref. [267] and displays YSR states at $+\alpha = +450\,\mu\mathrm{eV}$, $-\beta = -450\,\mu\mathrm{eV}$, and $\pm\gamma = \pm 200\,\mu\mathrm{eV}$, which is in very good agreement with the values that we obtained for statistically distributed Mn atoms in Figure 4.16. The spatial distributions[151,152] of this atom's YSR states are shown in Figure 4.16d, where the leftmost panel is an STM image of the adatom, and the remaining panels are constant-contour $\mathrm{d}I/\mathrm{d}V$-maps (see Subsection 3.1.4).

As I have shown in Subsections 3.3.2 and 4.1.1, Mn adatoms are stably adsorbed in the fourfold-coordinated hollow sites of Ta(110) and Nb(110), respectively. This adsorption geometry belongs to the C_{2v} point group. Here, the d_{xy}-, d_{xz}- and d_{yz}-orbitals are assigned to different irreducible representations of the group and should, therefore, have one scattering channel each, which can not hybridize with one another. On the other hand, the $d_{x^2-y^2}$- and d_{z^2}-orbitals may hybridize as they belong to the same irreducible representation. Therefore, we expect similar spatial

distributions for the YSR states of Mn adatoms on Ta(110) and on Nb(110) (see Subsection 4.1.1).
Indeed, we find spatial distributions which match the 2D projection of atomic d-orbitals onto the $x-y-$plane. However, the distinct spatial distribution of the particle-hole partners of the YSR state at $\pm 450\,\mu\text{eV}$ is rather unusual. While the one at negative biases resembles the d_{z^2}-orbital with slight contributions from $d_{x^2-y^2}$, the positive bias state quite clearly matches a d_{yz}-orbital. As the just described positive- and negative YSR states may not hybridize in an individual atom due to symmetry constraints, we interpret them as two distinct YSR states which are closer in energy than our experimental resolution allows us to distinguish. Along with a strong intensity asymmetry, which is given by a non-magnetic scattering term, the different spatial distributions for positive and negative biases explain the intensity asymmetries of these YSR states in Figures 4.16c and d.
On the other hand, the spatial distributions of the $\pm\gamma$-states are similar for positive and negative biases. They resemble the 2D projection of a d_{xy}-orbital, possibly with contributions from d_{xz}- and d_{yz}-orbitals. We do not find unambiguous signatures of a YSR state with dominant d_{xz} character, except for the minor contribution of the dumbbell-shape in the map at $-160\,\mu\text{eV}$. Alternatively, this YSR state could be hidden in the coherence peaks of the Ta substrate. A comparison of the YSR state energies of Mn/Ta(110) and Mn/Nb(110) is shown in Table 4.2.
Overall, we find very similar dominating YSR states for a single Mn atom on Ta(110) and Nb(110) (cf. Figure 4.16 and Figure 4.1). For example, we observe a YSR state close to the coherence peak of the substrate with a very strong particle-hole asymmetry and with a very local and spherical spatial distribution on top of Mn (d_{z^2}). Additionally, we find another YSR state with a more even particle-hole intensity distribution, which is located close to the Fermi level and has a more extended spatial shape located at the sides of the Mn atom (d_{xy} for Ta and d_{yz} for Nb, respectively). However, Table 4.2 shows that the energetic order of the d_{xz}, d_{yz}, and d_{xy}

Table 4.2.: Comparison of the YSR states of single Mn adatoms on Ta(110) and Nb(110) in units of the respective superconducting gap. YSR states that are not observed experimentally on Ta(110) are left blank.

d-orbital	$\epsilon_{\mathrm{YSR}}\ (\Delta_{\mathrm{Ta}})$	$\epsilon_{\mathrm{YSR}}\ (\Delta_{\mathrm{Nb}})^{(60)}$
$d_{z^2}, d_{x^2-y^2}$	0.65 (α)	0.79 (α)
d_{yz}	0.65 (β)	0.08 (δ)
d_{xy}	0.29 (γ)	0.70 (β)
d_{xz}		0.52 (γ)

YSR states is interchanged for Ta with respect to Nb.
Considering this comparison, we conclude that the Shiba bands of chains where the d_{z^2}-like YSR state dominates should be similar for Mn/Nb(110) and Mn/Ta(110). An example of such Shiba chains are the $1a - [001]$ Mn chains on Nb(110), that are discussed in Subsection 4.2.1 and Ref. [61]. For this chain geometry, we expect that the substrate's SOC strength contributes the main difference between both systems. We proceed to compare exactly those chains in Subsection 4.4.2. A more limited comparison is possible considering Shiba chains where the d_{yz}- or d_{xy}-like YSR states dominate the properties, as e.g. the $\sqrt{2}a$-$[1\bar{1}0]$ Mn chains on Nb(110) (see Subsection 4.2.2 and Ref. [62]). Since the starting energies E_0 of the relevant single impurity YSR states already vary significantly, we do not necessarily expect similar results. Nevertheless, $\sqrt{2}a$-$[1\bar{1}0]$ Mn chains on Ta(110) are presented in Subsection 4.4.3. While a detailed and spacing-dependent study of artificial dimers can contribute largely to the understanding of Shiba band formation[60], I refrain from doing so at this point for the sake of shortness. Interested readers are referred to Ref. [197].

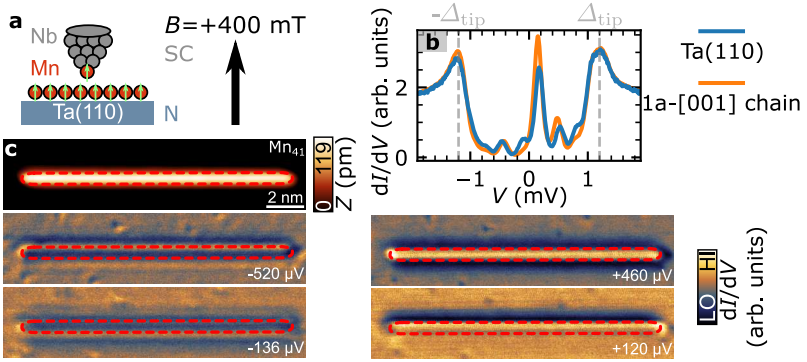

Figure 4.17.: a Sketch of the tunneling geometry employing the method of YSR SP-STM. **b** Two $\mathrm{d}I/\mathrm{d}V$-spectra measured on the Ta(110) substrate and on a Mn_{41} $1a-[001]$ chain using a superconducting Nb tip decorated with Mn atoms (illustrated in **a**). The same microtip was used for all panels and an out-of-plane magnetic field of $+400\,\mathrm{mT}$ was applied. **c** STM image and constant-contour $\mathrm{d}I/\mathrm{d}V$-maps measured at biases of the tip's YSR states, as indicated in the bottom right corner of each panel. The red dashed lines marks the spatial extent of the Mn chain. Measurement parameters: $V_{\mathrm{stab}} = -2\,\mathrm{mV}$, $I_{\mathrm{stab}} = 2\,\mathrm{nA}$, $V_{\mathrm{mod}} = 40\,\mu\mathrm{V}$ and $B = +400\,\mathrm{mT}$.

4.4.2. Magnetic and electronic properties of $1a-[001]$ Mn chains

Since we have discussed $1a-[001]$ Mn chains at an earlier stage of this thesis, I refer to the illustration of the atomic positions of this chain geometry in Figure 4.6a. We commence the comparison of $1a-[001]$ Mn chains on Ta(110) and Nb(110) by performing SP-STS and SP-STM measurements. For this purpose, I use a YSR state functionalized superconducting Nb tip (details on method in Ref. [59] and Figure 4.17a). SP-STS and SP-STM measurements on a Mn_{41} $1a-[001]$ chain are shown in Figures 4.17b and c. The substrate is quenched into its metallic phase by an out-of-plane magnetic field of $+400\,\mathrm{mT}$ throughout these measurements. Thereby, we avoid tunneling processes between YSR states of

the tip and YSR states of the sample, which could dramatically complicate the interpretation of the SP-STS data[149]. Furthermore, an external B-field stabilizes the magnetic moment of the tip apex in the field direction, which is required as we only pick up very few magnetic atoms. As shown recently, the particle-hole partners of the tip's YSR states have opposite spin orientations[56,144,271]. A $\mathrm{d}I/\mathrm{d}V$-spectrum measured on the Ta substrate (blue curve), which clearly demonstrates the presence of at least three YSR states on the tip, and a $\mathrm{d}I/\mathrm{d}V$-spectrum measured on the Mn_{41} $1a - [001]$ chain (orange curve) are shown in Figure 4.17b.
Let us discuss the influence of spin-polarized tunneling using the example of the YSR state at $\pm 130\,\mu V$. From the spectrum measured on the Ta(110) substrate, it is apparent that this state has a particle-hole asymmetry in the $\mathrm{d}I/\mathrm{d}V$-intensity, i.e. it has a higher intensity at $+130\,\mu V$ than at $-130\,\mu V$. Upon moving the tip onto the Mn_{41} $1a - [001]$ chain, a change in these YSR states' intensities occurs: The positive (negative) bias YSR states have larger (lower) intensities in the spectrum measured on the Mn chain than on the Ta substrate. We interpret this asymmetric intensity change of the particle-hole partners as a consequence of TMR[59,198,199,271].
To eventually determine the spin structure of the chain, we proceed to measure constant-contour $\mathrm{d}I/\mathrm{d}V$-maps over the Mn_{41} $1a - [001]$ chain, which are shown in Figure 4.17c. The $\mathrm{d}I/\mathrm{d}V$-maps reveal an intensity increase (decrease) of the YSR state at $+130\,\mu V$ ($-130\,\mu V$) throughout the entire chain in comparison to the substrate. We observe exactly the same behavior considering the YSR state at $\pm 500\,\mu V$. Furthermore, we observe that the $\mathrm{d}I/\mathrm{d}V$-signal on the chain is constant in all four $\mathrm{d}I/\mathrm{d}V$-maps. From the increased asymmetry of the tip's YSR states measured on the chain and the absence of any contrast changes along the chain we conclude that the chain is in a FM state in the external field of 400 mT. Since $1a - [001]$ Mn chains on Nb(110) are in a FM state as well, we proceed with the comparison of the in-gap band structure for chains on these two substrates.

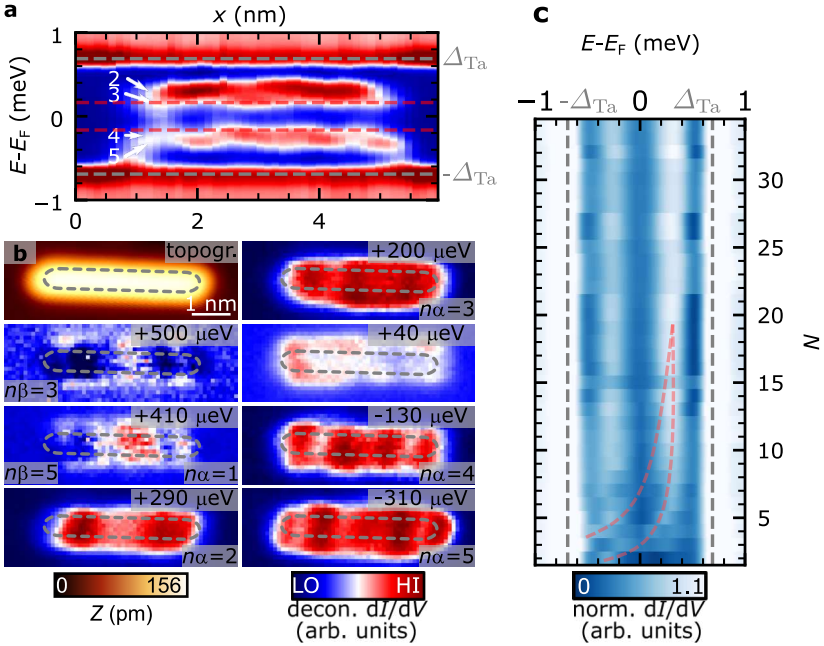

Figure 4.18.: a Exemplary $\mathrm{d}I/\mathrm{d}V$-line profile measured along the longitudinal axis of a Mn_{14} $1a-[001]$ chain on Ta(110). White arrows and labels indicate the number of maxima $n\alpha$ along the entire length of the chain for a particular energy. Red dashed horizontal lines indicate the edges of the minigap. **b** STM image and $\mathrm{d}I/\mathrm{d}V$-grid of a Mn_{14} chain evaluated at energy slices indicated in every panel's top right corner. Gray dashed lines mark the spatial extent of the chain. **c** Chain length-dependent $\mathrm{d}I/\mathrm{d}V$-spectra for Mn_2-Mn_{34} $1a-[001]$ chains. Each spectrum (row) was obtained by averaging over the $\mathrm{d}I/\mathrm{d}V$-line profile of the particular length. Red dashed lines are a guide to the eye. Measurement parameters: $V_{\mathrm{stab}}=-2.5\,\mathrm{mV}$, $I_{\mathrm{stab}}=1\,\mathrm{nA}$ and $V_{\mathrm{mod}}=20\,\mu\mathrm{V}$.

We reveal the Shiba band properties of $1a - [001]$ Mn chains on Ta(110) the same way as we have done it so far throughout this thesis: We subsequently construct a chain with increasing length starting form Mn_2 up to Mn_{34}. We measure a dI/dV-line profile for each of those lengths. An exemplary dI/dV-line profile of a Mn_{14} $1a - [001]$ chain is shown in Figure 4.18a and an additional data-set on a Mn_{33} $1a - [001]$ chain is shown in Figure A.1a. We find states with a very high dI/dV-intensity which dominate inside the superconducting gap of tantalum. They resemble standing waves with increasing numbers $n\alpha$ of maxima along the chain at decreasing energies, as indicated by white arrows and labels. For example, we observe $n = 2$,3,4 and 5 maxima at energies $+290\,\mu eV$, $+200\,\mu eV$, $-130\,\mu eV$ and $-310\,\mu eV$, respectively. As shown in the previous study of structurally identical Mn chains on Nb(110), these standing waves are assigned to confined BdG quasiparticles in a Shiba band which forms by the hybridization of YSR states of the chain's Mn atoms (see Subsection 4.2.1). Most importantly, we find that these states are again separated by a minigap around the Fermi level, as indicated by the red dashed horizontal lines in Figure 4.18a, which is visible in all dI/dV-line profiles for $N > 5$, see the length-dependent chain-averaged spectra in Figure 4.18c.

These dominant states are also uncovered by the dI/dV-grids at the respective energy slices shown in Figure 4.18b (see Figure A.1b for dI/dV-grids of a Mn_{33} $1a - [001]$ chain). The states are spatially localized on top of the longitudinal axis of the chain. They have a transversal extent that is similar to the most intense, d_{z^2} (α), single atom's YSR state, c.f. Figures 4.16c and d. As visible in the length-dependent investigation of averaged dI/dV-spectra, which is shown in Figure 4.18c, the confined states gradually evolve from the split α YSR states of the dimer. They continuously shift up in energy from $-350\,\mu eV$, cross the Fermi level, and saturate at $+400\,\mu eV$, which is the bottom of the corresponding Shiba band. Therefore, we conclude that the Shiba band producing these confined states primarily stems from hybridization of the single atom d_{z^2}

(α) YSR states.
In addition to these dominant states of the α band, we observe confined states which have an elongated intensity minimum directly on top of the chain, c.f. Figure 4.18b. This nodal line renders those states barely visible in the $\mathrm{d}I/\mathrm{d}V$-line profiles of Figures 4.18a and c. In contrast to the α states, these states are extended in the $[1\bar{1}0]$-direction, i.e. on both sides of the chain with an offset in $[1\bar{1}0]$-direction that compares to the spatial extent of the lobes of the single Mn atom's β and γ YSR states (cf. Figure 4.16d). Nevertheless, these states form standing waves along the longitudinal axis of the chain. We conclude that these states originate primarily from hybridization of the single atom's d_{yz} (β) and d_{xy} (γ) YSR states. Additional $\mathrm{d}I/\mathrm{d}V$-grids of a $1a-[001]$ Mn_{33} chain on Ta(110) are shown in Figure A.1. These measurements reveal that the observed side features remain bulk states and do not evolve to end states, even for longer chains.
In the following, we analyze the dispersions of these two bands. We obtain the α- and β/γ-Shiba bands by extracting the energy-dependent scattering vectors q from the average of 1D-FFTs of all $\mathrm{d}I/\mathrm{d}V$-line profiles for chains with lengths Mn_{14}-Mn_{34} (details in Subsection 4.2.1). The resulting averaged 1D-FFT is shown in Figure 4.19a. Additionally, the figure features an overlay of gray and orange dots which are manually evaluated points of scattering vectors q and energy E. We extract them from the confined states of the Shiba bands by plugging n, the number of maxima for a given energy, and the chain length N into the equation $q(E) = \pm 2n\pi/(N \cdot a)$.
By evaluating both sets of data points, the averaged 1D-FFT and the manually evaluated gray dots, we find that the α-Shiba band has a parabolic dispersion of scattering vectors with negative curvature ranging from $+400\,\mu\mathrm{eV}$ to $-600\,\mu\mathrm{eV}$. Similar to the α YSR state, whose $\mathrm{d}I/\mathrm{d}V$-intensity dominates all other YSR states, this band also dominates all other features in the averaged 1D-FFT. Most notably, a minigap in the α Shiba band is visible in Figure 4.19a, which we have identified

before in all $\mathrm{d}I/\mathrm{d}V$-line profiles for $N > 5$, see Figures 4.18a and c. To quantify the size of this minigap, we extract the spectral function at the q-value where the α band would cross E_F in an ungapped phase. This q-value is indicated by a dashed blue line in Figure 4.19a. The spectral function of the $1a - [001]$ Mn chains on Ta(110) is shown by the blue dots in Figure 4.19b. We fit the minigap using a Dynes function (Equation 2.25) and extract a width of $\Delta_\alpha = \pm(146 \pm 10)\,\mu\mathrm{eV}$ or $0.21\Delta_\mathrm{Ta}$. In order to compare this minigap size with the structurally identical chain of Mn on Nb(110), we proceed similarly, as shown by the black dots in Figure 4.19b, which results in $(164 \pm 4)\,\mu\mathrm{eV}$ or $0.11\Delta_\mathrm{Nb}$ for the Nb system.
Additionally to the gapped α-Shiba band, the averaged 1D-FFT reveals another band with a lower intensity and a nearly linear dispersion which extends from $+500\,\mu\mathrm{eV}$ at $\pm q/2 = 0.2\ \pi/a$ to $-500\,\mu\mathrm{eV}$ at $\pm q/2 = 0.64\ \pi/a$. From a comparison with the manually extracted $q(E)$-values of the confined $d_{\mathrm{yz}}/d_{\mathrm{xy}}$-like states (orange dots in the left panel of Figure 4.19a), we conclude that this band is the β/γ band. It is not gapped, but bypasses the minigap of the α Shiba band and the Fermi level continuously.
Now that we have extracted the crucial Shiba band properties of $1a - [001]$ Mn chains on Ta(110) and Nb(110), we can proceed to compare the results on both material platforms. Firstly, despite the larger SOC of Ta(110) in comparison to Nb(110), we do not observe indications for non-collinear spin structures in the $1a - [001]$ Mn chains on Ta(110). In fact, our results show quite the contrary. They indicate a FM ground state, i.e. the same magnetic state as for structurally identical chains on Nb(110)[59].
Secondly, we obtain similar results for the in-gap states on the single atom level: We find alike spatial distributions of the YSR states and a comparable energy of the d_{z^2}-like (α) YSR states, if taken in relation to the respective substrate's Δ. On the other hand, the remaining YSR states are energetically interchanged (Table 4.2) between both material platforms. Thirdly, due to these similarities of the spin structures and the single

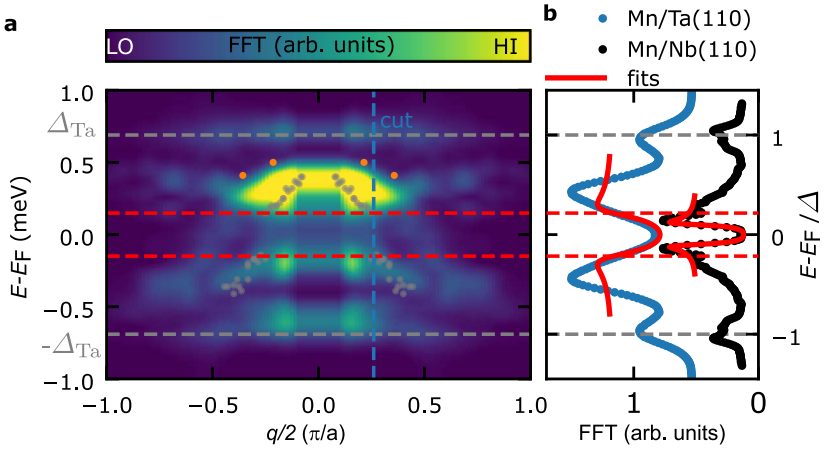

Figure 4.19.: a Averaged 1D-FFT of Mn $1a - [001]$ chains with lengths Mn_{14}-Mn_{34}. Gray and orange dots are an overlay of manually evaluated $q(E)$-values from the maxima visible on and besides the chain (e.g. from Figures 4.18a and b), respectively. Red dashed horizontal lines indicate the minigap of the α band. The blue dashed line marks the cut in q-space, where the α band would cross the Fermi level. **b** Symmetrized spectral functions[272] evaluated at the q-value where the α band is closest to E_F for $1a - [001]$ Mn chains on Ta(110) (blue) and on Nb(110) (black) (see Figure 4.7c), extracted from cuts through the 1D-FFTs. For the blue curve, the FFT intensity is offset by 0.5 arb. units for the sake of visibility. Red curves are fits of the spectra in vicinity of the minigaps using a Dynes function (Equation 2.25). Measurement parameters: see Figure 4.18 and Figure 4.6.

atom α YSR states, we expect, and in fact observe, very similar properties of the α Shiba bands for the two substrates: (I) The α band has a similar dispersion for both substrates with a sufficient band width such that it crosses the Fermi level. We can unambiguously conclude this from the fact that there are confined states with less maxima above and with more maxima below E_F[61]. (II) We observe a minigap in the α band around E_F for both substrates. We assign this gap to a topological gap induced by SOC-driven p-wave correlations[61]. If we determine the size of the minigap using the same method, we find that it is only $0.11\ \Delta_{Nb}$ for the Nb system while it is $0.21\Delta_{Ta}$ for Ta. This results in an increase by a factor of 1.9 (cf. Figure 4.19b).
In general it is not straightforward to pinpoint the origin of the increased minigap. As recently shown, it doesn't only depend on the SOC strength, but also on the normal state Fermi wave vector $k_{F,0}$ of the substrate and on the Fermi wave vector of the α band $k_{F,\alpha}$[62]. However, as the α Shiba band dispersions of the Ta(110)- and Nb(110)-based material platforms, which we compare here, are very similar ($k_{F,\alpha} = 0.24\pi/a$ for Ta, $k_{F,\alpha} = 0.19\pi/a$ for Nb) and since both substrates have very similar Fermi surfaces[261], we assume that the latter effects play a minor role. Therefore, to a large degree, we ascribe the increased minigap to the threefold-increased SOC[263] of the Ta(110) substrate compared to Nb(110). Even though the factor of 1.9 increase in the minigap size and the factor of 3-fold increase in SOC agree reasonably well, we note that there is probably a complex relation of substrate SOC and the SOC in the relevant Shiba bands. The strength of SOC in surface science related phenomena is usually determined by an intricate interplay of atomic contributions and wave function asymmetries[103,104], and requires further theoretical modeling in the case of Shiba bands.

4.4.3. Magnetic and electronic properties of $\sqrt{2}a - [1\bar{1}0]$ Mn chains

To begin the characterization of $\sqrt{2}a$-$[1\bar{1}0]$ Mn chains on Ta(110), we perform SP-STM and SP-STS with YSR-functionalized superconducting Nb tips as in the previous section. A $\mathrm{d}I/\mathrm{d}V$-spectrum measured on the bare substrate at an applied external magnetic field of $B = +200\,\mathrm{mT}$, i.e. where the substrate's superconductivity is fully quenched, using a functionalized superconducting tip, is shown in Figure 4.20a. We observe two pairs of YSR states. One is located at $\pm 110\,\mu\mathrm{eV}$ and the other at $\pm 530\,\mu\mathrm{eV}$. By comparing this curve with a spectrum that was measured on a Mn_{12} $\sqrt{2}a - [1\bar{1}0]$ chain, we find that there is an asymmetric intensity shift for the particle-hole partners of the YSR state at $\pm 530\,\mu\mathrm{eV}$. Therefore, we conclude that the tip has a net spin-polarization at the biases of the tip's YSR states at $\pm 530\,\mu\mathrm{eV}$. We verified this contrast by measurements over an AFM coupled $(\sqrt{3}/2)a - [1\bar{1}1]$ Mn chain, where alternating up-down contrast is easily achievable (see Figure 5.1).
Constant-contour $\mathrm{d}I/\mathrm{d}V$-maps measured at those two biases are shown in Figure 4.20b. We find that the $\mathrm{d}I/\mathrm{d}V$-signal is evenly decreased (increased) for the positive bias (negative bias) state along the entire chain. This absence of any further contrast modulation indicates a constant out-of-plane magnetization of all Mn atoms in the chain.
Strangely, using regular STM images, we observe additional contrast modulations. As opposed to the just presented SP-STS and SP-STM measurements, we reproducibly observe a periodic modulation in the Z-signal on $\sqrt{2}a$-$[1\bar{1}0]$ Mn chains with different chain lengths, at multiple different locations on the sample and employing multiple different microtips and even different bulk tips.
An example of this modulation is shown in Figure 4.20c. The STM image was obtained with a regular superconducting tip (without YSR functionalization) and displays a Mn_{19} $\sqrt{2}a - [1\bar{1}0]$ chain. It is apparent that the Mn atoms making up the chain have different heights. By bare eye, it is

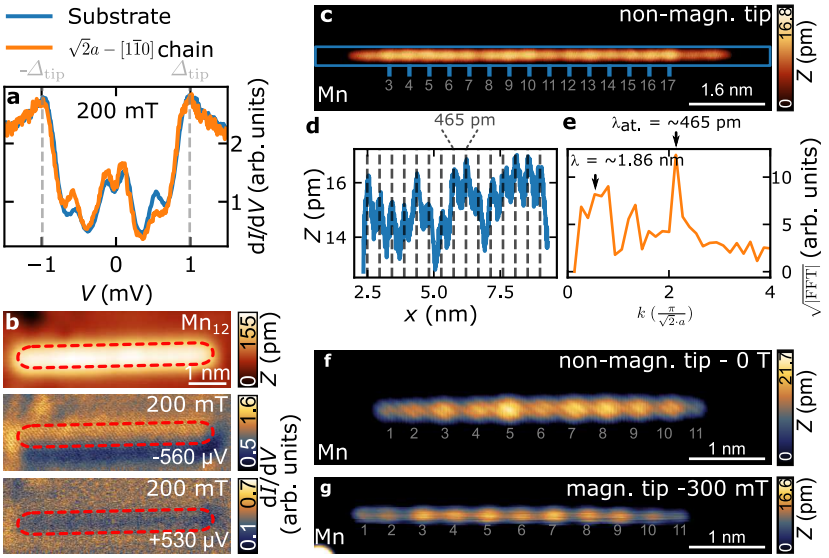

Figure 4.20.: **a** Two $\mathrm{d}I/\mathrm{d}V$-spectra measured on the substrate and on a $Mn_{12}\sqrt{2}a - [1\bar{1}0]$ chain using a functionalized superconducting Nb tip (see sketch in Figure 4.17). An external magnetic field of +200 mT was applied for this measurement and the ones shown in **b**. **b** STM image and constant-contour $\mathrm{d}I/\mathrm{d}V$-maps of a Mn_{12} $\sqrt{2}a - [1\bar{1}0]$ chain, measured at biases of the tip's YSR states . **c** STM image of a Mn_{19} $\sqrt{2}a - [1\bar{1}0]$ chain taken with a non-magnetic tip. The contrast is adjusted to highlight the height-modulation of individual atoms in the chain. The blue rectangle indicates the extraction region for the line profile along the longitudinal chain axis, which is shown in **d**. **d** Each Z-value of the line profile is obtained by averaging the pixels column wise, i.e. perpendicular to the chain axis. Grey dashed lines mark the positions of Mn atoms in the chain. **e** 1D-FFT of the line profile shown in **d**. Black arrows and labels mark the k-values of the interatomic distance in the chain and a broad peak around $k = 0.5(\pi/\sqrt{2}a)$. **f** and **g** are STM images of two different Mn_{11} $\sqrt{2}a - [1\bar{1}0]$ chains measured with a non-magnetic tip at 0 T (**f**) and a magnetic tip at −300 mT (**g**). Measurement parameters: **a** $V_{\mathrm{stab}} = 1.5\,\mathrm{mV}$, $I_{\mathrm{stab}} = 1\,\mathrm{nA}$ and $V_{\mathrm{mod}} = 40\,\mu\mathrm{V}$, **b** $V_{\mathrm{bias}} = 5\,\mathrm{mV}$, $I = 1\,\mathrm{nA}$, $V_{\mathrm{mod}} = 40\,\mu\mathrm{V}$, **c** $V_{\mathrm{bias}} = -20\,\mathrm{mV}$, $I = 200\,\mathrm{pA}$, **f** $V_{\mathrm{bias}} = 3\,\mathrm{mV}$, $I = 1\,\mathrm{nA}$ and **g** $V_{\mathrm{bias}} = 2\,\mathrm{mV}$, $I = 1\,\mathrm{nA}$.

difficult to identify a certain wavelength of this modulation. However, one can find regions with a $4 \cdot \sqrt{2}a$ period. We further analyze this by taking a line profile of the topography: The blue rectangle in Figure 4.20c marks the extraction region where we averaged each line perpendicular to the chain axis to end up with the profile shown in Figure 4.20d. For the sake of visibility, we reduce the Z-scale to the atoms 3-17 of the chain, as the first two and the last two Mn atoms of the chain appear much lower than the bulk.

In Figure 4.20d one can clearly observe the atomic modulation with a nearest-neighbor distance of 465 pm. In fact, the exact registry of the atomic distances in the chain with the underlying $[1\bar{1}0]$-direction of the Ta(110) substrate, is also observable in the STM image of Figure 3.7c, which was taken with an ultra-sharp STM tip. This precise and equal spacing of all nearest neighbors allows us to exclude an internal strain of the chain as the origin of the height-modulation. Apart from the period of $\lambda_{at.} = 465\,\text{pm}$, it is more apparent from Figure 4.20d that there is a modulation with $\lambda = 4 \cdot 465\,\text{pm}$. This additional modulation is observable in the 1D-FFT of the line profile, shown in Figure 4.20e, where one finds a broad peak around $k = \frac{1}{4}(\frac{2\pi}{\sqrt{2}a})$.

To demonstrate that this modulation is reproducible, we used different microtips and different $\sqrt{2}a - [1\bar{1}0]$ Mn_{11} chains, constructed at different locations on the sample, and recorded the STM images shown in Figures 4.20f and g. Further, I want to highlight that Figure 4.20f is measured while the substrate is in the superconducting state at 0 T. On the other hand, Figure 4.20g is measured in the normal metal state of the Ta(110) substrate at an external field of $-300\,\text{mT}$. A careful comparison of these two STM images shows that the same contrast modulation is observed in both: Starting with the leftmost atom (1), we find that the first two and the last two atoms have a lower apparent height than atoms in the rest of the chain. Starting from the 3$^{\text{rd}}$ atom on the left side, the Z-signal increases until it reaches a maximum at site five. For atom six we observe a sudden decrease of the apparent height, which increases greatly again

for atom seven and then drops off slowly for sites eight and nine.
Overall, we can not unambiguously determine the origin of this modulation. However, in the measurements shown above, we demonstrate that neither an out-of-plane magnetic structure, nor geometric anomalies or strain, nor electronic modulations caused by in-gap states (e.g. YSR states) can be its origin. Due to the independence of this contrast on the microtip and its existence with nonmagnetic tips, we speculate that weak in-plane non-collinear spin components in addition to the dominant FM out-of-plane contribution (Figure 4.20b) combined with tunneling anisotropic magnetoresistance could be the origin[273]. To confirm this hypothesis, one would have to conduct SP-STM with in-plane sensitive tips in a vector magnetic field or perform *ab-initio* calculations of the magnetic ground state.
An in-depth study of dimers oriented in $[1\bar{1}0]$-direction with a spacing of $\sqrt{2}a$, which is published in Ref. [197], and the SP-STM measurements shown in Figure 4.20 indicate that the corresponding chains are potentially interesting concerning the formation of Shiba bands. An illustration of the Mn sites for chains along this building direction is shown in Figure 4.9a. The spectroscopic results on the in-gap states of this type of chain are summarized in Figure 4.21. An exemplary $\mathrm{d}I/\mathrm{d}V$-line profile of a Mn_{13} chain is presented in Figure 4.21a. Well-defined in-gap states with a mirror symmetric spatial distribution around the center of the chain are clearly observable. This hallmark can be seen as an indicator for good crystallographic quality and the absence of defects. However, while the states seem to have a standing wave character, the dispersion is not as readily observable as for the $1a - [001]$ chains (Subsection 4.4.2).
The Shiba state with the highest $\mathrm{d}I/\mathrm{d}V$-intensity is found at $-470\,\mu\mathrm{eV}$ and is strongly localized on the edges of the chain (Figures 4.21a and b). We speculate that this trivial edge state could be the single impurity α state, which does not seem to hybridize and split in this crystallographic direction and interatomic spacing (see dimer in Ref. [197]). It should be noted, that all other Shiba states have a much lower $\mathrm{d}I/\mathrm{d}V$-intensity, and

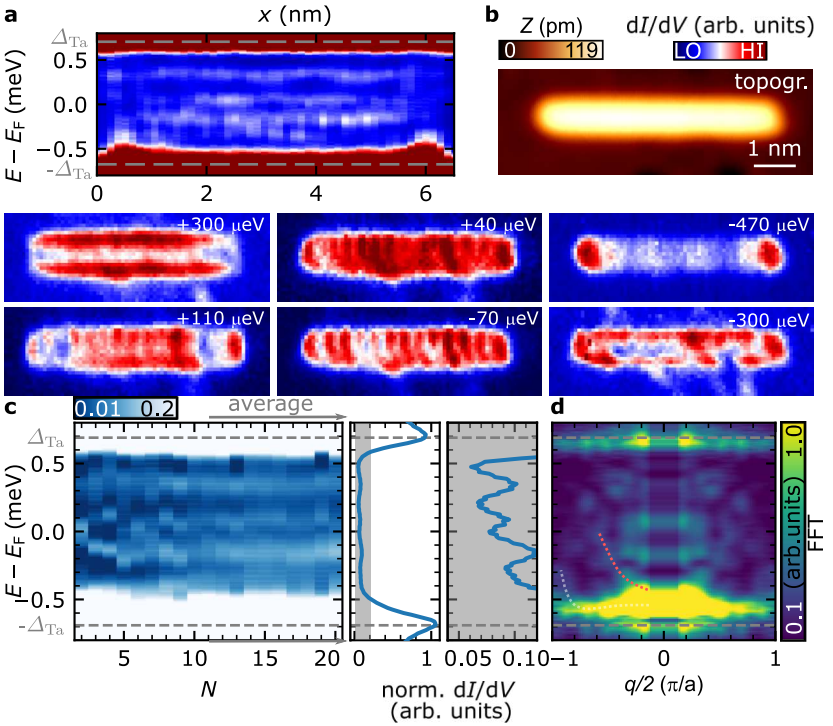

Figure 4.21.: a $\mathrm{d}I/\mathrm{d}V$-line profile measured along a the longitudinal axis of a Mn_{13} $\sqrt{2}a - [1\bar{1}0]$ chain. Dashed gray horizontal lines mark the coherence peaks of Δ_{Ta}. **b** STM image and $\mathrm{d}I/\mathrm{d}V$-grids of a Mn_{13} chain evaluated at energy slices where confined states of the Shiba bands are observed. **c** The leftmost panel displays chain length dependent $\mathrm{d}I/\mathrm{d}V$-spectra for $Mn_2 - Mn_{20}$ $\sqrt{2}a - [1\bar{1}0]$ chains. Each spectrum (column) was obtained by averaging over the $\mathrm{d}I/\mathrm{d}V$-line profile measured for a chain having this particular length. An average $\mathrm{d}I/\mathrm{d}V$-spectrum of the chains with lengths $Mn_{11} - Mn_{20}$ (indicated by the gray arrow) is shown in the middle panel. The rightmost panel is a magnification of the gray-shaded area in the middle panel to improve the visibility of states with a low $\mathrm{d}I/\mathrm{d}V$ intensity. Gray dashed vertical lines mark the coherence peaks $\pm\Delta_{Ta}$. **d** Averaged 1D-FFT of $\mathrm{d}I/\mathrm{d}V$-line profiles of Mn $\sqrt{2}a - [1\bar{1}0]$ chains with lengths Mn_8-Mn_{20}. The white and red dashed lines are guides to the eye. Measurement parameters: $V_{stab} = -2.5\,\mathrm{mV}$, $I_{stab} = 1\,\mathrm{nA}$ and $V_{mod} = 20\,\mu\mathrm{V}$.

are therefore likely ascribed to the β and γ YSR states.
One of those Shiba states is observed at $\pm 300\,\mu eV$, which is located everywhere along the longitudinal axis of the chain but has the spatial distribution of a dumbbell-like YSR state in $[001]$-direction , as shown in the dI/dV-maps of Figure 4.21b. Further, we observe a state at $40\,\mu eV$, which resembles a standing wave with four maxima along the chain, where the two inner ones are strongest. Additionally, we observe a state at $-70\,\mu eV$, which is located on every atomic site.
Overall, we obtain very similar results for all chain lengths, as apparent from the length-dependent chain-averaged dI/dV-spectra in Figure 4.21c. While details are difficult to extract form this plot, we may still conclude that there are dominant states at $-120\,\mu eV$, $+100\,\mu eV$ and $+300\,\mu eV$ for chains with $N > 8$.
The averaged 1D-FFT of the dI/dV-line profiles of all Mn chains with lengths of Mn_8-Mn_{20} is shown in Figure 4.21d. We find indications for multiple bands: One has its band bottom at the Γ-point and $-550\,\mu eV$. This Shiba band has an upwards dispersion, which is visible from its increase to $\sim -300\,\mu eV$ close to the Brillouin zone boundary at $q/2 > 0.7\,(\frac{\pi}{a})$ (white dashed line). The band has a strong particle-hole asymmetry, as it is not observed for positive energies. The strong particle-hole asymmetry, the elevated spectral intensity and spatial distribution of the state at $-470\,\mu eV$ (Figure 4.21b) indicate that this could be the α band.
A second upwards dispersing Shiba band is observed in Figure 4.21d. It has its band bottom at $q/2 = 0$ and $-400\,\mu eV$. Starting from the band bottom, the Shiba band increases to $0\,\mu eV$ at $q/2 \approx 0.5\,(\frac{\pi}{a})$, as indicated by the red dashed line. Its dispersion seems to be closer to a parabolic shape than the α band's dispersion. We can't tell whether the second Shiba band crosses the Fermi level or not within our experimental resolution.
Overall, we find that Mn chains in $[1\bar{1}0]$-direction with an interatomic spacing of $\sqrt{2}a$ have multiple bands with multiple different orbital origins (Figures 4.21b and d). Unfortunately, an unambiguous extraction of

the Shiba band structure including the clear respective orbital origin was not possible for $\sqrt{2}a - [1\bar{1}0]$ chains. This is partly caused by the limited energy resolution on the small-gap superconductor Ta ($T_c = 4.39\,\mathrm{K}$) at our measurement temperature of 320 mK together with the multi-orbital character of the bands giving rise to a plethora of states in the gap. An additional problem is the low $\mathrm{d}I/\mathrm{d}V$-intensity of the second Shiba band, which is apparent from Figure 4.21c.

4.4.4. Conclusion

In conclusion, we learn multiple important facts from the study of Mn chains on Ta(110), and by comparing these new results to the Mn/Nb(110) platform. To begin with, we find that the d_{z^2}-like YSR state of single Mn atoms on Ta(110) has very similar properties as on Nb(110). As this YSR state is crucial for the Shiba bands of $1a - [001]$ Mn chains on Ta(110) and on Nb(110) (see Subsections 4.2.1 and 4.4.2) we performed a comparative study on the influence of the substrate's SOC on Shiba band properties of $1a - [001]$ Mn chains. The striking result of this comparison is the observation of a minigap in $1a - [001]$ Mn chains on Ta(110), that is 1.9 times larger (related to the respective substrate gaps) than the one observed in structurally identical chains on Nb(110). Therefore, we conclude that higher substrate SOC can indeed lead to a larger topological minigap in Shiba bands.
A second valuable lesson is learned from the $\sqrt{2}a$-$[1\bar{1}0]$ chains on Ta(110). While it is clearly found that YSR states hybridize and form bands (probably two), we find that the reduced gap size of Ta(110) compared to Nb(110) makes a clear allocation of in-gap features difficult. This is easily explainable, if we consider an experiment where Mn chains on Nb(110) and on Ta(110) have the same Shiba band structure (normalized to Δ). In $\mathrm{d}I/\mathrm{d}V$-spectra, we would expect to find the same amount of in-gap states for both systems. However, for Ta(110) these states are all located

in a much smaller gap, leading to smaller absolute energy differences between Shiba states, which makes them difficult to distinguish from one another. Therefore, I conclude that the ideal material platform to investigate MSH structures should be Nb-based.
These two conclusions highlight the need of superconducting heterostructures, which are composed of a high-Z metal deposited on Nb(110)[175,274]. Such proximitized high-Z films might be the ideal candidates to incorporate all the required ingredients for the realization of MBS. I proceed to study two examples of such heterostructures in Section 4.5.

4.5. Proximitized Ir and Au films as substrates for MSHs

In Section 4.4 we demonstrate that employing a high-Z material with a high SOC as the substrate for Shiba chains can increase the strength of SOC in the relevant Shiba bands as well, and hence it can increase the size of a topological gap. Therefore, we proceed to investigate the growth of two high-Z materials — Ir and Au — on Nb(110), which we then use as substrates for magnetic structures.
The experimental data, the figures and parts of the text on the growth study of Ir on clean Nb(110), which are presented and discussed in Subsections 4.5.1 and 4.5.3, are published in the article

> Philip Beck, Lucas Schneider, Lydia Bachmann, Jens Wiebe and Roland Wiesendanger
>
> *Structural and superconducting properties of ultrathin Ir films on Nb(110)*
>
> Physical Review Materials, **6**, 024801 (2022).

The experimental data, the figures and parts of the text describing the study of 1 ML Au thin films grown on clean Nb(110) as well as the Fe adatom structures assembled on top (Subsections 4.5.2 and 4.5.4), are written up in the preprint

> Philip Beck, Bendegúz Nyári, Lucas Schneider, Levente Rózsa, András Lászlóffy, Krisztián Palotás, László Szunyogh, Balázs Ujfalussy, Jens Wiebe and Roland Wiesendanger
>
> *Search for large topological gaps in atomic spin chains on proximitized superconducting high-Z layers*
>
> Manuscript submitted to Nano Letters (2022).

The remaining results on the growth of 2 and 4 ML thick Au films (included in Subsection 4.5.2), and the STS studies of single Fe adatoms on 4 ML Au/Nb(110) (included in Subsection 4.5.4) and 10 ML Ir/Nb(110) (Subsection 4.5.5) are unpublished up to this date.
All dI/dV-spectra measured at ultra-low temperature, i.e. all dI/dV-spectra of the superconducting gaps were obtained with the bulk Nb tip described in Subsection 3.3.3. The spectra are numerically deconvoluted as described in Subsection 3.1.2, unless indicated otherwise.

Contributions

The STM and STS data presented in this section were measured by Dr. Lucas Schneider and myself. The measurements on 0.3, 1 and 2 ML thick Ir films were supported by Lydia Bachmann in the scope of her Bachelor thesis[275]. STM images were analyzed using Gwyddion[248] and the spectroscopic data was processed using a self-written Python code.

Introduction

As we have shown in Sections 4.1, 4.2 and 4.3, recent research efforts in the quest to realize MBS have been devoted to employing Nb(110) as a substrate for artificial magnetic structures composed of Fe[244,276], Cr[63,174,265] and Mn[60–62] adatoms. All of those STS studies found that in-gap features become clearly observable and distinguishable using typical ultra-low temperature STMs (operation temperatures 300 mK-1.4 K) due to the large gap and high critical temperature $T_C = 9.2$ K of Nb. Additionally, Nb(110) enables highly reproducible STM tip-induced atom manipulation. These two points clearly emphasize its advantages over substrates as Re(0001)[55,58] or Ta(110) (see Section 4.4) which have lower critical temperatures, and Pb(110)[53,54,56,57] where atom manipulation is not possible in a reproducible manner.

However, while we have shown that considerable SOC is present in Nb based MSH systems in Section 4.1 and Ref. [60], we also found that SOC effects turn out to be too low in Section 4.2. Additionally, low DM interaction strengths resulting in dominantly collinear magnetic ground states were calculated[216] and experimentally observed[59] for most Mn chains on Nb(110).
In this chapter, we prepare superconducting heterostructures consisting of a thin film of a high-Z metal grown on the (110) surface of a Nb single crystal. The approach is centered around the idea, that the latter component provides its excellent superconducting properties (i.e. the large superconducting gap), while the former serves to increase SOC (see Section 4.4) and the DM interaction within the nanostructure assembled on top, which should favor non-collinear magnetic ground states.
We expect that superconductivity is induced into the high-Z metal overlayer by proximity, which was discussed in Subsection 2.2.3, as long as the film's thickness is kept low enough[277–279]. Furthermore, we expect that the spin-carrying states of magnetic nanostructures constructed on the high-Z metal/Nb(110) heterostructures will hybridize with the electronic states of the high-Z metal overlayer, which should induce strong SOC in the nanostructure. This approach follows the ideas that atomic SOC contributions roughly scale with multiple powers of the atomic number Z of the species and that the asymmetry of the wave functions in the magnetic nanostructure may be increased by the hybridization with the high-Z metal overlayer (see Section 4.4).
Therefore, such systems should be ideal to realize TSC in 1D and 2D magnetic nanostructures. Concerning the choice of a high-Z metal to use as an overlayer, we expect that Ir and Au are particularly well-suited candidates. The former is appropriate, since Ir(111) surfaces have already been shown to serve as a template for the realization of spin-spiral and skyrmion phases[280–283], where the non-collinear magnetic states are stabilized by a large contribution of the DM interaction. The latter appears to be a suitable candidate, since Au is well known to exhibit

large SOC, e.g. in its surface state[100,284]. Furthermore, it was experimentally demonstrated that the proximity to Au has enhanced SOC-induced effects in light elements, including the scattering rate[285], the Rashba splitting[103,286] and the magnetocrystalline anisotropy energy[287]. Additionally, previous work hints at the possibility to prepare pseudomorphic thin films of Au on Nb(110)[288], which is desirable, since anisotropic YSR states enable the tailoring of systems into the single Shiba band regime as shown in Subsection 4.2.2.
In the following subsections, I present coverage-dependent growth studies of Ir (Subsection 4.5.1) and Au on Nb(110) (Subsection 4.5.2), where I use STM and LEED to determine the crystal structures of thin films. Afterwards, I discuss the usability of films with varying thicknesses for single adatom and Shiba chain experiments in Subsection 4.5.3. In Subsection 4.5.4, I proceed to perform the proposed experiments on Fe adatoms and Shiba chains on 1 and 4 monolayer (ML) thick Au films deposited on Nb(110). Last, I present a STS study on the influence of single Fe adatoms on 10 ML thick Ir films on Nb(110) in Subsection 4.5.5 and, finally, finish this section with a discussion and conclusions in Subsection 4.5.6.

4.5.1. Growth study of Ir on Nb(110)

In this subsection I subsequently discuss Ir films with a coverage of 0.3 ML, 1 ML, 2 ML and $\sim$ 10 ML on Nb(110). All samples, excluding the latter, were prepared and investigated in the experimental set-up referred to as the VT-STM in Subsection 3.2.2. The sample with an Ir coverage of $\sim$ 10 ML was investigated in the ultra low-temperature STM with a base temperature of 320 mK (see Subsection 3.2.1).
Throughout the following sample preparations, the Ir coverage of the Nb(110) surface is calculated by calibration measurements for films thicker than 1 ML: We measured the ion current of the evaporator and the evaporation time for a calibration sample. Subsequently, we analyzed the

Ir coverage of the Nb(110) sample (required to be < 1 ML) using an STM. The determined evaporation rate was then used to calculate an estimated coverage for all following sample preparations. A separate calibration was carried out for the two experimental setups. We obtained the following rates for the VT-STM: At a power of 23 W and an ion current of 29 nA we achieved a rate of 0.024 ML/min. In the 320 mK lab a power of 53 W and an ion current of 22 nA yielded a rate of 0.065 ML/min. Since this method assumes a pseudomorphic ML and doesn't account for structural changes in the Ir film with increasing layer thickness, it should be seen as an estimate for coverages larger than 1 ML.

Sub-ML coverage

To begin with, a sample with an iridium coverage of ~ 0.3 ML is shown in Figure 4.22. Large-scale overview STM images which highlight the quality and homogeneity of the Ir islands are shown in Figures 4.22a and b. As apparent from the irregularly shaped step edges in Figure 4.22a, in comparison to those of a clean single crystal (see Figure 3.6d), we conclude that iridium grows via step-edge decoration and step-flow, as well as in a free-standing island mode.
Both, the islands and the substrate appear to be atomically flat with the exception of few randomly distributed point-like defects. Furthermore, the Ir islands mostly have approximately rectangular shapes, whose edges are preferably oriented along the directions indicated by black lines in Figure 4.22b. The atomic resolution image taken on the substrate (inset in the bottom left corner of Figure 4.22b) shows the atomic structure of bare Nb(110), i.e. a centered rectangular unit cell with edges along the $[1\bar{1}0]$- and $[001]$-direction. The fact that large areas of clean Nb(110) are still found, even after Ir evaporation and post-annealing processes, is crucial to highlight the good quality of the Ir/Nb(110) interface.
This conclusion is further supported by the $\mathrm{d}I/\mathrm{d}V$-spectra taken on bare

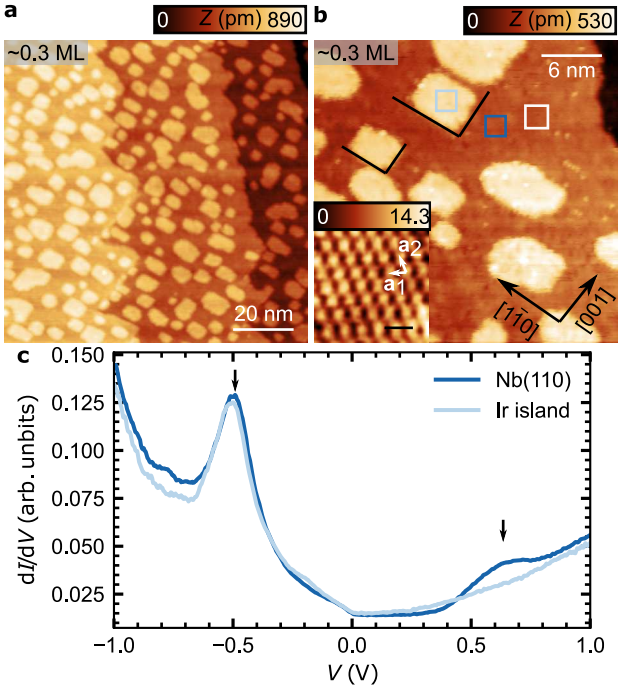

Figure 4.22.: **a** and **b** Overview STM images of an Ir/Nb(110) sample with a coverage of $\sim$ 0.3 ML. Black arrows and labels in **b** denote crystallographic directions and are valid for panel **a** as well. An atomic resolution STM image taken at the location of the white box is shown as an inset in panel **b**. The black scale bar corresponds to a length of 500 pm. A Gaussian filter was applied in order to highlight the atomic resolution. White arrows and labels mark lattice vectors ($\mathbf{a}_1$ and $\mathbf{a}_2$) of the clean Nb(110) substrate. The remaining color-coded boxes in **b** mark the areas, where the $\mathrm{d}I/\mathrm{d}V$-spectra shown in **c** were measured. **c** Averaged $\mathrm{d}I/\mathrm{d}V$-spectra obtained while stabilizing on bare Nb(110) and on an Ir island. Black arrows mark the characteristic peaks of Nb(110). Measurement parameters: **a** and **b** $V_{\mathrm{bias}} = -1\,\mathrm{V}$, $I = 1\,\mathrm{nA}$, inset of **b** $V_{\mathrm{bias}} = -10\,\mathrm{mV}$, $I = 5\,\mathrm{nA}$ and **c** $V_{\mathrm{stab}} = -1\,\mathrm{V}$, $I_{\mathrm{stab}} = 1\,\mathrm{nA}$.

Nb(110) and an Ir island in Figure 4.22c. The $\mathrm{d}I/\mathrm{d}V$-spectrum taken on bare Nb(110) (dark blue curve) agrees very well with recent results from the literature[206]: We observe a pronounced peak at $-500\,\mathrm{mV}$ (marked by the left black arrow), which is characteristic for clean Nb(110). Furthermore, we observe a step at a positive bias of approximately $+500\,\mathrm{mV}$. Upon moving the STM tip onto an Ir island, we find that the $\mathrm{d}I/\mathrm{d}V$-spectrum (light blue curve) is altered. While the pronounced peak at -500 mV is still found, the step feature at positive biases is no longer observable. Instead one finds a nearly linear increase of the $\mathrm{d}I/\mathrm{d}V$-signal for positive biases. Since the $\mathrm{d}I/\mathrm{d}V$-spectrum measured on bare Nb(110) fully resembles literature spectra and we observe the expected bcc(110) surface in atomic resolution images of the substrate (inset in Figure 4.22b), we conclude that there is no intermixing of Ir into the topmost layers of Nb(110). Furthermore, we conclude that the observed islands cannot be caused by Ir patches intercalated beneath the topmost layers of Nb(110), as tunneling spectra taken on their locations no longer resemble the spectrum of bare Nb(110). This indicates that the islands are formed by iridium ontop of the Nb(110) surface.
Obviously, we can largely exclude oxygen diffusion from the bulk crystal to the surface or the deposition of impurities from the evaporator beam. The conclusion holds true, also for the further preparations with higher iridium coverages, as long as the post-annealing protocol is not altered.
Last, a comparison of the crystallographic directions and the preferred edge orientation of the iridium islands (both highlighted in Figure 4.22b) hints towards a rectangular crystal structure of the Ir islands. Obtaining clear atomic resolution images of the Ir islands was not possible in this experiment, but conclusive experiments on 1 ML and 2 ML thick Ir films in the following subsections further indicate a rectangular crystal structure.

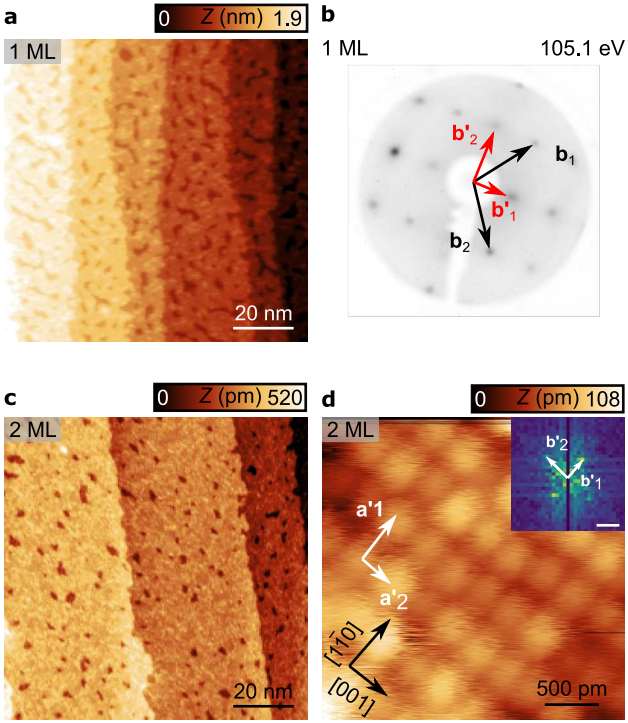

Figure 4.23.: a STM image and **b** LEED pattern characterizing the growth of 1 ML Ir on clean Nb(110). The LEED pattern was obtained with a beam energy of 105.1 eV. Black arrows and labels in **b** denote reciprocal lattice vectors, which were observed for clean Nb(110). Red ones mark LEED spots observed only after the growth of 1 ML Ir. **c** and **d** STM images of an Ir/Nb(110) sample with a coverage of 2 ML. **d** Black arrows denote crystallographic directions as obtained from Figure 4.22b and white arrows mark the lattice vectors ($\mathbf{a}_1^{'}$ and $\mathbf{a}_2^{'}$) determined from the visible superstructure. The 2D-FFT is shown as an inset. Here, white arrows and labels mark the reciprocal lattice vectors. The white scale bar represents a length of 2.3 nm^{-1}. Measurement parameters: **a** $V_{\mathrm{bias}} = -1\,\mathrm{V}$, $I = 20\,\mathrm{pA}$, **c** $V_{\mathrm{bias}} = -1\,\mathrm{V}$, $I = 20\,\mathrm{pA}$ and **d** $V_{\mathrm{bias}} = -20\,\mathrm{mV}$, $I = 8\,\mathrm{nA}$.

One and two ML: Ultrathin film limit

Now that we have established that Ir grows in an ordered and flat fashion, and that the Ir/Nb(110) interface remains clean even after applying post-annealing, we proceed to study samples with a higher coverage of Ir, which are needed for the purpose of single atom experiments or for the growth of metallic transition metal thin films onto Ir thin films. A large-scale STM image obtained for a sample with a coverage of 1 ML Ir is shown in Figure 4.23a. It is apparent, that the first ML isn't fully closed, as there are still holes in the film. Furthermore, irregularly shaped step edges indicate that the formation of a second ML might have begun. Flat connected areas are visible between the holes of the first ML, which are only disrupted by point-like defects that we already observed for samples with sub-ML coverage (see Figure 4.22d) as well.
We performed a LEED measurement on this sample, which results in the pattern shown in Figure 4.23b. The data obtained from this measurement allows us to derive a model of the crystal structure for the first ML of Ir on Nb(110). To begin with, the LEED spots of bare Nb(110) (cf. Figure 3.6f) are still observed in this measurement and are marked by black arrows which are labeled by $\mathbf{b}_1$ and $\mathbf{b}_2$. Additional sharp and bright spots are observed at locations marked by red arrows, which are labeled $\mathbf{b}_1^{'}$ and $\mathbf{b}_2^{'}$. Since the emergence of these new LEED spots is linked to a coverage of the Nb(110) substrate with an ultrathin Ir film, we can link them to the surface structure of the Ir films. The newly observed LEED spots, marked by $\mathbf{b}_1^{'}$ and $\mathbf{b}_2^{'}$ lie directly in between $\mathbf{b}_1$ and $\mathbf{b}_2$ or $\mathbf{b}_1$ and $-\mathbf{b}_2$, respectively. Therefore, they can be described as linear combinations of the reciprocal lattice vectors of Nb(110):

$$\mathbf{b}_1^{'} = \frac{\mathbf{b}_1}{2} + \frac{\mathbf{b}_2}{2} \tag{4.6}$$

and

$$\mathbf{b}_2^{'} = \frac{\mathbf{b}_1}{2} - \frac{\mathbf{b}_2}{2} \tag{4.7}$$

which enables a calculation of the real-space lattice vectors of this structure. Using reciprocal lattice vectors of the bcc(110) Nb surface for $\mathbf{b}_1$ and $\mathbf{b}_2$ and inserting them into Equations 4.6 and 4.7, we calculate the real-space lattice vectors of the Ir film to be

$$\mathbf{a}_1^{'} = \begin{pmatrix} 0 \\ \sqrt{2} \end{pmatrix} \cdot a \tag{4.8}$$

and

$$\mathbf{a}_2^{'} = \begin{pmatrix} 1 \\ 0 \end{pmatrix} \cdot a. \tag{4.9}$$

Here, x and y correspond to the $[001]$- and $[1\bar{1}0]$-direction, respectively, and $a = 330\,\mathrm{pm}$ is the lattice constant of Nb(110) as determined from the atomic resolution image in the inset of Figure 4.22d. Therefore, we find a rectangular unit cell with lattice vectors of $|\mathbf{a}_1^{'}| = 467\,\mathrm{pm}$ and $|\mathbf{a}_2^{'}| = 330\,\mathrm{pm}$ for the first ML of Ir, on the centered rectangular unit cell of bare Nb(110). We speculate that the crystal structure observed for the first ML of Ir on Nb(110) was also present in the islands of Figure 4.22 due to the predominant rectangular shape of the islands.
Afterwards, we prepared samples with an Ir coverage of 2 ML, to determine whether they grow in a similar crystal structure. From the large-scale images in Figure 4.23c, we find that the second ML is not fully closed either, as there are holes with atomic step height. However, in contrast to the sample with 1 ML coverage (Figure 4.23a), we find that the step edges are straight which might indicate the absence of step-flow growth of a third ML.
The atomic resolution image shown in Figure 4.23d, taken on a clean part of the terrace, clearly shows a simple rectangular lattice, whose lattice vec-

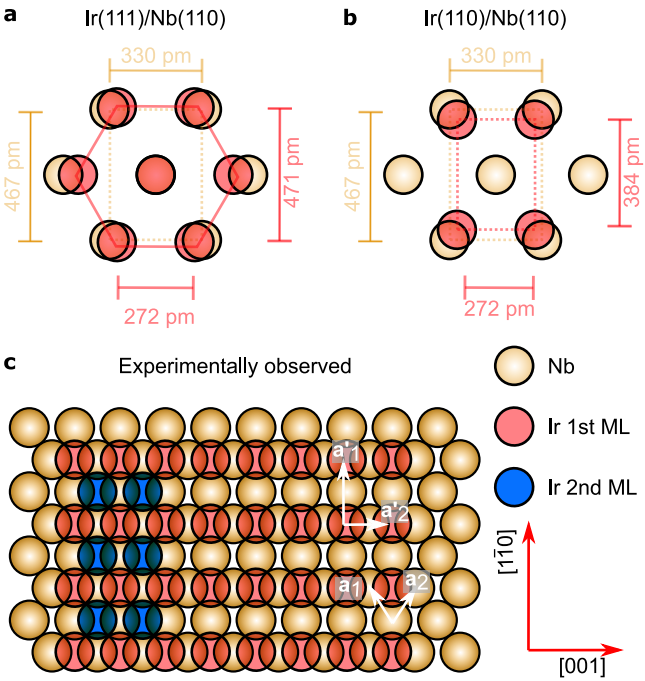

Figure 4.24.: a and **b** Ball models of two different possible crystallographic orientations for the growth of Ir on Nb(110). The yellow and pink spheres represent niobium and iridium atoms, respectively. Panel **a** shows the unrelaxed hexagonal unit cell of Ir(111), and **b** shows the unrelaxed one of Ir(110) on top of the unrelaxed pseudohexagonal unit cell of Nb(110). **c** Structural model for one and two ML of Ir on Nb(110) suggested by the STM images and LEED pattern in Figure 4.23. Blue spheres correspond to Ir atoms forming the second ML. White arrows indicate the lattice vectors of the Nb(110) substrate ($\mathbf{a}_1$ and $\mathbf{a}_2$) and of the first ML Ir ($\mathbf{a}_1^{'}$ and $\mathbf{a}_2^{'}$). Red arrows in the bottom right corner of the figure mark crystallographic directions, valid for all three panels.

tors are indicated by white arrows and labels. Black arrows highlight the crystallographic directions of the underlying Nb(110) lattice as obtained from Figure 4.22d. Analyzing the 2D -FFT of this atomic resolution image (inset of Figure 4.22d) confirms the existence of a simple rectangular lattice and yields absolute values for $|\mathbf{a}_1^{'}| = 480\,\mathrm{pm}$ and $|\mathbf{a}_2^{'}| = 340\,\mathrm{pm}$ which are in very good agreement with the values calculated from the LEED pattern of the first Ir ML in Figure 4.23b. We conclude that the 2nd ML growth occurs in the same crystal structure as the 1st ML of Ir.
To investigate the origin of this experimentally observed superstructure, the mismatches of Ir(111) and Ir(110) surfaces as grown on Nb(110) are illustrated in Figure 4.24a and Figure 4.24b, respectively. The literature values of the lattice constants for bulk bcc Nb (330 pm) and fcc Ir (384 pm)[258] were used to calculate the nearest neighbor distances in $[001]_{\mathrm{Nb}}$- and $[1\bar{1}0]_{\mathrm{Nb}}$-directions. An analysis of the unrelaxed crystal structure in the orientation Ir(111)/Nb(110), as illustrated in Figure 4.24a, reveals that there is a very small mismatch $(a_{\mathrm{Ir}} - a_{\mathrm{Nb}})/a_{\mathrm{Ir}}$ in $[1\bar{1}0]$-direction of only 0.8 %. However, the mismatch in [001]-direction, $-21.3\,\%$, is comparably large. Moving to the growth orientation of Ir(110)/Nb(110) (Figure 4.24b), the mismatch in the [001]-direction remains the same as for the Ir(111)/Nb(110) orientations. However, it is drastically increased to $-21.6\,\%$ in the $[1\bar{1}0]$-direction.
As suggested by the experimentally measured crystal structures and lattice parameters of the samples with Ir coverages of 1 ML and 2 ML, the Ir films most probably grow in an Ir(110)/Nb(110)-oriented superlattice. If we assume, that the Ir atoms energetically prefer the four-fold coordinated hollow adsorption site on the Nb(110) surface, we end up with the structural model illustrated in Figure 4.24(c). The resulting tensile strains $\epsilon = (a_{\mathrm{exp.}} - a_{\mathrm{Ir}(110)})/a_{\mathrm{Ir}(110)}$ of the Ir layer along the [001]- and $[1\bar{1}0]$-directions are 21.3 % and 21.6 %, compared to the unrelaxed Ir(110) surface.

Ten ML: Thin film limit

Since the surface structure we observed for ultrathin films is not very densely packed and appears slightly disordered, it seems to be unsuitable for single atom experiments, since adatoms could intermix with the film, STM tip-induced atom manipulation might not be reproducible and YSR states might be influenced by the defects[212]. To eventually achieve a hexagonal surface symmetry with lattice vectors similar to that of Ir(111), we evaporated Ir with a higher coverage. Since Ir(111) is a common stable surface of an Ir single crystal, we expect that the crystal structure of films on Nb(110) will eventually relax into this hexagonal crystal surface with increasing film thickness, once the strain energy accumulated in the first Ir layers exceeds the Ir/Nb interface energy. Hence, we prepare a sample with an Ir coverage of 10 ML to investigate if there is a structural transition for thicker Ir films.
An overview STM image and an atomically resolved STM image of the resulting sample are shown in Figures 4.25a and b, respectively. Similar to the ultrathin films discussed in Figures 4.22 and 4.23, the Ir thin film does not perfectly grow in a layer-by-layer fashion for the used post annealing power and time. We rather observe islands, which commonly are hexagonal in shape, have sharp edges, mostly show 120° corners (marked in Figure 4.25a) and are atomically flat and clean. The atomic resolution image shown in Figure 4.25b reveals that these islands indeed have a hexagonal surface structure. To highlight this symmetry and structure, a conventional unit cell and the lattice vectors $\mathbf{a}_1^*$ and $\mathbf{a}_2^*$ are marked by black arrows and labels. The absolute length of the direct lattice vectors may be calculated to be $|\mathbf{a}_1^*| = |\mathbf{a}_2^*| = 227\,\mathrm{pm}$. As indicated in Figure 4.24a, the ideal value for a perfect Ir(111) surface would be $\sim 272\,\mathrm{pm}$, which results in a compressive strain of $-16.5\,\%$.
We speculate that the compression of the hexagonal lattice compared to bulk Ir(111) is a result of the structural transition from the Ir(110)-oriented superlattice to the Ir(111)-oriented structure: The lattice constants of the

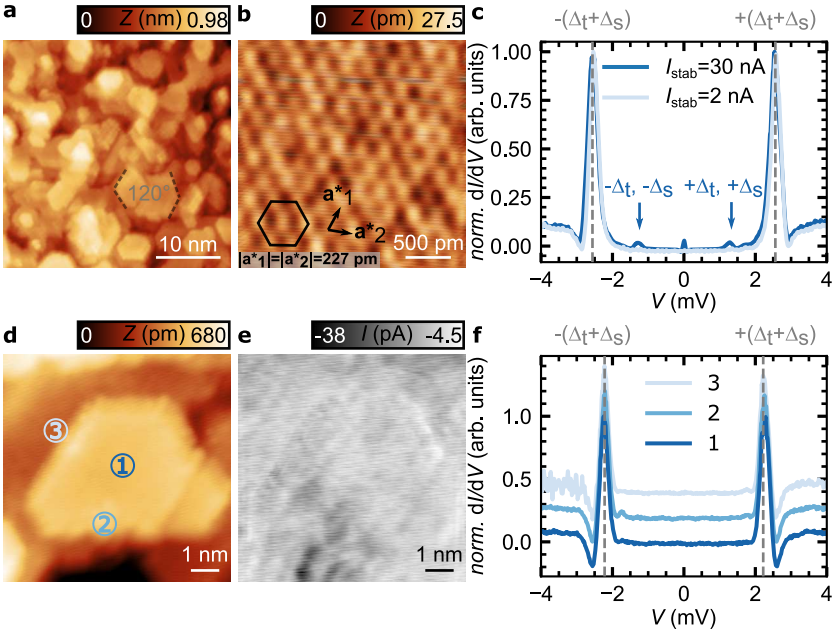

Figure 4.25.: a Overview STM image of a sample with ~ 10 ML of Ir coverage. Dashed lines mark common angles enclosed by the edges of Ir islands. **b** Atomic resolution STM image displaying a hexagonal lattice as indicated by the black hexagon marking a conventional unit cell of the lattice. Black arrows and labels denote the lattice vectors $\mathbf{a}_1^*$ and $\mathbf{a}_2^*$. **c** $\mathrm{d}I/\mathrm{d}V$-spectrum taken on an Ir island, using a bulk Nb tip at two different stabilization currents. The spectra are normalized by their respective maximum value. Gray and blue labels mark the superconducting coherence peaks at $\pm(\Delta_\mathrm{t} + \Delta_\mathrm{s})$ and the merged MAR's at $\pm\Delta_\mathrm{t}$ and $\pm\Delta_\mathrm{s}$. **d** STM image of an exemplary Ir island on which we measured $\mathrm{d}I/\mathrm{d}V$-spectra at the locations indicated by color-coded numbers. **e** Constant-contour current map taken at $V_\mathrm{bias} = -1.95\,\mathrm{mV}$ using the Z-signal from image **d**. **f** Tunneling spectra taken at the locations marked in panel **d**. Gray vertical lines mark the coherence peaks. The spectra are offset by 0.2 arb. units for the sake of visibility. Measurement parameters: **a** $V_\mathrm{bias} = -10\,\mathrm{mV}, I = 2\,\mathrm{nA}$, **b** $V_\mathrm{bias} = -10\,\mathrm{mV}, I = 1\,\mathrm{nA}$, **c** $V_\mathrm{stab} = -4\,\mathrm{mV}$, I_stab is given in the legend, **d** $V_\mathrm{bias} = -10\,\mathrm{mV}, I = 1\,\mathrm{nA}$, **e** $V_\mathrm{bias} = -1.95\,\mathrm{mV}$ and **f** $V_\mathrm{stab} = -4\,\mathrm{mV}, I_\mathrm{stab} = 1\,\mathrm{nA}$.

Ir(110)-oriented superlattice will approach the unrelaxed values indicated by red lines in Figure 4.24b with increasing film thickness. The Ir(110) to Ir(111) transition could then occur by the occupation of the center of the rectangular unit cell by an additional Ir atom, resulting in a nearest neighbor distance of 235 pm. A comparison to the experimentally extracted value of 227 pm yields good agreement and supports this theory.
Apart from the crystal structure, proximity-induced superconductivity is another crucial physical property of the Ir films on Nb(110), which is required to realize the experiments proposed in the introduction of this section. Two important criteria to judge the proximity-induced superconductivity in the Ir film are the size of the superconducting gap Δ_s and whether it is a fully pronounced "hard" gap, i.e. $\mathrm{d}I/\mathrm{d}V \sim$ DOS approaches zero inside the superconductor's gap. As we have seen in Figure 2.4c, both of those quantities crucially depend on the layer thickness of the normal-metal overlayer.
To evaluate these criteria, two $\mathrm{d}I/\mathrm{d}V$-spectra obtained on the Ir film are shown in Figure 4.25c. One one hand, a $\mathrm{d}I/\mathrm{d}V$-spectrum with a small tip-sample distance is shown in dark blue. Apart from a typical superconducting energy gap with coherence peaks at $\pm|\Delta_s + \Delta_t| = \pm 2.56\,\mathrm{mV}$, where Δ_t is the superconducting gap of the tip, a Josephson peak becomes apparent at zero bias. Further in-gap states are observed at $\pm 1.28\,\mathrm{mV}$, which we determine to be multiple Andreev reflections (MARs)[196]. MARs are expected to occur at $\pm|\Delta_s|$ and $\pm|\Delta_t|$. Since only one pair of MARs is observed in Figure 4.25c, we conclude that both $\pm|\Delta_t|$ and $\pm|\Delta_s|$ are $\pm 1.28\,\mathrm{meV}$ large, which matches precisely with the observation of coherence peaks at $\pm 2.56\,\mathrm{mV}$. Compared to typical values of $\pm|\Delta_s|$ for bare Nb(110) at 320 mK ($1.50\,\mathrm{meV}$[60]), the proximity-induced superconducting energy gap is reduced by only 14.7 %.
Additionally, a $\mathrm{d}I/\mathrm{d}V$-spectrum with common stabilization parameters of $V_{\mathrm{stab}} = -4\,\mathrm{mV}$, $I_{\mathrm{stab}} = 2\,\mathrm{nA}$ is shown in Figure 4.25c. We observe a clear superconducting energy gap with coherence peaks at $\pm|\Delta_s + \Delta_t| = \pm 2.56\,\mathrm{mV}$. Furthermore, the $\mathrm{d}I/\mathrm{d}V$-signal drops to zero

between the coherence peaks and $\pm|\Delta_t| = \pm 1.28\,\mathrm{mV}$, indicating a hard superconducting gap. To further judge the spatial homogeneity of these properties, additional $\mathrm{d}I/\mathrm{d}V$-spectra and a constant-contour current map taken at a bias voltage close to a coherence peak are shown in Figures 4.25d-f. An overview STM image of the investigated Ir island is shown in Figure 4.25d. Color-coded numbers mark the measurement locations of the $\mathrm{d}I/\mathrm{d}V$-spectra shown in Figure 4.25f, which were measured (1) in the center of the island, (2) on a defect close to the edge of the island and (3) on the Ir layer underneath the Ir island.
Overall, the three $\mathrm{d}I/\mathrm{d}V$-spectra measured at different locations have similar characteristics. The coherence peaks are found at $\pm 2.22\,\mathrm{mV}$ for all three $\mathrm{d}I/\mathrm{d}V$-spectra, as highlighted by the gray dashed vertical line in Figure 4.25f. Furthermore, the gap is fully pronounced in all three cases. A closer look at spectrum (2), which was taken on a defect close to the edge of the island, reveals a pair of in-gap states at $\pm 1.72\,\mathrm{mV}$. This indicates that the defect has a magnetic moment, which gives rise to YSR states, as discussed in Subsection 2.2.4. The origin of this defect is unknown.
The constant-contour current map allows us to evaluate the spatial homogeneity of the superconducting gap. While the bias was not set to the center of the coherence peak, $-1.95\,\mathrm{mV}$ still lies on the dropping edge of the coherence peak. Therefore, the measured current signal is very sensitive to changes of the intensity or the energy of the coherence peak (e.g. caused by a locally varying sample gap Δ_s) or to the local emergence of in-gap states, as the ones observed in spectrum (2) of Figure 4.25f. For example, a higher current signal (dark spot) is measured at location (2), due to the observed in-gap state of the defect. Further dark spots are observed at the edge to the hole underneath the island. Otherwise, the island, the layer underneath it and an additional hole to the top right of the island all appear to have the same current signal. Therefore, we conclude that the superconductivity is homogeneous across at least these three layers.

4.5.2. Growth study of Au on Nb(110)

In this section I present and discuss the structural properties of Au films grown on clean Nb(110), where I focus on three thicknesses of the gold overlayer. In particular, I investigate Au films consisting of 1, 2 and 4 atomic layers, all of which are prepared and studied in the set-up equipped with the 320 mK STM (description in Subsection 3.2.1). The Au coverage of the Nb(110) surface for samples with thicknesses > 1 ML, where it is no longer straightforward to determine the coverage from STM images, are estimated by a calibration measurement and subsequent STM investigation of a sample with a coverage below one ML. For all preparations discussed in the following, we evaporate the Au onto the freshly flashed Nb(110) samples as fast as possible and don't apply any post-annealing.
This section is separated into three parts. I subsequently discuss the surface structure and growth mode of the first ML, the second ML and the fourth ML of Au on Nb(110).

One ML of Au on Nb(110)

An STM image of a sample with an estimated coverage of ~ 1 ML Au is shown in Figure 4.26a. The presence of holes in the first atomic layer of Au shows that the first layer of Au is not fully closed at the evaporation parameters and sample temperature of the preparation performed here. However, the second atomic layer of Au is already partly beginning to form. It grows in the step-edge decoration and step-flow, as well as in the free-standing island mode. One of these regions is illustrated in the bottom panel of Figure 4.26a, where a height profile and the underlying layer structure are shown. Fe atoms are deposited onto the sample while keeping it cooled to $T < 6$ K. Apart from these adatoms and the aforementioned holes, the first atomic layer of Au on Nb(110) appears very

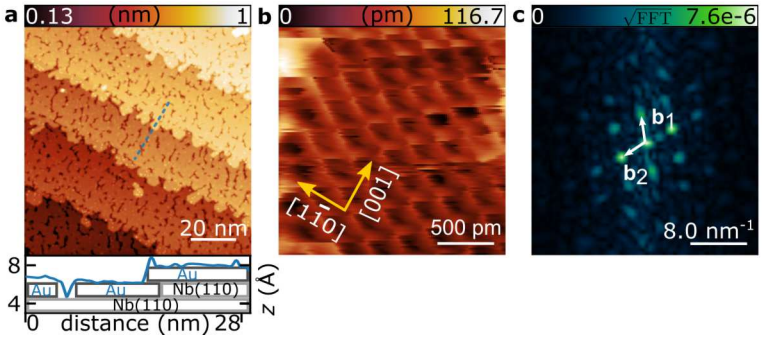

Figure 4.26.: **a** Overview STM image of a Nb(110) sample covered by ~ 1 ML of Au and subsequently deposited Fe atoms, which were evaporated onto the surface while keeping the sample at cryogenic temperatures $T < 6$ K. The blue dashed line marks the height profile shown in the bottom panel. Gray boxes underneath the blue curve indicate the local layer structure of the Nb(110) substrate, the first- and the second atomic layer of gold. **b** Manipulated atom image obtained while dragging/pushing an Fe atom in the lateral manipulation mode. Yellow arrows and white labels indicate crystallographic directions. **c** 2D-FFT of the STM image shown in **b**. White arrows and labels mark the reciprocal lattice vectors. Measurement parameters: **a** $V_{\text{bias}} = 50\,\text{mV}$, $I = 100\,\text{pA}$ and **b** $V_{\text{bias}} = -3\,\text{mV}$, $I = 100\,\text{nA}$.

flat and defect-free.
Since it was not possible to obtain atomic resolution STM images using a regular imaging mode, we measured atom manipulation images with an Fe adatom, as shown in Figure 4.26b. The resulting structure of the adsorption sites matches that of a bcc(110) surface. This is further highlighted by the 2D-FFT of the STM image, which is shown in Figure 4.26c. Here, one can clearly see that the first ML of Au on Nb(110) has a centered rectangular unit cell, with reciprocal lattice vectors as indicated by white arrows and labels. We determine a nearest neighbor distance of 260 pm, which agrees reasonably well, with the nearest neighbor distance of Nb(110) (285 pm). Therefore, we conclude that the first ML of Au on Nb(110) grows pseudomorphic and we attribute the mismatch of the determined atomic spacing to an inaccurate calibration of the piezo tube. Furthermore, the atom manipulation image allows us to determine the adsorption site of Fe adatoms on Nb(110): As the pattern observed in Figure 4.26b matches the lattice of the topmost layer of a Nb(110) surface, we conclude that there is only one stable adsorption site. Therefore, we expect that Fe adatoms adsorb in the four-fold coordinated hollow site, which is further discussed in Subsection 4.5.4.

Two ML of Au on Nb(110)

As apparent from the overview STM image in Figure 4.26a, there are areas on the sample, where a second layer of Au on Nb(110) has formed. Firstly, we find free-standing islands, which are easily identified as the second ML of Au on Nb(110). Secondly, there are additional areas growing from the step-edges that can be identified by an irregular shape (compared to a clean single crystal surface, cf. Figure 3.6d). One further characteristic difference between both layers is the apparent height of Fe adatoms, which is much larger on the second ML of Au. An STM image of a free-standing 2 ML high island is shown in Figure 4.27a, where Fe adatoms

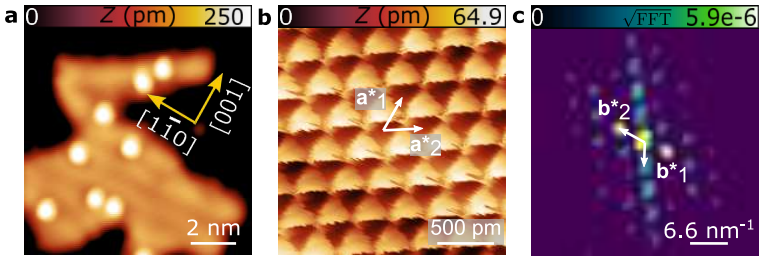

Figure 4.27.: a STM image of a free standing Au island which consists of two atomic layers of gold on Nb(110). The STM measurements were performed on the sample shown in Figure 4.26a. Yellow arrows indicate crystallographic directions, which are obtained from Figure 4.26b and are valid for **b** as well. **b** Manipulated atom image obtained while manipulating an Fe adatom. White arrows and letters mark the lattice vectors. **c** 2D-FFT of the STM image shown in **b**. White arrows and labels indicate the reciprocal lattice vectors. Measurement parameters: **a** $V_{\text{bias}} = 6\,\text{mV}$, $I = 200\,\text{pA}$ and **b** $V_{\text{bias}} = 3\,\text{mV}$, $I = 50\,\text{nA}$.

are visible as bright protrusions.

From the manipulated atom image shown in Figure 4.27b, we find that the film has undergone a structural transition. To begin with, we now observe two different adsorption sites of Fe adatoms, which is concluded from the presence of two distinct types of triangles that have different apparent heights and are rotated by 180° with respect to one another.

Focusing on only one type of the triangles, e.g. the darker ones, we find that they are arranged in a hexagonal lattice, which is characterized by the lattice vectors indicated by white arrows and labels. The hexagonal arrangement of the adsorption sites is confirmed by the 2D-FFT of the atom manipulation image, which is shown in Figure 4.27c. The reciprocal lattice vectors $\mathbf{b}_1^*$ and $\mathbf{b}_2^*$ are marked by white arrows. We obtain a nearest neighbor distance of the Au adsorption sites of 250 pm. We conclude that the second ML of Au on Nb(110) has transitioned to a Au(111)-like structure.

This structural change allows us to identify the two adsorption sites

observed in Figure 4.27b as the fcc and hexagonal close-packed (hcp) sites, which are well known on fcc(111) surfaces and have been investigated by STM[213]. The adsorption sites differ by the coordination of the adsorbate with surface atoms: The hcp site is characterized by a Au atom located directly underneath it in the subsurface Au layer. On the other hand, there is no Au atom in the subsurface Au layer underneath the fcc site. The equally large triangles in the atom manipulation image (Figure 4.27b) indicate that the adsorption sites are energetically nearly equal.
Since there is a mismatch of the first pseudomorphic Au ML and the Au(111)-like second ML ($-32\,\%$ in $[001]$-direction and $-8\,\%$ in $[1\bar{1}0]$-direction, calculated in analogy to Subsection 4.5.1 using the extracted lattice constants), we expect that the second ML is strained, which could be relaxed by a superstructure. However, due to the limited size of the islands we do not clearly observe such a superstructure. Only small hints, such as slight depression lines extended in $[1\bar{1}0]$-direction (Figure 4.27a) and extended regions in the $[1\bar{1}0]$-direction, where the adsorption sites are brighter/darker (Figure 4.27b), indicate that the strain in the $[001]$-direction is relieved by a superstructure that is periodic in $[001]$-direction.

Four ML of Au on Nb(110)

Last, we investigate a sample with an approximate coverage of $\sim 4\,\mathrm{ML}$ Au, where an STM overview image, two atomically resolved STM images and $\mathrm{d}I/\mathrm{d}V$-spectra characterizing the superconducting properties are shown in Figure 4.28. To begin with, we find that the surface morphology has changed again, moving from the second atomic layer of Au to the fourth atomic layer. With the applied evaporation parameters and sample temperature during the evaporation, we do not obtain closed layers, but rather observe large terraces with few holes and hexagonal islands. Furthermore, the step-edges are not straight but are washed out by the step-flow growth.

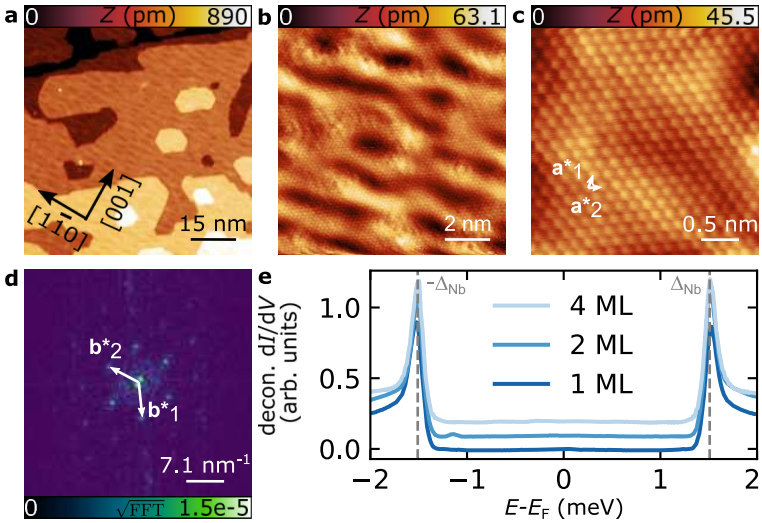

Figure 4.28.: **a** Overview STM image of a Nb(110) sample with ~ 4 ML of Au coverage. Black arrows and labels indicate crystallographic directions (obtained from Figure 4.26b), which are valid for panels **b** and **c** as well. **b** and **c** Atomic resolution STM images of the sample shown in **a**. White arrows and labels denote the lattice vectors $\mathbf{a}_1^*$ and $\mathbf{a}_2^*$. **d** 2D-FFT of the STM image shown in panel **c**. White arrows and labels indicate the reciprocal lattice vectors. **e** Normalized and deconvoluted $\mathrm{d}I/\mathrm{d}V$-spectra taken on the first (Figure 4.26), the second (Figure 4.27) and the fourth (**a-c**) atomic layers of Au on Nb(110). Gray dashed vertical lines mark the superconducting gap of niobium, which is typically observed at $T = 320\,\mathrm{mK}$ ($\Delta_{\mathrm{Nb}} = 1.51\,\mathrm{meV}$)[60]. The $\mathrm{d}I/\mathrm{d}V$-spectra are vertically offset by 0.1 arb. units for the sake of visibility. Measurement parameters: **a** $V_{\mathrm{bias}} = 200\,\mathrm{mV}$, $I = 200\,\mathrm{pA}$, **b** $V_{\mathrm{bias}} = 20\,\mathrm{mV}$, $I = 1\,\mathrm{nA}$, **c** $V_{\mathrm{bias}} = -6\,\mathrm{mV}$, $I = 1\,\mathrm{nA}$, **e** $V_{\mathrm{stab}} = -4\,\mathrm{mV}$, $I_{\mathrm{stab}} = 1\,\mathrm{nA}$.

Most strikingly, we find a superstructure on the terraces. It appears as bright/dark stripes oriented in the $[1\bar{1}0]$-direction which have a periodic arrangement in the [001]-direction of the Nb(110) substrate, with an average spacing of 1.95 nm. This superstructure might be a result of the strain induced by the mismatch of the pseudomorphic first ML of Au on Nb(110) and the hexagonal lattice structure of the following atomic layers (see previous subsection).
From the atomic resolution image in Figure 4.28c and its 2D-FFT in Figure 4.28d, we find that the fourth ML of Au still has a hexagonal surface structure with a nearest neighbor distance of 260 pm, i.e. the same value that we found for the second atomic layer of Au.
Last, we investigate the superconducting properties of the three Au thin films discussed before. One deconvoluted $\mathrm{d}I/\mathrm{d}V$-spectrum obtained on each film investigated previously is shown in Figure 4.28e. The dashed vertical lines indicate the typical superconducting gap of a Nb(110) sample at our measurement temperature of 320 mK. Apart from the coherence peaks and a small contribution of a close-by Fe impurity in the $\mathrm{d}I/\mathrm{d}V$-spectrum of the 2 ML, the $\mathrm{d}I/\mathrm{d}V$-spectra are featureless and the $\mathrm{d}I/\mathrm{d}V$-signal reaches zero in between the coherence peaks. Furthermore, we find that the coherence peaks are at 1.51 meV for all three Au film thicknesses, i.e. the gap sizes are indistinguishable from bare Nb(110) within our experimental resolution.

4.5.3. Discussion of the growth modes and usability of proximitized thin films as substrates for MSHs

Ir thin films grown on clean Nb(110) undergo a transition of the crystal structure from an Ir(110)-oriented superlattice at low coverages (1-2 ML), to an Ir(111)-oriented hexagonal crystal structure at 10 ML. This structural behavior differs drastically from other growth modes of fcc transition metals such as Ag, Pt and Pd on clean Nb(110), which were

investigated by LEED[288–290]. Those elements grow on Nb(110) by forming a pseudomorphic wetting layer, followed by an fcc(111)-like growth for thicker films, which is exactly the mode that we have confirmed in the case of Au films grown on clean Nb(110) in the second part of this section. However, in contrast to the aforementioned studies which only employ LEED[288], we perform STM measurements. This allows us to locally determine the high quality, the large defect-free terrace size and the superconducting properties of Au thin films on Nb(110) very accurately. Indeed, we observe the formation of a pseudomorphic Au layer at a coverage of one ML on Nb(110). Already at two atomic layers of Au, we find the structural transition to a hexagonal fcc(111)-like structure. However, we observe a strain-induced superstructure upon increasing the Au coverage to four ML.

Regarding the application of the studied heterostructures as substrates for MSH systems, we conclude that the samples with an Ir coverage of 10 ML, which display a hexagonal lattice, and the sample with a Au coverage of 1 ML, which grows commensurate to Nb(110), are very promising to proceed with the study of single transition metal atoms. In the following I will present the arguments and reasons for this conclusion: The crystal structure and quality are the decisive factor considering both overlayer materials. The Ir(110)-oriented superlattice has a comparably large unit cell, which could lead to intermixing effects upon the deposition of transition metal species and may prevent reproducible STM tip-induced atom manipulation. Nevertheless, the observation of a strained Ir(110)-oriented superstructure with a rectangular unit cell for one and two ML might be interesting from another perspective. Since the Ir(110) surface stabilizes by forming (311) facets[291,292], the preparation of a clean and unreconstructed Ir(110) surface seems to be unachievable starting from an Ir single crystal. Therefore, the growth of ultrathin films of Ir on Nb(110) could enable the study of the Ir(110) surface, and could be of interest for further experiments.

In the case of Au thin films grown on Nb(110), the sample covered by

four atomic layers of Au has a periodic superstructure, which leads to an inhomogeneous potential landscape and could, therefore, eventually result in a strong location dependence of the YSR states of given transition metal species. Furthermore, with regards to constructing Shiba chains the pseudomorphic first ML of Au on Nb(110) has the advantage of a lower symmetry compared to a hexagonal surface, which should lead to anisotropic YSR states of single magnetic impurities and should, therefore, allow a selective coupling of those.

4.5.4. Tailoring a single Shiba band system in Fe chains on Au/Nb(110)

In this subsection I present a STS study of Fe adatoms deposited onto thin films of Au on Nb(110) in the limit of 1 ML (sample shown in Figure 4.26) and 4 ML (sample shown in Figure 4.28). Unless indicated otherwise, $\mathrm{d}I/\mathrm{d}V$-spectra were obtained with the following measurement parameters: $V_{\mathrm{stab}} = 6\,\mathrm{mV}$, $I_{\mathrm{stab}} = 1\,\mathrm{nA}$ and $V_{\mathrm{mod}} = 20\,\mu\mathrm{V}$.

Fe atoms, artificial dimers and chains on 1 ML of Au on Nb(110)

All Fe adatoms which are positioned far from any other Fe atoms or defects show similar $\mathrm{d}I/\mathrm{d}V$-spectra. An example of such a $\mathrm{d}I/\mathrm{d}V$-spectrum is shown in Figure 4.29a (blue curve). Single Fe atoms display two pairs of YSR states, which are induced in the superconducting gap of the proximitized Au ML on Nb(110). We mark those states by black arrows and greek letters. The first YSR state is energetically located close to the superconducting gap edge at $\pm 1.23\,\mathrm{meV}$ and is labeled $\pm\alpha$. The second YSR state ($\pm\beta$) has a lower energy and lies close to the Fermi level E_{F} with an energy of $\pm 0.27\,\mathrm{meV}$. Using constant-contour $\mathrm{d}I/\mathrm{d}V$-maps (see Subsection 3.1.4) we resolve the spatial distributions of both YSR states in Figure 4.29c[151,152].

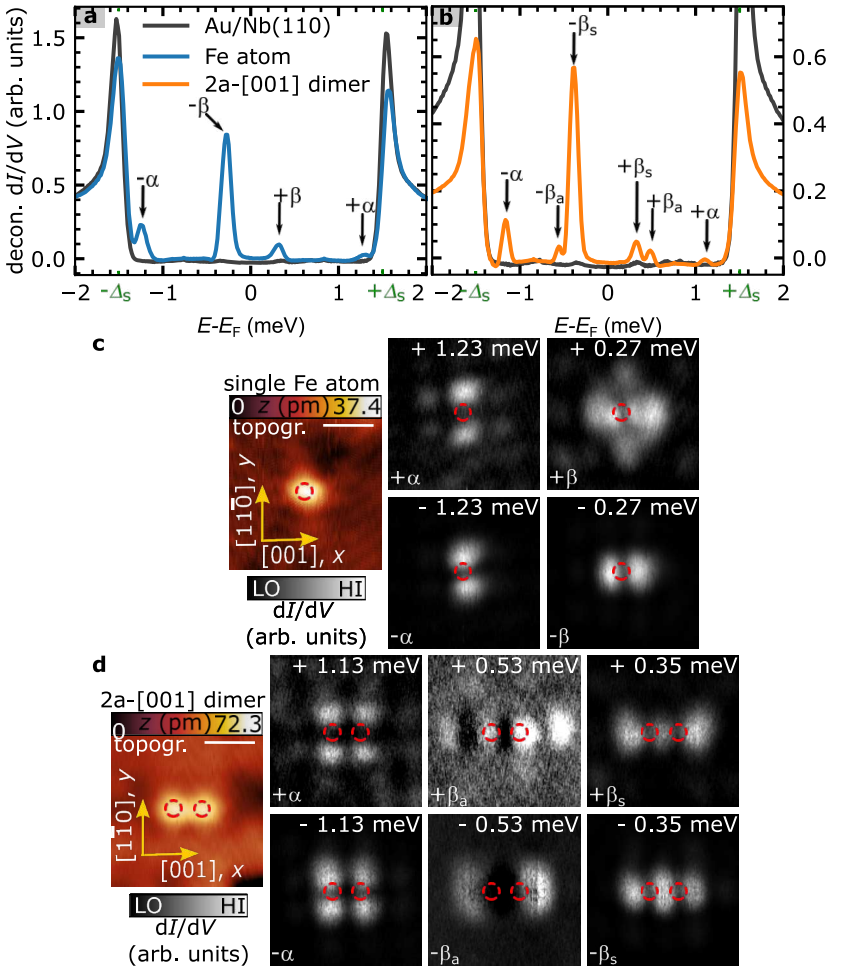

Figure 4.29.: a and **b**, Deconvoluted $\mathrm{d}I/\mathrm{d}V$-spectra measured on the first ML of Au on Nb(110), a single Fe atom and in the center of a $2a - [001]$ Fe dimer. Black arrows and greek letters label YSR states. Green ticks mark the positions of the superconducting energy gap of the sample $\Delta_\mathrm{s} = 1.50\,\mathrm{meV}$ as extracted from Figure 4.28e. **c** and **d** are STM images and constant-contour $\mathrm{d}I/\mathrm{d}V$-maps of a single Fe atom (**c**) and a $2a - [001]$ Fe dimer (**d**). Yellow arrows indicate crystallographic directions, red dashed circles depict the positions of the Fe atoms as determined from the STM images, and white scale bars represent a length of 1 nm. Measurement parameters as indicated above.

The $\pm\alpha$ state has a spatial distribution resembling that of a d_{yz}-orbital with two lobes pointing along the $[1\bar{1}0]$-direction. On the other hand, a spatial distribution resembling that of a d_{xz}-orbital extended along the $[001]$-direction is observed for the $\pm\beta$ state. Note, that the shapes of the $+\beta$ and the $-\beta$ state are somewhat different since the former has additional faint lobes along the $[1\bar{1}0]$-direction, which probably indicates contributions from a $d_{x^2-y^2}$-like YSR state. The spatial distributions of the YSR states are not surprising: As we have shown in Subsections 4.1.1 and 4.4.1, the spatial distributions of YSR states are governed by the symmetry of the adsorbed impurity. Fe atoms on 1 ML Au/Nb(110) are adsorbed similar to Mn adatoms on Nb(110) and Ta(110). Since all those systems are described by the same point group (C_{2v}), their YSR states are strikingly similar regarding their spatial distribution, even though we expect a completely different electronic environment for the Fe adatoms on Au/Nb(110).

In light of the comparison between Mn/Nb(110) and Mn/Ta(110) in Section 4.4, it should be noted, that the energetic order of the YSR states for Fe on Au/Nb(110) is completely different compared to those systems. Furthermore, we only observe two YSR states states and we do not find any indications for a d_{z^2}- or d_{xy}-like YSR state. Therefore, we find that the electronic properties of the Au/Nb(110) system are considerably different than bare Nb(110) or Ta(110). Hence, I want to highlight that a comparison of the Fe/Au/Nb(110) system with the Mn/Nb(110) or Mn/Ta(110) should not be overstressed.

Before we continue with the investigation of artificial structures from Fe atoms, let us consider some intuitive ideas about the most promising orientations of chains that we can construct from individual Fe atoms towards the goal of topologically gapped Shiba bands. As found in Section 4.2, a sufficient hybridization of a YSR state, which is already close to E_F, while at the same time minimizing the hybridizations of all the other YSR states far from E_F, may lead to a single Shiba band overlapping with E_F. Together with SOC, this can be an adequate condition for the

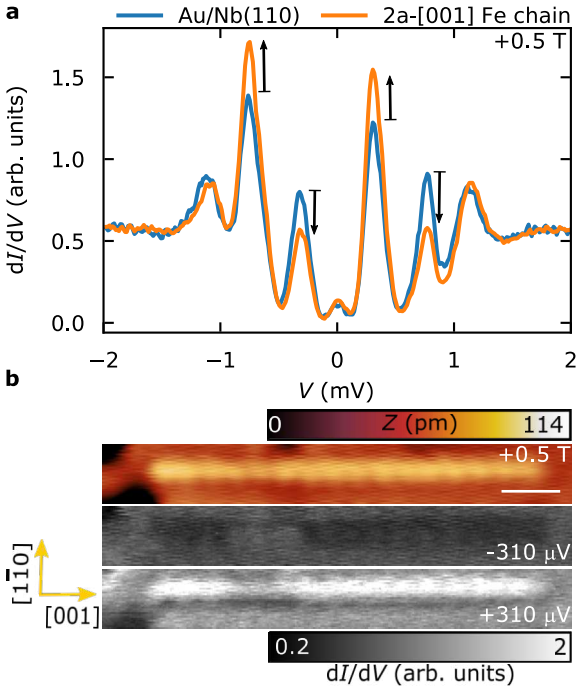

Figure 4.30.: **a** $\mathrm{d}I/\mathrm{d}V$-spectrum measured in a magnetic field of $+0.5\,\mathrm{T}$ using a superconducting tip which is functionalized by Fe atoms. The blue curve was obtained on the first Au ML on Nb(110) and the orange curve was obtained on a Fe_{16} $2a-[001]$ chain. Black arrows indicate an increase or decrease in the $\mathrm{d}I/\mathrm{d}V$-signal of the tip's YSR states when comparing the substrate and the chain spectrum ($V_{\mathrm{mod}} = 40\,\mu\mathrm{V}$). **b** Constant-contour $\mathrm{d}I/\mathrm{d}V$-maps of the 16-atom-long $2a-[001]$ Fe chain in a magnetic field of $+0.5\,\mathrm{T}$. The top panel shows the STM image, serving as the contour for the lower panels. The white scale bar represents a length of 1.5 nm and is valid for all three panels. Measurement parameters as indicated above with the exception that $V_{\mathrm{mod}} = 40\,\mu\mathrm{V}$ in **b**.

opening of a topologically non-trivial gap in the lowest energy Shiba band. Starting from the experimentally detected shapes and energies of the α and β YSR states in Figure 4.29, we thus regard chains along the [001]-direction as most promising. For this orientation, we expect a weak hybridization of the α YSR states which are far from the Fermi level. Considering the energetically low-lying β YSR states on the other hand, we expect strong hybridization effects. We are able to tune the system into the above condition using dimers with an interatomic spacing of $2a$ along the [001]-direction (see STM image in Figure 4.29d). It should be noted that it was not possible to create $1a - [001]$ Fe dimers by means of STM tip-induced atom manipulation.
To verify the speculations above, we construct a $2a - [001]$ Fe dimer artificially using STM tip-induced atom manipulation. A $\mathrm{d}I/\mathrm{d}V$-spectrum measured above the center of the dimer as well as constant-contour $\mathrm{d}I/\mathrm{d}V$-maps of the spatial distributions of the three evident YSR states are displayed in Figures 4.29b and d. In this configuration, the $\pm\alpha$ YSR states of the two atoms do not overlap significantly such that they do not split into hybridized states, but only slightly shift in energy. In contrast, the $\pm\beta$ YSR states of the two atoms strongly overlap and split into an energetically higher one, with a clear nodal line in the center between both impurities ($\pm\beta_\mathrm{a}$), and another energetically lower one with an increased intensity in the center of the dimer ($\pm\beta_\mathrm{s}$).
Having identified a promising orientation and interatomic spacing from the investigation of the single atom and the dimer above, we move on to study artificial chains with the same interatomic separation, called $2a - [001]$ chains in the following. A sketch illustrating this geometry and an STM image of a nine Fe atoms long (Fe_9) $2a - [001]$ chain are shown in the top panels of Figures 4.31a and b. In order to determine the magnetic ground state of the chains, we perform SP-STS and SP-STM measurements on a Fe_{19} $2a - [001]$ chain, as shown in Figure 4.30. We employ the same method as in Subsections 4.4.2 and 4.4.3, i.e. we use a functionalized superconducting STM tip for the measurements.

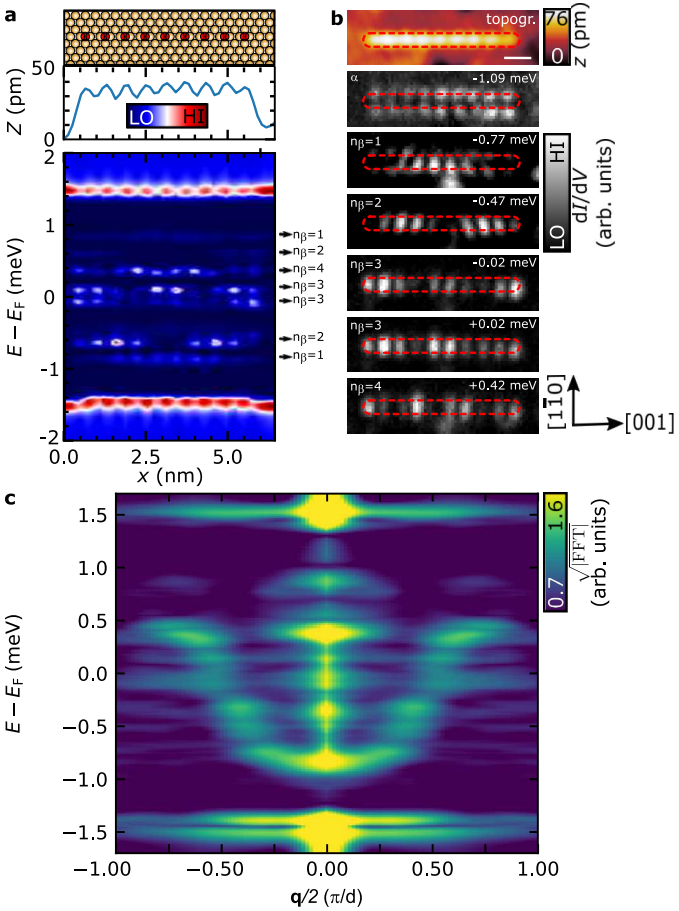

Figure 4.31.: a, Deconvoluted $\mathrm{d}I/\mathrm{d}V$-line profile (bottom panel) and corresponding topographic line profile (middle panel) measured along the longitudinal axis of a Fe_9 $2a - [001]$ chain, as illustrated in the top panel. Black arrows mark the energies in the bottom panel at which n_β maxima are observed along the chain. **b** STM image and $\mathrm{d}I/\mathrm{d}V$-grids of a Fe_9 $2a - [001]$ chain, obtained at energies indicated in the top right corner of each panel. The red lines mark the spatial extent of the chain in the STM image. The white scale bar represents a length of 1 nm. **c**, Averaged 1D-FFT obtained from $\mathrm{d}I/\mathrm{d}V$-line profiles of Fe_N $2a - [001]$ chains with lengths N ranging from seven to fourteen atoms. Measurement parameters as indicated above.

A $\mathrm{d}I/\mathrm{d}V$-spectrum taken on the Au/Nb(110) film using a functionalized STM tip at an external B-field of $+500\,\mathrm{mT}$, which quenches the superconductivity in the substrate, is shown in Figure 4.30a. We find that the tip has three pairs of YSR states in total. One of those pairs is located at $0\,\mathrm{mV}$ and, therefore, appears as a single peak. A $\mathrm{d}I/\mathrm{d}V$-spectrum taken on the Fe chain with the same microtip is shown in Figure 4.30a (orange curve). The $\mathrm{d}I/\mathrm{d}V$-intensities of the individual YSR states are considerably altered compared to the spectrum taken on the substrate. Using the YSR states at $\pm 310\,\mu\mathrm{V}$ as an example, we find that the state at negative bias voltage has a much lower $\mathrm{d}I/\mathrm{d}V$-signal in the measurement on top of the chain than it is the case on the substrate. However, its positive-bias counterpart has an increased $\mathrm{d}I/\mathrm{d}V$-intensity. A similar behavior, although inverted for the positive- and negative-bias YSR states, is observed for the higher energy YSR state at $\pm 760\,\mu\mathrm{V}$.
As demonstrated in Refs. [59, 271], this behavior is explainable by TMR. Constant-contour $\mathrm{d}I/\mathrm{d}V$-maps measured on the YSR states at $\pm 310\,\mu\mathrm{V}$ are shown in Figure 4.30b. Since the $\mathrm{d}I/\mathrm{d}V$-intensity is continuously increased (decreased) at $+310\,\mu\mathrm{V}$ ($-310\,\mu\mathrm{V}$) along the entire chain, we conclude that the spins in this chain configuration are FM aligned.
We now proceed to investigate the Shiba band properties using similar methods as e.g. in Subsections 4.4.2 and 4.4.3: We perform a length-dependent study of $\mathrm{d}I/\mathrm{d}V$-line profiles measured along the longitudinal chain axis. An exemplary $\mathrm{d}I/\mathrm{d}V$-line profile for a Fe_9 $2a - [001]$ chain is shown in Figure 4.31a (bottom panel) alongside the acquired stabilization height profile (middle panel). The first apparent characteristic of this measurement is the modulation of every feature with the interatomic spacing of $2a$. This modulation is also visible in the height profile. It should be emphasized that this is not a feature of the chain's in-gap band structure but just due to the lattice periodic part of the wave function. However, we find additional states with different well-defined numbers of maxima at increasing energy and also very close to E_F as indicated by the labels n_β ($n_\beta - 1$) for the numbers of maxima (nodes). Note that all

these states have particle-hole partners occurring on the other side of E_F with the same energetic distance to E_F and equal numbers of maxima and nodes. However, they mostly have much smaller dI/dV-intensities such that they are barely visible. These pairs of states can thus be assigned to confined BdG quasiparticles residing in a Shiba band induced by the finite magnetic chain on the superconductor[61].

To determine the orbital origin of these states, we show dI/dV-grids of the Fe_9 2a-[001] chain in Figure 4.31b. We find that the confined BdG states identified before in Figure 4.31a are localized inside the spatial extent of the chain deduced from the STM image (dashed red elliptical circumference). We assign those states to a Shiba band formed by the strong hybridization of the $\pm\beta$ YSR states of the single adatoms as they are expected to be largely localized along the longitudinal axis of the chain. Additionally, there is a state at a similar energy as the single adatom's and dimer's $\pm\alpha$ YSR states around ± 1.09 meV. This state has exactly as many maxima as there are atoms in the chain (nine) which are spatially localized along both sides of the chain with a similar distance to the chain axis as the lobes of the single adatom's and dimer's $\pm\alpha$ YSR states (cf. Figures 4.29c and d). Therefore, we assign this state to the very weakly hybridizing $\pm\alpha$ YSR states of the single atom. It is not observed in the dI/dV-line profile of Figure 4.31a due to its nodal line along the longitudinal chain axis.

In order to measure the dispersion of the confined BdG states from the β Shiba band we perform a 1D-FFT of the dI/dV-line profiles of chains with lengths ranging from $N = 7$ to $N = 14$ atoms in Figure 4.31c. The obtained dispersion is closely linked to the β Shiba band structure. We find that this Shiba band has an approximately parabolic dispersion ranging from -0.9 meV at $q/2 = 0$ to $+0.5$ meV at $q/2 = \pi/d$, where d is defined as $2a$. Note that the particle-hole partner of this band has a much lower intensity, as already discussed for the dI/dV line profiles above. It is only visible around the Brillouin zone center ($q/2 = 0$) in our measurements. Most importantly, the β Shiba band smoothly crosses E_F

without any indications of a minigap opening within our experimental energy resolution. These results are further discussed in Subsection 4.5.6.

Fe adatoms on four ML of Au on Nb(110)

Let us move on to investigate Fe adatoms on 4 ML thick Au films on Nb(110), whose structural properties are presented in Figure 4.28. An overview of the spectroscopic results obtained on an individual Fe atom is shown in Figure 4.32. To begin with, an atom manipulation image which is measured with an Fe adatom on the 4 ML thick Au films on Nb(110) is shown in Figure 4.32a. We find two possible adsorption sites, which are apparent from two equally spaced triangles in the manipulation image, that both form a hexagonal lattice, but are rotated by 60° with respect to each other. As these Au films structurally resemble a Au(111) surface, we expect that these two adsorption sites are the fcc and hcp sites[213]. Since both species of triangles in Figure 4.32a are equally sized, we conclude that both adsorption sites are similarly stable and neither one is largely energetically favored. Throughout the spectroscopic investigation of Fe adatoms on 4 ML Au on Nb(110) we do not observe any indications for spectroscopic differences between Fe adatoms located in either site. Therefore, I refrain from discussing the existence of two adsorption sites in the following.
An STM image of a single Fe adatom on the 4 ML thick Au film is shown in Figure 4.32b. An averaged $\mathrm{d}I/\mathrm{d}V$-spectrum over the adatom extent and a substrate spectrum are shown in Figure 4.32c. We find signatures of two clear pairs of YSR states. Considering this particular atom, we find one pair of YSR states at $E_1 = \pm 1.44\,\mathrm{meV}$ appearing as shoulder of the coherence peaks and another pair at $E_0 = \pm 0.18\,\mathrm{meV}$. Constant-contour $\mathrm{d}I/\mathrm{d}V$-maps taken over the Fe adatom at exactly the aforementioned energies are shown in Figure 4.32d. We find that the YSR states resemble triangles. Interestingly, the triangles of the particle-hole partners of a given

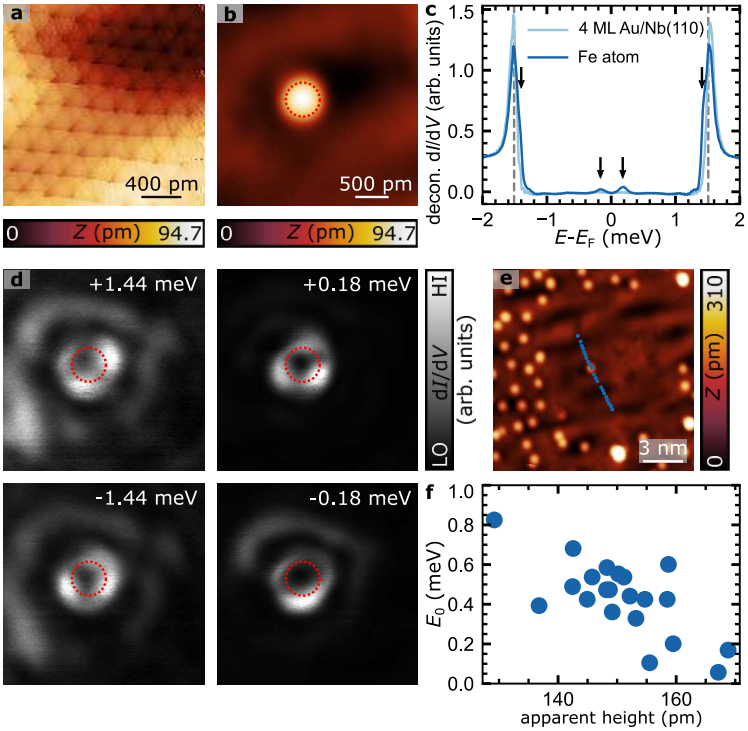

Figure 4.32.: **a** Manipulated atom image obtained with an Fe adatom on 4 ML of Au on Nb(110) (see Figure 4.28). **b** STM image of a single Fe atom. **c** Deconvoluted dI/dV-spectra measured on the 4 ML thick Au film on Nb(110) and on an Fe adatom. Black arrows mark the positions of YSR states. **d** Constant-contour dI/dV-maps measured on the single Fe adatom shown in **b** and **c**. **e** STM image of an Fe adatom positioned in an environment where all other impurities are removed. Blue dots indicate all locations where the adatom is moved and a dI/dV-spectrum is measured. **f** The apparent height of the Fe adatom in each adsorption site of **d** was evaluated and is plotted against the corresponding energetic position of the low-energy YSR state. Measurement parameters as indicated above.

YSR state are rotated by 60° with respect to one another. Furthermore, the triangular shapes of the YSR states at $+1.44\,\mathrm{meV}$ and $+0.18\,\mathrm{meV}$ are rotated by 60° as well. The same holds true for the negative bias YSR states.
This drastically different shape of the YSR states compared to all other single impurity YSR states that were investigated throughout this thesis is again explained by the symmetry of the adsorption geometry. An Fe adatom on the hexagonal 4 ML thick Au film on Nb(110) belongs to the C_{3v} point group. The symmetry of the ligand field results in a hybridization of the Fe atom's *d*-orbitals with *p*-orbitals. Therefore, the YSR states states no longer resemble the characteristic shapes of the *d*-orbitals, as it was the case for C_{2v} symmetric substrates in Figures 4.1, 4.16 and 4.29. We rather obtain threefold symmetric YSR states (Figure 4.32d). Similar spatial distributions were observed for Fe impurities on Pb(111)[151], which have the same C_{3v} point group symmetry.
As we know from the investigation of the structural properties in Subsection 4.5.2, a pronounced superstructure is observed on the fourth ML Au on Nb(110). This superstructure is clearly visible in Figures 4.32a,b and e as well. To investigate the influence of the superstructure on the YSR states of a single adatom and to investigate whether such a thin film could be used as a substrate for Shiba chains, we perform a novel kind of experiment: To begin with a sufficiently large region (approximately $7\,\mathrm{nm} \times 7\,\mathrm{nm}$) is cleared from all Fe adatoms except for one (Figure 4.32e). Thereby, I make sure that the observed YSR states solely stem from the single adatom and not from long-range hybridizations with other impurities. I then proceed to manipulate the single adatom along the line which is indicated by the blue dots in Figure 4.32e. For each of the adsorption sites, I measure a $\mathrm{d}I/\mathrm{d}V$-spectrum on the Fe atom and obtain an STM image.
Using this data set, I extract the energies of the low-lying YSR states $\pm E_0$ and the apparent height of the Fe adatom for each adsorption site. By linking these two pieces of information, I obtain the plot shown in

Figure 4.32f. To begin with, it is apparent that the energy of the low-lying YSR state varies considerably from 50 µeV to 850 µeV throughout this measurement series. Additionally, we find that there is a clear correlation between the apparent height of the Fe adatom in a particular adsorption site and the respective YSR state's energy. With increasing apparent height, we observe a decrease of the YSR state's energy.
The observed relationship is easily explainable by considering Equation 4.5. If the exchange coupling J of the impurity spin to the substrate is altered, the YSR state's energy changes. It is reasonable to assume that a change of the apparent height of a given Fe adatom results in a change of this parameter and, therefore, a change of the YSR state's energy. The observed behavior is similar to that investigated in a study of manganese phthalocyanine on Pb(111), where the YSR states of the molecules vary energetically due to Moiré-like variations in the molecular film[270]. Unfortunately, this strong local variation of the coupling strength of the Fe adatoms and the gold film renders these thick films of 4 ML Au on Nb(110) useless for studying Shiba chains. Since the YSR states of individual atoms would vary drastically along the chain, the Shiba band structure would vary locally as well, resulting in regions of distinct Shiba band properties along the chain. Shiba chains exposed to a locally varying potential — although on a much larger length-scale and induced by the domain walls of a charge density wave — are studied in Ref. [238].

4.5.5. Single Fe impurities on proximitized films of Ir on Nb(110)

The last example of a proximitized thin film used as a substrate for magnetic adatoms, which I present in the course of this thesis, is the promising 10 ML thin Ir film that was prepared in Subsection 4.5.1. We proceed, as with all samples investigated so far, and deposit a $3d$ transition metal

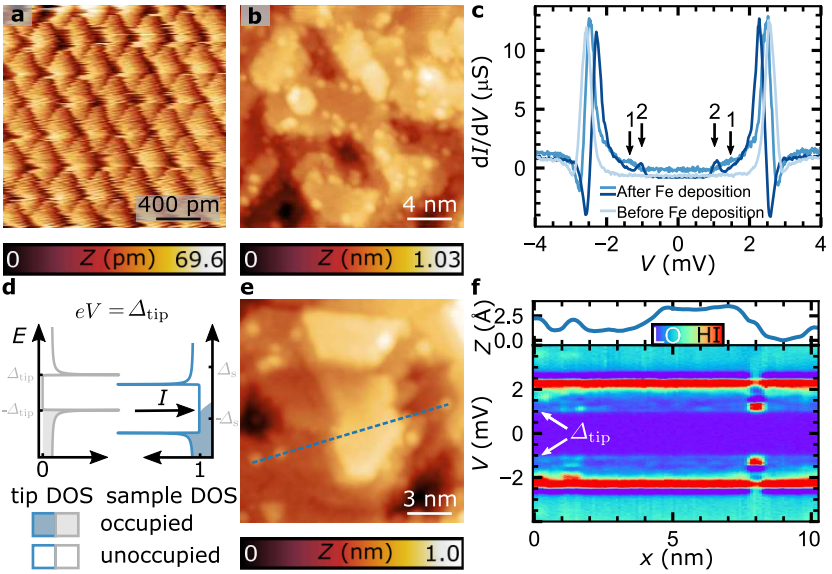

Figure 4.33.: a Manipulated atom image obtained with an Fe adatom on 10 ML of Ir on Nb(110) (see Figure 4.25). **b** Overview STM image of a sample consisting of 10 ML Ir on Nb(110) covered by statistically distributed Fe atoms. **c** Three $\mathrm{d}I/\mathrm{d}V$-spectra measured on the sample shown in **b**. The light blue curve was measured before the deposition of Fe atoms. The two darker curves were obtained afterwards. Black arrows mark the positions of Δ_{tip} in the $\mathrm{d}I/\mathrm{d}V$-spectra, which were obtained with microtips 1 and 2, as indicated by the labels. **d** Schematic illustration of the tunneling processes leading to the peaks at Δ_{tip} in **c**. **e** Overview STM image of the sample consisting of 10 ML Ir on Nb(110) covered by statistically distributed Fe atoms. The dashed blue line marks the position of the $\mathrm{d}I/\mathrm{d}V$-line profile shown in **f**. **f** The bottom (top) panel displays the $\mathrm{d}I/\mathrm{d}V$-line profile (Z profile). Measurement parameters: **a** $V_{\mathrm{bias}} = -3\,\mathrm{mV}$, $I = 200\,\mathrm{nA}$, **b** $V_{\mathrm{bias}} = 50\,\mathrm{mV}$, $I = 1\,\mathrm{nA}$, **c** $V_{\mathrm{stab}} = 4\,\mathrm{mV}$, $I_{\mathrm{stab}} = 1\,\mathrm{nA}$, $V_{\mathrm{mod}} = 20\,\mu\mathrm{V}$, **e** $V_{\mathrm{bias}} = -4\,\mathrm{mV}$, $I = 1\,\mathrm{nA}$ and **f** $V_{\mathrm{stab}} = -4\,\mathrm{mV}$, $I_{\mathrm{stab}} = 1\,\mathrm{nA}$, $V_{\mathrm{mod}} = 20\,\mu\mathrm{V}$.

adatom species, in this case Fe, at temperatures below $< 7\,\mathrm{K}$, which results in a statistical distribution of the adatoms. Two exemplary overview STM images are shown in Figures 4.33b and c. As illustrated by the manipulated atom image in Figure 4.33a, we find that STM tip-induced atom manipulation is easily possible. As the Ir film studied here has an Ir(111)-like surface structure, we find two stable adsorption sites. Following a similar line of argumentation as for Figure 4.32a, we conclude that there are nearly equally stable fcc and hcp adsorption sites for Fe adatoms on the hexagonal Ir films.

Two $\mathrm{d}I/\mathrm{d}V$-spectra obtained on the bare surface of the 10 ML Ir film on Nb(110) after the deposition of Fe atoms are shown in Figure 4.33c. These two $\mathrm{d}I/\mathrm{d}V$-spectra are very distinct from all other substrate spectra that were discussed in the course of this thesis and, in particular they differ from the previously obtained $\mathrm{d}I/\mathrm{d}V$-spectrum on the Ir films on Nb(110) prior to the deposition of Fe atoms (light blue in Figure 4.33c): While we observe regular coherence peaks at $\pm(\Delta_{\mathrm{tip}} + \Delta_{\mathrm{s}})$, we find that the $\mathrm{d}I/\mathrm{d}V$-signal does not sharply drop to zero inside of the superconducting gap region. It rather appears as if the coherence peaks are smeared out and as if the $\mathrm{d}I/\mathrm{d}V$-intensity approaches zero only very slowly. Right before the $\mathrm{d}I/\mathrm{d}V$-intensity would reach zero, we find additional peaks in the $\mathrm{d}I/\mathrm{d}V$-spectra. We mark them by black arrows and their labels indicate that the two $\mathrm{d}I/\mathrm{d}V$-spectra were obtained with two different microtips (labeled 1 and 2). From additional spectroscopic data we find that the energies of these peaks coincide with the energetic positions of one of the MARs, which indicates that they are located at Δ_{tip} or Δ_{s}.

Our measurement temperature of 320 mK allows us to rule out thermally activated tunneling processes as the origin for the additional peaks. Therefore, I conclude that either the tip or the sample DOS is non-zero at the Fermi level. In order to determine which of both scenarios is true, I display two $\mathrm{d}I/\mathrm{d}V$-spectra obtained with different microtips in Figure 4.33c. Since the low energy peak varies energetically between the two tips 1 and 2, I conclude that the sample DOS is non-zero at the Fermi

level: If the sample DOS is non-zero at the Fermi level, and we consider finite temperatures, tunneling may occur at $\pm\Delta_{\mathrm{tip}}$ (see Figure 4.33d). If the tip DOS was non-zero at the Fermi level on the other hand, we would expect peaks at $\pm\Delta_{\mathrm{s}}$. However, these peaks would be fixed in energy and would be independent of the microtip. Therefore, we can conclude that the DOS of the sample is non-zero at the Fermi level, which is evidently connected to the coverage of the Ir film with Fe adatoms.
To investigate if these peaks vanish if we move far away from any impurity, I perform $\mathrm{d}I/\mathrm{d}V$-line profiles as illustrated in Figures 4.33e and f. The dashed blue line indicates the location of the $\mathrm{d}I/\mathrm{d}V$-line profile shown in Figure 4.33f. The STM image shows that the left end of the line profile starts in close proximity to two Fe atoms but then moves onto an island without any impurities nearby. It is then terminated on an Fe adatom on the right-hand side.
The $\mathrm{d}I/\mathrm{d}V$-intensity of the peaks at $\pm\Delta_{\mathrm{tip}}$ is enhanced at the positions of the Fe atoms in Figure 4.33f. Additional broad in-gap states between $\pm\Delta_{\mathrm{tip}}$ and $\pm(\Delta_{\mathrm{tip}}+\Delta_{\mathrm{s}})$ are visible at those locations. However, the increase of the peaks' intensities (at $\pm\Delta_{\mathrm{tip}}$) appears very local. Within 1 nm distance from the impurities, the $\mathrm{d}I/\mathrm{d}V$-intensity of the peaks at $\pm\Delta_{\mathrm{tip}}$ drops down to a relatively constant value. Most importantly, this value is observed throughout the entire central region of the $\mathrm{d}I/\mathrm{d}V$-line profile. At no point of this $\mathrm{d}I/\mathrm{d}V$-line profile does the spectral intensity at the energy of this peak disappear nor is the superconducting gap considerably restored. Therefore, we find that the superconducting state of the proximitized Ir layer is already considerably quenched by this dilute coverage of Fe adatoms. Unfortunately, this renders the material platform hardly usable for studying Shiba chains.

4.5.6. Discussion & Conclusion

In conclusion, we grew thin films of Ir and Au on Nb(110) at various coverages and determined the structural properties layer-dependently in Subsections 4.5.1 and 4.5.2. We identify the coverages which have a structure that likely enables single atom experiments (Subsection 4.5.3) and we determine the proximity-induced superconductivity for both material platforms. We find fully pronounced hard superconducting gaps for all Au films that were investigated. Considering the 10 ML Ir film on Nb(110), we found a hard gap, whose size was slightly reduced compared to that of bare Nb(110) by 14.7 %. Thereby, we have identified two proximitized high-Z thin films which are promising for the realization of Shiba chains exposed to high SOC or strong DM interactions:

- a single pseudomorphic layer of Au on Nb(110), which yields a high degree of tunability for the Shiba band structure by choosing an appropriate crystal direction and interatomic spacing
- ten ML Ir films, which have a strained Ir(111)-like surface structure, which is well known to lead to large DM interaction in transition metal films deposited on top.

We study both of these interesting platforms in combination with single Fe adatoms.
To begin with, we find spatially anisotropic YSR states for Fe atoms on the first layer of Au on Nb(110). These YSR states enable us to tailor Fe chains along a certain crystal direction with a particular interatomic spacing, where it is likely that we realize a one-band system ($2a - [001]$). We perform a length-dependent study of this chain type and extract the Shiba band structure from the QPI of BdG quasiparticles. Indeed we find a single Shiba band crossing the Fermi level. However, the Shiba band is not gapped out around E_F by p-wave correlations, as one could have expected due to the high SOC of the substrate. Furthermore, chains of this

type are in a FM ground state. So far unpublished *ab initio* calculations (based on the method presented in Ref. [223]) indicate that the absence of a non-collinear magnetic ground state of the chains may be the limiting factor for the absence of a topological gap and MBS in this type of chains. Recent first-principles calculations of the magnetic interaction parameters in ultrathin film systems have demonstrated that the connection between the formation of a spin-spiral state and SOC is complicated. In particular, the DM interaction preferring a non-collinear spin alignment is typically weak when a 3*d* transition metal is deposited on a Au surface compared to other 5*d* substrates[293–295], which may be tentatively attributed to the fully occupied 5*d* band of Au having a reduced effect on the DM interaction. Proximity to a Au layer is known to give rise to strong Heisenberg exchange interactions and anisotropy[287] in the magnetic layer instead, both of which prefer a collinear spin alignment and the latter being induced by the SOC. Our results indicate that a strong SOC itself is not sufficient for inducing topological superconductivity, but its role may be more complex, similarly to the competition between DM interaction and anisotropy terms in the formation of non-collinear spin structures.

Considering these conclusions, the 10 ML Ir films on Nb(110) with a Ir(111)-like structure appear even more promising. However, we find that the superconducting gap of the proximitized Ir film is considerable changed when Fe adatoms are evaporated onto it. In particular, we observe that the gap is beginning to fill up and does not recover its original state, even if one moves away (> 5 nm) form single Fe adatoms. The exact origin of this effect is unknown so far. Recent theoretical calculations[296,297] and experimental results[298] suggest that Ir is a strong paramagnet, i.e. that it is close to fulfilling the Stoner criterion. Screened KKR calculations for a single Fe adatom on Ir(111) find that a finite magnetic moment is induced in the Ir atoms underneath the impurity. These moments are even observed if one moves multiple sites away from the impurity center[296]. Therefore, I speculate that a finite magnetic

moment could be induced in the topmost Ir layer by the statistically distributed Fe atoms, which would slightly fill up the superconducting gap. Unfortunately, the filling of the substrate's superconducting gap renders the platform useless for the construction of Shiba chains and for the realization of MBS.
Nevertheless, the growth of proximitized high-Z films on Nb(110) and the investigation of Shiba chains on such films can still be considered as a great success. The herein presented results prove that it is experimentally possible to grow heterostructures of a high-Z metal on a superconductor with a high T_c as a substrate for the deposition of transition metal atoms and to construct defect-free 1D structures in an excellent quality. In fact, the thin film and chain quality is so good that we even observe QPI of BdG quasiparticles, which has only been observed for Shiba chains constructed directly on single crystals so far. Therefore, our work opens a great perspective for the growth of other high-Z materials on Nb(110) as a substrate for Shiba chains, which can eventually lead to the realization of MBS in a hard topological gap.

5 Spin dynamics across a superconducting transition

The magnetization dynamics of AFM coupled spin chains positioned on a superconducting substrate are investigated in this chapter. The new aspect of this study is the possibility to switch the substrate between the SC state and the normal metal state, which drastically modifies the availability of substrate charge carriers at the Fermi level. The experimental results and the corresponding discussion are so far unpublished. An introduction to the basic theoretical framework of single atom magnetism and magnetic switching between two Néel states is given in Sections 2.1 and 2.3, respectively. The measurement method and the data analysis procedure are introduced in Subsection 3.1.4.

Contributions

The experiments presented in this chapter were carried out by Dr. Lucas Schneider and myself. The extraction of lifetimes and switching rates was performed using a group internal program. Self-written Python code and Gwyddion[248] were used for further analysis of the data and the presentation of data in figures.

5.1. Introduction

The underlying microscopic processes of magnetization dynamics and the time evolution of artificially prepared magnetic states are funda-

mental for potential future applications in the broad field of nanoscale spintronics[299,300] and are even more decisive for future applications which aim to prepare, manipulate and measure individual quantum states of spins on surfaces[301]. The STM has proven to be a powerful tool to investigate static magnetic properties of individual nanomagnets on surfaces with atomic resolution using SP-STM[48], giving it a lead over spatially averaging techniques such as X-ray magnetic circular dichroism (XMCD) measurements[302]. In the last decade, SP-STM has been further developed to gain access to the time domain and to spin dynamics. Breakthroughs were mainly achieved using the following three methods:
(I) From an experimental standpoint, telegraph noise switching was the first realized method which enabled the direct measurement of spin dynamics[49]. It relies solely on the effect of TMR[199] (see Subsection 3.1.3), which induces current changes if a nanomagnet switches its magnetization between two opposite spin states relative to the probe magnetization. Therefore, this technique is limited by the bandwidth of the transimpedance amplifier and typically enables a time resolution on the order of $> 1\,\mathrm{ms}$. After this method was pioneered on relatively large magnetic islands (approximately $5\,\mathrm{nm} \times 5\,\mathrm{nm}$) where it uncovered the role of spin-transfer torque, Joule heating, the Oersted field of tunneling electrons and temperature[49,50,303–305], the method was subsequently applied to artificially constructed clusters and chains with tailored properties on different substrates as metals and ultrathin decoupling layers[74,184,187,306,307].
(II) By employing a pump-probe scheme, in which a short pump pulse of spin-polarized electrons locally excites a nanomagnet and one subsequently detects the spin state with a probe pulse after a varying delay time Δt one can measure the temporal evolution of spin states. This method enables the measurement of dynamics at shorter times scales down to the nanosecond regime[51,308].
(III) Last, recent efforts have combined STM and electron spin resonance (ESR), where microwave radiation is guided into the tunnel junc-

tion in order to drive spin transitions of individual atoms and small dimers positioned on thin decoupling layers on metallic substrates, which can then be detected as resonances in the tunnel current[309–315].
One particularly interesting aspect for spin dynamics of a given spin chain is the role of the substrate's itinerant electron bath, to which the system is coupled. So far, research has focused on metallic surfaces covered by an ultra-thin decoupling layer (e.g. CuN on Cu(100)[184,316]) and bare metallic surfaces[306,307]. Therefore, the question arises how a superconducting substrate influences the spin dynamics of individual atoms, molecules and artificial structures. Inelastic scanning tunneling spectroscopy[317] is the only tool employed, so far, to address such material systems. These studies come to the conclusion that a superconducting substrate increases the lifetime of magnetic states and spin excitations due to the absence of substrate electrons that could spin-flip scatter with the spins[318–320].
Let us now consider AFM coupled spin chains, which are described by the model introduced in Section 2.3 and Refs. [64, 65]. In this model, external perturbations and scattering with substrate electrons are predicted to cause a decoherence of the quantum ground- and excited states, which lead to a bistability of the Néel states and quasiclassical switching between the two Néel states. In the absence of any substrate electrons or other influences leading to decoherence, the spin chain is expected to be in a pure quantum limit and, thus, in a superposition of the two quantum states.
In this section, we proceed to investigate the transition between those two limits by studying the switching behavior of artificially-constructed AFM coupled Mn $\sqrt{3}/2a$-$[1\bar{1}1]$ chains on Ta(110)[222] using the spin-state telegraph noise method. Since Ta(110) is a type-I SC, it has a sharp phase transition to the normal metal state once a critical field of $H_{\mathrm{C,Ta}} = 84\,\mathrm{mT}$[321] is exceeded, which enables us to study the switching behavior of the chains in the superconducting and in the normal metal phase of the substrate, i.e. without and with substrate electrons at the Fermi level,

respectively. Furthermore, we tune the influence of other perturbations by employing multiple types of STM tips: On the one hand, we employ Cr bulk tips with a Mn cluster at the tip apex which has a stray field. On the other hand, functionalized superconducting Nb tips are used, which screen magnetic fields and are expected to exhibit a low stray field as their spin contrast is generated by YSR states and not by a magnetized cluster. Thereby, we control the degree of perturbing B-fields that the spin chain is exposed to and have an additional parameter to hopefully switch between spin chains in the pure quantum case and the quasiclassical one.

5.2. Antiferromagnetic spin chains

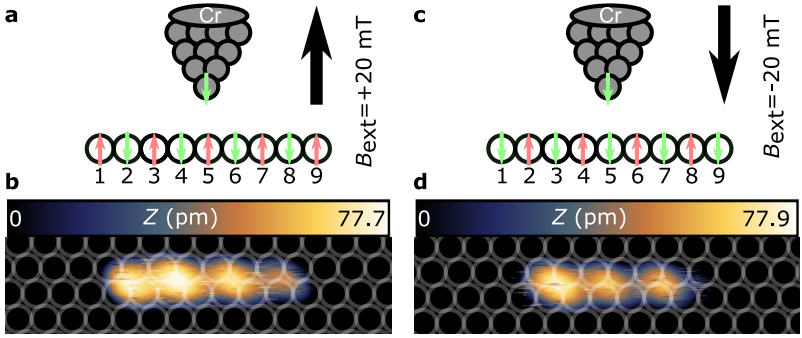

Figure 5.1.: a and **c** Illustrations of the STM tip including the magnetization of the apex, the externally applied out-of-plane magnetic field B_{ext} and the spin orientations of all atoms in the Mn_9 $\sqrt{3}/2a$-$[1\bar{1}1]$ chain, which were investigated in **b** and **d**. **b** and **d** STM images (4 nm × 1 nm) of a Mn_9 $\sqrt{3}/2a$-$[1\bar{1}1]$ chain on Ta(110), measured in an out-of-plane field of $+20$ mT and -20 mT, respectively. White circles mark the atomic positions of Ta atoms in the underlying layer. Note that the first and last atoms of the chain are not visible in the STM images due to the adjusted contrast. Measurement parameters: $V_{\mathrm{bias}} = 1$ mV, $I = 200$ pA. A Cr tip was used for all measurements.

To experimentally demonstrate the AFM ground state of $\sqrt{3}/2a$-$[1\bar{1}1]$ Mn chains on Ta(110), we perform SP-STM on such artificially constructed structures using a stable out-of-plane magnetized Cr bulk tip in the following. We prepared the tip by picking up several dozens of Mn atoms until a magnetically stable tip was achieved (demonstrated in Figures 5.1 and 5.4). Nevertheless, for the sake of simplicity, I will refer to the tip as a Cr bulk tip in the following unless the apex and its properties are relevant.

A sketch of the measurement set-up, including the assumed magnetization of the STM tip as well as of the atoms of a Mn_9 $\sqrt{3}/2a$-$[1\bar{1}1]$ chain, is shown in Figures 5.1a and c. From measurements with multiple different tips we find that the AFM coupled chains are typically in a state where their net magnetic moment is aligned with the external B-field, as illustrated in Figures 5.1a and c. This behavior is demonstrated by the SP-STM measurements presented in Figures 5.1b and d, which were performed with the aforementioned stable out-of-plane magnetized Cr bulk tip. Let us consider the first SP-STM measurement shown in Figures 5.1a and b: Without the loss of generality we assume that the tip apex atom is oriented antiparallel to the external magnetic field due to the magnetic field history of the tip. The SP-STM image in Figure 5.1b shows an alternating contrast modulation with four atomic sites that display an elevated height, and three with a reduced height.

Upon changing the B-field to $-20\,\mathrm{mT}$ (Figures 5.1c and d), which is too low to cause an inversion of the magnetic moment of the stable Cr tip, we are in a configuration in which three brighter and two darker atomic sites are visible in the SP-STM image shown in Figure 5.1d. These results are consistent with the sketches of the magnetization of the chain shown at the top of panels Figures 5.1a and d: For positive fields, atoms 3, 5, and 7 are magnetized antiparallel to the tip and appear darker while atoms 2, 4, 6, and 8 are magnetized parallel to the tip and appear brighter. For negative fields, the atoms 3, 5, and 7 are magnetized parallel to the tip and appear brighter while atoms 2, 4, 6, and 8 are magnetized antiparallel

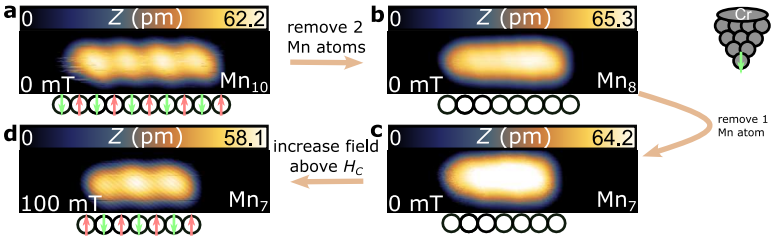

Figure 5.2.: **a-c** Series of STM images (4 nm × 1 nm) showing a $\sqrt{3}/2a$-$[1\bar{1}1]$ Mn chain, whose length is subsequently reduced from $N = 10$, over $N = 8$ to $N = 7$ by STM tip-induced atom manipulation. **d** In a last step, an out-of-plane field of $+100$ mT is applied. Black spheres and arrows located underneath each STM image indicate the atomic positions and the spin alignment deduced from the SP-STM images. Measurement parameters: $V_{\text{bias}} = 1$ mV, $I = 200$ pA. A Cr tip was used for all measurements.

to the tip and appear darker. Note, that the first and last atom of the chain have a lower apparent height compared to the bulk chain atoms. Hence, they are not visible in the adjusted contrast of Figure 5.1d. Presumably this is the reason why we only observe three bright atomic sites in the SP-STM image shown in Figure 5.1d, compared to the naively expected five sites. Additionally, it could be that the magnetizations of atoms 1 and 9 are canted with respect to the z-direction.

As already demonstrated throughout most experiments in Chapter 4, STM tip-induced atom manipulation is an incredibly powerful tool to study spin chains length-dependently. We can exploit this tool to investigate if there is a lower length limit, below which we no longer observe an AFM ground state in SP-STM measurements. We commence this investigation with an SP-STM image of an artificially constructed Mn_{10} $\sqrt{3}/2a$-$[1\bar{1}1]$ chain in zero magnetic field, which is displayed in Figure 5.2a. We find that the chain is in a stable AFM ground state which displays four maxima. Again, it should be noted that we observe a state with four maxima instead of the naively expected five maxima due to the different

apparent height of the edge atoms (or due to the canting of the edge atoms' magnetizations). Overall, it is interesting that we observe a stable AFM contrast for a spin chain with an even number of atoms at all. In principle, both antiferromagnetic configurations of the spins (↑↓↑↓) and (↓↑↓↑) are expected to be degenerate and neither of the states should be preferred. It could be, that a nearby magnetically stable FM cluster on the Ta(110) surface is coupled to the chain (e.g. via the RKKY interaction) and therefore stabilizes one of the two spin configurations. Additionally, one can not rule out that an influence of the tip magnetization breaks the degeneracy: Spin-torque or exchange interactions could favor one of the two states and, thereby, stabilize it.
As shown in Figures 5.2b and c, the chain length is sequentially reduced to Mn_8 and to Mn_7. Indeed, we no longer observe any contrast modulation along the chain in both of the STM images. We do, however, observe streaky features at the edges of the chain, which could be explained by a very fast magnetic switching (see Section 5.3). As the disappearance of contrast upon decreasing the chain length is a reversible process i.e. the magnetic contrast is recovered upon attaching three Mn atoms to the Mn_7 chain, we conclude that a tip change can't explain the absence of contrast on chains shorter than nine atoms. Additionally, if we increase the magnetic field to $+100\,\mathrm{mT}$, which is above the critical field of Ta(110) in this measurement configuration, we find a contrast modulation that is consistent with AFM order for the Mn_7 chain.

5.3. Magnetic switching of AFM chains

Careful readers of the previous section may have noticed that I avoided to discuss the streaky features in the SP-STM measurements of Figures 5.1b and d, as well as in Figures 5.2a and d. That is, because I will proceed to discuss them in-depth in this section. In particular, two STM images

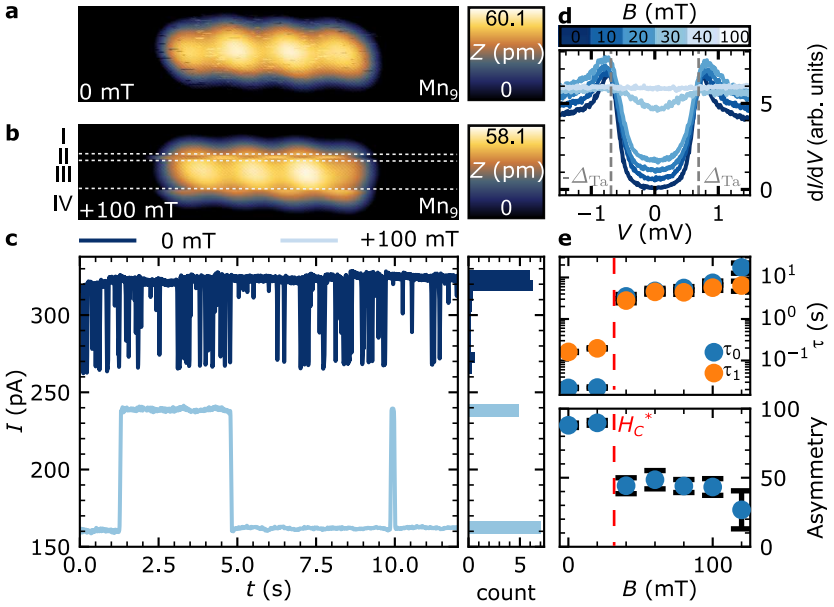

Figure 5.3.: **a** and **b** STM images of a Mn_9 $\sqrt{3}/2a$-$[1\bar{1}1]$ chain in an out-of-plane magnetic field of 0 mT and +100 mT, respectively. **c** Time traces recorded on the left end atom of the Mn_9 chain shown in **a** and **b**. The curve at 0 mT is offset by 100 pA for the sake of visibility. The right panel displays histograms of the full time traces of the cutouts shown in the left panel. **d** B-field-dependent $\mathrm{d}I/\mathrm{d}V$-spectra measured on the Ta(110) substrate. The spectra are offset by 0.5 arb. units for the sake of visibility. **e** Magnetic field-dependent lifetimes and asymmetries of the Mn_9 $\sqrt{3}/2a$-$[1\bar{1}1]$ chain displayed in **a** and **b**. The red vertical line marks the effective critical field H_C^* of Ta in this measurement series. Measurement parameters: **a-c** $V_{\mathrm{bias}} = 1\,\mathrm{mV}$, $I = 200\,\mathrm{pA}$, **d** $V_{\mathrm{stab}} = +1.5\,\mathrm{mV}$, $I_{\mathrm{stab}} = 2\,\mathrm{nA}$ and **e** $V_{\mathrm{stab}} = +2\,\mathrm{mV}$, $I_{\mathrm{stab}} = 200\,\mathrm{pA}$. A Cr tip was used for all measurements.

of a Mn_9 $\sqrt{3}/2a$-$[1\bar{1}1]$ chain in magnetic fields of 0 mT and +100 mT are shown in Figures 5.3a and b. Apart from the clear alternating contrast modulation with four (Figure 5.3a) and three (Figure 5.3b) maxima on top of the chains, that we have ascribed to AFM aligned spins in Section 5.2, we find similar streaky features as in the STM images mentioned before. However, the STM image shown in Figure 5.3b allows us to determine the origin of these streaks, as they are not only few pixels wide but even extend over multiple scanned lines.

It is instructive to separate the image into four sections where the chain appears differently in order to understand the effect: Those sections are marked by white dashed horizontal lines and are labeled on the left side of the panel. In regions I and III the contrast modulation on top of the chain has three maxima. Opposed to that, the alternating contrast is shifted by one site and displays four maxima in regions II and IV. Therefore, we interpret the streaky lines to be a result of magnetic switching of the chain from one Néel state to the other Néel state, which is characterized by an inversion of every spin in the chain.

To further evaluate the switching between the two Néel states, we position the STM tip over the leftmost atom of the Mn_9 chain and turn off the feedback loop at stabilization parameters of $V_{stab} = 1\,mV$ and $I_{stab} = 200\,pA$ (see Subsection 3.1.4 for details on the measurement procedure). We can then record time traces of the current channel. Two exemplary cutouts of such time traces are shown in Figure 5.3c. Apart from a slight noise contribution of $\sim 5\,pA$, we find that the current signal switches between two states in both curves, which corresponds to the chain being in one of the two Néel states: If the tip magnetization and the moment of the leftmost chain atom are parallel (antiparallel) the current signal is high (low). The observed current difference of the two alignments is on the order of 70 pA for both magnetic fields (slightly larger at +100 mT).

Apart from the fact that the current switches between two states, both time traces have very different characteristics: It is clearly visible that the

switching rate is much higher at 0 mT than at +100 mT. Furthermore, the lifetime of the low current state at 0 mT is very short compared to that of the high current state, while at +100 mT, the lifetimes of both states are not only much longer but also more evenly distributed between both of the Néel states. These findings are fully supported by histograms (Figure 5.3c, right panel) of the time traces which evaluate not only the cutout shown in the left panel, but include the entire measurement over a longer period of time.

To investigate if these changes occur continuously with an increasing magnetic field, we perform a B-field-dependent study in Figures 5.3d and e. To begin with, we measure $\mathrm{d}I/\mathrm{d}V$-spectra on the Ta(110) substrate field-dependently to obtain information on the electronic structure of the substrate. These $\mathrm{d}I/\mathrm{d}V$-spectra are shown in Figure 5.3d. It should be noted, that the spectra are offset by 0.5 arb. units for the sake of visibility. Taking this into account, we find that the four $\mathrm{d}I/\mathrm{d}V$-spectra measured at $B = 0$, 10, 20 and 30 mT all lie exactly on top of each other and display coherence peaks at the superconducting gap of tantalum $\Delta_{\mathrm{Ta}} = 690\,\mu\mathrm{eV}$. After increasing the B-field to 40 mT the $\mathrm{d}I/\mathrm{d}V$-spectrum is drastically altered. The superconducting gap of the substrate is no longer clearly visible, but only a very shallow dip around 0 mV remains. At 100 mT, the $\mathrm{d}I/\mathrm{d}V$-signal is almost constant in the measurement range, which indicates that tantalum is in the metallic phase. These finding are in line with the expected behavior of the type-I SC Ta, with the exception that the reference value of tantalum's critical field is 84 mT[321]. Therefore, we refer to the observed critical field as $H_{\mathrm{C}}^{*} = 40\,\mathrm{mT}$. It should be noted that this behavior is reproducible using a Cr bulk tip and that it is independent of the magnetic field's orientation.

Similar time traces as the ones shown in Figure 5.4c were obtained in 20 mT steps up to a magnetic field of +120 mT. We extract the lifetimes of both Néel states and their asymmetry according to the procedure described in Subsection 3.1.4. The extracted values are shown in Figure 5.3e as a function of the B-field. The qualitative description of the results,

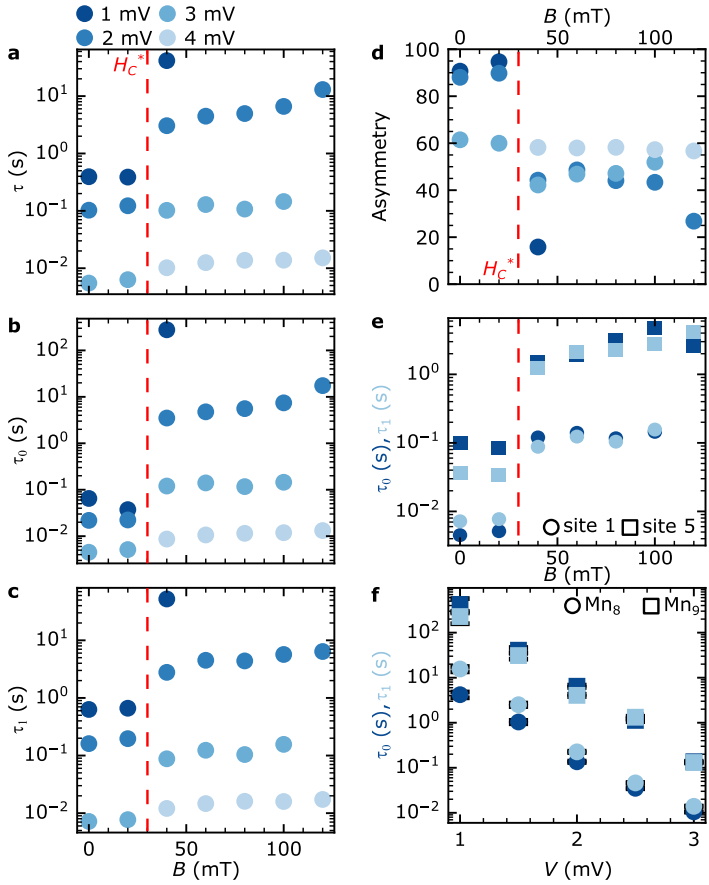

Figure 5.4.: a - d Magnetic field-dependent lifetimes τ, τ_0 and τ_1 and their asymmetries extracted for multiple stabilization biases. All measurements were performed on the same end atom of a Mn_9 $\sqrt{3}/2a$-$[1\bar{1}1]$ chain. The red vertical lines mark the effective critical field H_C^* of Ta in this measurement series. **e** B-field-dependent lifetimes ($V_{stab} = 3\,mV$) evaluated on two different sites of the Mn_9 chain discussed in **a-c**. **f** Bias-dependent lifetimes which were obtained on the left-most end atom of a Mn_8 and Mn_9 chain at a constant magnetic field of $+100\,mT$ and using the same micro-tip. Measurement parameters: Prior to all time traces, the tip was stabilized at $I_{stab} = 200\,pA$. A Cr tip was used for all measurements.

which I performed above, is confirmed by these values: As soon as the magnetic field is increased above H_C^*, the properties change abruptly and drastically. The lifetimes of both Néel states are increased by two orders of magnitude. Furthermore, the asymmetry changes across the superconducting transition of the substrate as well. Below the effective critical field H_C^* the lifetime of the Néel state "0" (τ_0) is more than one order of magnitude lower than that of the Néel state "1" (τ_1), which results in an asymmetry of $\sim$ 90 %. However, above the effective critical field, the asymmetry of both states is reduced below 50 %, which highlights that τ_0 is now slightly larger than τ_1.

In Figure 5.4, we proceed to investigate how the lifetimes of the Néel states and their asymmetry depend on other parameters such as the stabilization bias V_{stab}, the atomic site above which the STM tip is positioned and the chain length. To begin with, we find that an increase of V_{stab} reduces the lifetimes of both Néel states (Figures 5.4b and c) as well as their average lifetime τ (Figure 5.4a). This finding is equally true above H_C^* and below H_C^*. For example, note that the switching at 4 mV and 0 mT is too fast to be accurately measured in our set-up, while lifetimes on the order of $\sim$ 1 s are observed for 1 mV. Similarly, the average lifetimes for $V_{stab} = 1$ mV and 4 mV are four orders of magnitude apart at 40 mT, i.e. above H_C^*. This effect can be explained by the fact that the tunneling electrons have a higher energy with increasing bias voltage and are thus more likely to induce the spin flip to the other respective Néel state[307,322].

Overall, we find a similar sudden increase of the lifetimes for all stabilization biases once the B-field exceeds H_C^* and the SC of Ta is quenched, as we have observed for $V_{stab} = 2$ mV in Figure 5.3e. Additionally, the lifetimes increase exponentially once the critical field H_C^* is exceeded.

The previously discussed behavior of the Néel states' asymmetry across the superconductor-metal phase transition of the substrate is observed for all investigated bias voltages as shown in Figure 5.4d, i.e. it drops from a high value close to unity below H_C^* to nearly 50 % above H_C^*.

However, we do not observe a clear trend in the lifetime asymmetry at fields larger than H_C^*, which we attribute to the low B-field range in this measurement series and a correspondingly small Zeeman effect. As I will show later, larger magnetic fields favor the Néel state which has the net magnetic moment of the chain aligned with the field over the other Néel state (see Figure 5.5e). Moving to very high fields, this should yield a lifetime asymmetry close to one.

Apart from the previously discussed strong bias voltage dependence on the switching rate, we also uncover a pronounced relation of the lateral tip position and the Néel states' lifetimes. In Figure 5.4e, we display the extracted lifetimes of both Néel states τ_0 and τ_1 at $V_{\text{stab}} = 3\,\text{mV}$ while the tip was positioned over the left edge atom (site 1 — circles) and the middle atom (site 5 — squares). In the entire B-field range considered in this measurement series, we find that both lifetimes τ_0 and τ_1 are at least one order of magnitude larger on site 5, compared to site 1 at the same field strength. As we observe this effect of increased lifetimes at the chain's center in comparison to both ends of the chain and since it is independent of the actual micro-tip, we ascribe this effect to the switching mechanism between the two Néel states, and not only to an asymmetry of the tip.

An additional interesting feature of the measurement series in Figure 5.4e is the site-dependence of the lifetime asymmetry. From the color-coded lifetimes τ_0 (dark blue) and τ_1 (light blue) it is apparent that the asymmetries are inverted below the effective critical field H_C^*, i.e.: state '1' has a longer lifetime than state '0' if the measurement is performed on site 1, as opposed to site 5, where $\tau_0 > \tau_1$. Note that site 1 and site 5 have aligned spins for a given Néel state, which excludes the trivial explanation that τ_0 and τ_1 are linked to a different Néel state in each case.

Finally, we move on to investigate the effect of the chain length on the lifetimes. Bias voltage-dependent extracted lifetimes for a Mn_8 (circles) and a Mn_9 (squares) $\sqrt{3}/2a$-$[1\bar{1}1]$ chain obtained at a constant magnetic field of $+100\,\text{mT}$ are shown in Figure 5.4f. Besides the fact, that the

lifetimes τ_0 and τ_1 of both chains exponentially decrease with increasing bias voltages, it is apparent that the lifetimes are enhanced by more than one order of magnitude for the one atom longer Mn_9 chain compared to the Mn_8 chain, which is a well known effect from other studies of spin dynamics on AFM-coupled chains[184].

5.4. On the influence of the probe

To investigate the influence of the STM probe on the switching behavior, we performed a measurement series using a functionalized superconducting Nb tip. As described in Subsection 3.3.3, we picked up Mn atoms from the Ta(110) substrate, in order to achieve a spin-polarized tip. A SP-STM image of a Mn_{11} $\sqrt{3}/2a$-$[1\bar{1}1]$ chain measured at 0 mT is shown in Figure 5.5a. A small contrast-modulation with a period of $\sim$ 500 pm is visible on top of the chain and is in good agreement with the measurements which we performed with a Cr bulk tip (cf. Figure 5.3a). Therefore, we interpret this height modulation as AFM contrast resulting from spin-polarized tunneling. One minor difference between the two measurements with different tips is the lower amplitude of the contrast modulation which is approximately one order of magnitude smaller than with the Cr tip.
A striking difference, however, is the absence of any streaky lines, which would indicate the presence of magnetic switching and which is clearly visible using a Cr bulk tip (cf. Figure 5.3a). In fact, we do not observe any indications for magnetic switching at all, as long as the Ta(110) substrate is in the superconducting phase. This is apparent from the light blue time trace in Figure 5.5c, which was obtained with $V_{\mathrm{stab}} = 3$ mV at 0 mT, and from the histogram illustrating the current distribution, which only shows a single centered broad peak.
We proceed to perform B-field dependent measurements as we did in

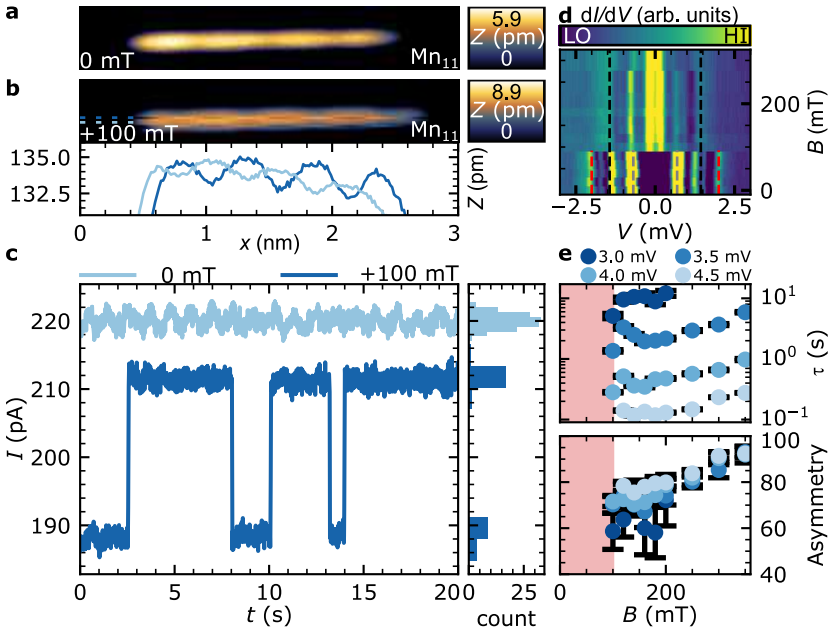

Figure 5.5.: **a** and **b** STM images (3 nm × 500 pm) of a Mn_{11} $\sqrt{3}/2a$-$[1\bar{1}1]$ chain in an out-of-plane magnetic field of 0 mT and +100 mT, respectively. The bottom panel in **b** displays two line profiles, which were extracted at the vertical positions indicated by two color-coded dashed horizontal lines. **c** Time traces recorded on the left end atom of the Mn_{11} chain shown in **a** and **b**. The right panel displays histograms of the full time traces of the cutouts shown in the left panel. **d** B-field-dependent $\mathrm{d}I/\mathrm{d}V$-spectra measured on the Ta(110) substrate. Dashed vertical lines indicate the superconducting gap of Ta $\Delta_{\mathrm{Ta}} = \pm 0.69$ meV (gray), the superconducting gap of the Nb tip $\Delta_{\mathrm{Nb}} = \pm 1.31$ meV (black) and the sum of both $\pm(\Delta_{\mathrm{Ta}} + \Delta_{\mathrm{Nb}}) = 2.00$ meV (red). **e** Magnetic field-dependent lifetimes and asymmetries of the Mn_{11} $\sqrt{3}/2a$-$[1\bar{1}1]$ chain displayed in **a** and **b**. The red shaded area marks the magnetic field region where no switching is observed. Measurement parameters: **a-c** $V_{\mathrm{bias}} = 3$ mV, $I = 200$ pA, **d** $V_{\mathrm{stab}} = +4$ mV, $I_{\mathrm{stab}} = 1$ nA and **e** $I_{\mathrm{stab}} = 200$ pA. A functionalized Nb tip was used for all measurements.

Section 5.3. To begin with, $\mathrm{d}I/\mathrm{d}V$-spectra taken with the functionalized tip on the Ta(110) are shown in Figure 5.5d as a function of the external field. The overall shape of the spectra is more complex than in Figure 5.3d, due to the use of a SC tip with a magnetic apex. In the range of 0 mT to 100 mT we observe four pairs of maxima in the $\mathrm{d}I/\mathrm{d}V$-spectra. The outermost peaks are the coherence peaks at $\pm(\Delta_{\mathrm{Ta}} + \Delta_{\mathrm{Nb}}) = 2.00\,\mathrm{meV}$, which are marked by the red dashed lines. Additionally we observe three pairs of YSR states at $\pm 1.71\,\mathrm{meV}$, $\pm 1.40\,\mathrm{meV}$ and $\pm 0.19\,\mathrm{meV}$. Since the Ta substrate has a clean SC gap, we do not observe any peaks in between $\Delta_{\mathrm{Ta}} = \pm 0.69\,\mathrm{meV}$. This area is marked by the gray dashed lines.
Once we exceed a B-field of 100 mT, the $\mathrm{d}I/\mathrm{d}V$-spectra change considerably: First of all, the coherence peaks $\pm(\Delta_{\mathrm{Ta}} + \Delta_{\mathrm{Nb}})$ vanish. The highest energy peak is now found at $\Delta_{\mathrm{Nb}} = \pm 1.31\,\mathrm{meV}$, as marked by the black line. Therefore, we conclude that the SC is quenched in the Ta(110) substrate and we now obtain a critical field of $H_{\mathrm{C}} = 100\,\mathrm{mT}$ that is in good agreement with reference values. Note that the coherence peaks are no longer extremely sharp and high in $\mathrm{d}I/\mathrm{d}V$-intensity, as we are now in a N/S tunneling geometry. Apart from the coherence peaks we still observe three pairs of YSR states (the highest energy one is faint) at energies, that are decreased by $\Delta_{\mathrm{Ta}} = 0.69\,\mathrm{meV}$ with respect to the $\mathrm{d}I/\mathrm{d}V$-spectra taken at $B < 100\,\mathrm{mT}$. At B-fields larger than 100 mT the $\mathrm{d}I/\mathrm{d}V$-spectra only change slightly due to external parameters such as, e.g., additional noise at higher fields. The tip remains superconducting in the entire measurement range due to finite size effects.
Returning to the switching behavior of the chains, we find that it is drastically changed, once the superconductivity is quenched in the Ta(110) substrate. A STM image obtained at $+100\,\mathrm{mT}$ is shown in Figure 5.5b, alongside with two color-coded height profiles in the panel below. The height profiles indicate that the chain has switched between the two AFM Néel states in between the measurement of the two lines. The occurrence of magnetic switching is further clarified by the time trace shown in Figure 5.5c.

The B-field dependence of the lifetimes and their asymmetry are shown in Figure 5.5e. The red shaded regions indicate that we don't observe any magnetic switching in the field range $B_{\mathrm{ext}} < H_{\mathrm{C}}$. In the normal metal state of Ta(110), however, we do observe switching in the investigated bias range. After a short decrease of the lifetimes in the B-field range of $100\,\mathrm{mT} - 180\,\mathrm{mT}$, they increase exponentially. Furthermore, we find that the asymmetry of the lifetimes increases nearly linearly and approaches unity for high magnetic fields.
Another interesting series of experiments is shown in Figure 5.6. After performing a B-field sweep and after subsequently ramping the magnet to 0 mT we prepare a superconducting tip which has a trapped magnetic flux (indicated by red currents and the B-field vector in Figure 5.6a). This is an effect of the hysteresis loop of type-II superconductors. If one applies the Bean model to a cylindrical SC wire one obtains an average remanent magnetization of $\langle M \rangle = -J_C^{\mathrm{Bean}} R/3$ at zero field, where J_C^{Bean} is the material specific critical current density and R is the cylinder radius of the wire[114]. After heating the STM to 7 K and subsequently cooling it down to 300 mK we reset the sample into the virgin SC state, while the Nb tip retains the trapped magnetic flux. This way, we can artificially induce a larger tip stray field.
Experimental proof for the success of this procedure is shown in Figure 5.6c, where B-field-dependent $\mathrm{d}I/\mathrm{d}V$-spectra of the substrate are plotted. Comparing this plot to the previous one obtained with the same tip in the virgin SC state (cf. Figure 5.5d), one observes a striking difference. All in-gap features continuously shift to higher energies if the $|B|$-field is increased. For example the coherence peaks at $\pm(\Delta_{\mathrm{Ta}} + \Delta_{\mathrm{Nb}})$ shift from $\pm 1.85\,\mathrm{meV}$ at 0 mT to $\pm 2.00\,\mathrm{meV}$ at $-100\,\mathrm{mT}$. At a magnetic field of $-120\,\mathrm{mT}$ the SC of Ta is quenched. The observed behavior is only explainable by the aforementioned trapped flux in the SC tip at zero field, which is subsequently compensated by the external field, up to a value of $-100\,\mathrm{mT}$. This subsequent compensation gives rise to an increasing gap $\pm\Delta_{\mathrm{Nb}}$ for an increasing $|B|$-field.

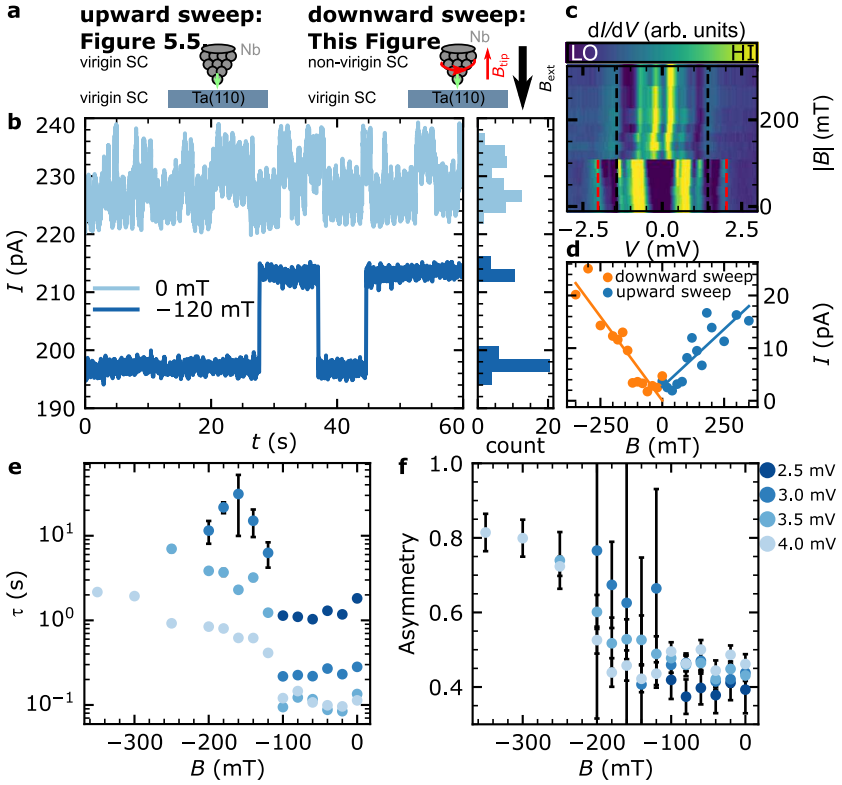

Figure 5.6.: a Illustration of the magnetic field history of the STM tip. After an upward sweep of the magnetic field (as in Figure 5.5), it was ramped down to approximately 0 mT. The STM was heated to 7 K, in order to reset the sample into the virgin SC state. However, the tip maintains some trapped flux and is not reset to the virgin state at this temperature. Such a tip is used for the following measurements. **b** Time traces recorded on the left end atom of a Mn_{11} chain at two exemplary magnetic fields. The right panel displays histograms of the full time traces of the cutouts shown in the left panel. **c** B-field-dependent dI/dV-spectra measured on the Ta(110) substrate. **d** Magnetic field-dependent evaluation of the magnetic contrast-modulation caused by the AFM order of a Mn_{11} $\sqrt{3}/2a$-$[1\bar{1}1]$ chain, which was extracted from constant-height current maps. **e** and **f** Magnetic field-dependent lifetime and lifetime asymmetry of the Mn_{11} $\sqrt{3}/2a$-$[1\bar{1}1]$ chain discussed in **b**. Measurement parameters: **a-c** $V_{bias} = 3\,mV$, $I = 200\,pA$, **d** $V_{stab} = +4\,mV$, $I_{stab} = 1\,nA$ and **e** $I_{stab} = 200\,pA$. A functionalized Nb tip was used for all measurements.

As apparent from the time traces and their histograms in Figure 5.6b, magnetic switching is obviously observed for fields of 0 mT and −120 mT. The average lifetime and the lifetime asymmetry are shown in Figures 5.6e and f. Qualitatively, we observe the same behavior as we did for the Cr tip in Figures 5.3 and 5.4, besides the fact that the average lifetime is increased, due to the two additional atoms of the Mn_{11} chain compared to the Mn_9 chain in Section 5.3.

5.5. Discussion & Conclusion

The most intriguing properties of the spin chains that we have uncovered in the previous sections are: (I) the abrupt change of the lifetimes of Néel states and their asymmetry across the superconducting transition of the substrate, (II) the fact that the lifetimes are shorter in the SC state of the substrate than in the normal metal phase, even though scattering with quasiparticles from the substrate should be suppressed in the former case, and (III) the absence of switching in the measurement series performed with a virgin-state SC tip.
In the following I will discuss these findings using the model introduced in Section 2.3. To begin with, we found that there is a lower chain length limit of $N = 9$, below which we do not observe any spin contrast at zero magnetic field (even though the tip is spin-polarized). However, if the substrate is in the normal metal state, AFM contrast is recovered. In Ref. [64] critical chain lengths below which the spin chain is in the quantum limit are calculated for Fe on CuN/Cu(001). Considering this particular system, spin chains are in the quantum limit for $N \leq 4$ at a measurement temperature of 300 mK. However, we expect to have a drastically decreased Γ (Equation 2.36), as there are no substrate electrons at the Fermi level of a SC (see Equation 2.23 and Figure 2.3b). Therefore, we expect that this critical chain length is increased for our material system,

as long as the substrate is in the SC state. Once we quench this state and the spin chain is coupled to a normal metal bath of itinerant substrate electrons, which are expected to stabilize the Néel states by decoherence, we observe AFM contrast again.

Points I and II are also explainable in the framework of this theory. Naively thinking, one would expect that the absence of scattering charge carriers should increase the spin lifetimes and the lifetime of magnetic states, as demonstrated in Refs. [318, 319]. However, AFM coupled spin chains are an exception. Here, the lifetime is given by Equation 2.35, which can be converted to $\tau \propto \Gamma/2V^2 \propto NT_{\mathrm{atom}}(E_{\mathrm{F}})/2V^2$. In the SC case, where $NT_{\mathrm{atom}}(E_{\mathrm{F}})$ approaches zero, lifetimes are low. In the normal metal state of the substrate, this term increases and, therefore, the lifetimes increase as well. Note, that the spin chains measured with a Cr bulk tip and a large Mn cluster at the apex in Figures 5.3 and 5.4 at $B_{\mathrm{ext}} \leq H_{\mathrm{C}}^{*}$ are not in the quantum limit. Presumably, this is caused by a significant stray field of the tip and by the fact that the spin chain is not screened from external fields, which energetically separates the two Néel states and therefore reduces their coupling V.

In order to explain the observations of point III, I will begin to exclude two possible trivial explanations for the observed behavior, one being that the spin-polarization of the tip might be too low to observe switching in Figure 5.5 and the other being that the stabilization biases are too high if a SC tip is employed.

An analysis of the contrast-modulation in SP-STM images (constant height mode) for both measurement series performed with a superconducting tip is shown in Figure 5.6d. It is apparent, that the observed SP-STM contrast is equal in strength for both sweeps. Since spin-switching telegraph noise was clearly observed in the second measurement series (Figure 5.6) with the same level of spin contrast, we can exclude a lack of spin-contrast to be the origin of the absence of switching in Figure 5.5.

One could also argue that the absence of switching in Figure 5.5 is

related to a characteristic of SIS tunnel junctions, that all features are shifted to higher bias voltages by Δ_{tip}. This leads to coherence peaks at $\pm(\Delta_{\mathrm{Ta}} + \Delta_{\mathrm{Nb}}) = 2.00\,\mathrm{meV}$, which are separated from one another by a gap (see Figure 5.5d). Due to this gap, we only performed measurements at bias voltages sufficiently larger than $\pm(\Delta_{\mathrm{Ta}} + \Delta_{\mathrm{Nb}}) = 2.00\,\mathrm{mV}$ in order to reliably stabilize the tip. As the expected lifetimes in this bias voltage range (see Figures 5.4a-c) are at the lower limit of lifetimes that can be detected experimentally, it could be that the switching is too fast to be observed at the accessible biases. However, if we recall the lifetime of $\tau \approx 10\,\mathrm{s}$ that we obtain at $+100\,\mathrm{mT}$ and $V_{\mathrm{stab}} = 3\,\mathrm{mV}$ (Figure 5.5e) and we use the information from the investigation with a Cr tip (Figures 5.4a-c), where we found that the lifetimes are decreased by approximately two orders of magnitude upon entering the superconducting state, one would expect to be in a regime where magnetic switching lifetimes are well within the observable time scale for 3 mV, even below H_{C}. Therefore, we can exclude that this effect is only caused by the high stabilization biases. Therefore, we explain the absence of switching in the measurement series with a virgin-state superconducting tip by the assumption, that the spin chain is no longer in a quasi-classical limit but its rather in the quantum limit: The SC tip in a virgin state locally screens perturbing magnetic fields and has a low stray field on its own. Therefore, we argue that the spin chain is decoupled from its environment as far as possible, where the only external influence is caused by the tunneling electrons. The fact that we still obtain slight AFM contrast below the critical magnetic field (see Figure 5.5a) could be explained by a minor stray field of the tip, which causes a slight asymmetry between both spin states that can be detected by time averaging SP-STM measurements.

Overall, the spin dynamics of AFM coupled chains on superconducting substrates are highly interesting. In contrast to common believe, the absence of quasiparticles at the Fermi level does not lead to a stabilization of the spins. We rather find that the dynamics is too fast to be observed with random telegraph switching if external influences are screened (e.g.

by a superconducting tip) considering the case of AFM coupled spin chains. However, if we expose the spin chain to local B-fields, either using a non-virgin state SC tip or a bulk Cr tip with a Mn apex we observe enhanced lifetimes, which we explain by a decoherence of the chain's quantum states.

In conclusion, our results motivate a theoretical study of single Mn adatoms and $\sqrt{3}/2a$-$[1\bar{1}1]$ chains on Ta(110): To begin with, *ab initio* calculations to determine the magnetic moment of a Mn adatom, the direction- and distance-dependent exchange couplings (direct and RKKY), as well as the DM interaction and magnetic anisotropy energy (MAE) would be highly useful as input parameters for a spin Hamiltonian. This Hamiltonian could be used to set up a Master equation to determine the spin dynamics of the AFM coupled chains in the normal metal state of the substrate. Additionally, one could extend the model of Ref. [64] to superconductors and check if our interpretation of the results is confirmed by the theory. Furthermore, it would be interesting to investigate the role of YSR states on the spin dynamics of $\sqrt{3}/2a$-$[1\bar{1}1]$ coupled Mn chains, which we neglect in our discussion so far.

Additionally, a position-dependent investigation of the lifetimes in combination with theoretical modeling of the system could be a powerful tool to learn something about the dynamics of the actual switching process, which is not accessible in regular random telegraph switching measurements due to the limits set by the bandwidth of the transimpedance amplifier (1 kHz) and the time scale of the actual switching process ($\sim$ ps). The strong dependence of the switching rate on the lateral position of the STM tip in our measurements could indicate that spin waves drive the switching between both Néel states[187].

From the experimental side, it would be highly interesting to further investigate the set-up in which the spin chain is in the quantum limit (Figure 5.5). Using a pulsed pump-probe scheme or by employing ESR-STM one could attempt to initialize the spin chain in one of the quantum states and subsequently attempt to measure the Rabi oscillations between both

Néel states. Ultimately, if pulsed ESR schemes allow a precise control and readout of the spin state, one could design a novel type of qubit.

Extended Data

A

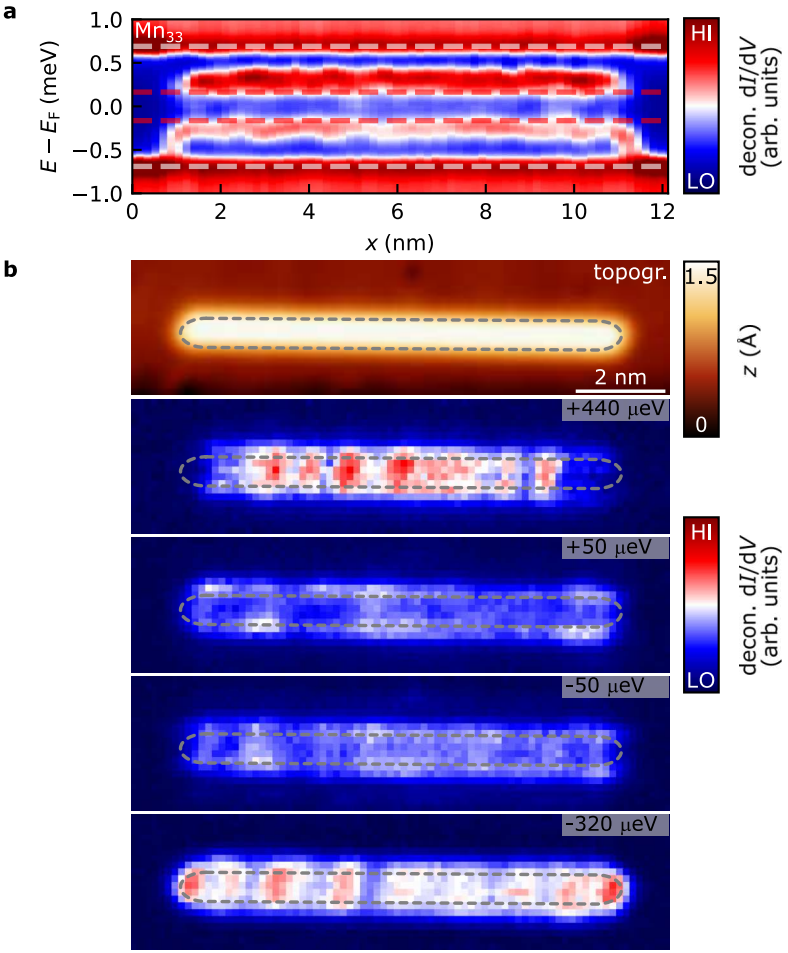

Figure A.1.: a $\mathrm{d}I/\mathrm{d}V$-line profile measured along the longitudinal axis of a Mn_{33} $1a - [001]$ chain on Ta(110). Red dashed horizontal lines indicate the edges of the minigap. **b** STM image and $\mathrm{d}I/\mathrm{d}V$-grid of a Mn_{33} chain evaluated at energy slices indicated in every panel's top right corner. Gray dashed lines mark the spatial extent of the chain. Measurement parameters: $V_{\mathrm{stab}} = -2.5\,\mathrm{mV}$, $I_{\mathrm{stab}} = 1\,\mathrm{nA}$ and $V_{\mathrm{mod}} = 20\,\mu\mathrm{V}$.

Bibliography

[1] *Top 500 supercomputers ranked by their performance on the LINPACK Benchmark*, URL: https://www.top500.org/lists/top500/list/2022/06/ (accessed on 16.6.2022), cited on page(s): 1.

[2] L. Wang and S. U. Khan, *Review of performance metrics for green data centers: a taxonomy study*. The Journal of Supercomputing **63**, 639–656 (2013), cited on page(s): 1.

[3] *Report to Congress on Server and Data Center Energy Efficiency Public Law 109-431*, URL: https://www.energystar.gov/ia/partners/prod_development/downloads/EPA_Datacenter_Report_Congress_Final1.pdf (accessed on 13.6.2022), cited on page(s): 1.

[4] I. Žutić, J. Fabian, and S. Das Sarma, *Spintronics: Fundamentals and applications*. Reviews of Modern Physics **76**, 323–410 (2004), cited on page(s): 1.

[5] T. D. Ladd, F. Jelezko, R. Laflamme, Y. Nakamura, C. Monroe, and J. L. O'Brien, *Quantum computers*. Nature **464**, 45–53 (2010), cited on page(s): 1.

[6] I. Buluta and F. Nori, *Quantum Simulators*. Science **326**, 108–111 (2009), cited on page(s): 1.

[7] F. Arute, K. Arya, R. Babbush, D. Bacon, J. C. Bardin, R. Barends, R. Biswas, S. Boixo, F. G. S. L. Brandao, D. A. Buell, B. Burkett, Y. Chen, Z. Chen, B. Chiaro, R. Collins, W. Courtney, A. Dunsworth, E. Farhi, B. Foxen, A. Fowler, C. Gidney, M. Giustina, R. Graff, K. Guerin, S. Habegger, M. P. Harrigan, M. J. Hartmann, A. Ho, M. Hoffmann, T. Huang, T. S. Humble, S. V. Isakov, E. Jeffrey, Z. Jiang, D. Kafri, K. Kechedzhi, J. Kelly, P. V. Klimov, S. Knysh, A. Korotkov, F. Kostritsa, D. Landhuis, M. Lindmark, E. Lucero, D. Lyakh, S. Mandrà, J. R. McClean, M. McEwen, A. Megrant, X. Mi, K. Michielsen, M. Mohseni, J. Mutus, O. Naaman, M. Neeley, C. Neill, M. Y. Niu, E. Ostby, A. Petukhov, J. C. Platt, C. Quintana, E. G. Rieffel, P. Roushan, N. C. Rubin, D. Sank, K. J. Satzinger, V.

Smelyanskiy, K. J. Sung, M. D. Trevithick, A. Vainsencher, B. Villalonga, T. White, Z. J. Yao, P. Yeh, A. Zalcman, H. Neven, and J. M. Martinis, *Quantum supremacy using a programmable superconducting processor*. Nature **574**, 505–510 (2019), cited on page(s): 1.

[8] A. Kitaev, *Fault-tolerant quantum computation by anyons*. Annals of Physics **303**, 2–30 (2003), cited on page(s): 1, 2, 33.

[9] R. LaPierre, *Topological Quantum Computing*, *Introduction to Quantum Computing*, chap. 26, 347–357, Springer (2021), cited on page(s): 1.

[10] *The Nobel Prize in Physics 2016*, URL: `https://www.nobelprize.org/prizes/physics/2016/summary/` (accessed on 9.6.2022), cited on page(s): 1.

[11] M. El-Batanouny, *Advanced Quantum Condensed Matter Physics: One-Body, Many-Body, and Topological Perspectives*, Cambridge University Press (2020), cited on page(s): 1, 15, 17.

[12] B. A. Bernevig, T. L. Hughes, and S.-C. Zhang, *Quantum Spin Hall Effect and Topological Phase Transition in HgTe Quantum Wells*. Science **314**, 1757–1761 (2006), cited on page(s): 2.

[13] M. König, S. Wiedmann, C. Brüne, A. Roth, H. Buhmann, L. W. Molenkamp, X.-L. Qi, and S.-C. Zhang, *Quantum Spin Hall Insulator State in HgTe Quantum Wells*. Science **318**, 766–770 (2007), cited on page(s): 2.

[14] C. Brüne, C. X. Liu, E. G. Novik, E. M. Hankiewicz, H. Buhmann, Y. L. Chen, X. L. Qi, Z. X. Shen, S. C. Zhang, and L. W. Molenkamp, *Quantum Hall Effect from the Topological Surface States of Strained Bulk HgTe*. Physical Review Letters **106**, 126803 (2011), cited on page(s): 2.

[15] C. Beenakker, *Search for Majorana fermions in superconductors*. Annual Review of Condensed Matter Physics **4**, 113–136 (2013), cited on page(s): 2, 34.

[16] F. von Oppen, Y. Peng, and F. Pientka, *Topological superconducting phases in one dimension*. Topological Aspects of Condensed Matter Physics, École de Physique des Houches , 387–447 (2015), cited on page(s): 2, 34, 36.

[17] L. Fu and C. L. Kane, *Superconducting Proximity Effect and Majorana Fermions at the Surface of a Topological Insulator*. Physical Review Letters **100**, 096407 (2008), cited on page(s): 2, 34.

[18] L. Fu and C. L. Kane, *Josephson current and noise at a superconductor/quantum-spin-Hall-insulator/superconductor junction*. Physical Review B **79**, 161408 (2009), cited on page(s): 2, 34.

[19] T. D. Stanescu, J. D. Sau, R. M. Lutchyn, and S. Das Sarma, *Proximity effect at the superconductor–topological insulator interface*. Physical Review B **81**, 241310 (2010), cited on page(s): 2, 34.

[20] H.-H. Sun, K.-W. Zhang, L.-H. Hu, C. Li, G.-Y. Wang, H.-Y. Ma, Z.-A. Xu, C.-L. Gao, D.-D. Guan, Y.-Y. Li, C. Liu, D. Qian, Y. Zhou, L. Fu, S.-C. Li, F.-C. Zhang, and J.-F. Jia, *Majorana Zero Mode Detected with Spin Selective Andreev Reflection in the Vortex of a Topological Superconductor*. Physical Review Letters **116**, 257003 (2016), cited on page(s): 2, 34.

[21] P. Zhang, K. Yaji, T. Hashimoto, Y. Ota, T. Kondo, K. Okazaki, Z. Wang, J. Wen, G. D. Gu, H. Ding, and S. Shin, *Observation of topological superconductivity on the surface of an iron-based superconductor*. Science **360**, 182–186 (2018), cited on page(s): 2, 35.

[22] D. Wang, L. Kong, P. Fan, H. Chen, S. Zhu, W. Liu, L. Cao, Y. Sun, S. Du, J. Schneeloch, R. Zhong, G. Gu, L. Fu, H. Ding, and H.-J. Gao, *Evidence for Majorana bound states in an iron-based superconductor*. Science **362**, 333–335 (2018), cited on page(s): 2, 35.

[23] G. Li, S. Zhu, D. Wang, Y. Wang, and H.-J. Gao, *Recent progress of scanning tunneling microscopy/spectroscopy study of Majorana bound states in the* $FeTe_{0.55}Se_{0.45}$ *superconductor*. Superconductor Science and Technology **34**, 073001 (2021), cited on page(s): 2, 35.

[24] D. Wang, R. Zhong, G. Gu, and R. Wiesendanger, *Surface orbital order and chemical potential inhomogeneity of the iron-based superconductor* $FeTe_{0.55}Se_{0.45}$ *investigated with special STM tips*. Physical Reviews Research **3**, L032055 (2021), cited on page(s): 2, 3, 35.

[25] J. D. Sau, R. M. Lutchyn, S. Tewari, and S. Das Sarma, *Generic New Platform for Topological Quantum Computation Using Semiconductor Heterostructures*. Physical Review Letters **104**, 040502 (2010), cited on page(s): 2, 35.

[26] R. M. Lutchyn, J. D. Sau, and S. Das Sarma, *Majorana Fermions and a Topological Phase Transition in Semiconductor-Superconductor Heterostructures*. Physical Review Letters **105**, 077001 (2010), cited on page(s): 2, 35.

[27] V. Mourik, K. Zuo, S. M. Frolov, S. R. Plissard, E. P. A. M. Bakkers, and L. P. Kouwenhoven, *Signatures of Majorana Fermions in Hybrid Superconductor-Semiconductor Nanowire Devices*. Science **336**, 1003–1007 (2012), cited on page(s): 2, 35.

[28] S. Gazibegovic, D. Car, H. Zhang, S. C. Balk, J. A. Logan, M. W. A. de Moor, M. C. Cassidy, R. Schmits, D. Xu, G. Wang, P. Krogstrup, R. L. M. O. het Veld, K. Zuo, Y. Vos, J. Shen, D. Bouman, B. Shojaei, D. Pennachio, J. S. Lee, P. J. van Veldhoven, S. Koelling, M. A. Verheijen, L. P. Kouwenhoven, C. J. Palmstrøm, and E. P. A. M. Bakkers, *Epitaxy of advanced nanowire quantum devices*. Nature **548**, 434–438 (2017), cited on page(s): 2, 35.

[29] W. Chang, S. M. Albrecht, T. S. Jespersen, F. Kuemmeth, P. Krogstrup, J. Nygård, and C. M. Marcus, *Hard gap in epitaxial semiconductor—superconductor nanowires*. Nature Nanotechnology **10**, 232–236 (2015), cited on page(s): 2, 35.

[30] S. M. Albrecht, A. P. Higginbotham, M. Madsen, F. Kuemmeth, T. S. Jespersen, J. Nygård, P. Krogstrup, and C. M. Marcus, *Exponential protection of zero modes in Majorana islands*. Nature **531**, 206–209 (2016), cited on page(s): 2.

[31] M. T. Deng, S. Vaitiekėnas, E. B. Hansen, J. Danon, M. Leijnse, K. Flensberg, J. Nygård, P. Krogstrup, and C. M. Marcus, *Majorana bound state in a coupled quantum-dot hybrid-nanowire system*. Science **354**, 1557–1562 (2016), cited on page(s): 2, 35.

[32] Y. Oreg, G. Refael, and F. von Oppen, *Helical Liquids and Majorana Bound States in Quantum Wires*. Physical Review Letters **105**, 177002 (2010), cited on page(s): 2.

[33] T.-P. Choy, J. M. Edge, A. R. Akhmerov, and C. W. J. Beenakker, *Majorana fermions emerging from magnetic nanoparticles on a superconductor without spin-orbit coupling*. Physical Review B **84**, 195442 (2011), cited on page(s): 2.

[34] F. Pientka, L. I. Glazman, and F. von Oppen, *Topological superconducting phase in helical Shiba chains*. Physical Review B **88**, 155420 (2013), cited on page(s): 2.

[35] J. Klinovaja, P. Stano, A. Yazdani, and D. Loss, *Topological Superconductivity and Majorana Fermions in RKKY Systems*. Physical Review Letters **111**, 186805 (2013), cited on page(s): 2, 35.

[36] S. Nadj-Perge, I. K. Drozdov, B. A. Bernevig, and A. Yazdani, *Proposal for realizing Majorana fermions in chains of magnetic atoms on a superconductor*. Physical Review B **88**, 020407 (2013), cited on page(s): 2.

[37] J. Li, H. Chen, I. K. Drozdov, A. Yazdani, B. A. Bernevig, and A. H. MacDonald, *Topological superconductivity induced by ferromagnetic metal chains*. Physical Review B **90**, 235433 (2014), cited on page(s): 2.

[38] M. Schecter, K. Flensberg, M. H. Christensen, B. M. Andersen, and J. Paaske, *Self-organized topological superconductivity in a Yu-Shiba-Rusinov chain*. Physical Review B **93**, 140503 (2016), cited on page(s): 2, 3, 35.

[39] J. F. Steiner, C. Mora, K. J. Franke, and F. von Oppen, *Quantum Magnetism and Topological Superconductivity in Yu-Shiba-Rusinov Chains*. Physical Review Letters **128**, 036801 (2022), cited on page(s): 2, 35.

[40] S. Frolov, *Quantum computing's reproducibility crisis: Majorana fermions*. Nature **592**, 350–352 (2021), cited on page(s): 3.

[41] D. Castelvecchi, *Evidence of elusive Majorana particle dies — but computing hope lives on*. Nature **591**, 354–355 (2021), cited on page(s): 3.

[42] P. Yu, J. Chen, M. Gomanko, G. Badawy, E. P. A. M. Bakkers, K. Zuo, V. Mourik, and S. M. Frolov, *Non-Majorana states yield nearly quantized conductance in proximatized nanowires*. Nature Physics **17**, 482–488 (2021), cited on page(s): 3, 91.

[43] M. Kayyalha, D. Xiao, R. Zhang, J. Shin, J. Jiang, F. Wang, Y.-F. Zhao, R. Xiao, L. Zhang, K. M. Fijalkowski, P. Mandal, M. Winnerlein, C. Gould, Q. Li, L. W. Molenkamp, M. H. W. Chan, N. Samarth, and C.-Z. Chang, *Absence of evidence for chiral Majorana modes in quantum anomalous Hall-superconductor devices*. Science **367**, 64–67 (2020), cited on page(s): 3.

[44] S. Zhu, L. Kong, L. Cao, H. Chen, M. Papaj, S. Du, Y. Xing, W. Liu, D. Wang, C. Shen, F. Yang, J. Schneeloch, R. Zhong, G. Gu, L. Fu, Y.-Y. Zhang, H. Ding, and H.-J. Gao, *Nearly quantized conductance plateau of vortex zero mode in an iron-based superconductor*. Science **367**, 189–192 (2020), cited on page(s): 3.

[45] G. Binnig, H. Rohrer, C. Gerber, and E. Weibel, *Tunneling through a controllable vacuum gap*. Applied Physics Letters **40**, 178–180 (1982), cited on page(s): 3, 45.

[46] G. Binnig, H. Rohrer, C. Gerber, and E. Weibel, *Surface Studies by Scanning Tunneling Microscopy*. Physical Review Letters **49**, 57–61 (1982), cited on page(s): 3, 45.

[47] R. Wiesendanger, H.-J. Güntherodt, G. Güntherodt, R. J. Gambino, and R. Ruf, *Observation of vacuum tunneling of spin-polarized electrons with the scanning tunneling microscope*. Physical Review Letters **65**, 247–250 (1990), cited on page(s): 3, 54.

[48] R. Wiesendanger, *Spin mapping at the nanoscale and atomic scale*. Reviews of Modern Physics **81**, 1495–1550 (2009), cited on page(s): 3.

[49] M. Bode, O. Pietzsch, A. Kubetzka, and R. Wiesendanger, *Shape-Dependent Thermal Switching Behavior of Superparamagnetic Nanoislands*. Physical Review Letters **92**, 067201 (2004), cited on page(s): 3, 5, 192.

[50] S. Krause, L. Berbil-Bautista, G. Herzog, M. Bode, and R. Wiesendanger, *Current-Induced Magnetization Switching with a Spin-Polarized Scanning Tunneling Microscope*. Science **317**, 1537–1540 (2007), cited on page(s): 3.

[51] S. Loth, M. Etzkorn, C. P. Lutz, D. M. Eigler, and A. J. Heinrich, *Measurement of Fast Electron Spin Relaxation Times with Atomic Resolution*. Science **329**, 1628–1630 (2010), cited on page(s): 3, 192.

[52] D. M. Eigler and E. K. Schweizer, *Positioning single atoms with a scanning tunnelling microscope*. Nature **344**, 524–526 (1990), cited on page(s): 3, 67.

[53] S. Nadj-Perge, I. K. Drozdov, J. Li, H. Chen, S. Jeon, J. Seo, A. H. MacDonald, B. A. Bernevig, and A. Yazdani, *Observation of Majorana fermions in ferromagnetic atomic chains on a superconductor*. Science **346**, 602–607 (2014), cited on page(s): 3.

[54] M. Ruby, F. Pientka, Y. Peng, F. von Oppen, B. W. Heinrich, and K. J. Franke, *End States and Subgap Structure in Proximity-Coupled Chains of Magnetic Adatoms*. Physical Review Letters **115**, 197204 (2015), cited on page(s): 3.

[55] H. Kim, A. Palacio-Morales, T. Posske, L. Rózsa, K. Palotás, L. Szunyogh, M. Thorwart, and R. Wiesendanger, *Toward tailoring Majorana bound states in artificially constructed magnetic atom chains on elemental superconductors*. Science Advances **4**, eaar5251 (2018), cited on page(s): 3.

[56] S. Jeon, Y. Xie, J. Li, Z. Wang, B. A. Bernevig, and A. Yazdani, *Distinguishing a Majorana zero mode using spin-resolved measurements*. Science **358**, 772–776 (2017), cited on page(s): 3.

[57] B. E. Feldman, M. T. Randeria, J. Li, S. Jeon, Y. Xie, Z. Wang, I. K. Drozdov, B. Andrei Bernevig, and A. Yazdani, *High-resolution studies of the Majorana atomic chain platform*. Nature Physics **13**, 286–291 (2017), cited on page(s): 3.

[58] L. Schneider, S. Brinker, M. Steinbrecher, J. Hermenau, T. Posske, M. dos Santos Dias, S. Lounis, R. Wiesendanger, and J. Wiebe, *Controlling in-gap end states by linking nonmagnetic atoms and artificially-constructed spin chains on superconductors*. Nature Communications **11**, 4707 (2020), cited on page(s): 4.

[59] L. Schneider, P. Beck, J. Wiebe, and R. Wiesendanger, *Atomic-scale spin-polarization maps using functionalized superconducting probes*. Science Advances **7**, eabd7302 (2021), cited on page(s): 4.

[60] P. Beck, L. Schneider, L. Rózsa, K. Palotás, A. Lászlóffy, L. Szunyogh, J. Wiebe, and R. Wiesendanger, *Spin-orbit coupling induced splitting of Yu-Shiba-Rusinov states in antiferromagnetic dimers*. Nature Communications **12**, 2040 (2021), cited on page(s): 4.

[61] L. Schneider, P. Beck, T. Posske, D. Crawford, E. Mascot, S. Rachel, R. Wiesendanger, and J. Wiebe, *Topological Shiba bands in artificial spin chains on superconductors*. Nature Physics **17**, 943–948 (2021), cited on page(s): 4.

[62] L. Schneider, P. Beck, J. Neuhaus-Steinmetz, L. Rózsa, T. Posske, J. Wiebe, and R. Wiesendanger, *Precursors of Majorana modes and their length-dependent energy oscillations probed at both ends of atomic Shiba chains*. Nature Nanotechnology **17**, 384–389 (2022), cited on page(s): 4.

[63] F. Küster, S. Brinker, R. Hess, D. Loss, S. Parkin, J. Klinovaja, S. Lounis, and P. Sessi, *Non-Majorana modes in diluted spin chains proximitized to a superconductor*. arXiv:2112.05708 [cond-mat.supr-con] , (2021), cited on page(s): 4.

[64] J.-P. Gauyacq and N. Lorente, *Decoherence-governed magnetic-moment dynamics of supported atomic objects*. Journal of Physics: Condensed Matter **27**, 455301 (2015), cited on page(s): 5.

[65] F. Delgado, S. Loth, M. Zielinski, and J. Fernández-Rossier, *The emergence of classical behaviour in magnetic adatoms*. Europhysics Letters **109**, 57001 (2015), cited on page(s): 5.

[66] F. Hund, *Zur Deutung der Molekelspektren. I*. Zeitschrift für Physik **40**, 742–764 (1927), cited on page(s): 7.

[67] F. Hund, *Zur Deutung der Molekelspektren. III*. Zeitschrift für Physik **43**, 805–826 (1927), cited on page(s): 7.

[68] R. Skomski, *Simple models of magnetism*, Oxford University Press on Demand (2008), cited on page(s): 8.

[69] W. Demtröder, *Experimentalphysik 3: Atome, Moleküle und Festkörper*, Springer-Verlag (2016), cited on page(s): 8, 15.

[70] J. M. Coey, *Magnetism and magnetic materials*, Cambridge university press (2010), cited on page(s): 8, 9.

[71] C. Rudowicz and C. Y. Chung, *The generalization of the extended Stevens operators to higher ranks and spins, and a systematic review of the tables of the tensor operators and their matrix elements*. Journal of Physics: Condensed Matter **16**, 5825–5847 (2004), cited on page(s): 9.

[72] K. W. H. Stevens, *Matrix Elements and Operator Equivalents Connected with the Magnetic Properties of Rare Earth Ions*. Proceedings of the Physical Society. Section A **62**, 209 (1952), cited on page(s): 9.

[73] D.-J. Choi, N. Lorente, J. Wiebe, K. von Bergmann, A. F. Otte, and A. J. Heinrich, *Colloquium: Atomic spin chains on surfaces*. Reviews of Modern Physics **91**, 041001 (2019), cited on page(s): 9, 12.

[74] J. Hermenau, S. Brinker, M. Marciani, M. Steinbrecher, M. dos Santos Dias, R. Wiesendanger, S. Lounis, and J. Wiebe, *Stabilizing spin systems via symmetrically tailored RKKY interactions*. Nature Communications **10**, 2565 (2019), cited on page(s): 12, 192.

[75] I. Dzyaloshinsky, *A thermodynamic theory of "weak" ferromagnetism of antiferromagnetics*. Journal of Physics and Chemistry of Solids **4**, 241–255 (1958), cited on page(s): 12.

[76] T. Moriya, *New mechanism of anisotropic superexchange interaction*. Physical Review Letters **4**, 228–230 (1960), cited on page(s): 12.

[77] M. Kleiber, M. Bode, R. Ravlić, and R. Wiesendanger, *Topology-Induced Spin Frustrations at the Cr(001) Surface Studied by Spin-Polarized Scanning Tunneling Spectroscopy*. Physical Review Letters **85**, 4606–4609 (2000), cited on page(s): 12.

[78] M. Waśniowska, S. Schröder, P. Ferriani, and S. Heinze, *Real space observation of spin frustration in Cr on a triangular lattice*. Physical Review B **82**, 012402 (2010), cited on page(s): 12.

[79] K. Kim, M.-S. Chang, S. Korenblit, R. Islam, E. E. Edwards, J. K. Freericks, G.-D. Lin, L.-M. Duan, and C. Monroe, *Quantum simulation of frustrated Ising spins with trapped ions*. Nature **465**, 590–593 (2010), cited on page(s): 12.

[80] A. Kubetzka, M. Bode, O. Pietzsch, and R. Wiesendanger, *Spin-Polarized Scanning Tunneling Microscopy with Antiferromagnetic Probe Tips*. Physical Review Letters **88**, 057201 (2002), cited on page(s): 12, 108.

[81] M. Bode, M. Heide, K. V. Bergmann, P. Ferriani, S. Heinze, G. Bihlmayer, A. Kubetzka, O. Pietzsch, S. Blügel, and R. Wiesendanger, *Chiral magnetic order at surfaces driven by inversion asymmetry*. Nature **447**, 190–193 (2007), cited on page(s): 12.

[82] P. Ferriani, K. von Bergmann, E. Y. Vedmedenko, S. Heinze, M. Bode, M. Heide, G. Bihlmayer, S. Blügel, and R. Wiesendanger, *Atomic-Scale Spin Spiral with a Unique Rotational Sense: Mn Monolayer on W(001)*. Physical Review Letters **101**, 027201 (2008), cited on page(s): 12.

[83] P. Ferriani, K. von Bergmann, E. Y. Vedmedenko, S. Heinze, M. Bode, M. Heide, G. Bihlmayer, S. Blügel, and R. Wiesendanger, *Erratum: Atomic-Scale Spin Spiral with a Unique Rotational Sense: Mn Monolayer on W(001) [Phys. Rev. Lett. 101, 027201 (2008)]*. Physical Review Letters **102**, 019901 (2009), cited on page(s): 12.

[84] K. Di, V. L. Zhang, H. S. Lim, S. C. Ng, M. H. Kuok, J. Yu, J. Yoon, X. Qiu, and H. Yang, *Direct Observation of the Dzyaloshinskii-Moriya Interaction in a Pt/Co/Ni Film*. Physical Review Letters **114**, 047201 (2015), cited on page(s): 12.

[85] P. W. Anderson, *New Approach to the Theory of Superexchange Interactions*. Physical Review **115**, 2–13 (1959), cited on page(s): 13.

[86] „The Magnetic Hamiltonian“, *Quantum Theory of Magnetism: Magnetic Properties of Materials*, Berlin, Heidelberg: Springer Berlin Heidelberg (2007), 33–83, cited on page(s): 13.

[87] X. Chen, Y.-S. Fu, S.-H. Ji, T. Zhang, P. Cheng, X.-C. Ma, X.-L. Zou, W.-H. Duan, J.-F. Jia, and Q.-K. Xue, *Probing Superexchange Interaction in Molecular Magnets by Spin-Flip Spectroscopy and Microscopy*. Physical Review Letters **101**, 197208 (2008), cited on page(s): 13.

[88] M. A. Ruderman and C. Kittel, *Indirect Exchange Coupling of Nuclear Magnetic Moments by Conduction Electrons*. Physical Reviews **96**, 99–102 (1954), cited on page(s): 13.

[89] T. Kasuya, *A Theory of Metallic Ferro- and Antiferromagnetism on Zener's Model*. Progress of Theoretical Physics **16**, 45–57 (1956), cited on page(s): 13.

[90] K. Yosida, *Magnetic Properties of Cu-Mn Alloys*. Physical Reviews **106**, 893–898 (1957), cited on page(s): 13.

[91] A. A. Khajetoorians, J. Wiebe, B. Chilian, S. Lounis, S. Blügel, and R. Wiesendanger, *Atom-by-atom engineering and magnetometry of tailored nanomagnets*. Nature Physics **8**, 497–503 (2012), cited on page(s): 13.

[92] L. Zhou, J. Wiebe, S. Lounis, E. Vedmedenko, F. Meier, S. Blügel, P. H. Dederichs, and R. Wiesendanger, *Strength and directionality of surface Ruderman–Kittel–Kasuya–Yosida interaction mapped on the atomic scale*. Nature Physics **6**, 187–191 (2010), cited on page(s): 13.

[93] M. Steinbrecher, R. Rausch, K. T. That, J. Hermenau, A. A. Khajetoorians, M. Potthoff, R. Wiesendanger, and J. Wiebe, *Non-collinear spin states in bottom-up fabricated atomic chains*. Nature Communications **9**, 2853 (2018), cited on page(s): 14, 109.

[94] W. E. Lamb and R. C. Retherford, *Fine Structure of the Hydrogen Atom. Part I*. Physical Review **79**, 549–572 (1950), cited on page(s): 15.

[95] M. Grundmann, *The Physics of Semiconductors*, 3rd ed., Springer (2010), cited on page(s): 15.

[96] A. Fert, *Magnetic and Transport Properties of Metallic Multilayers*, Trans Tech Publications Ltd (1990).

[97] Y. A. Bychkov and E. I. Rashba, *Oscillatory effects and the magnetic susceptibility of carriers in inversion layers*. Journal of Physics C: Solid State Physics **17**, 6039–6045 (1984), cited on page(s): 16.

[98] Y. A. Bychkov and E. I. Rashba, *Properties of a 2D electron-gas with lifted spectral degeneracy*. Soviet Physics JETP Letters **39**, 78 (1984), cited on page(s): 16.

[99] A. Manchon, H. C. Koo, J. Nitta, S. M. Frolov, and R. A. Duine, *New perspectives for Rashba spin–orbit coupling*. Nature Materials **14**, 871–882 (2015), cited on page(s): 16.

[100] S. LaShell, B. A. McDougall, and E. Jensen, *Spin Splitting of an Au(111) Surface State Band Observed with Angle Resolved Photoelectron Spectroscopy*. Physical Review Letters **77**, 3419–3422 (1996), cited on page(s): 17, 152.

[101] M. Hoesch, M. Muntwiler, V. N. Petrov, M. Hengsberger, L. Patthey, M. Shi, M. Falub, T. Greber, and J. Osterwalder, *Spin structure of the Shockley surface state on* Au(111). Physical Review B **69**, 241401 (2004), cited on page(s): 17.

[102] G. Nicolay, F. Reinert, S. Hüfner, and P. Blaha, *Spin-orbit splitting of the L-gap surface state on Au(111) and Ag(111)*. Physical Review B **65**, 033407 (2001), cited on page(s): 17.

[103] G. Bihlmayer, Y. Koroteev, P. Echenique, E. Chulkov, and S. Blügel, *The Rashba-effect at metallic surfaces*. Surface Science **600**, 3888–3891 (2006), cited on page(s): 17, 140, 152.

[104] L. Petersen and P. Hedegård, *A simple tight-binding model of spin–orbit splitting of sp-derived surface states*. Surface Science **459**, 49–56 (2000), cited on page(s): 17, 140.

[105] G. Theurich and N. A. Hill, *Self-consistent treatment of spin-orbit coupling in solids using relativistic fully separable ab initio pseudopotentials*. Physical Review B **64**, 073106 (2001), cited on page(s): 17.

[106] A. D. Corso and A. M. Conte, *Spin-orbit coupling with ultrasoft pseudopotentials: Application to Au and Pt*. Physical Review B **71**, 115106 (2005), cited on page(s): 17.

[107] D. Smith, *New mechanisms for magnetic anisotropy in localised S-state moment materials*. Journal of Magnetism and Magnetic Materials **1**, 214–225 (1976), cited on page(s): 18.

[108] A. Fert and P. M. Levy, *Role of Anisotropic Exchange Interactions in Determining the Properties of Spin-Glasses*. Physical Review Letters **44**, 1538–1541 (1980), cited on page(s): 18.

[109] A. Fert, N. Reyren, and V. Cros, *Magnetic skyrmions: advances in physics and potential applications*. Nature Reviews Materials **2**, 17031 (2017), cited on page(s): 18.

[110] *The Nobel Prize in Physics 1913*, URL: `https://www.nobelprize.org/prizes/physics/1913/summary/` (accessed on 10.3.2022), cited on page(s): 20.

[111] W. Meissner and R. Ochsenfeld, *Ein neuer Effekt bei Eintritt der Supraleitfähigkeit*. Naturwissenschaften **21**, 787–788 (1933), cited on page(s): 20.

[112] K. Mendelssohn and J. R. Moore, *Supraconducting alloys*. Nature **135**, 826–827 (1935), cited on page(s): 20.

[113] W. J. De Haas and J. M. Casimir-Jonker, *Penetration of a magnetic field into supraconductive alloys*. Nature **135**, 30–31 (1935), cited on page(s): 20.

[114] P. Mangin and R. Kahn, *Superconductivity: an introduction*, Springer (2016), cited on page(s): 20, 21, 207.

[115] A. A. Abrikosov, *On the magnetic properties of superconductors of the second group*. Soviet Physics JETP **5**, 1174–1182 (1957), cited on page(s): 20.

[116] J. Auer and H. Ullmaier, *Magnetic Behavior of Type-II Superconductors with Small Ginzburg-Landau Parameters*. Physical Review B **7**, 136–145 (1973), cited on page(s): 21.

[117] J. Bardeen, L. N. Cooper, and J. R. Schrieffer, *Theory of Superconductivity*. Physical Reviews **108**, 1175–1204 (1957), cited on page(s): 21.

[118] R. K. Werner Buckel, *Supraleitung*, 6th ed., Wiley VCH Verlag GmbH (2012), cited on page(s): 21, 22, 24.

[119] J. Cayao, C. Triola, and A. M. Black-Schaffer, *Odd-frequency superconducting pairing in one-dimensional systems*. The European Physical Journal Special Topics **229**, 545–575 (2020), cited on page(s): 22.

[120] L. N. Cooper, *Bound Electron Pairs in a Degenerate Fermi Gas*. Physical Reviews **104**, 1189–1190 (1956), cited on page(s): 22.

[121] E. Maxwell, *Isotope Effect in the Superconductivity of Mercury*. Physical Reviews **78**, 477–477 (1950), cited on page(s): 22.

[122] C. A. Reynolds, B. Serin, and L. B. Nesbitt, *The Isotope Effect in Superconductivity. I. Mercury*. Physical Reviews **84**, 691–694 (1951), cited on page(s): 22.

[123] S. L. Bud'ko, G. Lapertot, C. Petrovic, C. E. Cunningham, N. Anderson, and P. C. Canfield, *Boron Isotope Effect in Superconducting* MgB_2. Physical Review Letters **86**, 1877–1880 (2001), cited on page(s): 22.

[124] J. B. Ketterson, S. N. Song, and B. Ketterson J., *Superconductivity*, 1st ed., Cambridge University Press (2003), ISBN: 0521565626, cited on page(s): 22, 24.

[125] R. C. Dynes, V. Narayanamurti, and J. P. Garno, *Direct Measurement of Quasiparticle-Lifetime Broadening in a Strong-Coupled Superconductor*. Physical Review Letters **41**, 1509–1512 (1978), cited on page(s): 25, 96.

[126] I. Giaever, *Electron Tunneling Between Two Superconductors*. Physical Review Letters **5**, 464–466 (1960), cited on page(s): 25.

[127] I. Giaever, *Energy Gap in Superconductors Measured by Electron Tunneling*. Physical Review Letters **5**, 147–148 (1960), cited on page(s): 25.

[128] J. Nicol, S. Shapiro, and P. H. Smith, *Direct Measurement of the Superconducting Energy Gap*. Physical Review Letters **5**, 461–464 (1960), cited on page(s): 25.

[129] K. M. Bastiaans, D. Chatzopoulos, J.-F. Ge, D. Cho, W. O. Tromp, J. M. van Ruitenbeek, M. H. Fischer, P. J. de Visser, D. J. Thoen, E. F. C. Driessen, T. M. Klapwijk, and M. P. Allan, *Direct evidence for Cooper pairing without a spectral gap in a disordered superconductor above* T_C. Science **374**, 608–611 (2021), cited on page(s): 25.

[130] A. Gilabert, *Effet de Proximite entre un Metal Normal et un Supraconducteur*. Annales de Physique **2**, 203–252 (1977), cited on page(s): 25.

[131] E. L. Wolf, *Principles of electron tunneling spectroscopy*, OUP Oxford (2011), cited on page(s): 25.

[132] T. Klapwijk, *Proximity effect from an Andreev perspective*. Journal of superconductivity **17**, 593–611 (2004), cited on page(s): 25, 28.

[133] B. Pannetier and H. Courtois, *Andreev reflection and proximity effect*. Journal of low temperature physics **118**, 599–615 (2000), cited on page(s): 25, 28.

[134] K. D. Usadel, *Generalized Diffusion Equation for Superconducting Alloys*. Physical Review Letters **25**, 507–509 (1970), cited on page(s): 25, 28.

[135] S. Guéron, H. Pothier, N. O. Birge, D. Esteve, and M. H. Devoret, *Superconducting Proximity Effect Probed on a Mesoscopic Length Scale*. Physical Review Letters **77**, 3025–3028 (1996), cited on page(s): 25, 28, 29.

[136] A. K. Gupta, L. Crétinon, N. Moussy, B. Pannetier, and H. Courtois, *Anomalous density of states in a metallic film in proximity with a superconductor*. Physical Review B **69**, 104514 (2004), cited on page(s): 25.

[137] A. F. Andreev Soviet Physics JETP **46**, 1823 (1964), cited on page(s): 27.

[138] G. Csire, B. Újfalussy, J. Cserti, and B. Győrffy, *Multiple scattering theory for superconducting heterostructures*. Physical Review B **91**, 165142 (2015), cited on page(s): 29.

[139] G. Csire, J. Cserti, I. Tüttő, and B. Újfalussy, *Prediction of superconducting transition temperatures of heterostructures based on the quasiparticle spectrum*. Physical Review B **94**, 104511 (2016), cited on page(s): 29.

[140] G. Csire, J. Cserti, and B. Újfalussy, *First principles based proximity effect of superconductor–normal metal heterostructures*. Journal of Physics: Condensed Matter **28**, 495701 (2016), cited on page(s): 29.

[141] L. Yu, *Bound state in superconductors with paramagnetic impurities*. Acta Physica Sinica **21**, 75 (1968), cited on page(s): 29, 129.

[142] H. Shiba, *Classical Spins in Superconductors*. Progress of Theoretical Physics **40**, 435–451 (1968), cited on page(s): 29, 30, 129.

[143] A. I. Rusinov, *Superconductivity near a paramagnetic impurity*. Soviet Physics JETP **9**, (1969), cited on page(s): 29, 31, 129.

[144] A. V. Balatsky, I. Vekhter, and J.-X. Zhu, *Impurity-induced states in conventional and unconventional superconductors*. Reviews of Modern Physics **78**, 373–433 (2006), cited on page(s): 29.

[145] B. W. Heinrich, J. I. Pascual, and K. J. Franke, *Single magnetic adsorbates on s -wave superconductors*. Progress in Surface Science **93**, 1–19 (2018), cited on page(s): 30–32.

[146] K. J. Franke, G. Schulze, and J. I. Pascual, *Competition of Superconducting Phenomena and Kondo Screening at the Nanoscale*. Science **332**, 940–944 (2011), cited on page(s): 31, 129.

[147] N. Hatter, B. W. Heinrich, D. Rolf, and K. J. Franke, *Scaling of Yu-Shiba-Rusinov energies in the weak-coupling Kondo regime*. Nature Communications **8**, 2016 (2017), cited on page(s): 31.

[148] L. Farinacci, G. Ahmadi, G. Reecht, M. Ruby, N. Bogdanoff, O. Peters, B. W. Heinrich, F. von Oppen, and K. J. Franke, *Tuning the Coupling of an Individual Magnetic Impurity to a Superconductor: Quantum Phase Transition and Transport*. Physical Review Letters **121**, 196803 (2018), cited on page(s): 31, 130.

[149] H. Huang, R. Drost, J. Senkpiel, C. Padurariu, B. Kubala, A. L. Yeyati, J. C. Cuevas, J. Ankerhold, K. Kern, and C. R. Ast, *Quantum phase transitions and the role of impurity-substrate hybridization in Yu-Shiba-Rusinov states*. Communications Physics **3**, 199 (2020), cited on page(s): 31, 134.

[150] S.-H. Ji, T. Zhang, Y.-S. Fu, X. Chen, X.-C. Ma, J. Li, W.-H. Duan, J.-F. Jia, and Q.-K. Xue, *High-Resolution Scanning Tunneling Spectroscopy of Magnetic Impurity Induced Bound States in the Superconducting Gap of Pb Thin Films*. Physical Review Letters **100**, 226801 (2008), cited on page(s): 31.

[151] M. Ruby, Y. Peng, F. von Oppen, B. W. Heinrich, and K. J. Franke, *Orbital Picture of Yu-Shiba-Rusinov Multiplets*. Physical Review Letters **117**, 186801 (2016), cited on page(s): 31.

[152] D.-J. Choi, C. Rubio-Verdú, J. de Bruijckere, M. M. Ugeda, N. Lorente, and J. I. Pascual, *Mapping the orbital structure of impurity bound states in a superconductor*. Nature Communications **8**, 15175 (2017), cited on page(s): 31, 130, 173.

[153] M. Ruby, F. Pientka, Y. Peng, F. von Oppen, B. W. Heinrich, and K. J. Franke, *Tunneling Processes into Localized Subgap States in Superconductors*. Physical Review Letters **115**, 087001 (2015), cited on page(s): 31.

[154] A. Yazdani, B. A. Jones, C. P. Lutz, M. F. Crommie, and D. M. Eigler, *Probing the Local Effects of Magnetic Impurities on Superconductivity*. Science **275**, 1767–1770 (1997), cited on page(s): 31.

[155] J. Ortuzar, S. Trivini, M. Alvarado, M. Rouco, J. Zaldivar, A. L. Yeyati, J. I. Pascual, and F. S. Bergeret, *Yu-Shiba-Rusinov states in two-dimensional superconductors with arbitrary Fermi contours*. Physical Review B **105**, 245403 (2022), cited on page(s): 33.

[156] G. C. Ménard, S. Guissart, C. Brun, S. Pons, V. S. Stolyarov, F. Debontridder, M. V. Leclerc, E. Janod, L. Cario, D. Roditchev, P. Simon, and T. Cren, *Coherent long-range magnetic bound states in a superconductor*. Nature Physics **11**, 1013–1016 (2015), cited on page(s): 33.

[157] H. Kim, L. Rózsa, D. Schreyer, E. Simon, and R. Wiesendanger, *Long-range focusing of magnetic bound states in superconducting lanthanum*. Nature Communications **11**, 4573 (2020), cited on page(s): 33.

[158] E. Majorana, *Teoria simmetrica dell'elettrone e del positrone*. Il Nuovo Cimento (1924-1942) **14**, 171–184 (1937), cited on page(s): 33.

[159] C. Nayak, S. H. Simon, A. Stern, M. Freedman, and S. Das Sarma, *Non-Abelian anyons and topological quantum computation*. Reviews of Modern Physics **80**, 1083–1159 (2008), cited on page(s): 33.

[160] J. Alicea, *New directions in the pursuit of Majorana fermions in solid state systems*. Reports on Progress in Physics **75**, 076501 (2012), cited on page(s): 34.

[161] Y. Maeno, H. Hashimoto, K. Yoshida, S. Nishizaki, T. Fujita, J. G. Bednorz, and F. Lichtenberg, *Superconductivity in a layered perovskite without copper*. Nature **372**, 532–534 (1994), cited on page(s): 34.

[162] T. M. Rice and M. Sigrist, Sr_2RuO_4*: an electronic analogue of* ^{3}*He?*. Journal of Physics: Condensed Matter **7**, 643–648 (1995), cited on page(s): 34.

[163] G. Baskaran, *Why is* Sr_2RuO_4 *not a high* T_C *superconductor? Electron correlation, Hund's coupling and p-wave instability*. Physica B: Condensed Matter **223-224**, 490–495 (1996), cited on page(s): 34.

[164] C. Kallin and A. J. Berlinsky, *Is* Sr_2RuO_4 *a chiral p-wave superconductor?*. Journal of Physics: Condensed Matter **21**, 164210 (2009), cited on page(s): 34.

[165] R. M. Lutchyn, E. P. A. M. Bakkers, L. P. Kouwenhoven, P. Krogstrup, C. M. Marcus, and Y. Oreg, *Majorana zero modes in superconductor–semiconductor heterostructures*. Nature Reviews Materials **3**, 52–68 (2018), cited on page(s): 35.

[166] B. Jäck, Y. Xie, and A. Yazdani, *Detecting and distinguishing Majorana zero modes with the scanning tunnelling microscope*. Nature Reviews Physics **3**, 541–554 (2021), cited on page(s): 35.

[167] A. I. Rusinov, *Theory of gapless superconductivity in alloys containing paramagnetic impurities*. Soviet Physics JETP **29**, 1101 (1969), cited on page(s): 36, 84, 129.

[168] M. E. Flatté and D. E. Reynolds, *Local spectrum of a superconductor as a probe of interactions between magnetic impurities*. Physical Review B **61**, 14810–14814 (2000), cited on page(s): 36.

[169] D. K. Morr and N. A. Stavropoulos, *Quantum interference between impurities: Creating novel many-body states in s -wave superconductors*. Physical Review B **67**, 020502 (2003), cited on page(s): 36.

[170] D. K. Morr and J. Yoon, *Impurities, quantum interference, and quantum phase transitions in s-wave superconductors*. Physical Review B **73**, 224511 (2006), cited on page(s): 36, 72.

[171] M. Ruby, B. W. Heinrich, Y. Peng, F. von Oppen, and K. J. Franke, *Wave-Function Hybridization in Yu-Shiba-Rusinov Dimers*. Physical Review Letters **120**, 156803 (2018), cited on page(s): 36, 73.

[172] D.-J. Choi, C. G. Fernández, E. Herrera, C. Rubio-Verdú, M. M. Ugeda, I. Guillamón, H. Suderow, J. I. Pascual, and N. Lorente, *Influence of Magnetic Ordering between Cr Adatoms on the Yu-Shiba-Rusinov States of the β-Bi_2Pd Superconductor*. Physical Review Letters **120**, 167001 (2018), cited on page(s): 36.

[173] S. Kezilebieke, M. Dvorak, T. Ojanen, and P. Liljeroth, *Coupled Yu-Shiba-Rusinov States in Molecular Dimers on $NbSe_2$*. Nano Letters **18**, 2311–2315 (2018), cited on page(s): 36, 73.

[174] F. Küster, S. Brinker, S. Lounis, S. S. P. Parkin, and P. Sessi, *Long range and highly tunable interaction between local spins coupled to a superconducting condensate*. Nature Communications **12**, 6722 (2021), cited on page(s): 36, 101, 150.

[175] H. Ding, Y. Hu, M. T. Randeria, S. Hoffman, O. Deb, J. Klinovaja, D. Loss, and A. Yazdani, *Tuning interactions between spins in a superconductor*. Proceedings of the National Academy of Sciences **118**, e2024837118 (2021), cited on page(s): 36, 101, 148.

[176] A. Y. Kitaev, *Unpaired Majorana fermions in quantum wires*. Physics-Uspekhi **44**, 131–136 (2001), cited on page(s): 36, 97.

[177] *Topology in condensed matter: tying quantum knots*, URL: `https://topocondmat.org/` (accessed on 16.3.2022), cited on page(s): 37.

[178] C. W. Groth, M. Wimmer, A. R. Akhmerov, and X. Waintal, *Kwant: a software package for quantum transport*. New Journal of Physics **16**, 063065 (2014), cited on page(s): 37.

[179] S. Ryu, A. P. Schnyder, A. Furusaki, and A. W. W. Ludwig, *Topological insulators and superconductors: tenfold way and dimensional hierarchy*. New Journal of Physics **12**, 065010 (2010), cited on page(s): 37.

[180] B. Braunecker, G. I. Japaridze, J. Klinovaja, and D. Loss, *Spin-selective Peierls transition in interacting one-dimensional conductors with spin-orbit interaction*. Physical Review B **82**, 045127 (2010), cited on page(s): 40, 107.

[181] J.-P. Gauyacq, S. M. Yaro, X. Cartoixà, and N. Lorente, *Correlation-Mediated Processes for Electron-Induced Switching between Néel States of Fe Antiferromagnetic Chains*. Physical Review Letters **110**, 087201 (2013), cited on page(s): 42, 43.

[182] B. Barbara and E. M. Chudnovsky, *Macroscopic quantum tunneling in antiferromagnets*. Physics Letters A **145**, 205–208 (1990), cited on page(s): 42.

[183] F. D. Novaes, N. Lorente, and J.-P. Gauyacq, *Quenching of magnetic excitations in single adsorbates at surfaces: Mn on CuN/Cu(100)*. Physical Review B **82**, 155401 (2010), cited on page(s): 43.

[184] S. Loth, S. Baumann, C. P. Lutz, D. M. Eigler, and A. J. Heinrich, *Bistability in Atomic-Scale Antiferromagnets*. Science **335**, 196–199 (2012), cited on page(s): 43.

[185] J. des Cloizeaux and J. J. Pearson, *Spin-Wave Spectrum of the Antiferromagnetic Linear Chain*. Physical Review **128**, 2131–2135 (1962), cited on page(s): 43.

[186] J. P. Gauyacq and N. Lorente, *Excitation of spin waves by tunneling electrons in ferromagnetic and antiferromagnetic spin-1/2 Heisenberg chains*. Physical Review B **83**, 035418 (2011), cited on page(s): 43.

[187] A. Spinelli, B. Bryant, F. Delgado, J. Fernández-Rossier, and A. F. Otte, *Imaging of spin waves in atomically designed nanomagnets*. Nature Materials **13**, 782–785 (2014), cited on page(s): 43, 192, 212.

[188] R. W. Gurney and E. U. Condon, *Wave Mechanics and Radioactive Disintegration*. Nature **122**, 439–439 (1928), cited on page(s): 45.

[189] A. Sonntag, *Magnetoelectric Coupling and Thermally Driven Magnetization Dynamics Studies on the Atomic Scale*, PhD thesis, Universität Hamburg (2014), cited on page(s): 46.

[190] *The Nobel Prize in Physics 1986*, URL: `https://www.nobelprize.org/prizes/physics/1986/summary/` (accessed on 27.5.2022), cited on page(s): 47.

[191] J.-L. Basdevant and J. Dalibard, *Quantum mechanics*, Springer Science & Business Media (2005), cited on page(s): 47, 49.

[192] R. Wiesendanger, *Scanning Probe Microscopy and Spectroscopy: Methods and Applications*, Cambridge University Press (1994), cited on page(s): 49–51.

[193] J. B. Pendry, A. B. Pretre, and B. C. H. Krutzen, *Theory of the scanning tunnelling microscope*. Journal of Physics: Condensed Matter **3**, 4313–4321 (1991), cited on page(s): 49.

[194] J. Bardeen, *Tunneling from a many-particle point of view*. Physical Review Letters **6**, 57 (1961), cited on page(s): 50.

[195] J.-D. Pillet, C. H. L. Quay, P. Morfin, C. Bena, A. L. Yeyati, and P. Joyez, *Andreev bound states in supercurrent-carrying carbon nanotubes revealed*. Nature Physics **6**, 965–969 (2010), cited on page(s): 52.

[196] M. Ternes, W.-D. Schneider, J.-C. Cuevas, C. P. Lutz, C. F. Hirjibehedin, and A. J. Heinrich, *Subgap structure in asymmetric superconducting tunnel junctions*. Physical Review B **74**, 132501 (2006), cited on page(s): 52, 163.

[197] P. Beck, L. Schneider, R. Wiesendanger, and J. Wiebe, *Systematic study of Mn atoms, artificial dimers and chains on superconducting Ta(110)*. arXiv:2205.10073 [cond-mat.supr-con] , (2022), cited on page(s): 53.

[198] M. Julliere, *Tunneling between ferromagnetic films*. Physics Letters A **54**, 225–226 (1975), cited on page(s): 53, 134.

[199] J. C. Slonczewski, *Conductance and exchange coupling of two ferromagnets separated by a tunneling barrier*. Physical Review B **39**, 6995–7002 (1989), cited on page(s): 54, 134, 192.

[200] L. Schneider, *Realizing topological boundary modes in bottom-up constructed magnetic nanostructures on superconducting surfaces*, PhD thesis, Universität Hamburg (2021), cited on page(s): 58.

[201] J. Wiebe, A. Wachowiak, F. Meier, D. Haude, T. Foster, M. Morgenstern, and R. Wiesendanger, *A 300* mK *ultra-high vacuum scanning tunneling microscope for spin-resolved spectroscopy at high energy resolution*. Review of Scientific Instruments **75**, 4871–4879 (2004), cited on page(s): 58.

[202] J. Wiebe, *Aufbau einer 300 mK-Ultrahochvakuum-Rastertunnelmikroskopie-Anlage mit 14 T-Magnet und Untersuchung eines stark ungeordneten zweidimensionalen Elektronensystems*, PhD thesis, Universität Hamburg (2003), cited on page(s): 58.

[203] „Piezoelectric Motor", WO/1993/019494, S. Pan., 1993 (cit. on p. 60).

[204] S. Kuck, J. Wienhausen, G. Hoffmann, and R. Wiesendanger, *A versatile variable-temperature scanning tunneling microscope for molecular growth*. Review of Scientific Instruments **79**, 083903 (2008), cited on page(s): 62.

[205] P. Beck, *Spectroscopy of the Yu-Shiba-Rusinov States of Artificial Arrys of Mn Atoms on Clean Nb (110)*, MA thesis, Universität Hamburg (2019), cited on page(s): 62, 71.

[206] A. B. Odobesko, S. Haldar, S. Wilfert, J. Hagen, J. Jung, N. Schmidt, P. Sessi, M. Vogt, S. Heinze, and M. Bode, *Preparation and electronic properties of clean superconducting Nb(110) surfaces*. Physical Review B **99**, 115437 (2019), cited on page(s): 62.

[207] T. Eelbo, V. Zdravkov, and R. Wiesendanger, *STM study of the preparation of clean Ta(110) and the subsequent growth of two-dimensional Fe islands*. Surface Science **653**, 113–117 (2016), cited on page(s): 64, 125.

[208] B. Engelkamp, H. Wortelen, H. Mirhosseini, A. B. Schmidt, D. Thonig, J. Henk, and M. Donath, *Spin-polarized surface electronic structure of Ta(110): Similarities and differences to W(110)*. Physical Review B **92**, 085401 (2015), cited on page(s): 64.

[209] C. Sürgers, M. Schöck, and H. v. Löhneysen, *Oxygen-induced surface structure of Nb(110)*. Surface Science **471**, 209–218 (2001), cited on page(s): 64.

[210] I. Arfaoui, J. Cousty, and H. Safa, *Tiling of a Nb(110) surface with NbO crystals nanosized by the NbO/Nb misfit*. Physical Review B **65**, 115413 (2002), cited on page(s): 64.

[211] M. V. Kuznetsov, A. S. Razinkin, and A. L. Ivanovskii, *Oxide nanostructures on an Nb surface and related systems: experiments and ab initio calculations*. Physics-Uspekhi **53**, 995–1014 (2010), cited on page(s): 65.

[212] A. Odobesko, D. Di Sante, A. Kowalski, S. Wilfert, F. Friedrich, R. Thomale, G. Sangiovanni, and M. Bode, *Observation of tunable single-atom Yu-Shiba-Rusinov states*. Physical Review B **102**, 174504 (2020), cited on page(s): 65.

[213] J. A. Stroscio and R. J. Celotta, *Controlling the Dynamics of a Single Atom in Lateral Atom Manipulation*. Science **306**, 242–247 (2004), cited on page(s): 67, 169, 181.

[214] N. Ashcroft, *Festkörperphysik*, Oldenbourg, R (2012), cited on page(s): 68.

[215] L. Szunyogh, B. Újfalussy, and P. Weinberger, *Magnetic anisotropy of iron multilayers on Au(001): First-principles calculations in terms of the fully relativistic spin-polarized screened KKR method*. Physical Review B **51**, 9552–9559 (1995), cited on page(s): 74.

[216] A. Lászlóffy, K. Palotás, L. Rózsa, and L. Szunyogh, *Electronic and Magnetic Properties of Building Blocks of Mn and Fe Atomic Chains on Nb(110)*. Nanomaterials **11**, 1933 (2021), cited on page(s): 74.

[217] A. Ptok, S. Głodzik, and T. Domański, *Yu-Shiba-Rusinov states of impurities in a triangular lattice of* $NbSe_2$ *with spin-orbit coupling*. Physical Review B **96**, 184425 (2017), cited on page(s): 74.

[218] M. Mashkoori, A. G. Moghaddam, M. H. Hajibabaee, A. M. Black-Schaffer, and F. Parhizgar, *Impact of topology on the impurity effects in extended s-wave superconductors with spin-orbit coupling*. Physical Review B **99**, 014508 (2019), cited on page(s): 74.

[219] C. Moca, E. Demler, B. Jankó, and G. Zaránd, *Spin-resolved spectra of Shiba multiplets from Mn impurities in* MgB_2. Physical Review B **77**, 174516 (2008), cited on page(s): 84.

[220] J. Spethmann, S. Meyer, K. von Bergmann, R. Wiesendanger, S. Heinze, and A. Kubetzka, *Discovery of Magnetic Single- and Triple-***q** *States in* Mn/Re(0001). Physical Review Letters **124**, 227203 (2020), cited on page(s): 86.

[221] R. L. Conte, M. Bazarnik, K. Palotás, L. Rózsa, L. Szunyogh, A. Kubetzka, K. von Bergmann, and R. Wiesendanger, *Coexistence of Antiferromagnetism and Superconductivity in Mn/Nb(110)*, 2021, cited on page(s): 86, 108.

[222] L. Schneider, P. Beck, L. Rózsa, T. Posske, J. Wiebe, and R. Wiesendanger, *Manuscript in Preparation.* 2022, cited on page(s): 86, 193.

[223] B. Nyári, A. Lászlóffy, L. Szunyogh, G. Csire, K. Park, and B. Ujfalussy, *Relativistic first-principles theory of Yu-Shiba-Rusinov states applied to Mn adatoms and Mn dimers on Nb(110)*. Physical Review B **104**, 235426 (2021), cited on page(s): 86, 189.

[224] H. Schmid, J. F. Steiner, K. J. Franke, and F. von Oppen, *Quantum Yu-Shiba-Rusinov dimers*. Physical Review B **105**, 235406 (2022), cited on page(s): 86.

[225] R. Pawlak, M. Kisiel, J. Klinovaja, T. Meier, S. Kawai, T. Glatzel, D. Loss, and E. Meyer, *Probing atomic structure and Majorana wavefunctions in mono-atomic Fe chains on superconducting Pb surface*. npj Quantum Information **2**, 16035 (2016), cited on page(s): 89, 91.

[226] A. Damascelli, Z. Hussain, and Z.-X. Shen, *Angle-resolved photoemission studies of the cuprate superconductors*. Reviews of Modern Physics **75**, 473–541 (2003), cited on page(s): 89.

[227] L. Kipp, M. Skibowski, R. L. Johnson, R. Berndt, R. Adelung, S. Harm, and R. Seemann, *Sharper images by focusing soft X-rays with photon sieves*. Nature **414**, 184–188 (2001), cited on page(s): 90.

[228] S. Hellmann, T. Ott, L. Kipp, and K. Rossnagel, *Vacuum space-charge effects in nano-ARPES*. Physical Review B **85**, 075109 (2012), cited on page(s): 90.

[229] M. F. Crommie, C. P. Lutz, and D. M. Eigler, *Imaging standing waves in a two-dimensional electron gas*. Nature **363**, 524–527 (1993), cited on page(s): 90.

[230] Y. Hasegawa and P. Avouris, *Direct observation of standing wave formation at surface steps using scanning tunneling spectroscopy*. Physical Review Letters **71**, 1071–1074 (1993), cited on page(s): 90.

[231] C. Wittneven, R. Dombrowski, M. Morgenstern, and R. Wiesendanger, *Scattering States of Ionized Dopants Probed by Low Temperature Scanning Tunneling Spectroscopy*. Physical Review Letters **81**, 5616–5619 (1998), cited on page(s): 90.

[232] J. E. Hoffman, K. McElroy, D.-H. Lee, K. M. Lang, H. Eisaki, S. Uchida, and J. C. Davis, *Imaging Quasiparticle Interference in* $Bi_2Sr_2CaCu_2O_{8+\delta}$. Science **297**, 1148–1151 (2002), cited on page(s): 90.

[233] D. J. Derro, E. W. Hudson, K. M. Lang, S. H. Pan, J. C. Davis, J. T. Markert, and A. L. de Lozanne, *Nanoscale One-Dimensional Scattering Resonances in the CuO Chains of* $YBa_2Cu_3O_{6+x}$. Physical Review Letters **88**, 097002 (2002), cited on page(s): 90.

[234] P. Roushan, J. Seo, C. V. Parker, Y. S. Hor, D. Hsieh, D. Qian, A. Richardella, M. Z. Hasan, R. J. Cava, and A. Yazdani, *Topological surface states protected from backscattering by chiral spin texture*. Nature **460**, 1106–1109 (2009), cited on page(s): 90.

[235] T. Zhang, P. Cheng, X. Chen, J.-F. Jia, X. Ma, K. He, L. Wang, H. Zhang, X. Dai, Z. Fang, X. Xie, and Q.-K. Xue, *Experimental Demonstration of Topological Surface States Protected by Time-Reversal Symmetry*. Physical Review Letters **103**, 266803 (2009), cited on page(s): 90.

[236] H. Beidenkopf, P. Roushan, J. Seo, L. Gorman, I. Drozdov, Y. S. Hor, R. J. Cava, and A. Yazdani, *Spatial fluctuations of helical Dirac fermions on the surface of topological insulators*. Nature Physics **7**, 939–943 (2011), cited on page(s): 90.

[237] B. Jäck, Y. Xie, B. Andrei Bernevig, and A. Yazdani, *Observation of backscattering induced by magnetism in a topological edge state*. Proceedings of the National Academy of Sciences **117**, 16214–16218 (2020), cited on page(s): 90.

[238] E. Liebhaber, L. M. Rütten, G. Reecht, J. F. Steiner, S. Rohlf, K. Rossnagel, F. von Oppen, and K. J. Franke, *Quantum spins and hybridization in artificially-constructed chains of magnetic adatoms on a superconductor*. Nature Communications **13**, 2160 (2022), cited on page(s): 90, 184.

[239] T. D. Stanescu, R. M. Lutchyn, and S. Das Sarma, *Dimensional crossover in spin-orbit-coupled semiconductor nanowires with induced superconducting pairing*. Physical Review B **87**, 094518 (2013), cited on page(s): 90.

[240] E. J. H. Lee, X. Jiang, M. Houzet, R. Aguado, C. M. Lieber, and S. D. Franceschi, *Spin-resolved Andreev levels and parity crossings in hybrid superconductor–semiconductor nanostructures*. Nature Nanotechnology **9**, 79–84 (2014), cited on page(s): 90.

[241] Y. Peng, F. Pientka, L. I. Glazman, and F. von Oppen, *Strong Localization of Majorana End States in Chains of Magnetic Adatoms*. Physical Review Letters **114**, 106801 (2015), cited on page(s): 97, 98, 105.

[242] J. Klinovaja and D. Loss, *Composite Majorana fermion wave functions in nanowires*. Physical Review B **86**, 085408 (2012), cited on page(s): 98, 102.

[243] K. V. Shanavas, Z. S. Popović, and S. Satpathy, *Theoretical model for Rashba spin-orbit interaction in d electrons*. Physical Review B **90**, 165108 (2014), cited on page(s): 98.

[244] D. Crawford, E. Mascot, M. Shimizu, L. Schneider, P. Beck, J. Wiebe, R. Wiesendanger, H. O. Jeschke, D. K. Morr, and S. Rachel, *Majorana modes with side features in magnet-superconductor hybrid systems*. cited on page(s): 99.

[245] Y. Qi, X. Ma, P. Jiang, S. Ji, Y. Fu, J.-F. Jia, Q.-K. Xue, and S. B. Zhang, *Atomic-layer-resolved local work functions of Pb thin films and their dependence on quantum well states*. Applied Physics Letters **90**, 013109 (2007), cited on page(s): 102.

[246] M. H. Upton, C. M. Wei, M. Y. Chou, T. Miller, and T.-C. Chiang, *Thermal Stability and Electronic Structure of Atomically Uniform Pb Films on Si(111)*. Physical Review Letters **93**, 026802 (2004), cited on page(s): 102.

[247] Y. Guo, Y.-F. Zhang, X.-Y. Bao, T.-Z. Han, Z. Tang, L.-X. Zhang, W.-G. Zhu, E. G. Wang, Q. Niu, Z. Q. Qiu, J.-F. Jia, Z.-X. Zhao, and Q.-K. Xue, *Superconductivity Modulated by Quantum Size Effects*. Science **306**, 1915–1917 (2004), cited on page(s): 102.

[248] David Necas and Petr Klapetek, *Gwyddion: an open-source software for SPM data analysis*. Open Physics **10**, 181–188 (2012), cited on page(s): 106.

[249] B. Karmakar, D. Venturelli, L. Chirolli, F. Taddei, V. Giovannetti, R. Fazio, S. Roddaro, G. Biasiol, L. Sorba, V. Pellegrini, and F. Beltram, *Controlled Coupling of Spin-Resolved Quantum Hall Edge States*. Physical Review Letters **107**, 236804 (2011), cited on page(s): 108.

[250] M. Kjaergaard, K. Wölms, and K. Flensberg, *Majorana fermions in superconducting nanowires without spin-orbit coupling*. Physical Review B **85**, 020503 (2012), cited on page(s): 108.

[251] J. Klinovaja and D. Loss, *Giant Spin-Orbit Interaction Due to Rotating Magnetic Fields in Graphene Nanoribbons*. Physical Review X **3**, 011008 (2013), cited on page(s): 108.

[252] M. M. Desjardins, L. C. Contamin, M. R. Delbecq, M. C. Dartiailh, L. E. Bruhat, T. Cubaynes, J. J. Viennot, F. Mallet, S. Rohart, A. Thiaville, A. Cottet, and T. Kontos, *Synthetic spin–orbit interaction for Majorana devices*. Nature Materials **18**, 1060–1064 (2019), cited on page(s): 108.

[253] M. Pratzer, H. J. Elmers, M. Bode, O. Pietzsch, A. Kubetzka, and R. Wiesendanger, *Atomic-Scale Magnetic Domain Walls in Quasi-One-Dimensional Fe Nanostripes*. Physical Review Letters **87**, 127201 (2001), cited on page(s): 108.

[254] J. J. Goedecke, L. Schneider, Y. Ma, K. T. That, D. Wang, J. Wiebe, and R. Wiesendanger, *Correlation of Magnetism and Disordered Shiba Bands in Fe Monolayer Islands on Nb(110)*. arXiv:2204.12391 [cond-mat.supr-con] , (2022), cited on page(s): 108.

[255] M. Menzel, Y. Mokrousov, R. Wieser, J. E. Bickel, E. Vedmedenko, S. Blügel, S. Heinze, K. von Bergmann, A. Kubetzka, and R. Wiesendanger, *Information Transfer by Vector Spin Chirality in Finite Magnetic Chains*. Physical Review Letters **108**, 197204 (2012), cited on page(s): 109.

[256] A. Lászlóffy, L. Rózsa, K. Palotás, L. Udvardi, and L. Szunyogh, *Magnetic structure of monatomic Fe chains on Re(0001): Emergence of chiral multispin interactions*. Physical Review B **99**, 184430 (2019), cited on page(s): 109.

[257] M. M. Bezerra-Neto, Y. O. Kvashnin, A. Bergman, R. B. Muniz, O. Eriksson, M. I. Katsnelson, and A. B. Klautau, *Incommensurate spin and orbital magnetism of Mn atomic chains on W(110) surface*. arXiv:2105.00348 [cond-mat.mtrl-sci] , (2021), cited on page(s): 109.

[258] N. Ashcroft, *Festkörperphysik*, Oldenbourg, R (2012), ISBN: 9783486713015, cited on page(s): 125, 160.

[259] H. B. Michaelson, *The work function of the elements and its periodicity*. Journal of Applied Physics **48**, 4729–4733 (1977), cited on page(s): 125.

[260] M. H. Halloran, J. H. Condon, J. E. Graebner, J. E. Kunzier, and F. S. L. Hsu, *Experimental Study of the Fermi Surfaces of Niobium and Tantalum*. Physical Review B **1**, 366–372 (1970), cited on page(s): 125.

[261] L. F. Mattheiss, *Electronic Structure of Niobium and Tantalum*. Physical Review B **1**, 373–380 (1970), cited on page(s): 125, 140.

[262] H. Wortelen, K. Miyamoto, H. Mirhosseini, T. Okuda, A. Kimura, D. Thonig, J. Henk, and M. Donath, *Spin-orbit influence on d_{z^2}-type surface state at Ta(110)*. Physical Review B **92**, 161408 (2015), cited on page(s): 125.

[263] D. Thonig, T. Rauch, H. Mirhosseini, J. Henk, I. Mertig, H. Wortelen, B. Engelkamp, A. B. Schmidt, and M. Donath, *Existence of topological nontrivial surface states in strained transition metals: W, Ta, Mo, and Nb*. Physical Review B **94**, 155132 (2016), cited on page(s): 125, 140.

[264] R. Linnen, D. L. Trueman, and R. Burt, *Tantalum and niobium*. Critical metals handbook , 361–384 (2014), cited on page(s): 125.

[265] F. Küster, A. M. Montero, F. S. M. Guimarães, S. Brinker, S. Lounis, S. S. P. Parkin, and P. Sessi, *Correlating Josephson supercurrents and Shiba states in quantum spins unconventionally coupled to superconductors*. Nature Communications **12**, 1108 (2021), cited on page(s): 125, 129, 150.

[266] P. Townsend and J. Sutton, *Investigation by Electron Tunneling of the Superconducting Energy Gaps in Nb, Ta, Sn, and Pb*. Physical Review **128**, 591–595 (1962), cited on page(s): 128.

[267] P. Beck, L. Schneider, R. Wiesendanger, and J. Wiebe, *Effect of substrate spin-orbit coupling on the topological gap size of Shiba chains*. arXiv:2205.10062 [cond-mat.supr-con] , (2022), cited on page(s): 128, 130.

[268] L. Schneider, M. Steinbrecher, L. Rózsa, J. Bouaziz, K. Palotás, M. dos Santos Dias, S. Lounis, J. Wiebe, and R. Wiesendanger, *Magnetism and in-gap states of 3d transition metal atoms on superconducting Re*. npj Quantum Materials **4**, 42 (2019), cited on page(s): 129.

[269] H. Huang, R. Drost, J. Senkpiel, C. Padurariu, B. Kubala, A. L. Yeyati, J. C. Cuevas, J. Ankerhold, K. Kern, and C. R. Ast, *Quantum phase transitions and the role of impurity-substrate hybridization in Yu-Shiba-Rusinov states*. Communications Physics **3**, 199 (2020), cited on page(s): 130.

[270] N. Hatter, B. W. Heinrich, M. Ruby, J. I. Pascual, and K. J. Franke, *Magnetic anisotropy in Shiba bound states across a quantum phase transition*. Nature Communications **6**, 8988 (2015), cited on page(s): 130, 184.

[271] L. Cornils, A. Kamlapure, L. Zhou, S. Pradhan, A. A. Khajetoorians, J. Fransson, J. Wiebe, and R. Wiesendanger, *Spin-Resolved Spectroscopy of the Yu-Shiba-Rusinov States of Individual Atoms*. Physical Review Letters **119**, 197002 (2017), cited on page(s): 134, 179.

[272] S. Manna, A. Kamlapure, L. Cornils, T. Hänke, E. M. J. Hedegaard, M. Bremholm, B. B. Iversen, P. Hofmann, J. Wiebe, and R. Wiesendanger, *Interfacial superconductivity in a bi-collinear antiferromagnetically ordered FeTe monolayer on a topological insulator*. Nature Communications **8**, 14074 (2017), cited on page(s): 139.

[273] M. Bode, S. Heinze, A. Kubetzka, O. Pietzsch, X. Nie, G. Bihlmayer, S. Blügel, and R. Wiesendanger, *Magnetization-Direction-Dependent Local Electronic Structure Probed by Scanning Tunneling Spectroscopy*. Physical Review Letters **89**, 237205 (2002), cited on page(s): 144.

[274] P. Beck, L. Schneider, L. Bachmann, J. Wiebe, and R. Wiesendanger, *Structural and superconducting properties of ultrathin Ir films on Nb(110)*. Physical Review Materials **6**, 024801 (2022), cited on page(s): 148.

[275] L. Bachmann, *Growth of Thin Films of Iridium on Nb(110)*, Bachelor's thesis, Universität Hamburg (2020), cited on page(s): 150.

[276] F. Friedrich, R. Boshuis, M. Bode, and A. Odobesko, *Coupling of Yu-Shiba-Rusinov states in one-dimensional chains of Fe atoms on Nb(110)*. Physical Review B **103**, 235437 (2021), cited on page(s): 150.

[277] W. Belzig, C. Bruder, and G. Schön, *Local density of states in a dirty normal metal connected to a superconductor*. Physical Review B **54**, 9443–9448 (1996), cited on page(s): 151.

[278] C. R. Reeg and D. L. Maslov, *Hard gap in a normal layer coupled to a superconductor*. Physical Review B **94**, 020501 (2016), cited on page(s): 151.

[279] T. Tomanic, M. Schackert, W. Wulfhekel, C. Sürgers, and H. V. Löhneysen, *Two-band superconductivity of bulk and surface states in Ag thin films on Nb*. Physical Review B **94**, 220503 (2016), cited on page(s): 151.

[280] K. von Bergmann, S. Heinze, M. Bode, G. Bihlmayer, S. Blügel, and R. Wiesendanger, *Complex magnetism of the Fe monolayer on Ir(111)*. New Journal of Physics **9**, 396–396 (2007), cited on page(s): 151.

[281] S. Heinze, K. von Bergmann, M. Menzel, J. Brede, A. Kubetzka, R. Wiesendanger, G. Bihlmayer, and S. Blügel, *Spontaneous atomic-scale magnetic skyrmion lattice in two dimensions*. Nature Physics **7**, 713–718 (2011), cited on page(s): 151.

[282] N. Romming, C. Hanneken, M. Menzel, J. E. Bickel, B. Wolter, K. von Bergmann, A. Kubetzka, and R. Wiesendanger, *Writing and Deleting Single Magnetic Skyrmions*. Science **341**, 636–639 (2013), cited on page(s): 151.

[283] N. Romming, A. Kubetzka, C. Hanneken, K. von Bergmann, and R. Wiesendanger, *Field-Dependent Size and Shape of Single Magnetic Skyrmions*. Physical Review Letters **114**, 177203 (2015), cited on page(s): 151.

[284] J. Henk, M. Hoesch, J. Osterwalder, A. Ernst, and P. Bruno, *Spin–orbit coupling in the L-gap surface states of Au(111): spin-resolved photoemission experiments and first-principles calculations*. Journal of Physics: Condensed Matter **16**, 7581–7597 (2004), cited on page(s): 152.

[285] G. Bergman, *Influence of Spin-Orbit Coupling on Weak Localization*. Physical Review Letters **48**, 1046–1049 (1982), cited on page(s): 152.

[286] D. Marchenko, A. Varykhalov, M. Scholz, G. Bihlmayer, E. Rashba, A. Rybkin, A. Shikin, and O. Rader, *Giant Rashba splitting in graphene due to hybridization with gold*. Nature Communications **3**, 1232 (2012), cited on page(s): 152.

[287] L. Szunyogh, B. Újfalussy, and P. Weinberger, *Magnetic anisotropy of iron multilayers on Au(001): First-principles calculations in terms of the fully relativistic spin-polarized screened KKR method*. Physical Review B **51**, 9552–9559 (1995), cited on page(s): 152, 189.

[288] M. W. Ruckman and L.-Q. Jiang, *Growth and thermal stability of Ag or Au films on Nb(110)*. Physical Review B **38**, 2959–2966 (1988), cited on page(s): 152, 172.

[289] X. Pan, M. W. Ruckman, and M. Strongin, *Electronic structure and chemical properties of Pt overlayers on Nb(110)*. Physical Review B **35**, 3734–3739 (1987), cited on page(s): 172.

[290] M. Strongin, M. El-Batanouny, and M. A. Pick, *Structure of Pd overlayers on Nb and Ta and the relationship to hydrogen uptake*. Physical Review B **22**, 3126–3129 (1980), cited on page(s): 172.

[291] R. Koch, M. Borbonus, O. Haase, and K. H. Rieder, *New aspects on the Ir(110) reconstruction: Surface stabilization on mesoscopic scale via (331) facets*. Physical Review Letters **67**, 3416–3419 (1991), cited on page(s): 172.

[292] J. Kuntze, S. Speller, and W. Heiland, *The Ir(110) surface studied by STM*. Surface Science **402-404**, 764–769 (1998), cited on page(s): 172.

[293] E. Simon, K. Palotás, B. Ujfalussy, A. Deák, G. M. Stocks, and L. Szunyogh, *Spin-correlations and magnetic structure in an Fe monolayer on 5d transition metal surfaces*. Journal of Physics Condensed Matter **26**, 186001 (2014), cited on page(s): 189.

[294] A. Belabbes, G. Bihlmayer, F. Bechstedt, S. Blügel, and A. Manchon, *Hund's Rule-Driven Dzyaloshinskii-Moriya Interaction at* $3d-5d$ *Interfaces*. Physical Review Letters **117**, 247202 (2016), cited on page(s): 189.

[295] E. Simon, L. Rózsa, K. Palotás, and L. Szunyogh, *Magnetism of a Co monolayer on Pt(111) capped by overlayers of* 5*d elements: A spin-model study*. Physical Review B **97**, 134405 (2018), cited on page(s): 189.

[296] C. Etz, J. Zabloudil, P. Weinberger, and E. Y. Vedmedenko, *Magnetic properties of single atoms of Fe and Co on Ir(111) and Pt(111)*. Physical Review B **77**, 184425 (2008), cited on page(s): 189.

[297] S. Bornemann, O. Šipr, S. Mankovsky, S. Polesya, J. B. Staunton, W. Wurth, H. Ebert, and J. Minár, *Trends in the magnetic properties of Fe, Co, and Ni clusters and monolayers on Ir(111), Pt(111), and Au(111)*. Physical Review B **86**, 104436 (2012), cited on page(s): 189.

[298] M. W. Prestel, M. Strohmeier, W. Belzig, and E. Scheer, *Revealing channel polarization of atomic contacts of ferromagnets and strong paramagnets by shot-noise measurements*. Physical Review B **104**, 115434 (2021), cited on page(s): 189.

[299] C. Chappert, A. Fert, and F. N. Van Dau, *The emergence of spin electronics in data storage*. Nature Materials **6**, 813–823 (2007), cited on page(s): 192.

[300] S. Bader and S. Parkin, *Spintronics*. Annual Review of Condensed Matter Physics **1**, 71–88 (2010), cited on page(s): 192.

[301] Y. Chen, Y. Bae, and A. J. Heinrich, *Harnessing the Quantum Behavior of Spins on Surfaces*. Advanced Materials , 2107534 (2022), cited on page(s): 192.

[302] P. Gambardella, A. Dallmeyer, K. Maiti, M. C. Malagoli, W. Eberhardt, K. Kern, and C. Carbone, *Ferromagnetism in one-dimensional monatomic metal chains*. Nature **416**, 301–304 (2002), cited on page(s): 192.

[303] S. Krause, G. Herzog, T. Stapelfeldt, L. Berbil-Bautista, M. Bode, E. Y. Vedmedenko, and R. Wiesendanger, *Magnetization Reversal of Nanoscale Islands: How Size and Shape Affect the Arrhenius Prefactor*. Physical Review Letters **103**, 127202 (2009), cited on page(s): 192.

[304] S. Krause, G. Herzog, A. Schlenhoff, A. Sonntag, and R. Wiesendanger, *Joule Heating and Spin-Transfer Torque Investigated on the Atomic Scale Using a Spin-Polarized Scanning Tunneling Microscope*. Physical Review Letters **107**, 186601 (2011), cited on page(s): 192.

[305] G. Herzog, S. Krause, and R. Wiesendanger, *Heat assisted spin torque switching of quasistable nanomagnets across a vacuum gap*. Applied Physics Letters **96**, 102505 (2010), cited on page(s): 192.

[306] A. A. Khajetoorians, B. Baxevanis, C. Hübner, T. Schlenk, S. Krause, T. O. Wehling, S. Lounis, A. Lichtenstein, D. Pfannkuche, J. Wiebe, and R. Wiesendanger, *Current-Driven Spin Dynamics of Artificially Constructed Quantum Magnets*. Science **339**, 55–59 (2013), cited on page(s): 192, 193.

[307] J. Hermenau, J. Ibañez-Azpiroz, C. Hübner, A. Sonntag, B. Baxevanis, K. T. Ton, M. Steinbrecher, A. A. Khajetoorians, M. dos Santos Dias, S. Blügel, R. Wiesendanger, S. Lounis, and J. Wiebe, *A gateway towards non-collinear spin processing using three-atom magnets with strong substrate coupling*. Nature Communications **8**, 642 (2017), cited on page(s): 192, 193, 202.

[308] S. Krause, A. Sonntag, J. Hermenau, J. Friedlein, and R. Wiesendanger, *High-frequency magnetization dynamics of individual atomic-scale magnets*. Physical Review B **93**, 064407 (2016), cited on page(s): 192.

[309] S. Müllegger, S. Tebi, A. K. Das, W. Schöfberger, F. Faschinger, and R. Koch, *Radio frequency scanning tunneling spectroscopy for single-molecule spin resonance*. Physical Review Letters **113**, (2014), cited on page(s): 193.

[310] S. Baumann, W. Paul, T. Choi, C. P. Lutz, A. Ardavan, and A. J. Heinrich, *Electron paramagnetic resonance of individual atoms on a surface*. Science **350**, 417–420 (2015), cited on page(s): 193.

[311] P. Willke, W. Paul, F. D. Natterer, K. Yang, Y. Bae, T. Choi, J. Fernández-Rossier, A. J. Heinrich, and C. P. Lutz, *Probing quantum coherence in single-atom electron spin resonance*. Science Advances **4**, eaaq1543 (2018), cited on page(s): 193.

[312] K. Yang, W. Paul, S.-H. Phark, P. Willke, Y. Bae, T. Choi, T. Esat, A. Ardavan, A. J. Heinrich, and C. P. Lutz, *Coherent spin manipulation of individual atoms on a surface*. Science **366**, 509–512 (2019), cited on page(s): 193.

[313] M. Steinbrecher, W. M. J. van Weerdenburg, E. F. Walraven, N. P. E. van Mullekom, J. W. Gerritsen, F. D. Natterer, D. I. Badrtdinov, A. N. Rudenko, V. V. Mazurenko, M. I. Katsnelson, A. van der Avoird, G. C. Groenenboom, and A. A. Khajetoorians, *Quantifying the interplay between fine structure and geometry of an individual molecule on a surface*. Physical Review B **103**, 155405 (2021), cited on page(s): 193.

[314] L. M. Veldman, L. Farinacci, R. Rejali, R. Broekhoven, J. Gobeil, D. Coffey, M. Ternes, and A. F. Otte, *Free coherent evolution of a coupled atomic spin system initialized by electron scattering*. Science **372**, 964–968 (2021), cited on page(s): 193.

[315] X. Zhang, C. Wolf, Y. Wang, H. Aubin, T. Bilgeri, P. Willke, A. J. Heinrich, and T. Choi, *Electron spin resonance of single iron phthalocyanine molecules and role of their non-localized spins in magnetic interactions*. Nature Chemistry **14**, 59–65 (2022), cited on page(s): 193.

[316] C. F. Hirjibehedin, C.-Y. Lin, A. F. Otte, M. Ternes, C. P. Lutz, B. A. Jones, and A. J. Heinrich, *Large Magnetic Anisotropy of a Single Atomic Spin Embedded in a Surface Molecular Network*. Science **317**, 1199–1203 (2007), cited on page(s): 193.

[317] A. J. Heinrich, J. A. Gupta, C. P. Lutz, and D. M. Eigler, *Single-Atom Spin-Flip Spectroscopy*. Science **306**, 466–469 (2004), cited on page(s): 193.

[318] B. W. Heinrich, L. Braun, J. I. Pascual, and K. J. Franke, *Protection of excited spin states by a superconducting energy gap*. Nature Physics **9**, 765–768 (2013), cited on page(s): 193, 210.

[319] K. Vaxevani, J. Li, S. Trivini, J. Ortuzar, D. Longo, D. Wang, and J. I. Pascual, *Extending the spin excitation lifetime of a magnetic molecule on a proximitized superconductor*. arXiv:2203.05613 [cond-mat.mes-hall] , (2022), cited on page(s): 193, 210.

[320] S. M. F. Shahed, F. Ara, M. I. Hossain, K. Katoh, M. Yamashita, and T. Komeda, *Observation of Yu–Shiba–Rusinov States and Inelastic Tunneling Spectroscopy for Intramolecule Magnetic Exchange Interaction Energy of Terbium Phthalocyanine (TbPc) Species Adsorbed on Superconductor $NbSe_2$*. ACS Nano **16**, 7651–7661 (2022), cited on page(s): 193.

[321] J. Eisenstein, *Superconducting Elements*. Reviews of Modern Physics **26**, 277–291 (1954), cited on page(s): 193, 200.

[322] A. A. Khajetoorians, B. Baxevanis, C. Hübner, T. Schlenk, S. Krause, T. O. Wehling, S. Lounis, A. Lichtenstein, D. Pfannkuche, J. Wiebe, and R. Wiesendanger, *Current-Driven Spin Dynamics of Artificially Constructed Quantum Magnets*. Science **339**, 55–59 (2013), cited on page(s): 202.

Publications

[1] X. Huang, R. Xiong, K. Volckaert, C. Hao, D. Biswas, M. Bianchi, P. Hofmann, P. Beck, J. Warmuth, B. Sa, J. Wiebe, and R. Wiesendanger, *Epitaxial growth of a two-dimensional topological insulator candidate: monolayer Si_2Te_2*. arXiv:2206.00919 [cond-mat.mtrl-sci] , (2022).

[2] P. Beck, L. Schneider, R. Wiesendanger, and J. Wiebe, *Effect of substrate spin-orbit coupling on the topological gap size of Shiba chains*. arXiv:2205.10062 [cond-mat.supr-con] , (2022).

[3] P. Beck, L. Schneider, R. Wiesendanger, and J. Wiebe, *Systematic study of Mn atoms, artificial dimers and chains on superconducting Ta(110)*. arXiv:2205.10073 [cond-mat.supr-con] , (2022).

[4] P. Beck, L. Schneider, L. Bachmann, J. Wiebe, and R. Wiesendanger, *Structural and superconducting properties of ultrathin Ir films on Nb(110)*. Phys. Rev. Materials **6**, 024801 (2022).

[5] L. Schneider, P. Beck, J. Neuhaus-Steinmetz, L. Rózsa, T. Posske, J. Wiebe, and R. Wiesendanger, *Precursors of Majorana modes and their length-dependent energy oscillations probed at both ends of atomic Shiba chains*. Nature Nanotechnology **17**, 384–389 (2022).

[6] D. Crawford, E. Mascot, M. Shimizu, L. Schneider, P. Beck, J. Wiebe, R. Wiesendanger, H. O. Jeschke, D. K. Morr, and S. Rachel, *Majorana modes with side features in magnet-superconductor hybrid systems*. arXiv:2109.06894 [cond-mat.supr-con] , (2021).

[7] P. Beck, L. Schneider, L. Rózsa, K. Palotás, A. Lászlóffy, L. Szunyogh, J. Wiebe, and R. Wiesendanger, *Spin-orbit coupling induced splitting of Yu-Shiba-Rusinov states in antiferromagnetic dimers*. Nature Communications **12**, 2040 (2021).

[8] L. Schneider, P. Beck, T. Posske, D. Crawford, E. Mascot, S. Rachel, R. Wiesendanger, and J. Wiebe, *Topological Shiba bands in artificial spin chains on superconductors*. Nature Physics **17**, 943–948 (2021).

[9] L. Schneider, P. Beck, J. Wiebe, and R. Wiesendanger, *Atomic-scale spin-polarization maps using functionalized superconducting probes*. Science Advances **7**, eabd7302 (2021).

[10] M. M. Ramin Moayed, S. Kull, A. Rieckmann, P. Beck, M. Wagstaffe, H. Noei, A. Kornowski, A. B. Hungria, R. Lesyuk, A. Stierle, and C. Klinke, *Function Follows Form: From Semiconducting to Metallic toward Superconducting PbS Nanowires by Faceting the Crystal*. Advanced Functional Materials **30**, 1910503 (2020).

[11] M. M. Ramin Moayed, F. Li, P. Beck, J.-C. Schober, and C. Klinke, *Anisotropic circular photogalvanic effect in colloidal tin sulfide nanosheets*. Nanoscale **12**, 6256–6262 (2020).

Contributed Talks

[1] P. Beck, L. Schneider, L. Rózsa, K. Palotás, A. Lászlóffy, L. Szunyogh, J. Wiebe, and R. Wiesendanger, *Scanning tunneling spectroscopy of atom-by-atom assembled magnetic nanostructures on Au/Nb (110)*, International Conference on Nanoscience + Technology 2021, Vancouver, Canada (2021).

[2] P. Beck, L. Schneider, L. Rózsa, J. Wiebe, and R. Wiesendanger, *Momentum-resolved Shiba bands in artificial spin chains coupled to a superconductor: From single atoms to chains*, SFB925 Annual Meeting, Hamburg, Germany (2020).

Contributed Posters

[1] P. Beck, L. Schneider, B. Nyári, L. Rózsa, A. Lászlóffy, K. Palotás, L. Szunyogh, B. Ujfalussy, J. Wiebe, and R. Wiesendanger, *Tuning the spin-orbit coupling in 1D magnetic structures on superconducting surfaces*, 769. WE-Heraeus-Seminar, Novel Quantum Phases in Superconducting Heterostructures, Bad Honnef, Germany (2022).

[2] K. That Ton, P. Beck, P. Lindner, S. Krause, and R. Wiesendanger, *Controlled dynamics in crafted spin arrays coupled to itinerant electron baths*, SFB925 Annual Meeting, Hohwacht, Germany (2021).

[3] P. Beck, J. Wiebe, S. Krause, and R. Wiesendanger, *Controlled dynamics in crafted spin arrays coupled to itinerant electron baths*, SFB925 Annual Meeting, Hohwacht, Germany (2019).

Danksagung

Obwohl eine Promotionszeit von drei Jahren vermutlich als schnell und unkompliziert abgetan werden kann, liegt es wahrscheinlich in der Natur des Unterfangens *Promotion*, dass man Höhen und Tiefen durchläuft. In meinem Fall waren Letztere vor allem durch die globale Pandemie, die Einstellung des experimentellen Betriebes und die damit einhergehenden Defekte in unseren Aufbauten bedingt. Zu den schönen Momenten und den Erfolgen hingegen haben wesentlich meine Mitmenschen beigetragen. Daher möchte ich dieses Kapitel den Personen widmen, die mich auf dem Weg zur Fertigstellung meiner Dissertation unterstützt haben.
Zunächst danke ich Herrn Prof. Dr. Roland Wiesendanger für die große Chance, in seiner exzellenten Forschungsgruppe zu promovieren. Insbesondere möchte ich hervorheben, dass Herr Prof. Dr. Wiesendanger und seine großartige Organisation der Forschungsgruppe uns Nachwuchswissenschaftlern stets ermöglicht haben, die Wissenschaft in den Vordergrund zu stellen. Dabei waren die vielen fachlichen Diskussionen in den Projektmeetings von hohem Wert für die Interpretation und die sachgerechte Darstellung unserer Ergebnisse.
Im Anschluss möchte ich Herrn PD Dr. Jens Wiebe zutiefst für seine Betreuung während meiner Promotionszeit danken. Sein fachliches Allwissen und seine beruhigende Art, komplizierte und verzwickte Situationen sowie technische Probleme zu lösen, und dabei auch in brenzligen Situationen kühlen Kopf und Zuversicht zu wahren, werde ich in Zukunft sehr vermissen. Nur durch die hervorragende Betreuung und das umfangreiche Korrigieren von Manuskripten durch Herrn PD Dr. Jens Wiebe war der Erfolg meiner Promotionszeit in dieser Form möglich.
Zudem möchte ich Herrn Dr. Lucas Schneider für die ausgiebige und lehrhafte Zusammenarbeit in Lab006 danken. Neben seiner großartigen Einweisung in die Methoden der Tieftemperaturrastertunnelmikroskopie

möchte ich besonders das beeindruckende physikalische Verständnis von Herrn Dr. Schneider hervorheben. Ohne die aufschlussreichen Modellrechnungen, die Herr Dr. Schneider angestellt hat – man bemerke, dass dies neben dem experimentellen Betrieb geschah – würden einige Daten uns wohl heute noch Kopfzerbrechen bereiten. Ich wünsche Herrn Dr. Schneider das Beste für seine akademische Laufbahn und bin überzeugt, dass er es weit bringen wird!
Ebenso möchte ich Herrn Dr. Xiaochun Huang dafür danken, dass er meinen fachlichen Horizont in den Bereichen MBE und 2D-Materialien erweitert hat — von meinem kulinarischen Wissen ganz zu schweigen.
Außerdem möchte ich meinen Kollaboratoren für die gute Zusammenarbeit danken. Ich danke Herrn Dr. Maciej Bazarnik und Herrn Dr. Roberto Lo Conte für die kurze Zusammenarbeit in Lab006 und den Theoriekollegen Herrn Dr. Levente Rózsa, Herrn Bendegúz Nyári, Herrn Dr. András Lászlóffy, Herrn Dr. Krisztián Palotás, Herrn Prof. Dr. László Szunyogh und Herrn Prof. Dr. Balázs Ujfalussy aus Budapest.
Zuletzt möchte ich meinen Freunden und meiner Familie danken, die mich in allen Lagen und Situationen ertragen und unterstützt haben.

Eidesstattliche Versicherung

Hiermit erkläre ich an Eides statt, dass ich die vorliegende Dissertationsschrift selbst verfasst und keine anderen als die angegebenen Quellen und Hilfsmittel benutzt habe.

Hamburg, den 02.08.2022

Philip Beck